TECHNIQUES FOR CHARACTERISATION AND APPLICATIONS OF LONG-LIFETIME LUMINESCENCE IN THE MICROSECOND REGION

By

Lixin Zhang

Department of Physics and Astronomy

Supervisors:

A/Prof. Dayong Jin,

A/Prof. Judith M. Dawes,

Prof. James A. Piper,

Prof. Ewa Goldys,

Dr. Aaron McKay

MACQUARIE University
SYDNEY·AUSTRALIA

FACULTY OF SCIENCE AND ENGINEERING

This thesis is presented for the degree of Doctor of Philosophy

March 2015

I certify that the work in this thesis has not previously been submitted for a degree nor has it been submitted as part of requirements for a degree to any other university or institution other than Macquarie University.

I also certify that the thesis is an original piece of research and it has been written by me. Any help and assistance that I have received in my research work and the preparation of the thesis itself have been appropriately acknowledged.

In addition, I certify that all information sources and literature used are indicated in the thesis.

Lixin Zhang 2-Mar-2015

Acknowledgements

Firstly, I would like to express my special appreciation and thanks to my principle supervisor A/Prof. Dayong Jin. He has been a tremendous mentor for me. I appreciate he provided me the opportunity to pursue my PhD degree in Macquarie University. I would like to thank him for providing me the valuable training on research and logical thinking, and priceless advice on my career development. His constructive suggestions and insightful feedbacks greatly speed up the progress of my PhD projects. His strong self-motivation, strategic planning, persistence on the dream and optimistic attitude in life always encourage me. Without his consistent guidance and inspiration, I cannot build such a solid track record with publications in top journals.

I would also like to thank my other supervisors: A/Prof Judith Dawes, Prof Jim Piper, Prof Ewa Goldys and Dr Aaron McKay. A/Prof Dawes, Prof Jim Piper and Dr Aaron provided their professional advice on my PhD project and give me thoughtful suggestion on my thesis draft. Prof Ewa Goldys spent time guiding me on the theoretical modelling involved in my projects. I really appreciate their efforts.

Apart from my supervisors, I would like to show my appreciations to my collaborators who contribute significantly to my PhD projects. Dr. Yiqing Lu helped me a lot during these years. He provided his big support and patient guidance for solving the troubles I met during the experiments; he offered his constructive suggestion on the analysis of experimental data and paper draft; and he also spent a lot of time in structuring and polishing my thesis. Besides, I also show my appreciations to my collaborators from other universities: Prof Xiaogang Liu and Mr Yuhai Zhang from National University of Singapore provided their colour-barcoded upconversion micro-rods; Prof Verelst and Dr Lechevallier from Paul Sabatier University, France provided their lanthanide doped nanoparticles. Prof. Jingli Yuan and A/Prof Zhiqiang Ye from Dalian University of Technology guided me to prepare the lanthanide chelate labelled bio-samples; I also show my thanks to Prof Tanya Monro and Dr Eric Schartner, who provided their microstructure optical fibres (MOF) and gave me training on the application of the MOF fibres in optical microscope system. I am also very grateful for

the help and support from Prof Peng Xi group from Peking University, and Prof Joerg Enderlein group from Gottingen University, Germany.

I also show my appreciations to my colleagues Dr Xavier Vidal Asensio, Mr Yujia Liu and Mr Xianlin Zheng, who provided their suggestion and help on my projects. I had thoroughly enjoyable experience with Dr Jiangbo Zhao, Dr Jie Lu, Dr Wei Deng, Dr Run Zhang and Mr Deming Liu, and other group members in Advanced Cytometry Labs@MQ. I am impressed and enhanced by their diverse skill sets and self-discipline minds. I will cherish the interactions with all of them.

I also received a lot of support from the people in MQ Biofocus Research Centre, including Prof. Andrei Zvyagin, Dr. Krystyna Drozdowicz-Tomsia, Dr. David Inglis, and Dr. Ayad Anwer; and the people from Macquarie OptoFab Node, Australian National Fabrication Facility, including Dr Benjamin Johnston. Thanks for their valuable suggestions for my work, which is beneficial for my research progress.

I present the special acknowledgements to my parents, sister and brother. Your love, understanding and support helped me overcome the hard time. I am also extremely gratitude for the encouragement from Lisa Li, who always delivers her positive and optimistic attitude to me, guiding me to be the person with “positive energy”!

Finally, I must acknowledge the International Macquarie Research Scholarship scheme of Macquarie University for the finance supports of my PhD study; I must acknowledge the generous HDR budget funding support from Department of Physics and Astronomy throughout my PhD projects; I must acknowledge the PGRF funding scheme of Macquarie University to support the conference travel and thus I had an opportunity to present my research to peers at international conferences.

List of Publications

[1]. **Lixin Zhang**, Aaron McKay, Dayong Jin. "High-throughput 3-Dimentional Time-resolved Spectroscopy: Simultaneous Characterisation of Luminescence Properties in Spectral and Temporal Domains", ***RSC Advances***, 3, 8670-8673, 2013**.**

[2]. Zhao J, Jin D, Schartner E, Lu Y, Liu Y, **Zhang L**, Zvyagin A, Dawes J, Xi P, Piper J, Goldys E, Monro T, "Single nanocrystal sensitivity achieved by enhanced upconversion luminescence", ***Nature Nanotechnology,*** 8, 729-734, 2013.171, 2013.

[3]. **Lixin Zhang**, Xianlin Zheng, Wei Deng, Yiqing, Lu, et al. "Practical Implementation, Characterization and Applications of a Multi-Colour Time-Gated Luminescence Microscope", ***Scientific Reports,*** 4: 6597, 2014.

[4]. Yuhai Zhang, **Lixin Zhang**, Renren Deng, Jing Tian, Yun Zong, Dayong Jin and Xiaogang Liu. "Multicolor Barcoding in a Single Upconversion Crystal", ***J. Am. Chem. Soc***., 136 (13), 4893–4896, 2014.

([1] - [4] are closely related to my PhD program)

[5]. Degui Kong, Qing Chang, Yachen Gao, Hong'an Ye, **Lixin Zhang**, et al. "Nonlinear absorption of CS2 at the wavelength of 400 nm with femtosecond pulses" ***Physica B: Condensed Matter***, 2012, 407(8),1279–1281.

([5] is from other project during my PhD candidature)

Abstract

High-resolution characterisation of lanthanide-based luminescence complexes and nanomaterials provides in-depth insights to understand the details of energy-transfer process and photon luminescence mechanisms, guiding new designs for probes and methods for advanced sensing applications. Comparing many recent developments of lanthanide luminescent materials, current spectrometer-based instruments are insufficient in characterising the optical properties of nanoscale and micro-scale luminescence samples. This PhD program of optoelectronics engineering explores time-resolved approaches through demonstrations of two purpose-built devices for comprehensive characterisation and advanced applications of long-lived luminescent materials.

The first part of this thesis describes a design of a multi-colour time-gated luminescence (TGL) microscope. Implementing a high-speed Xenon flash lamp and synchronised time-gated detection unit, we suggest a practical approach to upgrade a commercial microscope for low-background time-gated luminescence imaging at low cost, with high stability and simplicity. We applied this system for simultaneous inspection of pathogenic micro-organisms and evaluated its detection sensitivity by imaging single luminescent nanoparticles.

The second part of this thesis presents an imaging-spectroscopy platform for high-resolution simultaneous characterisation of lifetimes and spectra of long-lived luminescence materials. Incorporating a multi-channel photomultiplier tube as a linear array detector behind a spectrometer, we realised a three-dimensional time-resolved spectrometer; coupling the 3-D spectrometer to a purpose-built laser scanning confocal microscope; we demonstrated a microscope-based device for characterisation of nanoscale and micro-scale luminescent samples.

The third part of this thesis showcases new functionalities of the imaging-spectroscopy system by nanophotonic characterisation of the new generation of colour-coded upconversion micro-rods and single upconversion nanoparticles.

In addition to the main result chapters, I have obtained some preliminary results on the exploration of the relationship between the excitation power and luminescence lifetime using our time-resolved spectroscopy system. Moreover, I have also succeeded in demonstrating two other optical characterisation systems for measurement of luminescence quantum yield of upconversion activators, and characterisation of upconversion polarisation properties. These results are also included in this thesis as three appendices.

The advances brought to the characterisation systems in this thesis provide a set of new tools for exploring the rich optical properties of long-lived luminescence materials at the nanoscale and promoting novel luminescence materials for ultrasensitive and rapid sensing applications.

The three key result chapters of this thesis are presented by publication of four peer-reviewed journal papers. The introduction chapter is presented as a manuscript of a review article and the conclusion chapter is followed by three appendices containing the results of my work in parallel during the last three and half years of PhD research.

Key words: nanophotonics; fluorescence microscope; long-lived luminescence; lanthanide; nanoparticles; time-gated luminescence microscope; time-resolved; high throughput; high resolution

Contents

List of Acronyms (in Alphabetic Order)

AOM	Acoustic optical modulator
APS	3-amimopropyl (triethoxy) slilane
APD	Avalanched Photodiode
ARC	Arginine-rich peptide
BHHCT	4,4'-bis(1",1",1",2",2",3",3"-heptafluoro-4",6"-hexanedion-6"-yl)-chlorosulfo-*o*-terphenyl
BHHBCB	1, 2-bis [4'-(1 ", 1 ", 1 ", 2 ", 2 ", 3 ", 3 "-heptafluoro-4 ", 6 "-hexanedion-6 "-yl)-benzyl]-4-chlorosulfobenzene
BPTA	N, N, N1, N1-[2, 6-bis (3'-aminomethyl-1'-pyrzaolyl)-4-phenylpyridine] tetrakis
BSA	Bovine serum albumin
CMOS	Complementary metal-oxide-semiconductor
CW	Continuous wave
DELFIA	Dissociation enhanced lanthanide fluoroimmunoassay
DNA	Deoxyribonucleic acid
EMCCD	Electron multiplying charge coupled device
FD	Frequency-domain
FLIM	Fluorescence-lifetime imaging microscopy
FOV	Field of view
GALD	Gated auto-synchronous luminescence detection
ICCD	Intensified Charge Coupled Device
LD	Laser diode
LIM	Lifetime imaging microscopy

Ln	Lanthanide
LRET	Luminescence resonance energy transfer
MCP	Microchannel photomultiplier
MLC	Metallic ligand complexes
MOF	Metal-organic frameworks
NIR	Near infrared
NPTTA	[4′-(2, 4-dinitrophenyloxy)-2, 2′:6′, 2″-terpyridine-6, 6″-diyl]bis(methylenenitrilo) tetrakis(acetate)
OSAM	Orthogonal Scanning Automated Microscopy
PMT	Photomultiplier tube
PSLIM	Pinhole shifting lifetime imaging microscopy
QY	Quantum yield
RLD	Rapid lifetime determination
SNR	Signal-to-noise ratio
Ru-DCBPY	Ruthenium (II) tris (5, 5′-dicarboxy-2, 2′-bipyridine)
SPAD	Single-photon avalanche diode
SRL	Spatially resolved luminescence
TCSPC	Time-correlated single photon counting
TGL	Time-gated luminescence
TP-TREM	Two-photon time-resolved emission imaging microscopy
TRACE	Time-resolved amplified cryptate emission
TRL	Time-resolved luminescence
TRF	Time-resolved fluorescence
TR-FIA	Time-resolved fluoroimmunoassay
TR-OSAM	Time-resolved orthogonal scanning automated microscopy

TSLIM	Temporal sampling lifetime imaging microscope
UCNP	Upconversion nanoparticles
UV	Ultraviolet

Thesis Outline

Lanthanide-based luminescent materials have emerged as novel functional materials with unique optical properties, including a large Stokes shift (> 100 nm), long luminescence lifetimes in the microsecond to millisecond range, and multi-band sharp spectral emissions, suitable for a range of sensing applications. Major advances have been made in chemical synthesis, and both high-performance molecular probes and versatile nanoparticles have been demonstrated for the last decade. In addition, the unique excitation and emission spectra also require special consideration in designing characterisation schemes and implementing their applications through the use of advanced optical instruments that are not yet developed.

This engineering-based PhD program therefore has been motivated by these urgent needs, and I have succeeded in demonstrating several advanced optical instruments and photonics techniques for characterisation and applications of lanthanide-based luminescent materials. Since the nature of developing each type of instrumentation requires a long cycle of experiments, my PhD program for the last three and half years has been designed and carried out following a parallel structure with three major optical techniques developed (chapters 2 to 5). With these purpose-built devices, we have demonstrated rapid and high-resolution characterisation of a range of emerging luminescent materials towards the applications in sensing and analytical biotechnology. This thesis is presented in the form of five journal manuscripts/publications as steps in my PhD research journey.

Chapter 2 was presented as a published first-authored paper (*Scientific reports* 2014) for practical implementation, characterisation and applications of a multi-colour time-gated luminescent microscope. The previously reported time-gated luminescence microscopes require sophisticated engineering and costly components, and are only available in a few research labs. Most of them only image one colour at a time in the monochromatic mode, significantly affecting the detection throughput when multiple types of biological targets exist in a complex sample. These issues hinder the broad implementation of the time-gated imaging technique. This work reports a new engineering scheme of pulsed excitation and synchronised time-delayed detection

through demonstrating an excitation unit and a time-gated luminescence detection unit. This allows commercial fluorescence microscopes to achieve low-background multi-colour imaging at low cost, with high stability and simplicity. We realised the simultaneous dual-colour visualisation of two species of microorganisms, stained with a red-emitting europium-based probe and a green-emitting terbium-based probe respectively. We have further demonstrated a high detection sensitivity by imaging single europium-doped nanocrystals with size of around 150 nm.

Chapter 3 is another published first-authored paper (*RSC Advances* 2013) reporting a time-resolved spectroscopy system capable of high-speed acquisition of the high-resolution time-resolved spectra from the lanthanide-doped luminescence materials. The emphasis of this chapter is on upconversion materials because the conventional lanthanide-based down-conversion probes require ultraviolet (UV) excitation, which is not biologically compatible with photo-bleaching issues and detrimental damage on the bio-samples. The new generation of upconversion nanocrystals has emerged during my PhD period, but there is a lack of robust instruments for advanced characterisation to understand their complicated upconversion process within a single nanocrystal. This work incorporates an integrated multi-channel photon-sensing device, a 32 channel PMT as a linear array detector behind a spectrometer, to replace the single-channel avalanched photodiode (APD) in our home-built laser scanning confocal system. To demonstrate the powerful utility of the system, some mono-dispersed hexagonal-phase NaYF4: Yb20%, Er2% upconversion nanocrystals with 40 nm size were tested. It took less than 1 min for the system to complete 50 acquisitions and construct the time-resolved spectra with high spectral and temporal resolution. To the best of our knowledge, this is the first quantitative measurement showing the 3-D time-resolved emission spectra of upconversion nanocrystals.

Chapter 4 combines more characterisation results that I contributed to another two published papers as the co-authors. I have successfully demonstrated nanoscale time-resolved characterisation of multi-colour barcoded upconversion micro-rods (*Journal of America Chemistry Society* 2014) and wide-field imaging of single upconversion nanoparticles (*Nature Nanotechnology* 2013). Through the JACS project, I have developed a collaboration with a well-known research group in synthesising upconversion nanomaterials and carried out comprehensive optical characterisations of

the single colour-banded micro-rods. My data indicated that no energy transfer was observed between the neighbouring sections of rods doped by different lanthanide activators (Tm^{3+} and Er^{3+} ions). I have demonstrated the multi-modalities of my system suitable for self-correlated imaging and analysis: the wide field microscope is useful in rapidly finding the points of interest; the laser scanning confocal microscope provides high resolution scanning of a detailed area (junction) of a single micro-rod, followed by lifetime measurements to provide the luminescence decay properties with high spatial resolution. In the *Nature Nanotechnology* project, I used my system to obtain the evidence that the brightness of highly-doped upconversion crystals is power dependent. This supports our core discovery in this paper that a high excitation irradiance can alleviate concentration quenching in upconversion luminescence when combined with higher activator concentration. I have also used my system and demonstrated the highly doped single nanocrystals were directly imaged through the wide field microscope.

Chapter 5 summarises the key research outcomes and outputs of this thesis, and discusses the future prospects for developing advanced optical systems to explore the mechanisms and applications of the long-lifetime luminescence materials, including the effect of excitation power on the emission lifetime (Appendix I), quantum yield measurement for the doped activators in upconversion nanocrystals (Appendix II), and the emission polarisation measurement for upconversion micro-rods (Appendix II).

Flow chart for the thesis outline:

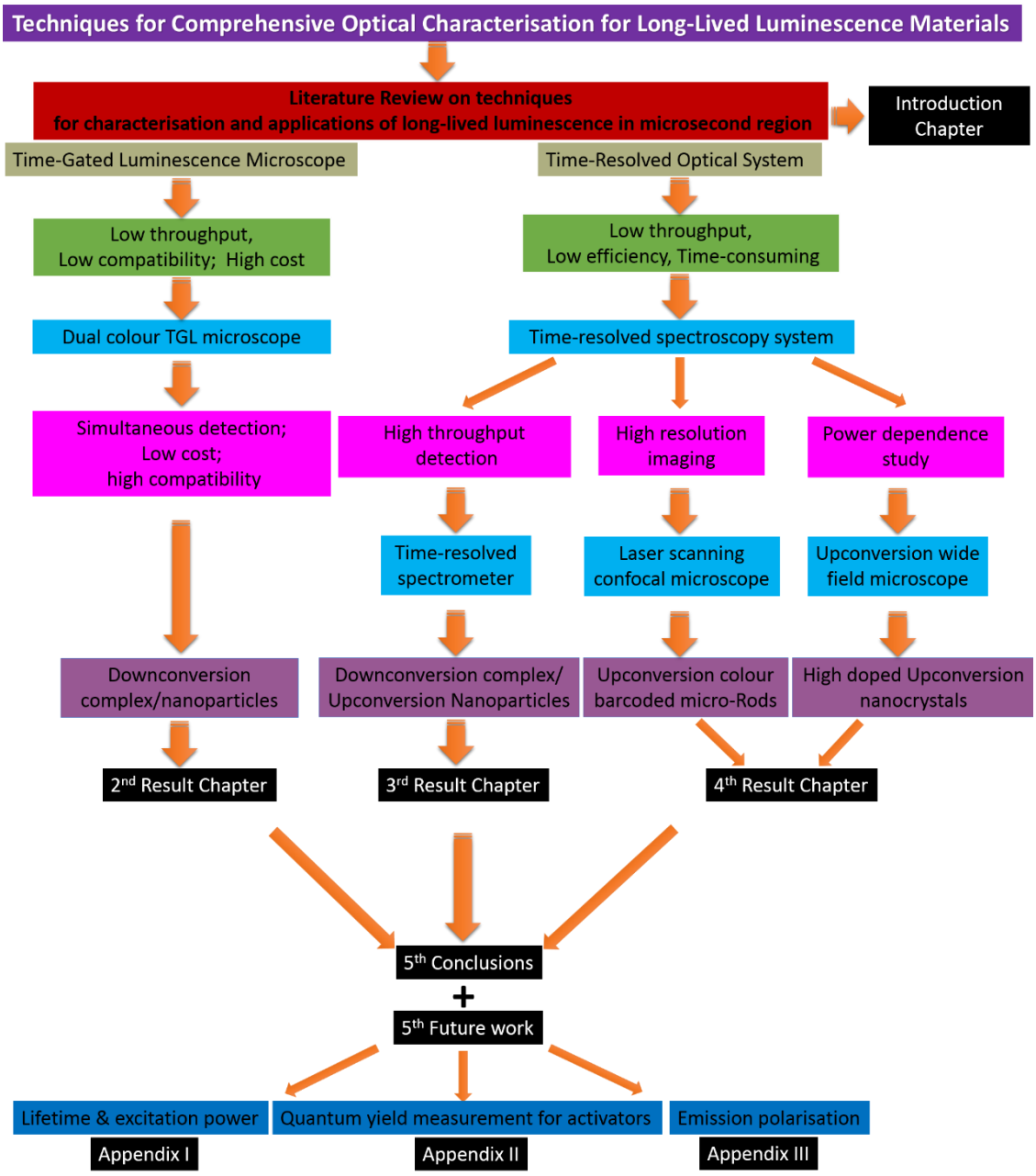

Chapter 1: Introduction and Literature Review

Time-resolved luminescence technique in the microsecond regime was first introduced to the field of analytical science more than 30 years ago[1, 2], and has been extensively applied for highly sensitive luminescence immunoassay[3], DNA hybridization assays[4], evaluation of enzyme activities[5], inspection of rare-event cell types [6], and detection of various intracellular analytes [7]. Taking advantage of long-lived luminescence probes, such as lanthanide complexes and nanoparticles with typical lifetimes ranging from tens of microseconds to a few milliseconds, simple time-delayed gated detection can provide high signal-to-background contrast by suppressing short-lived (in tens of nanoseconds) autofluorescence.

Like the partnership of inks and printers, the luminescent materials and time-resolved detection instrumentations have developed in parallel, resulting in great sensitivity, diversity, detection speed and analytical throughput for bioassays and bio-imaging applications. Over the past two decades, a variety of novel long-lived luminescent probes including organic complexes, nanoparticles and nanocrystals, have been designed and synthesized with improved luminescence brightness, photo-stability, emission-tunability, bio-compatibility and functionalities [8-12]. Because their rich optical properties involve sophisticated photon energy transfer processes, multiple energy levels and different designs of materials, existing commercial detection systems capable of spectra and lifetime measurements frequently fail to provide sufficient in-depth information for us to understand the photo-conversion mechanisms. Therefore, a range of purpose-built detection systems have been developed for characterisation and applications of luminescent probes [12-15].

This review focuses on the advances made in instrumentation for long-lifetime luminescence materials. Based on a brief review of long-lifetime luminescent complexes and nanomaterials and their luminescent mechanisms, we present the time-gated luminescence (TGL) techniques for spectroscopy and imaging applications; we then comprehensively review the methods for lifetime measurements in the microsecond regime, and then showcase the recent developments in time-resolved luminescence (TRL) techniques and perspective applications.

1.1 Long-Lived Luminescent Materials

In this section, the basic mechanisms that lead to long decay lifetimes in luminescent materials are briefly illustrated, and long-lived luminescent probes are categorized into lanthanide-based materials, transition metal ligands complexes, and non-metallic phosphors.

1.1.1 Mechanisms for long luminescent lifetime

The luminescent lifetime refers to the average time that a fluorophore stays in the excited state after excitation. Depending on the different electron distributions, inner structures and different relaxation processes of the excited ions, the luminescent lifetime varies from femtoseconds [16-18] up to tens of seconds and even to several hours [19]. Time-resolved lifetime measurements in the range of femtoseconds to nanoseconds requires sophisticated systems and expensive hardware, while luminescence with very long lifetimes compromise the signal strength due to the reduced photon emission. Compared with short-lived luminescent materials with lifetime less than nanoseconds and the more afterglow long-persistent luminescent materials with emission lifetime longer than several seconds, luminescent materials with emission lifetimes in the range of microseconds to milliseconds have useful properties for high-contrast analytical science and offer a balance between hardware requirements and the speed of analysis.

The long-lifetime luminescence phenomenon is governed by the electron spin selection rule and the Laporte selection rule in quantum mechanics. The spin selection rule states that electrons can only transit between energy levels with identical spin quantum number, while other transitions, e.g. between singlet states to triplet states, are spin forbidden. The Laporte rule is a spectroscopic selection rule that applies to centrosymmetric molecules and atoms. It states that in these cases, electronic transitions that conserve parity are forbidden, for instance, *d-d* transitions and *f-f* transitions. Allowed transitions must involve a change in parity, such as *d-f* transitions.

In reality, however, such forbidden transitions can happen, although usually with much lower probability compared to allowed transitions. An example of a forbidden transition is the well-known phosphorescence which relies on the radiative transitions from triplet excited states to the singlet ground state. Figure 1-1 shows the Jablonski

diagram of a typical absorption, fluorescence and phosphorescence processes, which encapsulates the photoluminescence. Transitions which involve redistributions of electrons within the same subshell are also weakly allowed, because atoms cannot strictly maintain perfect symmetry, which may be perturbed due to a variety of reasons such as asymmetric vibrations and the Jahn-Teller effect. These processes have kinetically smaller probability of occurrence, i.e., once excited, electrons decay to the ground state very slowly with longer emission lifetimes.

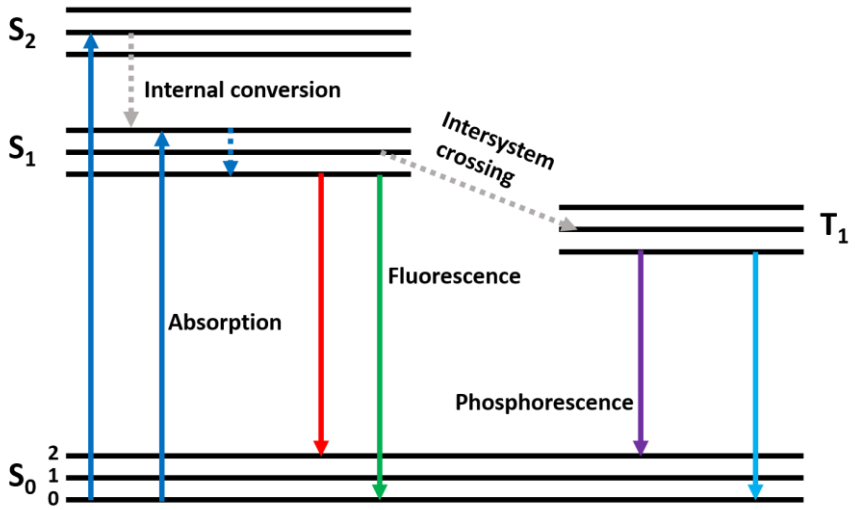

Figure 1-1. Jablonski diagram illustrates the process of photoluminescence in a singlet and triplet system. Reproduced from Ref. [20].

Based on these luminescent mechanisms, different types of long-lived luminescent materials have been designed and applied in many fields. These include the trivalent lanthanide doped materials and transition metal complexes, which show long lifetime emission via breaking the forbidden transitions, as well as some non-metal fluorophores. The detailed information for these long-lived luminescent materials is given in the following section.

Table.1 summarises typical metal ions that are often used to synthesise the long-lived luminescent materials. From the table, the long-lifetime (from several to hundreds of microseconds) of these luminescence materials arises either due to the energy transfer from the triple state to the singlet state or due to *f-f* transition, both of which are commonly considered as the forbidden transition processes as we discussed above. Considering the excitation and emission wavelengths, most of these rare earth ions

(except Yb-Tm and Yb-Er pairs of elements) exhibit down-conversion luminescence mechanism, absorbing excitation at shorter wavelengths and generating emission at longer wavelengths, when they are linked with organic frames/ligands.

TABLE 1-1 Long-lived luminescence probes.

Element	Mechanism	Example Form	Typical Peak Excitation (nm)	Typical Peak Emission (nm)	Typical Lifetime (μs)	Ref.
Ru*	T → S	bipyridine complex	460	620	0.20	[35]
Rh*	T → S	diimine complex	310	505	7.7	[34]
Pd*	T → S	porphyrin complex	380	660	1100	[33]
Os*	T → S	bipyridine complex	370	615	0.27	[32]
Ir*	T → S	diimine complex	280	560	2.7	[31]
Pt*	T → S	porphyrin complex	400	680	46	[30]
Eu†	4f → 4f	β-diketone complex	325	610	380	[29]
Tb†	4f → 4f	phenylpyridine complex	325	545	2700	[11]
Sm†	4f → 4f	trifluoroacetone complex	360	650	96	[28]
Dy†	4f → 4f	trifluoroacetone complex	315	575	27	[27]
Er†	4f → 4f	upconversion nanocrystal	980	540	20~550	[26]
Tm†	4f → 4f	upconversion nanocrystal	980	475	25~670	[25]
Au*	T → S	Cyclometalated complex	UV/Vis	530	5~270	[24]
Re*	T → S	Proteinbound luminophore	290	550	2.7	[23]
Ag*	T → S	Supramolecular complex	355	412	3.9, 4.9	[22]
Cd*	T → S	Coordination polymers	340	510	120 and 1200	[21]

Note: (*) indicates transition metal probes and (†) lanthanide probes. T: triplet stage; S: singlet state.

1.1.2 Lanthanide-based luminescent materials

1.1.2.1 Trivalent lanthanide ions

The lanthanide based materials commonly used as long-lifetime probes (with lifetimes in the range from hundreds of microseconds up to milliseconds), are generally composed of trivalent lanthanide metallic ions, including the elements from Lanthanum (La) with atomic number of 57 to Lutetium (Lu) with atomic number of 71. These are generally referred to as "lanthanides" with the informal chemical symbol Ln, due to their chemical similarities. This stems from their similar electron configurations associated with the unique 4*f* orbitals, which are

$$1s^2\ 2s^2\ 2p^6\ 3s^2\ 3p^6\ 3d^{10}\ 4s^2\ 4p^6\ 4d^{10}\ 4f^{0\sim14}\ 5s^2\ 5p^6\ 5d^{0\sim1}\ 6s^2$$

or in short [Xe]$4f^{0\sim14}\ 5d^{0\sim1}\ 6s^2$. Therefore, lanthanides are inclined to lose three outer-shell electrons to form trivalent cations Ln^{3+} in the form of [Xe] $4f^n$. Their chemical properties largely depend on the ionic radius, which decreases steadily from La^{3+} to Lu^{3+}.

1.1.2.2 Lanthanide-doped long-lived luminescent complexes and nanomaterials

Lanthanide-doped luminescent materials can be divided into two types according to the luminescent mechanisms: downconversion and upconversion luminescent materials. Downconversion materials require excitation by high-photon-energy light and emit low energy photons; and upconversion luminescent materials, conversely, absorb low-energy-photons and generate high-photon-energy emissions.

Ln^{3+} ions downconversion probes are usually composed of Ln^{3+} ions and organic frames/ligands with different structures to label biological samples [36-38]. For example, Ln chelates consist of Ln^{3+} ions coordinated with organic ligands, as shown in Figure 1-2, where the ligands work as the sensitisers to absorb the excitation energy and subsequently transfer the energy to the Ln^{3+} ions. Many major developments of lanthanide complexes have occurred over the last two decades, with recent comprehensive review papers published recently [39-41], and a few of these development are presented here. In early 1990s, Selvin *et al.* synthesised different types

of water-soluble Terbium (Tb) chelates and European (Eu) chelates, with luminescence lifetimes of a few milliseconds and a few hundreds of microseconds, respectively [42]. In 1998, Yuan and Matsumoto synthesised a new teradentate β-diketone chelate, 4,4'-bis(1", 1", 1", 2", 2", 3", 3"-heptafluoro-4",6"-hexanedion-6"-yl) chlorosulfo-o-terphenyl (BHHCT) for Eu^{3+}, with luminescence lifetime of 380 μs in an aqueous buffer (bound to BSA) [29]. In 2001, Yuan reported a new nonadentate ligand, N, N, N^1, N^1-[2, 6-bis (3'-aminomethyl-1'-pyrzaolyl)-4-phenylpyridine] tetrakis (acetic acid) (BPTA) to chelate Tb^{3+}, with a luminescence quantum yield of 1.00 and lifetime of 2.681 ms [11]. In 2012, Yuan *et al.* reported another new tetradentate β-diketonate europium complex 1,2-bis[4'-(1 ",1 ",1 ",2 ",2 ",3 ",3 "-heptafluoro-4 ",6 "-hexanedion-6 "-yl)-benzyl]-4-chlorosulfobenzene-Eu^{3+} (BHHBCB-Eu^{3+}) with long-lived Eu^{3+} luminescence decay of 500 μs and the quantum yield of 40% [43].

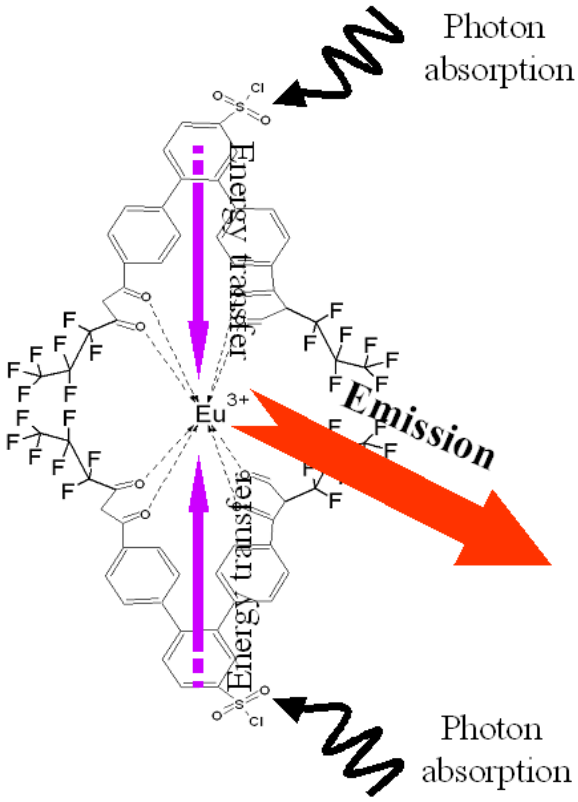

Figure 1-2. Schematic diagram illustrates luminescence from a lanthanide complex (lanthanide ion chelated by an organic antenna ligand). The antenna ligand absorbs the excitation photons then transfers the energy non-radiatively to the lanthanide ion that emits long-lived luminescence. Reprinted from Ref.[44].

Metal-organic frameworks (MOF) are an emerging class of porous material constructed from coordination networks of organic linkers that can hold and sensitise metals [45, 46]. In 2009, Bu *et al.* reported three synthesised 3D lanthanide anionic metal-organic frameworks $\{K_5\ [Ln_5\ (IDC)_4(ox)_4]\}_n \bullet\ (20H_2O)_n$ in an octahedral structure with Ln = Gd, Tb and Dy, respectively. The fluorescent lifetimes were measured in the range of ~ 160 to 800 µs depending on the chosen solvents [47]. Sun *et al.* reported 1D linear coordination polymers with a luminescence lifetime of several microseconds for Sm^{3+} ions, several milliseconds for Eu^{3+} and Tb^{3+} ions, but highly dependent on the temperature. According to authors, when the temperature increased from 75 K to 430 K, their lifetime decreased from 0.57 ms (73%) and 1.36 ms (27%) down to 75 µs (74%) and 200 µs (26%) [48].

Micro-emulsion wet chemistry techniques have been used to encapsulate lanthanide complexes and to make silica or polymer nanoparticles [49]. Other hybrid nanostructures have been explored to enhance the luminescence efficiency of lanthanide complexes, for example, nanoparticles using the noble metal of silver as core, silica as a spacer layer, and silica encapsulated lanthanide complex as the outer layer shell, as shown in Figure 1-3, have been synthesised. The localized nanoplasmonics effect can reduce luminescence lifetimes from hundreds of microseconds to tens of microseconds with enhanced brightness. Under the time-gated luminescence detection mode, the single high-brightness nanoparticles are visible to the naked eyes [50].

Eu and Tb doped oxide inorganic nanocrystals have been developed. Lechevallier *et al.* synthesized a series of Eu doped oxide nanoparticles (RE_2O_3: Eu, RE=Y, Gd), which absorb 254 nm excitation and generate the emission at 611 nm with luminescence lifetimes of 770 µs and 1.55 ms for Y_2O_3: Eu and Gd_2O_3: Eu, respectively [51]. Banski *et al.* recently reported the sub-10 nm Eu doped nanocrystals ($NaYF_4:Eu^{3+}$) that have been demonstrated with long luminescence lifetimes of 2.686 ms at 556 nm and 7.782 ms at 616 nm for 2% Eu doped nanocrystals with 395 nm excitation [52]. Aarts *et al.* used a low-phonon frequency host (KPb_2Cl5) to realise the downconversion emission for the well-known Er-Yb co-doped materials, which absorb the energy between 300 nm and 400 nm, resulting in two broad emission bands centred around 430 nm and 700 nm with a luminescence lifetime in the range of tens of microseconds[53].

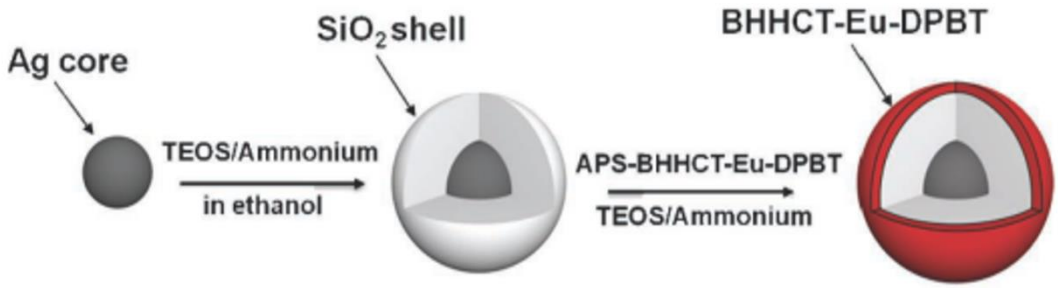

Figure 1-3. BHHCT-Eu-DPBT-doped Ag@SiO_2 nanocomposites. The silver core was first coated with a layer of silica with varied thickness (controlled using different amounts of tetraethyl orthosilicate (TEOS) catalysed by ammonia); and then 3-amimopropyl (triethoxy) slilane (APS)-linked BHHCT-Eu-DPBT (APS-BHHCT-Eu-DPBT) is covalently linked and embedded in the silica shell. Reprinted from Ref. [54].

Upconversion nanomaterials are crystalline hosts generally doped by pairs of Ln ions acting as sensitizers and emitters (also called activators). Commonly used host materials include fluorides ($NaYF_4$ [26, 55], $NaGdF_4$ [56, 57], $NaYbF_4$ [58, 59], $NaLuF_4$ [60]), and oxides (Y_2O_3 [61, 62], Gd_2O_3 [63]), where appropriate choice of the host can enhance the upconversion luminescence intensity. Among these nanocrystals, rare earth doped fluoride hosts have been universally considered as excellent host materials due to their low phonon energy, good thermal stability, optical stability, high transparency, high refractive index and high capacity for doping lanthanide ions [9, 64]. So far, most of the trivalent Ln ions (Er^{3+}, Tm^{3+}, Ho^{3+}, Pr^{3+}, Ce^{3+}, Nd^{3+}, Tb^{3+}, Dy^{3+}, Sm^{3+} and Eu^{3+}) have been employed as activators to improve the luminescent efficiency and tune the emission wavelengths from upconversion processes [65-67]; however, only a few (Yb^{3+}, Nd^{3+}) have generated relatively efficient upconversion emission under the laser irradiation when used as sensitizers[68, 69]. Recently, the corresponding core-shell structured nanoparticles (neutral [70, 71] and active shells [72, 73]) with passivation effect have also been extensively exploited due to their higher luminescent intensity compared to that of the corresponding bare nanoparticles [74].

Both core and core-shell upconversion nanocrystals absorb long-wavelength excitation, (~ 980 nm excitation), and generate short-wavelength emissions, as shown in Figure 1-4. The luminescence lifetime for these Ln^{3+} doped upconversion materials is typically hundreds of microseconds, but an increase in the shell thickness increases the

luminescent lifetime [75]. Furthermore, the luminescence lifetime also depends on the doping concentration and size of nanoparticles in addition to the effects of the surrounding medium. The increase of the Ln^{3+} ions doping concentration leads to a decrease of the luminescent lifetimes [75], while, for a fixed compositions and doping concentrations, the size decrease from 45 nm to 6 nm also leads to a reduction of the luminescent lifetime [26]. Furthermore, organic ligands can be covalently conjugated to functional biomolecules, or the surface of nanoparticles can be deliberately modified by ligand attraction [76], self-assembly [77], surface polymerization [78] or ligand engineering [79]. This biocompatibility enables them to be widely applied as the luminescent tags for a probe molecule for the targeted recognition, bio-detection and bio-imaging.

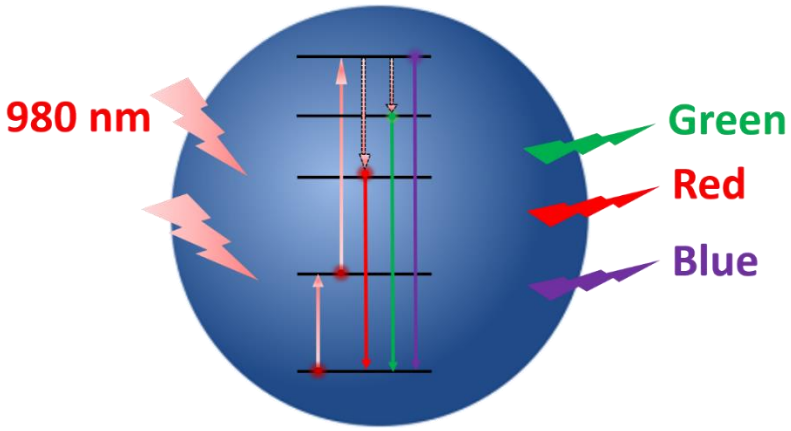

Figure 1-4. Schematic illustration of the luminescence mechanism for upconversion nanocrystals with NIR excitation at 980 nm and visible emission.

1.1.2.3 Optical properties

Apart from the long luminescence lifetimes, Ln^{3+} doped materials have large Stokes or anti-Stokes shifts, and well-defined sharp emission peaks. Ln^{3+} doped downconversion materials generally require ultraviolet (UV) excitation, which is usually not favourable in bio applications because it can cause photo-damage and strong autofluorescence background. Upconversion materials require NIR excitation, which is advantageous in producing less photo-toxicity and negligible autofluorescence, as well as in offering deeper penetration in tissue samples through the so-called “biological window”. Generally speaking, Ln^{3+} doped luminescent nanocrystals have excellent

photo-stability and brightness, but their intrinsic size and sophisticated surface conditions lead to challenges for specific bio applications.

1.1.3 Other types of long-lived luminescence materials

While the lanthanide-based luminescent materials dominate the long-lived luminescent materials, we here briefly introduce the other two types of long-lived luminescent materials, including the transition metal-ligand complexes and non-metal phosphors.

1.1.3.1 Transition metal-ligand complexes

Transition metal-ligand complexes (MLC) are complexes with a transition metal atom or ion element in the central position chelated by several ligands, as shown in Figure 1-5, taking Ru^{2+} ions as examples. In general, more number of ligands yield stronger bonds and greater thermodynamical stability of the complex [45]. Due to their unfilled *d* or *f* orbital electrons in the valence shell, MLC have a strong capability to bind multiple types of ligands. Ligands are commonly divided into two types: ionic ligands including Cl^-, H^-, OH^-, CN^-, and neutral ligands such as CO, H_2O and alkenes. This broad strong bonding feature enables MLC to be extensively involved in the catalysts [80, 81](e.g. polymers, pharmaceuticals), biochemistry (e.g. oxygen transport, photosynthesis, enzymes) [82, 83], organic chemistry methodology (e.g. M $(CO)_3$ arenes, Pd catalysed C-X (X=C, N, and S and O)) [84, 85] and biological and chemical imaging fields [86, 87].

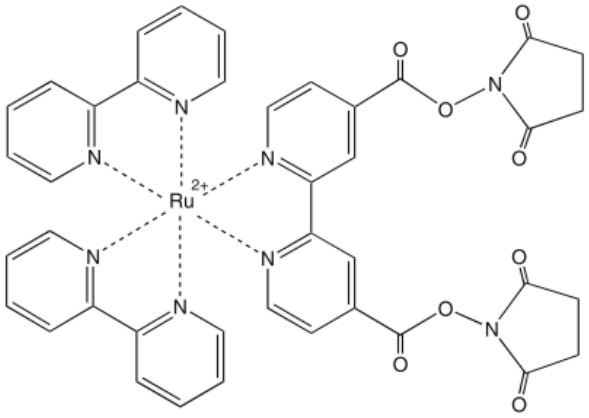

Figure 1-5. The chemical structure of a metal-ligand complex containing a Ru^{2+} ion is linked by other ligands. Reprinted from Ref. [88].

Common transition metal ligand complexes include Re(I), Ru(II), Os(II) and Rh(III) ions with d^6 electronic structures, Pt(II) ions with d^8 electronic structures, and Au(I) and Cu(I) ions with d^{10} electronic structures; these constitute most of the MLC photo-luminescent materials at room temperature [89]. In 2013, Buddha *et al.* reported that gold clusters in traditional fluorescence probes emit bright luminescence with short (up to 100 ns) and long lifetimes (up to 280 μs), and good photo-stability [90]. Wang *et al.* synthesised three novel 3D Cd(II) coordination polymers based on HIN as the organic linker: mononuclear-SBU($[Cd(IN)_2 \bullet H_2O]_n$, $[Cd_2(IN)_2(SO_4)(DMF)_2]_n$, $([Cd_3(IN)_{5.5}] \bullet 0.5OH^-])_n$. Three of them display luminescence with emission maxima in the deep blue, blue and green, respectively, with luminescent lifetime around 10 μs [91]. Morris *et al.* studied the photo-physical properties of a Ruthenium (II) tris (2, 2'-bipyridine)-doped Zirconium UiO-67 metal-organic framework, with the emission decaying exponentially for the concentration Ruthenium (II) tris (5, 5′-dicarboxy-2, 2′-bipyridine (Ru-DCBPY), but with non-exponential decay under high doping conditions [92].

1.1.3.2 Non-metal phosphors with long-lifetimes

Several non-metal complexes have been reported with long-lived luminescence emissions. In 2011, Asko Uri *et al.* developed protein-induced non-metal probes with luminescent lifetimes of 19 μs to 266 μs with flash excitation at 300-360 nm [93]. In 2012, the same group reported another novel non-metal optical probe (Arginine-Rich Peptide (ARC)-1063) with long-lifetime luminescence (115 μs) induced by association with the target protein kinase, which was used to measure the concentration of a catalytic subunit of protein kinase in complicated biological solutions [94]. Recently, Peng *et al.* reported a pure organic fluorophore without rare earth metal ions or heavy atoms, which displayed long luminescent decay lifetime of 22.11 μs (in deaerated ethanol) in oxygen-free condition, and 4.30 μs in normal aqueous condition. The mechanism of this long luminescent decay was proposed to be the thermal activation for the transition from the triplet to singlet excited states, and it has been employed in bio-imaging and bio-detection using time-resolved and confocal fluorescence imaging systems [95].

1.2 Time-Gating Instruments and Applications

Long-lived luminescence emission provides two opportunities for sensing: 1) time-gated luminescence (TGL) detection is simple and useful to suppress background interference from both optical systems and biological samples; 2) time-resolved luminescence (TRL) is useful in understanding the mechanisms of photon-luminescence and creating an additional optical dimension for multiplexed sensing applications.

This section focuses on TGL technique, the basic form of time-resolved techniques that takes advantage of the exceptionally long lifetimes for background-free luminescence detection. The working principles and various TGL approaches are discussed first, and then typical instruments for both practical analytical and imaging applications are showcased.

1.2.1 Time-gating techniques

1.2.1.1 Principles

As shown in Figure 1-6, time-gating techniques use periodical pulsed excitation and time-delayed detection to distinguish long-lived luminescence against a short lifetime background. That luminescent ‘ghost’ image remained on the screen long after the traditional TV was switched off suggests the idea behind the time-gated luminescence detection. A TGL detection cycle consists of an excitation phase, a time delay, and a detection phase. The pulsed excitation light only flashes during the excitation phase, while the photodetector is off. A time delay (typically from 1 to 10 μs) is preferred to allow the short-lived background, (such as autofluorescence and scattering of excitation light), to vanish promptly before the photodetector is rapidly switched on, so that only the luminescence signal at a relatively high level is detected with dramatically improved signal-to-background ratio [96]. Depending on the efficiency of the photodetector (electrical output per optical input), multiple TGL cycles are often required to accumulate sufficient luminescence.

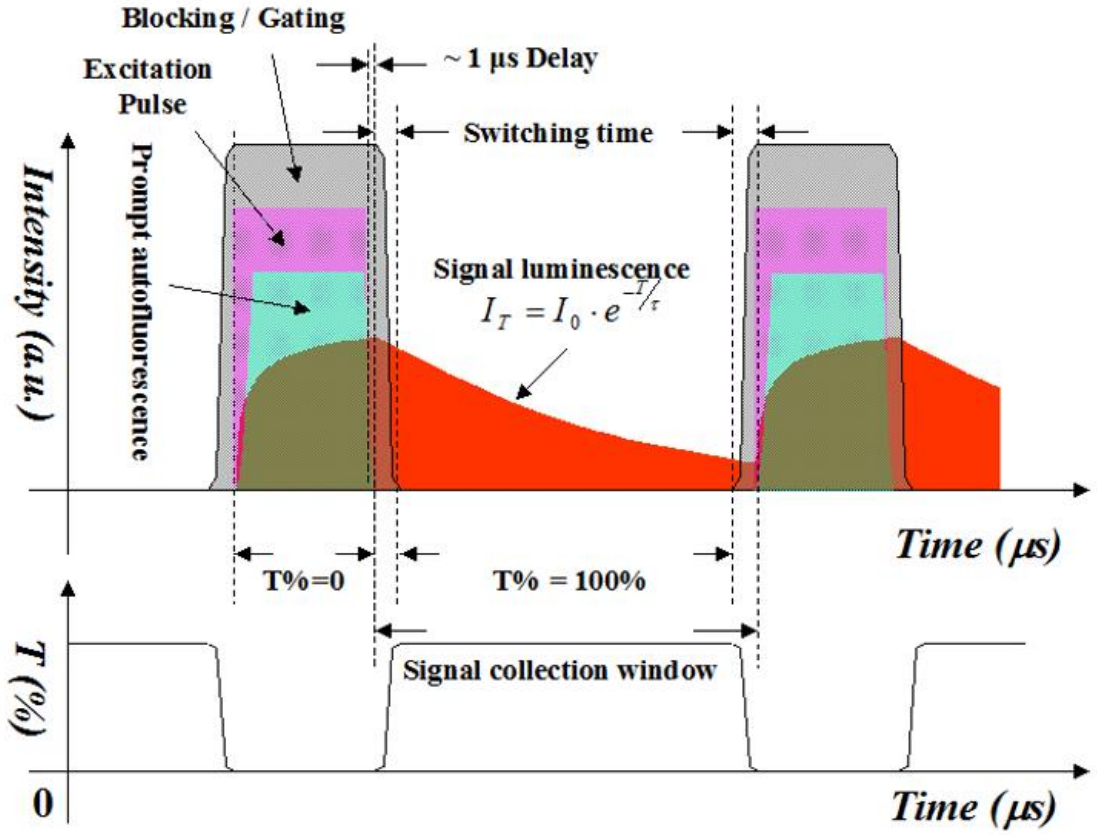

Figure 1-6. Schematic diagram illustrating the principle of time-gated luminescence detection for long-lived luminescence materials. During the excitation pulse, the signal detection window is off, avoiding all light. Following the switch off of the excitation pulse, a short time delay of a few microseconds allows the short-lived background to vanish before the detection window is opened to detect the long-lived luminescence without the interference from the background of autofluorescence and excitation scattering backgrounds. Reprinted from Ref. [96].

1.2.1.2 Methods for TGL detection

The key requirement enabling TGL detection is a pulsed excitation light source and a synchronised gated photodetector with accurate temporal control and rapid switching speed. A number of gating methods have been developed and are summarised in Table 1-2. The goal is to enable TGL detection with high efficiency, stability, and compatibility to the existing system at low cost.

Table 1-2. methods and devices to realize TGL detection

	Gating strategies	Gating components	Ref
Pulsed Excitation	External gating	Mechanical chopper	[33, 97-99]
		Acousto optical modulator	[30, 100]
	Internal gated sources	Xenon flash lamp	[36, 101-107]
		UV LED	[96, 108-114]
		Pulsed laser	[115]
Time-gated Detection	External shutters	Optical disk	[101]
		Mechanical chopper	[36, 96, 97, 103, 107, 112]
		Ferro-electric shutter	[33, 98, 99, 106]
		Gateable EMCCD	[113]
	Internal gated detectors	Gateable CPMT/PMT/ APD	[109]
	Internal gated cameras	Gateable monochrome CCD	[111]
		Gated monochrome ICCD	[114-116]
		Gateable EACCD	[110]

The most common TRL instruments in the recent decades have been time-gated luminescence microscopes. Either pulsed excitation or gated detection can be simply realised by using the gating methods shown in table 1-2. External gating methods based on acousto optical modulators (AOMs) or mechanical choppers are employed to produce pulsed excitation light from continuous Hg lamps or UV lasers; but more recently, new pulsed xenon flash lamps, pulsed solid-state lasers and current-switched UV light-emitting diodes (LEDs) have offered improvements. Therefore, although the TGL microscope initially required external gating devices in both the excitation and detection paths, as shown in Figure 1-7 (a) [117], now it only requires a gating device for detection, with an example shown in Figure 1-7 (b). With a mechanical chopper to gate the detection, the chopper must also provide the synchronisation to trigger the pulsed excitation using a built-in sensor to generate the output signal when the chopper blade passes [118, 119]. Other optical shutters such as ferro-electric liquid crystal shutters can be used in TGL instruments but typically suffer high insertion loss for the signal intensity [33, 98, 99, 106]. Thus the rotating disc chopper is considered to be the most effective way for mechanical gating [112], and recently a new derivative with blades taking the form of 45° mirrors, called gated auto-synchronous luminescence detection (GALD), has been demonstrated[120], as shown in Figure 1-7 (c).

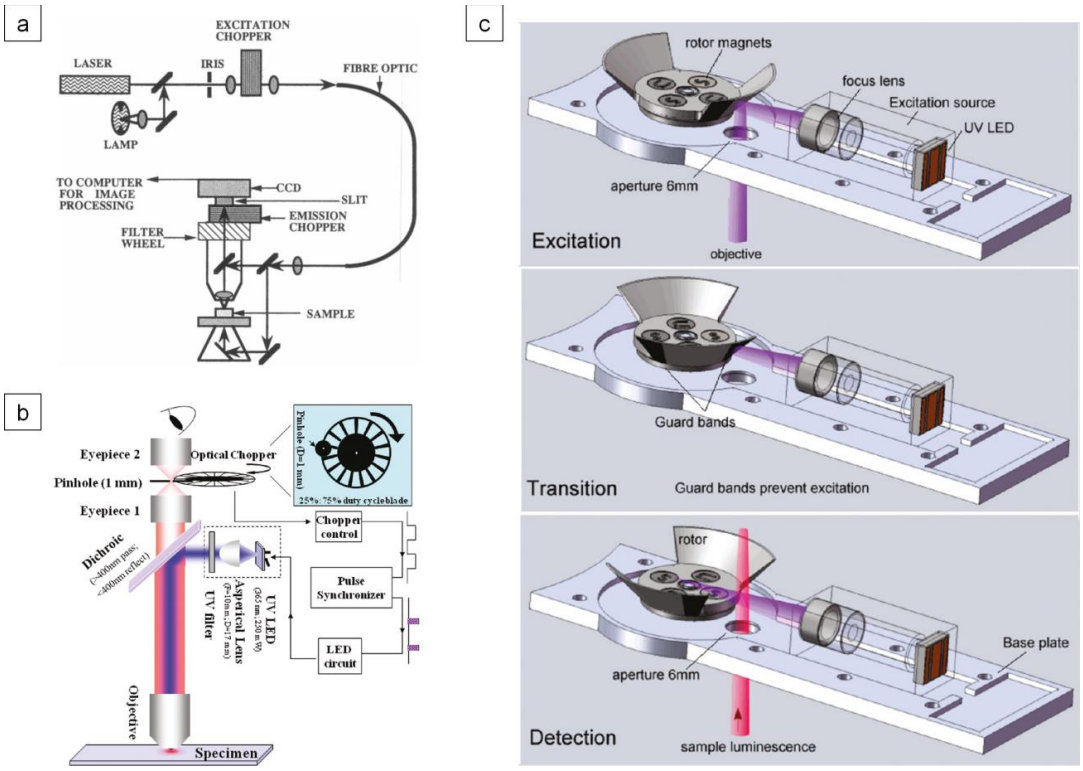

Figure 1-7. Schematic diagrams illustrate three types of mechanical time-gating. (a) reprinted from Ref. [117]; (b) reprinted from Ref.[112]; (c) reprinted from Ref. [120].

Gating a single element high-gain detector is now considered straightforward with time-gateable photo multiplier tubes (PMTs), semiconductor channel PMTs, and single photon counting avalanche diodes (SPAD). Gated intensified-CCD (ICCD) cameras or microchannel photomultipliers (MCP) coupled CCDs offer an effective means of time-delayed gating as fast as a few nanoseconds but are relatively expensive, with the problem of higher dark noise in low light sensing applications [100, 102, 104, 105, 114]. For the last decade, rapid developments in semiconductor technologies have made the electron multiplying charge coupled devices (EMCCDs) quieter, with a threefold improvement in quantum efficiency and with reduced cost, these currently dominate most low-light imaging applications. The design of EMCCDs requires an external shutter mechanism for longer exposure times to accumulate multiple TGL cycles of detection [113], and therefore external gating approaches are still essential, particularly if a multiple colour imaging is required. In contrast, recent optical approaches based on mechanical choppers can be practically implemented with existing imaging systems and cameras at low cost [97, 101, 103], and therefore they are more accessible to end-users in the biological, materials or chemical laboratories.

1.2.2 TGL fluorimeters and plate-readers

Fluorimeters are commonly used for fundamental characterisations of fluorescence and luminescence materials. These include an excitation source for irradiating the samples, a sample holder, and detectors for measuring luminescent intensity, absorbance, excitation spectrum, emission spectrum and luminescence lifetime. Due to their long lifetimes, the rotational motion of luminescent complexes and nanomaterials leads to non-polarised emission even under polarised excitation [121], so that the polarisation properties are usually not characterised. Band-pass filters simply select excitation wavelengths from a broad-band light source, and suitable band-pass emission filters are used to collect the emission. To achieve high accuracy and resolution, a monochromator is required to transmit a mechanically-selectable wavelength from the broad-band light source for excitation and a spectrometer is used for emission collection.

In the 1970s, time-resolved fluorimeters were introduced to measure long-lived luminescent complexes of rare earth ions (Eu, Tb, Sm, Dy) for immunoassays with high signal-to-noise ratio (SNR) [122, 123] , and commercial systems, such as PerkinElmer VICTOR™ EnLite™, Edinburg FS5, have been broadly used as fundamental tools for characterisation of novel long-lived luminescence materials [124]. To achieve high analytical throughput, plate readers with an array of sample containers/wells carried by a motorized stage are suitable for consecutive measurement of different samples. Commercial plate readers, such as the Spectramax series from Molecule Devices USA, FLx800 Fluorescence Microplate Reader from BioTek Cor, support time-resolved luminescence measurement [125].

Different types of time-resolved bioassay techniques based on lanthanide probes have been generated, including dissociation-enhanced lanthanide fluoroimmunoassay (DELFIA)[126-128], time-resolved amplified cryptate emission (TRACE)[129], multiple-label time-resolved fluoroimmunoassay (TR-FIA)[130], and enzyme amplified time-resolved fluorimeter[131]. Most of commercial time-resolved bioassays are based on the long-lived downconversion luminescence of Eu^{3+} or Tb^{3+} chelates, which require UV excitation.

Lanthanide-doped upconversion nanoparticles (UCNP) have been adapted as probes for bioassay methods recently due to their long luminescent lifetimes, high

photo-stability and visible/NIR excitation [10, 75, 132]. In 1999, Zijlmans *et al.* reported the first use of UCNPs in a bioassay, in which oxysulfide UCNPs were applied as analytical markers for detecting cells and tissue surface antigens using immunocytochemistry and immunohistochemistry [133]. In 2001, Hampl *et al.* demonstrated that erbium oxysulfide UCNPs could be applied in lateral flow assays as reporter particles to detect the human chorionic gonadotropin (hCG) [134]. In 2012, Chen *et al.* applied ultra-small CaF_2: Ce, Tb nanoprobes with sub-10 nm size for sensitive detection of avidin in homogenous time-resolved (TR) FRET and heterogeneous TRPL bioassays [135]; in 2014, Chen *at al*. developed a $LiLuF_4$: Ln^{3+} UCNP with higher quantum yield of 5.0% for Er^{3+} and 7.6% for Tm^{3+} for sensitive detection of the β subunit of human chorionic gonadotropin (β-hCG), an important pregnancy and tumor marker, for the heterogeneous upconversion luminescence bioassay[136].

1.2.3 TGL conventional microscopes

The first TGL microscope was reported by Beverloo *et al.* in 1991 by measuring Y_2O_2S: Eu particles with a luminescent lifetime of hundreds of microseconds [137]. The low brightness of the probes and slow TGL repetition rate at ~100 Hz resulted in a long signal accumulation times of tens of seconds for high quality image acquisition. In the late 1990s, highly efficient luminescent probes, particularly the lanthanide chelating complexes which can be functionalised with specific antibodies for cell staining, were reported [29]. The availability of these probes stimulates development of TGL techniques for high contrast imaging. Figure 1-8 displays an example of using time-gated luminescence microscopy to detect long-lifetime luminescence probe labelled cells among spectrally contaminated samples [112], with non-time-gated imaging shown in Figure 1-8(left) and time-gated imaging shown in Figure 1-8 (right).

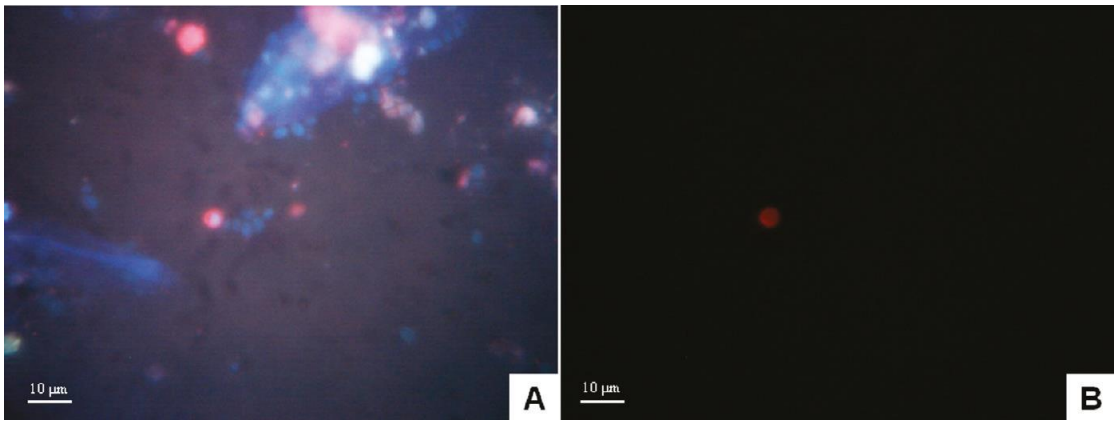

Figure 1-8. Non time-gated (A) and time-gated luminescence (B) images of a Eu^{3+} complex labelled Cryptosporidium parvum oocyst within fruit juice concentrate. Reprinted from Ref.[112].

The high cost has been a barrier to the extensive applications of TGL microscopes, although rapid evolutions in both excitation and detection have reduced cost [111, 137-139]. In 2011, Jin *et al.* reported a low-cost time-gated luminescence microscope with high detection efficiency, with the schematic diagram shown in Figure 1-7 (b). This work realised real-time observation of lanthanide labelled microorganisms by the naked eye or camera, with 18-fold improvement signal-to-noise ratio (SNR), compared to the non-time-gated mode [96]. Three independent approaches to build robust versions of time-gated luminescence microscopes for biological and material applications by modifying standard fluorescent microscopes to have been summarised into step-by-step protocols [140]. Although this low-cost time-gated luminescence microscope can carry out true-colour, high sensitivity detection for micro-organisms, the complicated assembly and low detection efficiency due to single colour detection hinder their wide spread adoption for biological imaging.

Further improvements of this TGL microscope with low cost, convenient operation and high compatibility were achieved by designing and engineering an excitation unit which was synchronised to a purposed-built time-gated luminescence detection unit. Both excitation and detection unit have been demonstrated with high compatibility and easy adaption to any commercial microscope to perform time-gated luminescence detection, with the detection unit shown in Figure 1-9. In addition, high throughput detection has also been demonstrated by simultaneously performing multi-colour imaging for different microorganisms [36].

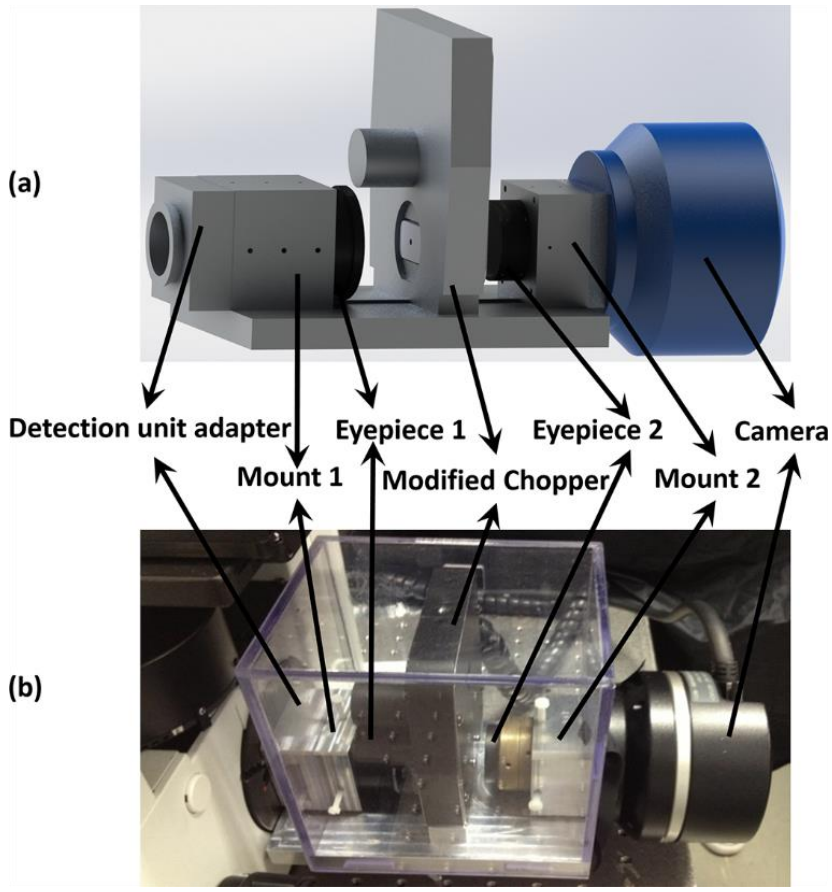

Figure 1-9. The time-gated detection unit consists of two eyepieces, one chopper and one camera, all of which are mounted on a common frame. Top: the schematics; Bottom: a photo of the real system. Reprinted from Ref. [36].

1.2.4 TGL scanning microscope

Lu *et al.* have developed and established a new generation of TGL techniques for automated, high speed, sensitive, quantitative and multiplexing bio-detection [6]. They first developed a wide-field scanning method to transform a manual TGL microscope into an automated workstation suitable for rare-event detection and counting. Figure 1-10 shows the schematics of the TGL scanning microscope.

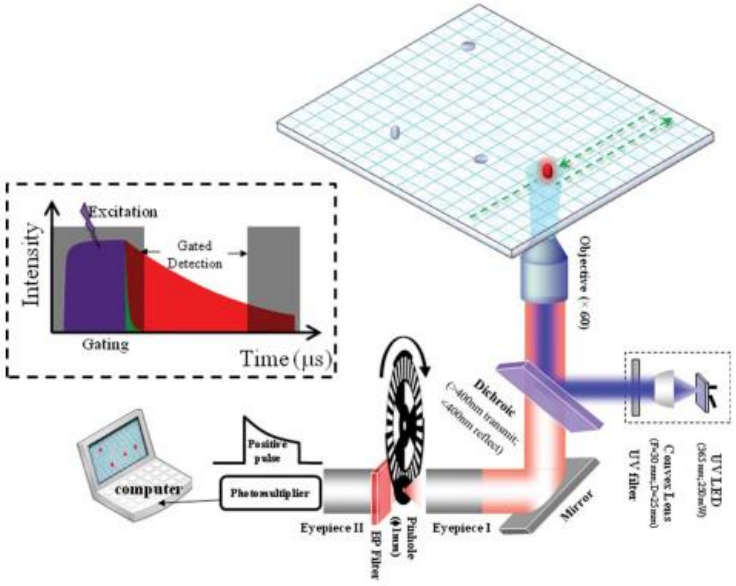

Figure 1-10. Prototype time-gated luminescence scanning microscope modified from a commercial inverted microscope (Diaphot-TMD, Nikon) with epi-fluorescence configuration. It uses a long-lived luminescence bioprobe to label the target microorganisms, so that a time-gated luminescence detection (shown in the dashed frame) renders both the scattered excitation light (purple) and autofluorescence background (green) invisible during the gated-detection phase. When a slide carrying the specimen is scanned in a grid pattern, instead of analysing each grid element, a single-element time-gated detector is capable of selectively determining and marking the "elements of interest" by the positive time gated pulses, so that the computer-guided system returns only to those elements for detailed imaging studies. In our prototype instrument, the time-gated detection was simply achieved by synchronizing a pulsed UV LED excitation to a compact optical chopper. Scanning was demonstrated by a computer-controlled 2-D mechanical stage. Reprinted from Ref. [6].

Using TGL detection, they applied the temporal rather than spectral discrimination to locate and identify target organisms. They used lanthanide-based bioprobes with luminescence lifetime of greater than 100 μs to label the target microorganisms. Instead of recording and analysing large numbers of images from the specimen, they applied a single-element time-gated photomultiplier tube (PMT) to rapidly scan all the samples on a small (75×75 μm^2) grid. Because time-gated detection renders the autofluorescence background invisible to the PMT, the long-lived luminescence from target organisms present in an individual element much have sufficient SNR to identify with certainty the

presence of a rare target event in any element of the certain 15 ×15 mm^2 sample. The microscope-computer system can determine the location of any grid element that appears to contain a target organism and return to only those elements for more detailed imaging studies. The method greatly reduces requirements for data storage, scene segmentation, analytical complicity and analysis time.

They then improved the TGL scanning system with rapid scanning of luminescence probe labelled cells with high sensitivity[141]. This is realised by invention of a new strategy called Orthogonal Scanning Automated Microscopy (OSAM). A novel two-step orthogonal scanning strategy was provided to realise on-the-fly, time-gated detection and precise location of targets, as shown in Figure 1-11. The resulting high-speed localisation of targets was demonstrated by scanning a 15 ×15 mm^2 slide area in only 3.3 minutes instead of 47 mins for detecting 1-μm lanthanide-doped microspheres distributed on the slide. The extremely low background levels achieved in OSAM have been realised to allow the collection of TGL signals as weak as 123 photoelectrons per 100 μs to be distinguished from background with high contrast and precise target locations. Lanthanide labelled *Giardia cysts* have also been analysed with two orders of magnitude improvement in the signal to noise ratio. Low-expressed cell surface antigens have been resolved using this high speed OSAM system [142]. The reduced sample scan time together with enhanced sensitivity and locational accuracy indicates that OSAM represents a very practical approach to high speed analysis for biological cell samples.

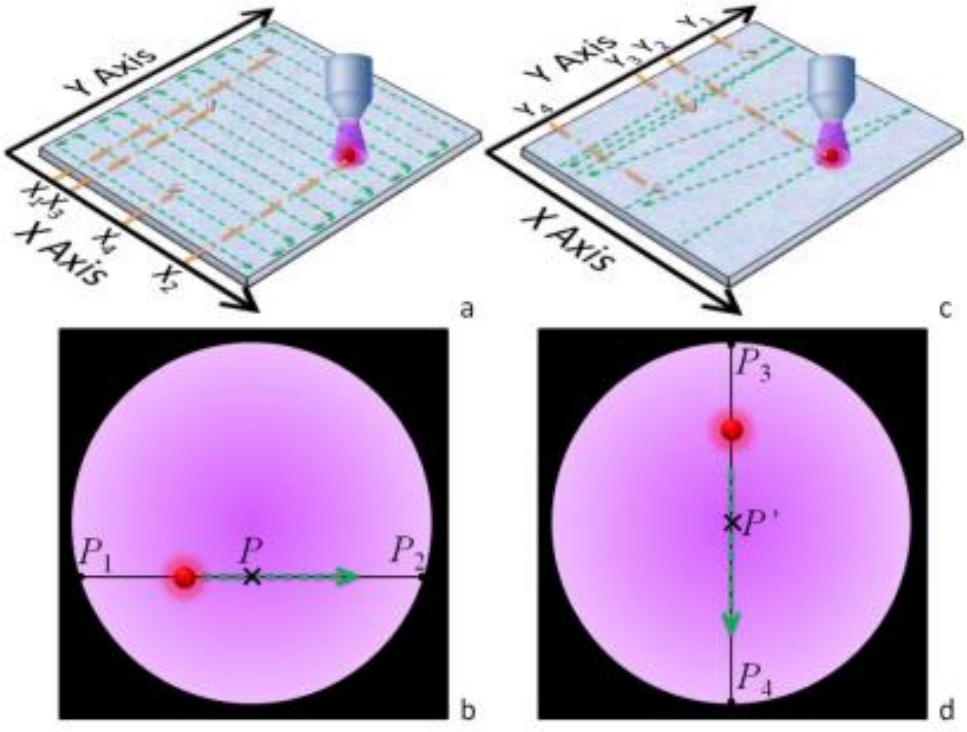

Figure 1-11. A schematic diagram showing the two-step orthogonal scanning method to discover and localise targets of interest. (a) The sample is first examined in a serpentine pattern, with continuous movement along X axis to obtain precise X coordinates and rough Y coordinates for each target. (b) the one target moves into the field of view (FOV), on-the-fly TGL scanning gives the X coordinates of P1 and P2, so that the precise X coordinate of the particles at (P) is obtained; (c) the targets are then scanned sequentially at precision X coordinates along Y-axis to obtain precise Y coordinates. (d) The precise X coordinate obtained in the first step scanning ensures that each target translates in the exact middle of the FOV. Since on-the-fly TGL scanning provides the Y coordinates of P3 and P4, the precise Y coordinate of the particle (at P') is determined. Reprinted from Ref.[141].

1.2.5 Pinhole-based TGL microscope

In 2008, Ramshesh *et al.* provided another type of TGL microscope using the pinhole shift method to gate the detection. This is the core technique in pinhole-shifting lifetime imaging microscopy (PSLIM). This is realised by the software-controlled pinhole displacement in both orthogonal and parallel directions, corresponding to the rastering the laser spot, according to the schematic diagram shown in Figure 1-12 [143].

When the detection pinhole is adjusted to the crossover of the rasting laser spot, the short-lived luminescence passes through the pinhole and then to the photodetector (Figure 1-12 A). However, when the pinhole is shifted in a suitable decay time regarding to the rasting laser spot, the long-lived luminescence is collected with rejection of short-lifetime luminescence (Figure 1-12 B). Therefore, this method is equivalent to the above mentioned time-gating technique. Furthermore, this method can also be applied to measure the fluorescent lifetime, as explained in the lifetime measurement section (section 4). Nevertheless, the requirement of laser beam scanning blocks the wide application.

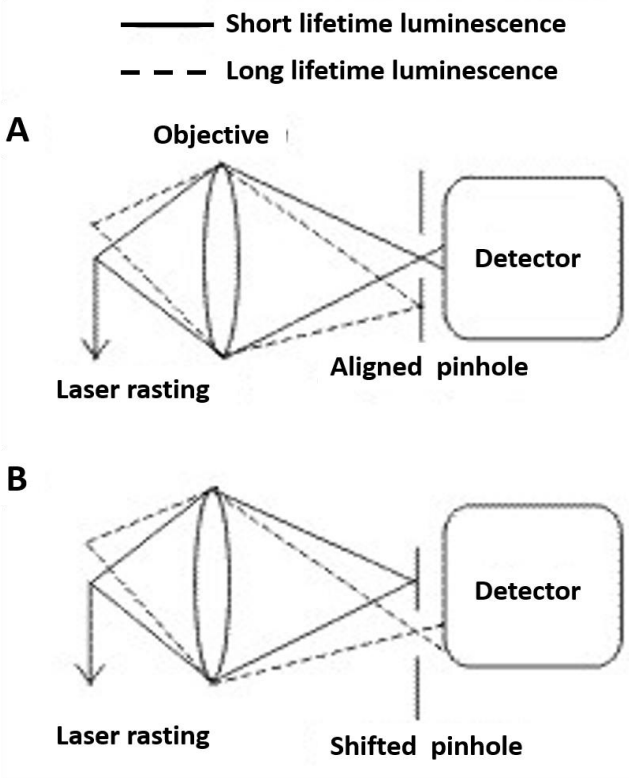

Figure 1-12. Schematic diagram of the pinhole shifting lifetime imaging microscope. A: without pinhole shifting for short-lived luminescence collection; B: with pinhole shift for long-lived luminescence collection. Revised from Ref. [143].

1.2.6 TGL flow cytometry

Flow cytometry is an automated technique capable of rapidly identifying rare cells contained within a large amount of samples. It relies on scattering or fluorescence

measurements that are generated when the cells or particles pass, usually in a single file, through a capillary flow cell.

Commercial flow cytometry instruments equipped with multiple spectral channels are capable of real-time rapid analysis with rates reaching 10,000 cells/s [144]. However, detecting very rare cells poses significant challenges in terms of accuracy due to the strong autofluorescence background from non-target particles/cells in the complex biological samples [144-147]. To overcome this issue, time-gated flow cytometry was proposed by Leif *et al.* to open up new opportunities using lanthanide chelates as fluorescent probes [148, 149]. A detailed theoretical analysis and discussion of TGL flow cytometer design concepts was presented by Condrau *et al*. in 1994 [150, 151] by using Eu chelates as probes with luminescence lifetime in the range from 10 µs to 2 ms [150]. However, the long luminescence lifetime of the probes required a slower flow rate than most commercial systems, which does not allow sufficient throughput to detect rare events in a reasonable period of time. Moreover, the laser system coupled with acousto-optic modulation resulted in a bulky, expensive and complex instrument.

Spatial-delay TGL flow cytometry was demonstrated in 2007. This provides many new opportunities to achieve high-speed cell analysis rates with 100% detection efficiency [152-154]. Figure 1-13 shows a schematic illustrating spatial-delayed TGL flow cytometry. The detection window is positioned downstream from the excitation with the openings and interval distance determined by the ratio of the temporal sequence and the sample speed. When the labelled cells travel in a rapid-flow stream, following excitation, the rapid flow spreads the long-lived emission spatially for detection.

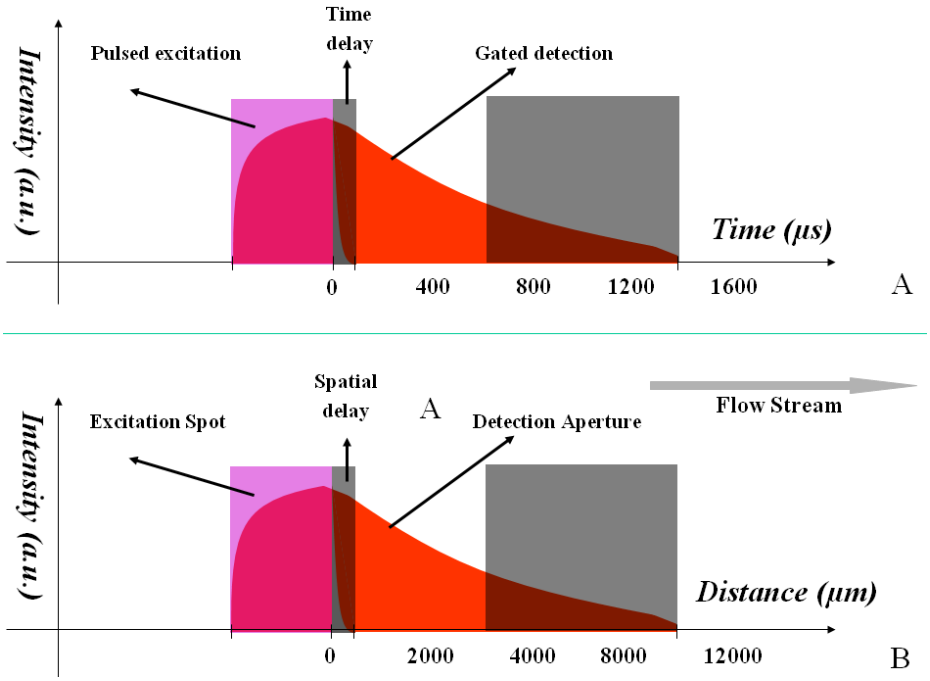

Figure 1-13. Temporal and spatial delay based TGL detection. (A) The general theory of TGL detection operation showing the large difference in luminescence decay in the temporal domain, where an appropriate time-gated detection window can eliminate both scattering and autofluorescence background; (B) Long-lifetime biomarkers in rapid flow can convert the temporal luminescence decay to a spatial decay along the flow axis (assuming luminescence lifetime τ=500 μs and flow velocity v=5 m/s). Correspondingly, the time-gated detection window in the temporal domain is analogous to the spatially resolved luminescence (SRL) aperture. Reprinted from Ref.[140].

However, in addition to the autofluorescence background, excitation light can be scattered along the flow stream, and this may be much brighter than the faint luminescent signal from the target organisms, rendering this simple approach impractical. A further implementation of TGL flow cytometry based on a spatial TGL system was carried out by adding a time-delay function to the detection, with the schematics of spatial and time-delay TGL flow cytometry shown in Figure 1-14.

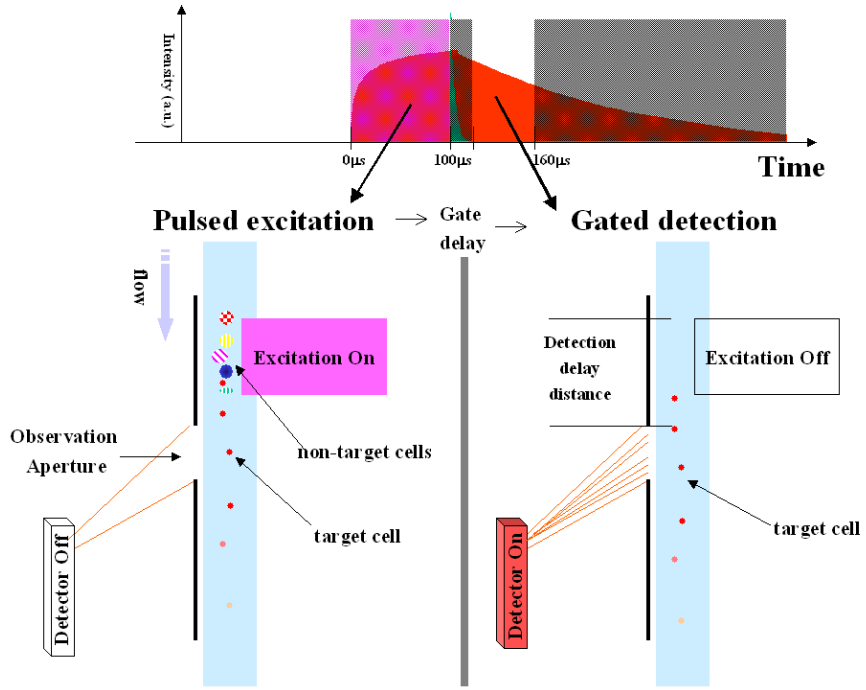

Figure 1-14. Schematics of TGL flow cytometry geometry. The detection of long-lifetime biomarker labelled target cells in the flow involves three steps (pulsed excitation, gate delay and gated detection) with both temporal and spatial considerations: During the period of pulsed excitation (e.g. 0 μs to 100μs shown in top), both autofluorescence from non-target particles and signal luminescence from target cells were detectable at the excitation spot, but the detector was positioned downstream from the excitation spot and switched off (bottom left). After an appropriate gate delay time, both light scattering and autofluorescence ceased and only long-lifetime luminescence from target cells remained to be detected. Revised from Ref. [153].

The labelled target organisms as well as other autofluorescence non-target cells were firstly illuminated by pulsed excitation in the excitation spot, during which the detector was switched off, as shown in Figure 1-14 (left). Once the excitation pulse is extinguished, the autofluorescence rapidly fades within 1 μs but the fluorescent signal from the target organisms/cells is almost unaffected. The opportunity for the time-delayed detection of the target cells exists at some point beyond the excitation zone, so the signal can be detected against a theoretically zero background with both temporal and spatial displacement, as shown in Figure 1-14 (right). To achieve a high target-organism count rate, the observation aperture was situated to permit a much shorter

luminescence measurement time (e.g. < 50 μs) rather than the typical ~1ms for luminescence from lanthanide chelates.

TGL flow cytometry using long-lived probes has the advantage of very high speed for rare event detection, high detection signal-to-noise ratio with the time-gated technique [154, 155] and high throughput detection by designing multi-channel simultaneous detection [156]. However, it requires a sophisticated labelling process (e.g. multi-colour staining) [157] and calibration quality controls [158, 159].

1.2.7 Summary

TGL based instruments have been widely used for bio-detection and bio-imaging by taking advantage of the long-lifetime probes to suppress the short-lived autofluorescence. This section reviews TGL based optical instruments and their applications in fluorimeters/plate-readers for measuring fluorescence intensity, spectrum, or lifetime *et al.*; several generations of TGL microscopes towards low-cost, high compatibility and high-speed detection, including scanning and pinhole-based TGL microscopes; and TGL flow cytometry for high-speed detection of rare events.

Apart from TGL-based optical instruments as discussed in this section, instruments/methods for characterising the luminescence lifetime also play an important role in materials science. This is because the luminescence lifetime offers information on the dynamic process, energy transfer, and intramolecular interactions for the luminescent materials. In the next section, we consider techniques and instruments for fluorescence lifetime measurement and lifetime-based applications.

1.3 Time-Resolved Methods, Instruments and Applications

Beyond basic time-gated detection, advances have been made to further measure the luminescence lifetimes. Not only do the lifetimes of slow-decaying luminescence indicate material characteristics and luminescence mechanisms, but also they offer distinctive optical signatures that can be used to distinguish different analytes for nanoscale sensing and high-throughput multiplexing applications. This section covers

the general principles for lifetime measurement in the microsecond region, the development of state-of-the-art instrumentation and a perspective on applications.

1.3.1 Principle of lifetime measurement

Conventionally, luminescence lifetimes can be obtained in either the time domain or the frequency domain. Both have mature techniques for short lifetimes in the nanosecond range [160-162], but these may be limited in practice for measuring long lifetimes in the microsecond range and beyond. Moreover, the slow decays of long-lived luminescence provide a unique opportunity to obtain the luminescence lifetime in the spatial domain. Here, we summarise the techniques that are applicable to long-lived luminescence materials.

1.3.1.1 Time-domain techniques

In general, the time-domain method aims to acquire the decay signals following pulsed excitation, from which lifetime values can be calculated. Based on different types of photodetectors, the following four techniques have been developed:

(a). The most straightforward approach is to record the entire decay curves, typically by a photodiode or a photomultiplier tube (PMT). The curve is then fitted to an exponential function via common algorithms such as least-squares or maximum likelihood, so that the lifetime parameters can be obtained. In the simple case of mono-exponential decay, the lifetime is the slope of the decay curve in log scale, as shown in Figure 1-15.

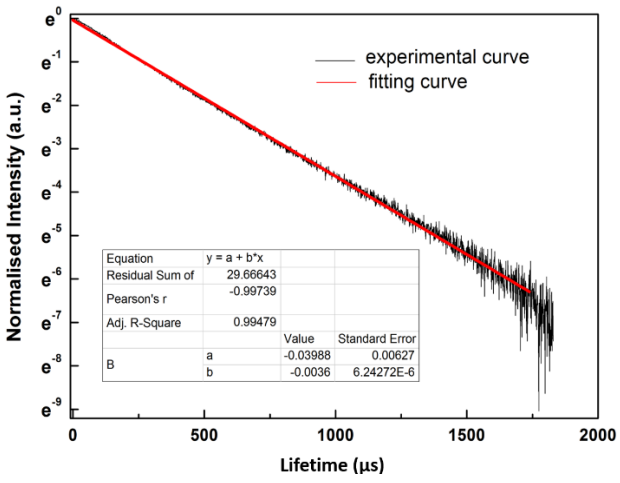

Figure 1-15. Experimental data (black line) and fitted decay curve (red line). The fitting formula and results are inserted in the figure with the absolute value of the gradient b, being the reciprocal of the luminescence lifetime.

(b). For image sensors, including charge-coupled devices (CCD) and complementary metal-oxide-semiconductor (CMOS), it is not feasible to record the entire decay curves; rather, they collect all photons arriving in a predetermined exposure period and convert them to one intensity value for each pixel. Providing that a series of intensity values are acquired from different exposure windows along the decayed signal, the luminescence lifetimes can be derived. For example, assuming that two exposure windows (A & B) with the same length are used on a mono-exponential curve without offset, as shown in Figure 1-16 (left). The integrated intensities N_A and N_B at these two detection windows are:

$$N_A = \int_0^{\Delta t} A \times e^{-t/\tau} dt$$
$$N_B = \int_t^{t+\Delta t} A \times e^{-t/\tau} dt \quad (1)$$

And the integrated intensity can be expressed by:

$$N_A = A \times \tau \times [1 - e^{-\Delta t/\tau}]$$
$$N_B = A \times \tau \times [e^{-t/\tau} - e^{-(\Delta t + t)/\tau}] \quad (2)$$

Therefore, the lifetime value τ is given by:

$$\tau = \frac{t}{\log(\frac{N_A}{N_B})} \quad (3)$$

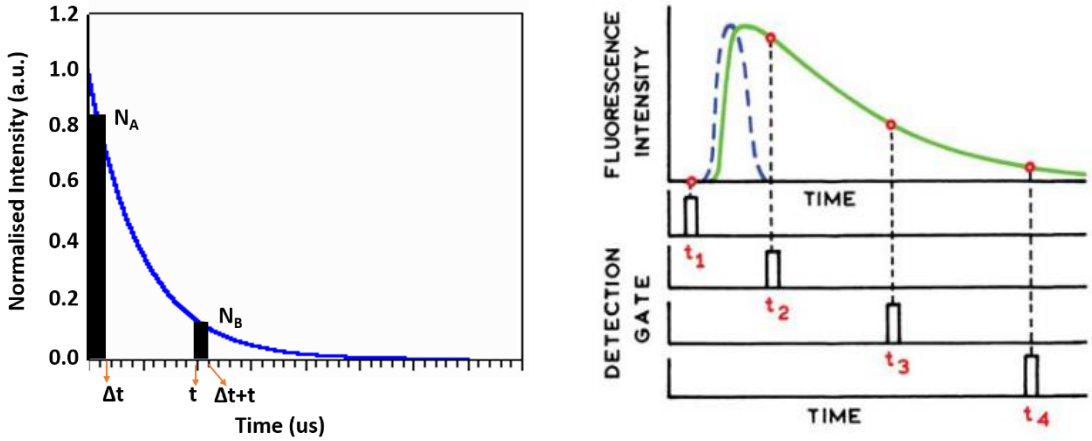

Figure 1-16. Decay sampling measurement. Left: the simplified sampling method with two detection windows. Right: the top curves show the excitation pulse (blue curve) and fluorescence signal (green curve); the bottom shows the sampling on the fluorescence signal as a function of time. Reprinted from [163].

To improve the accuracy, more than two detection windows along the decay signal are usually employed, as shown in Figure 1-16 (right), leading to different formulae to acquire the lifetime values, with a systematic derivation found in Ref [164]. In particular, using a digital delay gate generator (DGG) device for determining the delayed TTL pulses to trigger detectors, the luminescence decay can be sampled in a stroboscopic format as a function of time, with gate (time-delay) across the whole fluorescence decay [163, 165-167].

In addition to image sensors, this technique can also be applied with single-element detectors to reduce the data storage requirement and improve the processing speed.

(c). the above two techniques can also be implemented with photon counting devices, which present the luminescence intensity in an inherently discrete form. For example, a single-photon avalanche photodiode (SPAD) can be used to collect the emitted photons after pulsed excitation, and bin them to a series of time intervals, shown in Figure 1-17 [75]. Even if the entire decay is recorded, the lifetime can be obtained in an approach similar to the sampling technique, though curve fitting can be used as well. Apart from SPADs, intensifier CCDs (ICCD) that are capable of photon counting at ultrahigh frame rates have also been demonstrated for measuring lifetimes in the microsecond-region [168].

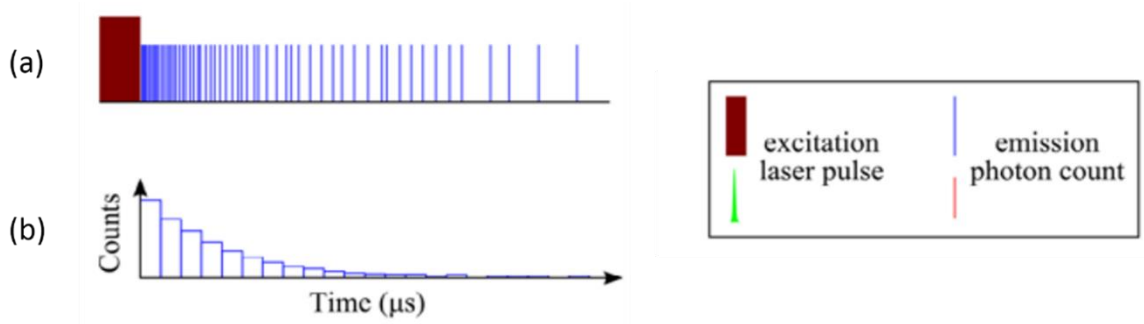

Figure 1-17. A scheme illustrates the principle of the time-gated photon tracking method for measuring luminescence lifetimes in the μs region. (a) Shows the distribution of emitted photons (blue line) in terms of time after excitation (red); and (b) shows the decreased numbers of collected emission photons at fixed time intervals with the increase of time after excitation. Reprinted from Ref. [75].

Note: for techniques (a)-(c), in principle only one excitation-detection cycle is required to recover the decay curves. Nevertheless, multiple cycles are often required to accumulate the signal and average the noise for probes with insufficient brightness.

(d). time-correlated single photon counting (TCSPC) has been extensively used to measure fluorescence lifetimes [163] through commercially available systems coupled with spectrometers, confocal and multi-photon microscopes. While the detailed principle can be found elsewhere [169, 170], briefly, it measures the statistics of the time interval between the pulsed excitation and the first emission photon, to obtain an equivalent decay curve in a statistical manner, as shown in Figure 1-18. The lifetime values can then be extracted via curve fitting to exponential functions.

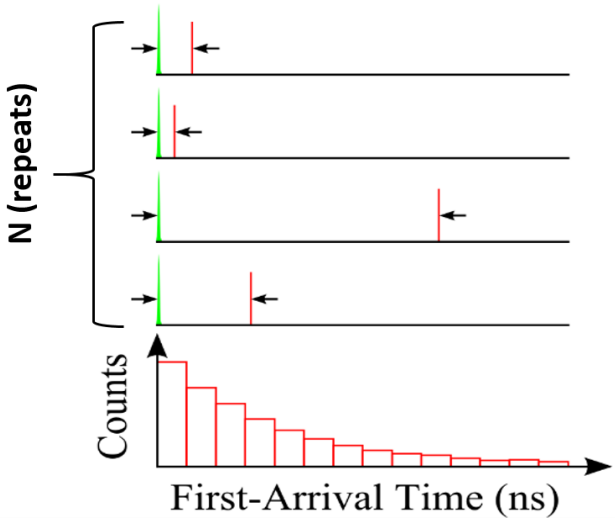

Figure 1-18. A scheme illustrates the traditional TCSPC method, which relies on statistical measurements of a single photon arrival time following pulsed excitation of picoseconds or even femtoseconds over many cycles to obtain a single lifetime decay curve. Reprinted from Ref. [163].

Nevertheless, TCSPC requires repetitive measurement of the photon arrival time, which on average is proportional to the luminescence lifetime. Moreover, to avoid distortion of decay curves, low excitation power has to be used to ensure no more than one photon is emitted per excitation pulse. Therefore, data acquisition using TCSPC becomes extremely slow for long-lived luminescence. Another critical issue when measuring long lifetimes using TCSPC is the increased possibility of false events due to optical and electronic noise, leading to biased results and reduced lifetime values. Noise

must be minimized, as straightforward compensation via deconvolution is not applicable to TCSPC, which is essentially a nonlinear measurement. Additionally, the repetition rate of the excitation pulses need to be adjusted accordingly, which complicates the instrumentation, especially with femtosecond-pulsewidth Ti: sapphire lasers that are commonly used in TCSPC systems. Nevertheless, the commercially available systems, especially for fluorescence-lifetime imaging microscopy (FLIM), have promoted the use of this technique with long-lived luminescent probes as a simple demonstration.

1.3.1.2 Frequency-domain techniques

The frequency-domain (FD) method applies modulated excitation to obtain the lifetime parameters from the phase delay and the modulation depths between the excitation and the emission [171]. As shown in Figure 1-19 (a), the excitation light source typically takes a sine-wave intensity modulation,

$$I(\mathrm{t}) = \alpha + \mathrm{bsin}(\omega \mathrm{t}) \tag{4}$$

where ω is the angular frequency of modulation, and b/a represents the modulation depth.

The emission exhibits the same oscillation frequency, but with a phase shift φ and a different modulation depth due to the time lag between the absorption and emission,

$$N(\mathrm{t}) = \mathrm{A} + \mathrm{Bsin}(\omega \mathrm{t} - \varphi) \tag{5}$$

where $\frac{B/A}{b/a}$ is the modulation depth of emission. $M = \frac{B/A}{b/a}$ is the demodulation factor. Assuming the impulse response of the fluorophore is a mono-exponential decay, it can be derived that [163] ,

$$\tau_{\varphi} = (\frac{1}{\omega})\tan\varphi \tag{6}$$

$$\tau_{M} = (\frac{1}{\omega})\sqrt{(1-\mathrm{M}^2)-1} \tag{7}$$

To improve the measurement accuracy, especially for those with multi-exponential lifetimes, the phase angle and modulation are measured over a wide range of frequencies, as shown in Figure 1-19 (b-c), to give the frequency response of the sample.

In multiple frequency measurement, when the modulation frequency is increased, the phase angle increases from 0 to 90 degree, and the modulation decreases from 1 to 0. However, the range of modulation frequencies required to recover the intensity decay depends strongly on the fluorescence lifetimes, which is the most critical when the phase is around 45 degree, because it is difficult to measure the phase angle approaching 90 degree according to Eq (6) [171].

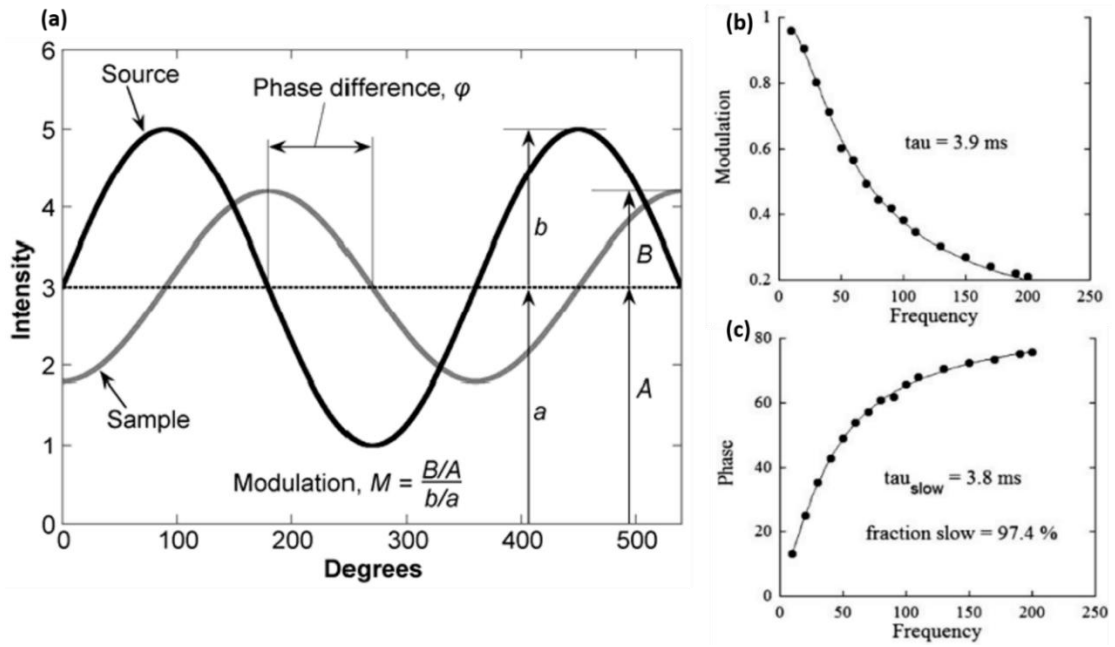

Figure 1-19. (a)Principle schematic for measuring lifetime using the FD measurement. Reprinted from Ref. [163]; (b) and (c) are multiple frequency measurements for calculating the lifetime with both modulation depth and phase. Reprinted from Ref. [172].

As early as 2006, Danielle *et al.* applied the FD method to measure the lifetime of conventional ruby with lifetime of 3 ms. Meanwhile, they mentioned that the required instrumentation in FD method is minimal and affordable by many laboratories [172]. In 2010, Iko Hyppanen *et al.* used the FD method to explore the temporal characteristics for two different Eu chelates in different solvents and under different temperatures. Their luminescence lifetimes for emission at 615 nm and 540 nm were in the range of several to hundreds of microseconds, measured using a modulated excitation beam with 200 modulation frequencies between 10 Hz and 100 kHz [171].

By comparing with the time-domain method, which is more accurate for low concentration lanthanide fluorophores due to the better signal-to-noise ratio, the FD method dominates when measuring multilevel systems or fluorescent materials with two or more closely spaced lifetimes [171].

1.3.1.3 Spatial domain methods

Apart from the time and frequency domain methods, the luminescence decay time of long-lived luminescence materials can also be measured on the basis of transformation of spatial domain to temporal domain. The spatial domain method uses the physical space shift to perform the lifetime measurement. To date, there are two types of spatial domain methods: pinhole shift method and microfluidic space domain method.

(1) Pinhole shift method

The pinhole shift method provides a spatial method to perform both luminescence lifetime measurements and background-free imaging. Here, we focus on the lifetime measurement. It relies on shifting the pinhole of a laser scanning confocal microscope with respect to the spot of laser beam scanning across the sample to detect the signal, with the schematic diagram shown in Figure 1-12. The collected lifetime ($\tau_{collected}$) for different pinhole shifts can be expressed by:

$$m\Delta t \le \tau_{collected} \le (\mathrm{m}+1)\Delta t \qquad (8)$$

where m is the pinhole shift in Airy units, corresponding to the diameter of the Airy disk projected on the pinhole plane; Δt is the dwell time of the laser spot. To test this method, the Eu microspheres with diameter of 1 μm were characterised with an average lifetime of 270 ± 2.8 μs [143]. At least two pinhole positions were needed to extract the lifetime in this method.

The pinhole shift method provides a faster method to measure the long luminescence lifetimes. However, it is not precise because only a few experimental points are captured with limited pinhole lags. Moreover, it depends on the use of a laser scanning confocal microscopes.

(2) Microflow space domain method

The microflow space domain method provides a simple and fast approach for exploring millisecond and sub-millisecond photo-kinetics. This method relies on the use of laminar microflows for time-resolved emission measurements with steady state excitation and detection. Passing a laminar flow through a short illuminated section of a microchannel provided an approach for pulsed-like photoexcitation of the moieties carried by the fluid. Imaging the microchannel flows carrying the photo-excited lanthanide chelates allowed us to extract their excited-state lifetimes from the spatial distribution of the changes in the emission intensity [173], as shown in Figure 1-20.

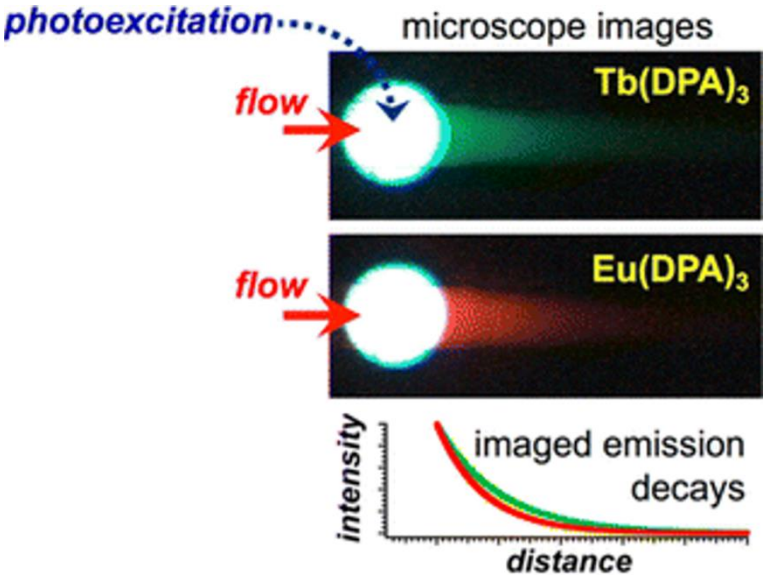

Figure 1-20. Microflow space domain method for lifetime measurement. Continuous-waveform (CW) illumination of a short stretch of a microchannel caused a pulse-like excitation of chromophores carried by the flow through the illuminated region, shown as white spots. Epi-fluorescence imaging of microflows after such confined CW illumination revealed the progress of radiative deactivation of the excited states of long-lived complexes. Reprinted from Ref.[173].

In 2013, Nunez *et al.* reported the microfluidic space domain method for studying time-resolved properties of long-lived Tb (III) and Eu (III) chelates with Pyridine-2, 6-dicarboxylate with lifetimes ranging from 500 μs to around 2 ms. According to the authors, simplicity and speed are the attractive features of this space-domain microfluidic technique. It is well-suited to the measurement of long lifetimes due to its

ability to discriminate against short-lived autofluorescence or scattered excitation beam [173].

1.3.2 Advanced systems and applications

The coordination chemistry used to design organic chelate complexes has also been broadly applied to design a series of molecularly-specific biosensors, to probe biomedical important molecules and ions, including the reactive oxygen/nitrogen species (such as singlet oxygen and nitric oxide) [174, 175], biomolecules (such as cysteine, homocysteine, and glutathione) [176], cations and anions (such as Hg^{2+}, S^{2-}, and Zn^{2+}). With the rapid development of bioprobes and similar luminescent materials, there are requirements for more specialized optical instruments for characterisation.

Based on the abovementioned principles of lifetime measurement, many optical instruments have been designed and developed for performing lifetime-related characterisation and sensing applications. In this section, we focus on these lifetime-based optical instruments and their applications.

1.3.2.1 Lifetime-based characterisation systems

(1) Commercial Time-Resolved Spectroscopes

On the basis of lifetime measurement methods mentioned above, commercial optical instruments have been developed for measuring the luminescent lifetimes in the range of hundreds of microseconds to several seconds. For example, the Delta Flex and Delta Prof from Horiba Corporation can measure the luminescence lifetimes in the range of several nanoseconds to 11 seconds based on the TCSPC technique; the EasyLife^{TM} X also from Horiba can capture luminescence lifetime from 50 picoseconds to 3 microseconds using the stroboscopic technique; the FLS920-m module and LifeSpec II spectrometer from Edinburgh Instruments measure the luminescence lifetimes from several picoseconds to 10 seconds using the TCSPC technique.

These commercial optical instruments provide a convenient measurements of luminescence lifetimes, especially for short-lived and intense luminescence signals. However, for long-lived luminescent materials, in particular for the lanthanide doped materials, they lack a suitable NIR excitation laser or suffer from low detection sensitivity. Consequently, some home-built optical systems have been designed and

established to meet the requirements of long-lifetime luminescence measurements. For example, Qin *et al.* used a modulated continuous wave (CW) visible laser to measure the time-resolved fluorescence spectra for the trivalent rare earth ions, Ho^{3+} (49 µs at 414 nm and 95 µs at 550 nm,) and Tb^{3+} (2 ms at 542 nm and 1. 9 ms at 1020 nm) [177]. Li *et al.* used a home-built laser scanning confocal system with 980 nm excitation to demonstrate Yb^{3+}-sensitised upconversion nanocrystals as luminescent labels [178].

(2) Time-Resolved Spectroscopy System

Time-resolved spectroscopy system provides a high-throughput and high-resolution method for simultaneous measurement of luminescence lifetime, spectrum and intensity for long-lifetime luminescence materials [179]. This incorporates an integrated multichannel photon-sensing device, a 32-channel PMT as a linear array detector attached to a spectrometer, to replace the single photon avalanched photodiode (SPAD) in the home-built laser scanning confocal microscopy system.

To demonstrate the robust capability of this system, the hexagonal-shaped upconversion nanocrystals $NaYF_4$:Yb20%, Er2% with 40 nm size were tested using 980 nm laser as excitation source. It took less than 1 minute for the system to complete 50 acquisitions and construct the three-dimensional time-resolved spectra with high temporal and spectral resolution, as shown in Figure 1-21[180].

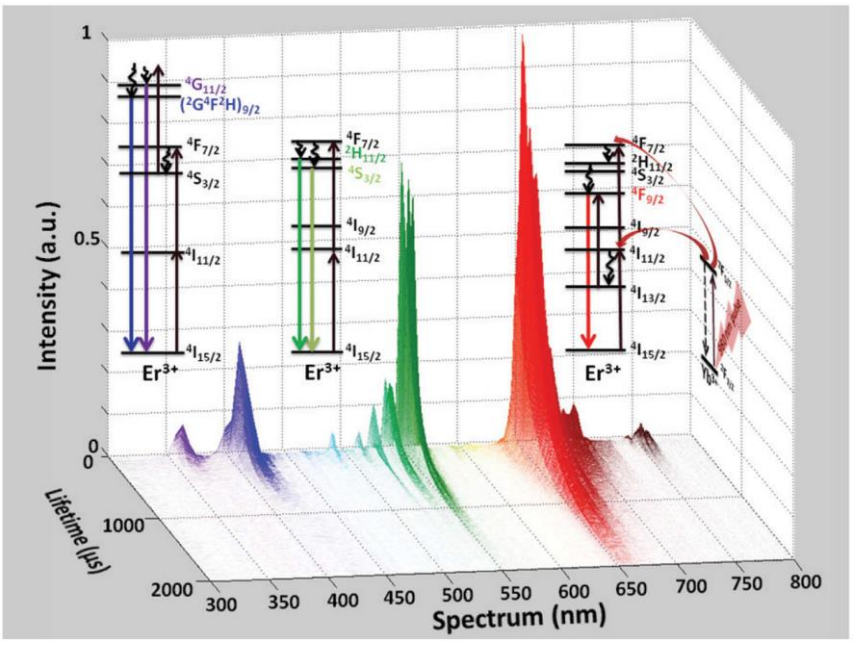

Figure 1-21. Time-resolved spectra for the upconversion nanocrystals ($NaYF_4$: Yb20%, Er2%). Reprinted from Ref.[180].

This time-resolved spectroscopy system provides an advanced characterisation modality to study long-lived lanthanide doped luminescence materials with high throughput, simultaneously measuring the temporal and spectral information with high resolution to resolve two neighbouring sections doped with different lanthanide emitters and high sensitivity for directly imaging single highly-doped upconversion nanocrystals. However, this requires further optimisation towards a fully automatic system with self-correlated functionalities to perform advanced nanoscale characterisations of luminescent materials.

(3) Quantum Yield Measurement of Lanthanide Activators

Lanthanide activators here refer to the lanthanide acceptors doped in upconversion crystals or linked by organic ligands. The quantum yield (QY) of these lanthanide doped activators contributes to the calculation of the energy transfer efficiency between sensitisers and acceptors, and the photo-physics of the lanthanide materials. To date, an indirect method has been used to measure this quantum yield Q_{Ln} by using one QY-known sample as the acceptor for the whole lanthanide ions doped/linked sample.

In 2001, Selvin *et al.* reported a simple and robust method to measure the quantum yield of lanthanide ions in a lanthanide chelate[181]. They considered the lanthanide chelate as a "black box", the sensitiser, and used fluorescein, whose quantum yield is known, as the acceptor, as shown in Figure 1-22. Q_a is the quantum yield of fluorescein; E is the energy transfer efficiency between the acceptor and the lanthanide chelate.

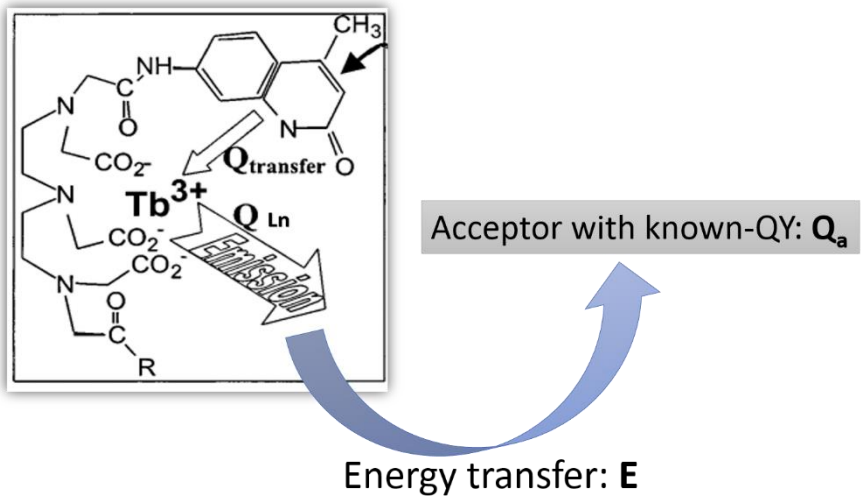

Figure 1-22. Q_{Ln} measurement of Tb^{3+} ions in the chelate (within the square) using quantum yield known acceptor. E is the efficiency of energy transfer between the chelate and acceptor. Reproduced from Ref.[181].

By comparing the spectral and lifetime measurements, the acceptors and sensitisers have the same E, which can be calculated from the lifetime of the donor luminescence (Eq 9, middle term) or lifetime of the sensitised emission (right-hand term of Eq 9), where sensitised emission is the delayed acceptor fluorescence due only to energy transfer from the sensitised emission[181]:

$$E = 1 - (\frac{\tau_{da}}{\tau_d}) = 1 - (\frac{\tau_{ad}}{\tau_d}) \quad \textbf{Di}$$

τ_{da} and τ_d are excited state lifetimes of donors in the presence and absence of acceptors, and τ_{ad} is the lifetime of sensitised emission. Here, τ_{ad} can be measured without interference from donor emission or from direct acceptor emission; donor emission lifetime can be obtained by time-gating method since the direct emission from acceptor is very short (ns) compared to sensitised emission (hundreds of microseconds to milliseconds).

The efficiency of energy transfer E can also be determined by measuring the intensity of sensitised emission (I_{ad}) and comparing it to the residual donor emission with acceptor (I_{da}):

$$E = (\frac{I_{ad}}{Q_a}) \Big/ (\frac{I_{ad}}{Q_a} + \frac{I_{da}}{Q_{Ln}}) \quad (10)$$

Eq (10) shows E is defined as the number of donor excitations that lead to acceptor excitations, divided by the total number of donor excitations. The numerator in Eq (8) is the number of excitations of the acceptors due to energy transfer; the denominator is the total number of excitations of the lanthanide donor, obtained from lanthanide donor excitations leading to donor emission without energy transfer I_{da}/Q_{Ln} and lanthanide excitations leading to energy transfer for exciting acceptors I_{ad}/Q_a . From Eq (8) and (9), we can obtain the QY value for the doped lanthanide ions[181].

$$Q_{Ln} = Q_a \times I_{da} \times (\tau_d - \tau_{ad})/(I_{ad} \times \tau_{ad}) \quad (11)$$

To measure I_{da} , I_{ad} and lifetimes τ_d and τ_{ad} , Selvin *et al.* used a home-built spectrometer system capable of measuring time-gated emission spectra and excited state lifetimes. For the time-gating measurement using a CCD as detector, a mechanical chopper was included in the emission path, generating a TTL signal to trigger the laser. When using the PMT as a detector, a function generator synchronised the laser and detector [182].

This method provides a simple and robust method for measuring the quantum yield of doped/linked lanthanide ions, with excellent precision. However, it strongly depends on the accuracy of the value of Q_a .

1.3.2.2 Lifetime-based application techniques

(1) Lifetime-Based Imaging Microscopy

Lifetime imaging microscopy (LIM), commonly called fluorescence lifetime imaging microscopy (FLIM), is an imaging technique for generating an image on the basic of the different fluorescence lifetimes from probes.

To capture one LIM image, three steps are required. Firstly, to capture the luminescence decay curves. All lifetime measurement methods can be employed for each pixel, including TCSPC, time-gating photon tracking method and phase modulation method, decay sampling method and pinhole shift method. Note that the LIM system using the decay sampling method to capture lifetime decay is also called

temporal sampling lifetime imaging microscopy (TSLIM); and the LIM system using the pinhole shift method is named pinhole shift lifetime imaging microscopy (PSLIM). Secondly, to extract lifetime values from the captured decay curves using the least squares iterative re-convolution method or called rapid lifetime determination (RLD) methods. Finally, it is the transformation of luminescence lifetimes into a colour code, so that different lifetime values are expressed by different colours and shown in one image, from which the obvious contrast among the mixture fluorophores can readily be distinguished.

In 2010, Frida *et al.* demonstrated that the frequency domain FLIM can be applied to monitor the long-lived (several microseconds) excited states of Ruthenium complex enantiomers in live and fixed cells [183]. The Maury group applied a TSLIM and PSLIM combined system to image cells stained by Eu based long-lived luminescence bio-probes $[Na]_3[EuL^{1G}_3]$ with millisecond luminescence lifetime [184]. Dragavon *et al.* applied FLIM-based detection of oxygen-sensitive porphyria microspheres with lifetime of tens of microseconds to study the effect of pathogenic bacteria on living macrophages [185]. In 2011, Becker *et al.* provided a lifetime imaging technique that simultaneously recorded fluorescence and phosphorescence lifetime images in laser scanning systems, which is based on modulating a high-frequency pulsed laser. Within one cycle, a high frequency pulsed laser is turned on only for a short period at the beginning of each pixel, and is turned off for the rest of the pixel time. This short period of laser "on" time allows the generation and collection of shorted-lived fluorescence decay, meanwhile building up the long-lived phosphorescence. When the laser is turned off, the phosphorescence decay can be collected [186]. In 2014, Baggaley *et al.* described "two-photon time-resolved emission imaging microscopy (TP-TREM)" based on a LIM system with the capability of discrimination between shorted-lived fluorescent and long-lived phosphorescent labels in multiply-stained cells and tissues. This system is a fluorescence/phosphorescence lifetime imaging microscope employing multiphoton excitation. The system was demonstrated by imaging long-lived (several microseconds) PtL^1Cl and short-lived (2.2 ns) Hoechst-33342 co-labelled live CHO-K1 cells in different detection windows, with lifetime images from constructed during 0~50 ns and 50~2000 ns timescales exactly matched with their corresponding intensity images [187].

Lifetime imaging systems are relatively unaffected by variations in chromophore concentrations or attenuation due to the sample absorption and the effect of photon scattering in thick layers of sample. Moreover, pulsed illumination allows the background free-detection for long-lived luminescence detection in each pixel. The detection resolution, accuracy and speed depend on the methods of lifetime measurement.

(2) Lifetime-Based Multiplexing Technique

The lifetime multiplexing technique takes advantage of different luminescence lifetimes instead of different emission colours to distinguish different probes or targets, adding a new dimension to multiplexing techniques [75].

In 2014, Lu *et al.* provided this new multiplexing concept by creating a temporal coding and decoding dimension. To demonstrate this concept, they first deliberately synthesised a series of sensitiser (Yb^{3+}) and activator (Tm^{3+}) doped upconversion nanocrystals with luminescence lifetimes in the range from tens to hundreds of microseconds, as shown in Figure 1-23, by adjusting the dopant concentrations of either activator (Tm^{3+}) or sensitiser (Yb^{3+}). They then applied three types of upconversion nanocrystals with three different lifetimes to demonstrate the lifetime decoding capability for document security as a blended picture composed of superimposed images printed by three different types of nanocrystals doped with different emitter concentrations as ink, as shown in Figure 1-24 (a). These three images could be distinguished separately using lifetime decoding method, shown in Figure 1-24 (b), but could not be distinguished by their intensities [75].

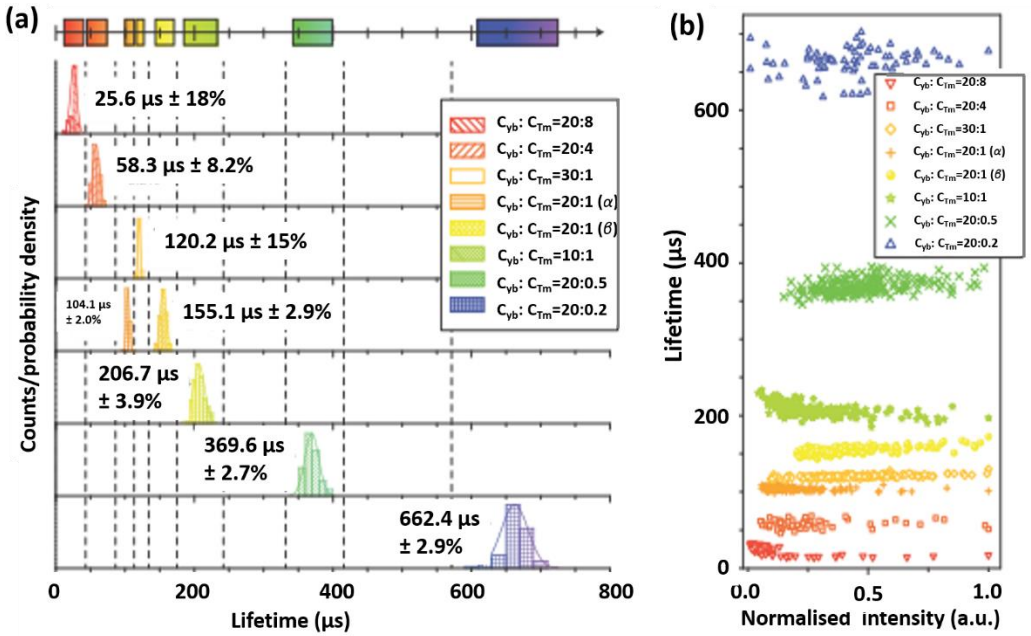

Figure 1-23. Lifetime encoded population of microspheres with unique lifetime identities. Emitter (Tm) variation within 0.2-8 mol% with constant Yb sensitizer (20 mol%) resulted in lifetime changes from 25.6 µs to 662.4 µs in the blue band. While when the Yb dopant concentration increased from 10 to 30 mol% with constant doping of Tm emitters (1 mol %), the blue emission remarkably decayed from 206.7 µs to 120.2 µs. Reprinted from Ref.[75].

According to the authors, several advantages of the lifetime multiplexing technique based on lanthanide doped nanocrystals can be summarised. Firstly, optical photo-stability resulting from the lanthanide probes; secondly, background-free detection deriving from the time-resolved detection of long-lived luminescence, avoiding the autofluorescence; thirdly, lifetime decoding is independent of the intensity, therefore less sensitive to the electronic noise, signal collection efficiency and other intensity-related factors; fourthly, combination with existing technique FLIM enables effective bio-imaging or bio-diagnostics; and finally, a simple optical system is required. One of the limitations of this technique is that the lanthanide probes must be individually synthesed with distinctive lifetimes.

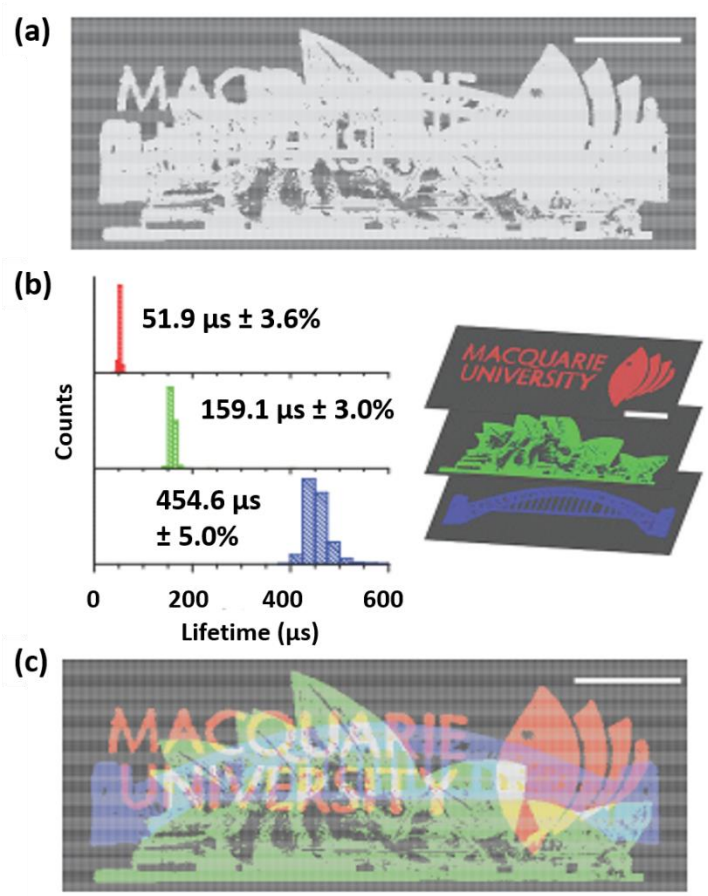

Figure 1-24. Demonstration of lifetime-encoded document security and photonic data storage. a: three overlapping patterns were prepared by three different nanocrystals with different emission lifetimes; b: decoded image using lifetime decoding method; c: pseudo-colour is applied to indicate the luminescence lifetimes. Reprinted from Ref. [75].

1.3.3 Summary

In this section, we review the commonly applied optical instruments/techniques from lifetime measurement to the long-lifetime based applications.We introduced the working principles and then some typical applications for both optical characterisation and sensing/bio-imaging application purposes.

1.4 Conclusions

Long-lived luminescence materials with good photo-stability, long luminescence lifetime and sharp narrow linewidth emission lines have been extensively explored and developed for lasers, sensing, bio-detection and bio-imaging applications. This has driven the rapid innovation and development of optical techniques for characterising their detailed luminescence properties and exploring their potential applications in different sensing and lighting fields.

We review the wide range of time-resolved luminescence techniques in the microsecond region aiming to provide a comprehensive and accurate introduction to the state of art optical instruments suitable for characterisation and application of long-lived luminescence materials. We first gave a brief review of long-lifetime luminescent materials and their luminescent mechanisms, and then illustrate the TGL technique based optical instruments. Further, we reviewed methods for lifetime measurements in the microsecond region, followed by showcasing the recent developments of time-resolved luminescence (TRL) techniques and relevant applications. This work aims to provide an overall introduction to techniques using long-lived luminescence materials as probes for researchers who are involved in this field, and a general understanding for those beyond this field.

1.5 References

[1] RC Leif SC, HG Gratzner, HG Haines, KV Rao, LM Vallarino. Automation of Uterine Cancer Cytology. Chicago, Ill. Wied, George L: Tutorials of Cytology; 1976.
[2] Soini E, Hemmila I. Fluoroimmunoassay: present status and key problems. Clinical chemistry. 1979;25:353-61.
[3] Charbonniere LJ, Hildebrandt N, Ziessel RF, Loehmannsroeben HG. Lanthanides to quantum dots resonance energy transfer in time-resolved fluoro-immunoassays and luminescence microscopy. Journal of the American Chemical Society. 2006;128:12800-9.
[4] Sueda S, Yuan JL, Matsumoto K. Homogeneous DNA hybridization assay by using europium luminescence energy transfer. Bioconjugate Chem. 2000;11:827-31.
[5] Bunzli JCG. Lanthanide Luminescence for Biomedical Analyses and Imaging. Chemical reviews. 2010;110:2729-55.
[6] Lu YQ, Jin DY, Leif RC, Deng W, Piper JA, Yuan JL, et al. Automated detection of rare-event pathogens through time-gated luminescence scanning microscopy. Cytom Part A. 2011;79A:349-55.
[7] Pershagen E, Nordholm J, Borbas KE. Luminescent Lanthanide Complexes with Analyte-Triggered Antenna Formation. Journal of the American Chemical Society. 2012;134:9832-5.
[8] Wang F, Han Y, Lim CS, Lu Y, Wang J, Xu J, et al. Simultaneous phase and size control of upconversion nanocrystals through lanthanide doping. Nature. 2010;463:1061-5.
[9] Zhang YH, Zhang LX, Deng RR, Tian J, Zong Y, Jin DY, et al. Multicolor Barcoding in a Single Upconversion Crystal. Journal of the American Chemical Society. 2014;136:4893-6.
[10] Zhao J, Jin D, Schartner EP, Lu Y, Liu Y, Zvyagin AV, et al. Single-nanocrystal sensitivity achieved by enhanced upconversion luminescence. Nature nanotechnology. 2013;8:729-34.
[11] Yuan JL, Wang GL, Majima K, Matsumoto K. Synthesis of a terbium fluorescent chelate and its application to time-resolved fluoroimmunoassay. Analytical chemistry. 2001;73:1869-76.
[12] Picot A, D'Aleo A, Baldeck PL, Grichine A, Duperray A, Andraud C, et al. Long-lived two-photon excited luminescence of water-soluble europium complex: Applications in biological imaging using two-photon scanning microscopy. Journal of the American Chemical Society. 2008;130:1532-+.
[13] Hanaoka K, Kikuchi K, Kobayashi S, Nagano T. Time-resolved long-lived luminescence imaging method employing luminescent lanthanide probes with a new microscopy system. Journal of the American Chemical Society. 2007;129:13502-9.
[14] Stohr RJ, Kolesov R, Xia KW, Reuter R, Meijer J, Logvenov G, et al. Super-resolution Fluorescence Quenching Microscopy of Graphene. Acs Nano. 2012;6:9175-81.
[15] Kolesov R, Reuter R, Xia KW, Stohr R, Zappe A, Wrachtrup J. Super-resolution upconversion microscopy of praseodymium-doped yttrium aluminum garnet nanoparticles. Physical Review B. 2011;84.
[16] Qin W, Liu H, Guyot-Sionnest P. Small Bright Charged Colloidal Quantum Dots. Acs Nano. 2014;8:283-91.

[17] Ghosh S, Chizhik AM, Karedla N, Dekaliuk MO, Gregor I, Schuhmann H, et al. Photoluminescence of Carbon Nanodots: Dipole Emission Centers and Electron-Phonon Coupling. Nano letters. 2014;14:5656-61.
[18] Schell AW, Engel P, Werra JFM, Wolff C, Busch K, Benson O. Scanning Single Quantum Emitter Fluorescence Lifetime Imaging: Quantitative Analysis of the Local Density of Photonic States. Nano letters. 2014;14:2623-7.
[19] Wu HY, Hu YH, Wang YH, Fu CJ. Influence on the luminescence properties of the lattice defects in Sr2MgSi2O7:Eu2+, M (M = Dy3+, La3+ or Na1+). J Alloy Compd. 2010;497:330-5.
[20] Lichtman JW, Conchello JA. Fluorescence microscopy. Nature methods. 2005;2:910-9.
[21] Salinas-Castillo A, Calahorro AJ, Choquesillo-Lazarte D, Seco JM, Rodriguez-Dieguez A. A new 2D cadmium chloride network with 2-aminopyrimidine displaying long lifetime photoluminescence emission. Polyhedron. 2011;30:1295-8.
[22] Ahern JC, Shilabin A, Henline KM, Pike RD, Patterson HH. Photophysical properties of {[Ag(CN)(2)](-)}(2) complexes trapped in a supramolecular electron-acceptor organic framework. Dalton T. 2014;43:12044-9.
[23] Guo XQ, Castellano FN, Li L, Lakowicz JR. Use of a long lifetime Re(I) complex in fluorescence polarization immunoassays of high-molecular weight analytes. Analytical chemistry. 1998;70:632-7.
[24] Hung FF, To WP, Zhang JJ, Ma CS, Wong WY, Che CM. Water-Soluble Luminescent Cyclometalated Gold(III) Complexes with cis-Chelating Bis(N-Heterocyclic Carbene) Ligands: Synthesis and Photophysical Properties. Chem-Eur J. 2014;20:8604-14.
[25] Lu Y, Lu J, Zhao J, Cusido J, Raymo FM, Yuan J, et al. On-the-fly decoding luminescence lifetimes in the microsecond region for lanthanide-encoded suspension arrays. Nature communications. 2014;5:3741.
[26] Zhao J, Lu Z, Yin Y, McRae C, Piper JA, Dawes JM, et al. Upconversion luminescence with tunable lifetime in NaYF4:Yb,Er nanocrystals: role of nanocrystal size. Nanoscale. 2013;5:944-52.
[27] Xu YY, Hemmila IA. Co-Fluorescence Enhancement System Based on Pivaloyltrifluoracetone and Yttrium for the Simultaneous Detection of Europium, Terbium, Samarium and Dysprosium. Anal Chim Acta. 1992;256:9-16.
[28] Xu YY, Hemmila I, Mukkala VM, Holttinen S, Lovgren T. Co-fluorescence of europium and samarium in time-resolved fluorimetric immunoassays. The Analyst. 1991;116:1155-8.
[29] Yuan JL, Matsumoto K, Kimura H. A new tetradentate beta-diketonate-Europium chelate that can be covalently bound to proteins for time-resolved fluoroimmunoasaay. Analytical chemistry. 1998;70:596-601.
[30] Hennink EJ, deHaas R, Verwoerd NP, Tanke HJ. Evaluation of a time-resolved fluorescence microscope using a phosphorescent Pt-porphine model system. Cytometry. 1996;24:312-20.
[31] Lo KKW, Ng DCM, Chung CK. First Examples of Luminescent Cyclometalated Iridium(III) Complexes as Labeling Reagents for Biological Substrates (vol 20, pg 4999, 2001). Organometallics. 2012;31:5668-.
[32] Yang TS, Xia A, Liu QA, Shi M, Wu HZ, Xiong LQ, et al. Polymer nanoparticles with an embedded phosphorescent osmium(II) complex for cell imaging. J Mater Chem. 2011;21:5360-7.

[33] de Haas RR, van Gijlswijk RPM, van der Tol EB, Veuskens J, van Gijssel HE, Tijdens RB, et al. Phosphorescent platinum/palladium coproporphyrins for time-resolved luminescence microscopy. Journal of Histochemistry & Cytochemistry. 1999;47:183-96.
[34] Leung SK, Kwok KY, Zhang KY, Lo KKW. Design of Luminescent Biotinylation Reagents Derived from Cyclometalated Iridium(III) and Rhodium(III) Bis(pyridylbenzaldehyde) Complexes. Inorg Chem. 2010;49:4984-95.
[35] Zhang R, Ye ZQ, Yin YJ, Wang GL, Jin DY, Yuan JL, et al. Developing Red-Emissive Ruthenium(II) Complex-Based Luminescent Probes for Cellular Imaging. Bioconjugate Chem. 2012;23:725-33.
[36] Zhang L, Zheng X, Deng W, Lu Y, Lechevallier S, Ye Z, et al. Practical implementation, characterization and applications of a multi-colour time-gated luminescence microscope. Scientific reports. 2014;4:6597.
[37] Cui GF, Ye ZQ, Chen JX, Wang GL, Yuan JL. Development of a novel terbium(III) chelate-based luminescent probe for highly sensitive time-resolved luminescence detection of hydroxyl radical. Talanta. 2011;84:971-6.
[38] Nishioka T, Yuan JL, Yamamoto Y, Sumitomo K, Wang Z, Hashino K, et al. New luminescent europium(III) chelates for DNA labeling. Inorg Chem. 2006;45:4088-96.
[39] Georges J. Lanthanide-Sensitized Luminescence and Applications to the Determination of Organic Analytes - a Review. The Analyst. 1993;118:1481-6.
[40] Selvin PR. Principles and biophysical applications of lanthanide-based probes. Annu Rev Bioph Biom. 2002;31:275-302.
[41] Yuan JL, Wang GL. Lanthanide-based luminescence probes and time-resolved luminescence bioassays. Trac-Trend Anal Chem. 2006;25:490-500.
[42] Li M, Selvin PR. Luminescent Polyaminocarboxylate Chelates of Terbium and Europium - the Effect of Chelate Structure. Journal of the American Chemical Society. 1995;117:8132-8.
[43] Zhang L, Wang YJ, Ye ZQ, Jin DY, Yuan JL. New Class of Tetradentate beta-Diketonate-Europium Complexes That Can Be Covalently Bound to Proteins for Time-Gated Fluorometric Application. Bioconjugate Chem. 2012;23:1244-51.
[44] Jin D, Lu Y, Leif RC, Yang S, Rajendran M, Miller LW. How to build a time-gated luminescence microscope. Current protocols in cytometry / editorial board, J Paul Robinson, managing editor [et al]. 2014;67:Unit 2 22.
[45] Zhou HC, Kitagawa S. Metal-organic frameworks (MOFs). Chemical Society reviews. 2014;43:5415-8.
[46] James SL. Metal-organic frameworks. Chemical Society reviews. 2003;32:276-88.
[47] Lu WG, Jiang L, Feng XL, Lu TB. Three-Dimensional Lanthanide Anionic Metal-Organic Frameworks with Tunable Luminescent Properties Induced by Cation Exchange. Inorg Chem. 2009;48:6997-9.
[48] Wang SJ, Tian YW, You LX, Ding F, Meert KW, Poelman D, et al. Solvent-regulated assemblies of 1D lanthanide coordination polymers with the tricarboxylate ligand. Dalton T. 2014;43:3462-70.
[49] Lim GK, Wang J, Ng SC, Gan LM. Nanosized hydroxyapatite powders from microemulsions and emulsions stabilized by a biodegradable surfactant. J Mater Chem. 1999;9:1635-9.
[50] Deng W, Sudheendra L, Zhao J, Fu J, Jin D, Kennedy IM, et al. Upconversion in NaYF(4):Yb, Er nanoparticles amplified by metal nanostructures. Nanotechnology. 2011;22:325604.

[51] Lechevallier S, Hammer P, Caiut JMA, Mazeres S, Mauricot R, Verelst M, et al. APTES-Modified RE2O3:Eu3+ Luminescent Beads: Structure and Properties. Langmuir. 2012;28:3962-71.
[52] Banski M, Afzaal M, Podhorodecki A, Misiewicz J, Abdelhady AL, O'Brien P. Passivation of lanthanide surface sites in sub-10 nm NaYF4:Eu3+ nanocrystals. J Nanopart Res. 2012;14.
[53] Aarts L, Jaeqx S, van der Ende BM, Meijerink A. Downconversion for the Er3+, Yb3+ couple in KPb2Cl5-A low-phonon frequency host. Journal of Luminescence. 2011;131:608-13.
[54] Deng W, Jin DY, Drozdowicz-Tomsia K, Yuan JL, Wu J, Goldys EM. Ultrabright Eu-doped plasmonic Ag@SiO2 nanostructures: time-gated bioprobes with single particle sensitivity and negligible background. Adv Mater. 2011;23:4649-54.
[55] Zhuang J, Yang X, Fu J, Liang C, Wu M, Wang J, et al. Monodispersed β-NaYF4 Mesocrystals: In Situ Ion Exchange and Multicolor Up-and Down-Conversions. Crystal Growth & Design. 2013;13:2292-7.
[56] Wang F, Deng RR, Liu XG. Preparation of core-shell NaGdF4 nanoparticles doped with luminescent lanthanide ions to be used as upconversion-based probes. Nat Protoc. 2014;9:1634-44.
[57] Zheng SH, Chen WB, Tan DZ, Zhou JJ, Guo QB, Jiang W, et al. Lanthanide-doped NaGdF4 core-shell nanoparticles for non-contact self-referencing temperature sensors. Nanoscale. 2014;6:5675-9.
[58] Chen GY, Shen J, Ohulchanskyy TY, Patel NJ, Kutikov A, Li ZP, et al. (alpha-NaYbF4:Tm3+)/CaF2 Core/Shell Nanoparticles with Efficient Near-Infrared to Near-Infrared Upconversion for High-Contrast Deep Tissue Bioimaging. Acs Nano. 2012;6:8280-7.
[59] Zhou LJ, Zheng XP, Gu ZJ, Yin WY, Zhang X, Ruan LF, et al. Mesoporous NaYbF4@NaGdF4 core-shell up-conversion nanoparticles for targeted drug delivery and multimodal imaging. Biomaterials. 2014;35:7666-78.
[60] Sun Y, Zhu XJ, Peng JJ, Li FY. Core-Shell Lanthanide Upconversion Nanophosphors as Four-Modal Probes for Tumor Angiogenesis Imaging. Acs Nano. 2013;7:11290-300.
[61] Gruzintsev AN, Ermolaeva YV, Matveevskaya NA, Bezkrovnyi AS, Tolmachev AV, Emel'chenko GA. Size-dependent luminescence of spherical Y2O3:Er nanoparticles. Inorg Mater+. 2014;50:1099-103.
[62] Gruzintsev AN. Anti-stokes luminescence of Y2O3:Er. Inorg Mater+. 2014;50:58-62.
[63] Huan J, Hu LF, Fang XS. Dense Assembly of Gd2O3:0.05X(3+) (X = Eu, Tb) Nanorods into Nanoscaled Thin-Films and Their Photoluminescence Properties. Acs Appl Mater Inter. 2014;6:1462-9.
[64] Greybush NJ, Saboktakin M, Ye XC, Della Giovampaola C, Oh SJ, Berry NE, et al. Plasmon-Enhanced Upconversion Luminescence in Single Nanophosphor-Nanorod Heterodimers Formed through Template-Assisted Self-Assembly. Acs Nano. 2014;8:9482-91.
[65] Wang R, Zhang W, Xu YL, Xing LL. Upconversion emissions in ZnNb2O6:Ho3+/Yb3+ ceramics. Opt Laser Technol. 2014;58:52-5.
[66] Zhang Y, Li PF, Wang CW, Bao ZJ, Zhao QZ. Two-photon-excited upconversion luminescence of Mn2+-doped germanate glass by infrared femtosecond laser irradiation. Optical Materials. 2014;36:1890-3.

[67] Silva JR, Bueno LA, Gouveia-Neto AS. Multicolor frequency upconversion luminescence in Eu3+/Tb3+/Yb3+ -codoped fluorogermanate glass excited at 980 nm. Journal of Luminescence. 2014;154:531-4.
[68] Wang F, Liu XG. Upconversion multicolor fine-tuning: Visible to near-infrared emission from lanthanide-doped NaYF4 nanoparticles. Journal of the American Chemical Society. 2008;130:5642-+.
[69] Lu D, Cho SK, Ahn S, Brun L, Summers CJ, Park W. Plasmon enhancement mechanism for the upconversion processes in NaYF4:Yb(3+),Er(3+) nanoparticles: Maxwell versus Forster. Acs Nano. 2014;8:7780-92.
[70] Li XM, Wang R, Zhang F, Zhao DY. Engineering Homogeneous Doping in Single Nanoparticle To Enhance Upconversion Efficiency. Nano letters. 2014;14:3634-9.
[71] Mai HX, Zhang YW, Sun LD, Yan CH. Highly efficient multicolor up-conversion emissions and their mechanisms of monodisperse NaYF4 : Yb,Er core and core/shell-structured nanocrystals. J Phys Chem C. 2007;111:13721-9.
[72] Zhu WJ, Chen DQ, Lei L, Xu J, Wang YS. An active-core/active-shell structure with enhanced quantum-cutting luminescence in Pr-Yb co-doped monodisperse nanoparticles. Nanoscale. 2014;6:10500-4.
[73] Vetrone F, Naccache R, Mahalingam V, Morgan CG, Capobianco JA. The Active-Core/Active-Shell Approach: A Strategy to Enhance the Upconversion Luminescence in Lanthanide-Doped Nanoparticles. Advanced Functional Materials. 2009;19:2924-9.
[74] Zhang F, Che R, Li X, Yao C, Yang J, Shen D, et al. Direct imaging the upconversion nanocrystal core/shell structure at the subnanometer level: shell thickness dependence in upconverting optical properties. Nano letters. 2012;12:2852-8.
[75] Lu YQ, Zhao JB, Zhang R, Liu YJ, Liu DM, Goldys EM, et al. Tunable lifetime multiplexing using luminescent nanocrystals. Nature Photonics. 2014;8:33-7.
[76] <4-2007-chem-mater-Water-Soluble NaYF4Yb,Er(Tm)NaYF4Polymer.pdf>.
[77] Liu Q, Chen M, Sun Y, Chen GY, Yang TS, Gao Y, et al. Multifunctional rare-earth self-assembled nanosystem for tri-modal upconversion luminescence/fluorescence/positron emission tomography imaging. Biomaterials. 2011;32:8243-53.
[78] Zhang F, Braun GB, Shi YF, Zhang YC, Sun XH, Reich NO, et al. Fabrication of Ag@SiO2@Y2O3:Er Nanostructures for Bioimaging: Tuning of the Upconversion Fluorescence with Silver Nanoparticles. Journal of the American Chemical Society. 2010;132:2850-+.
[79] Cao TY, Yang Y, Gao YA, Zhou J, Li ZQ, Li FY. High-quality water-soluble and surface-functionalized upconversion nanocrystals as luminescent probes for bioimaging. Biomaterials. 2011;32:2959-68.
[80] Hashiguchi BG, Bischof SM, Konnick MM, Periana RA. Designing catalysts for functionalization of unactivated C-H bonds based on the CH activation reaction. Accounts of chemical research. 2012;45:885-98.
[81] Fagnou K, Lautens M. Halide effects in transition metal catalysis. Angewandte Chemie. 2002;41:27-47.
[82] Gennari M, Gerey B, Hall N, Pecaut J, Collomb MN, Rouzieres M, et al. A bio-inspired switch based on cobalt(II) disulfide/cobalt(III) thiolate interconversion. Angewandte Chemie. 2014;53:5318-21.
[83] Hughes TF, Friesner RA. Systematic investigation of the catalytic cycle of a single site ruthenium oxygen evolving complex using density functional theory. The journal of physical chemistry B. 2011;115:9280-9.

[84] Ding F, Harman WD. Stereoselective tandem 1,4-addition reactions for benzenes: a comparison of Os(II), Re(I), and W(0) systems. Journal of the American Chemical Society. 2004;126:13752-6.
[85] Keane JM, Chordia MD, Mocella CJ, Sabat M, Trindle CO, Harman WD. Transition metal-stabilized arenium cations: protonation of arenes dihapto-coordinated to pi-basic metal fragments. Journal of the American Chemical Society. 2004;126:6806-15.
[86] Fernandez-Moreira V, Thorp-Greenwood FL, Coogan MP. Application of d(6) transition metal complexes in fluorescence cell imaging. Chemical communications. 2010;46:186-202.
[87] Berezin MY, Achilefu S. Fluorescence lifetime measurements and biological imaging. Chemical reviews. 2010;110:2641-84.
[88] Kim MS, Kim JH, Son BW, Kang JS. Dynamics of Bacteriophage R17 Probed with a Long-Lifetime Ru(II) Metal-Ligand Complex. J Fluoresc. 2010;20:713-8.
[89] Zhao Q, Huang CH, Li FY. Phosphorescent heavy-metal complexes for bioimaging. Chemical Society reviews. 2011;40:2508-24.
[90] Mali B, Dragan AI, Karolin J, Geddes CD. Photophysical Characterization and alpha-Type Delayed Luminescence of Rapidly Prepared Au Clusters. J Phys Chem C. 2013;117:16650-7.
[91] Gao S, Fan RQ, Qiang LS, Wang P, Chen S, Wang XM, et al. Effects of solvents and temperature on the luminescence properties of Cd-isonicotinic acid frameworks based on mono-, bi-, and trinuclear cluster units. Crystengcomm. 2014;16:1113-25.
[92] Maza WA, Morris AJ. Photophysical Characterization of a Ruthenium(II) Tris(2,2 ' bipyridine)-Doped Zirconium UiO-67 Metal Organic Framework. J Phys Chem C. 2014;118:8803-17.
[93] Enkvist E, Vaasa A, Kasari M, Kriisa M, Ivan T, Ligi K, et al. Protein-Induced Long Lifetime Luminescence of Nonmetal Probes. Acs Chem Biol. 2011;6:1052-62.
[94] Kasari M, Padrik P, Vaasa A, Saar K, Leppik K, Soplepmann J, et al. Time-gated luminescence assay using nonmetal probes for determination of protein kinase activity-based disease markers. Anal Biochem. 2012;422:79-88.
[95] Xiong XQ, Song FL, Wang JY, Zhang YK, Xue YY, Sun LL, et al. Thermally Activated Delayed Fluorescence of Fluorescein Derivative for Time-Resolved and Confocal Fluorescence Imaging. Journal of the American Chemical Society. 2014;136:9590-7.
[96] Jin D, Piper JA. Time-gated luminescence microscopy allowing direct visual inspection of lanthanide-stained microorganisms in background-free condition. Analytical chemistry. 2011;83:2294-300.
[97] Marriott G, Heidecker M, Diamandis EP, Yanmarriott Y. Time-Resolved Delayed Luminescence Image Microscopy Using an Europium Ion Chelate Complex. Biophys J. 1994;67:957-65.
[98] Verwoerd NP, Hennink EJ, Bonnet J, Vandergeest CRG, Tanke HJ. Use of Ferroelectric Liquid-Crystal Shutters for Time-Resolved Fluorescence Microscopy. Cytometry. 1994;16:113-7.
[99] Phimphivong S, Kolchens S, Edmiston PL, Saavedra SS. Time-Resolved, Total Internal-Reflection Fluorescence Microscopy of Cultured-Cells Using a Tb Chelate Label. Anal Chim Acta. 1995;307:403-17.

[100] de Haas RR, van Gijlswijk RPM, van der Tol EB, Zijlmans HJMAA, Bakker-Schut T, Bonnet J, et al. Platinum Porphyrins as Phosphorescent Label for Time-resolved Microscopy. Journal of Histochemistry & Cytochemistry. 1997;45:1279-92.
[101] Beverloo HB, Vanschadewijk A, Vangelderenboele S, Tanke HJ. Inorganic phosphors as new luminescent labels for immunocytochemistry and time-resolved microscopy. Cytometry. 1990;11:784-92.
[102] Connally R, Veal D, Piper J. Flash lamp-excited time-resolved fluorescence microscope suppresses autofluorescence in water concentrates to deliver an 11-fold increase in signal-to-noise ratio. Journal of biomedical optics. 2004;9:725-34.
[103] Seveus L, Vaisala M, Syrjanen S, Sandberg M, Kuusisto A, Harju R, et al. Time-resolved fluorescence imaging of europium chelate label in immunohistochemistry and in situ hybridization. Cytometry. 1992;13:329-38.
[104] Vereb G, Jares-Erijman E, Selvin PR, Jovin TM. Temporally and spectrally resolved imaging microscopy of lanthanide chelates. Biophys J. 1998;74:2210-22.
[105] Connally R, Veal D, Piper J. High resolution detection of fluorescently labeled microorganisms in environmental samples using time-resolved fluorescence microscopy. FEMS microbiology ecology. 2002;41:239-45.
[106] deHaas RR, Verwoerd NP, vanderCorput MP, vanGijlswijk RP, Siitari H, Tanke HJ. The use of peroxidase-mediated deposition of biotin-tyramide in combination with time-resolved fluorescence imaging of europium chelate label in immunohistochemistry and in situ hybridization. Journal of Histochemistry & Cytochemistry. 1996;44:1091-9.
[107] Seveus L, Vaisala M, Hemmila I, Kojola H, Roomans GM, Soini E. Use of Fluorescent Europium Chelates as Labels in Microscopy Allows Glutaraldehyde Fixation and Permanent Mounting and Leads to Reduced Autofluorescence and Good Long-Term Stability. Microscopy research and technique. 1994;28:149-54.
[108] Connally R, Jin D, Piper J. High intensity solid-state UV source for time-gated luminescence microscopy. Cytometry A. 2006;69:1020-7.
[109] Leif RC, Yang S, Jin DY, Piper J, Vallarino LM, Williams JW, et al. Calibration beads containing luminescent lanthanide ion complexes. Journal of biomedical optics. 2009;14.
[110] Hamey LGC, Connally RE, Yen SWT, Lawson TS, Piper JA, Iredell J. Luminescent Microspheres Resolved from Strong Background on an Automated Time-Gated Luminescence Microscopy Workstation. 2009 Digital Image Computing: Techniques and Applications (Dicta 2009). 2009:223-8.
[111] Leif RC, Yang S, Lu YQ, Jin DY, Chambers S. A cost-effective analog method to produce time-gated luminescence images. Imaging, Manipulation, and Analysis of Biomolecules, Cells, and Tissues X. 2012;8225.
[112] Jin DY. Demonstration of true-color high-contrast microorganism imaging for terbium bioprobes. Cytom Part A. 2011;79A:392-7.
[113] Connally R, Piper J. Solid-state time-gated luminescence microscope with ultraviolet light-emitting diode excitation and electron-multiplying charge-coupled device detection. Journal of biomedical optics. 2008;13.
[114] Gahlaut N, Miller LW. Time-resolved microscopy for imaging lanthanide luminescence in living cells. Cytom Part A. 2010;77A:1113-25.
[115] Ghose S, Trinquet E, Laget M, Bazin H, Mathis G. Rare earth cryptates for the investigation of molecular interactions in vitro and in living cells. J Alloy Compd. 2008;451:35-7.

[116] Kenjiro Hanaoka KK, ‡ Shigeru Kobayashi,§ and Tetsuo Nagano*,†. Time-Resolved Long-Lived Luminescence Imaging Method. J AM CHEM SOC. 2007;129:8.
[117] Marriott G, Clegg RM, Arndtjovin DJ, Jovin TM. Time Resolved Imaging Microscopy - Phosphorescence and Delayed Fluorescence Imaging. Biophys J. 1991;60:1374-87.
[118] Beverloo HB, Vanschadewijk A, Bonnet J, Vandergeest R, Runia R, Verwoerd NP, et al. Preparation and Microscopic Visualization of Multicolor Luminescent Immunophosphors. Cytometry. 1992;13:561-70.
[119] Seveus L, Vaisala M, Syrjanen S, Sandberg M, Kuusisto A, Harju R, et al. Time-Resolved Fluorescence Imaging of Europium Chelate Label in Immunohistochemistry and Insitu Hybridization. Cytometry. 1992;13:329-38.
[120] Connally R. A Device for Gated Autosynchronous Luminescence Detection. Analytical chemistry. 2011;83:4782-7.
[121] Lakowicz JR. Principles of fluorescence spectroscopy. 2nd ed. New York: Kluwer Academic/Plenum; 1999.
[122] Soini E, Kojola H. Time-resolved fluorometer for lanthanide chelates--a new generation of nonisotopic immunoassays. Clinical chemistry. 1983;29:65-8.
[123] Siitari H, Hemmila I, Soini E, Lovgren T, Koistinen V. Detection of Hepatitis-B Surface-Antigen Using Time-Resolved Fluoroimmunoassay. Nature. 1983;301:258-60.
[124] Ristiniemi N, Qin QP, Lindstrom V, Grubb A, Pettersson K. Quantification of cystatin C by time-resolved fluorometry-based immunoassays. Journal of immunological methods. 2012;378:56-61.
[125] Hagan AK, Zuchner T. Lanthanide-based time-resolved luminescence immunoassays. Analytical and bioanalytical chemistry. 2011;400:2847-64.
[126] Yeo KT, Bateman SW, Brownlee M, Beisswenger PJ. Development of a dissociation-enhanced lanthanide fluoroimmunoassay (DELFIA) for methylglyoxal-derived advanced glycation end-products. Clinical chemistry. 2001;47:A19-A20.
[127] Sammes PG, Yahioglu G. Modern bioassays using metal chelates as luminescent probes. Nat Prod Rep. 1996;13:1-28.
[128] Diamandis EP, Christopoulos TK. Europium Chelate Labels in Time-Resolved Fluorescence Immunoassays and DNA Hybridization Assays. Analytical chemistry. 1990;62:A1149-&.
[129] Bazin H, Trinquet E, Mathis G. Time resolved amplification of cryptate emission: a versatile technology to trace biomolecular interactions. Journal of biotechnology. 2002;82:233-50.
[130] Kimura H, Mukaida M, Wang GL, Yuan JL, Matsumoto K. Dual-label time-resolved fluoroimmunoassay of psychopharmaceuticals and stimulants in serum. Forensic Sci Int. 2000;113:345-51.
[131] Christopoulos TK, Diamandis EP. Enzymatically Amplified Time-Resolved Fluorescence Immunoassay with Terbium Chelates. Analytical chemistry. 1992;64:342-6.
[132] Jiang S, Zhang Y. Upconversion Nanoparticle-Based FRET System for Study of siRNA in Live Cells. Langmuir. 2010;26:6689-94.
[133] Zijlmans HJMAA, Bonnet J, Burton J, Kardos K, Vail T, Niedbala RS, et al. Detection of cell and tissue surface antigens using up-converting phosphors: A new reporter technology. Anal Biochem. 1999;267:30-6.

[134] Hampl J, Hall M, Mufti NA, Yao YM, MacQueen DB, Wright WH, et al. Upconverting phosphor reporters in immunochromatographic assays. Anal Biochem. 2001;288:176-87.
[135] Zheng W, Zhou SY, Chen Z, Hu P, Liu YS, Tu DT, et al. Sub-10nm Lanthanide-Doped CaF2 Nanoprobes for Time-Resolved Luminescent Biodetection. Angew Chem Int Edit. 2013;52:6671-6.
[136] Huang P, Zheng W, Zhou S, Tu D, Chen Z, Zhu H, et al. Lanthanide-doped LiLuF(4) upconversion nanoprobes for the detection of disease biomarkers. Angewandte Chemie. 2014;53:1252-7.
[137] Connally RE, Piper JA. Time-gated luminescence microscopy. Annals of the New York Academy of Sciences. 2008;1130:106-16.
[138] Leif RC, Yang SA. An analog method to produce time-gated images. Imaging, Manipulation, and Analysis of Biomolecules, Cells, and Tissues Viii. 2010;7568.
[139] Jin DY, Piper J, Yuan JL, Leif R. Time-gated real-time bioimaging system using multicolor microsecond-lifetime silica nanoparticles. Imaging, Manipulation, and Analysis of Biomolecules, Cells, and Tissues Viii. 2010;7568.
[140] Jin. D Y LYQ, Leif. R C, Yang. S, Rajendran. M, Miller. L W. . Current Protocols in Cytometry. Current Protocols in Cytometry. Wiley online library2014. p. 67: 2.22:2..1–2..36.
[141] Lu Y, Xi P, Piper JA, Huo Y, Jin D. Time-gated orthogonal scanning automated microscopy (OSAM) for high-speed cell detection and analysis. Scientific reports. 2012;2:837.
[142] Lu J, Martin J, Lu Y, Zhao J, Yuan J, Ostrowski M, et al. Resolving low-expression cell surface antigens by time-gated orthogonal scanning automated microscopy. Analytical chemistry. 2012;84:9674-8.
[143] Ramshesh VK. Pinhole shifting lifetime imaging microscopy. Journal of biomedical optics. 2008;13.
[144] Shapiro HM. Practical flow cytometry. fourth ed: A John Wiley & Sons, INC., publication; 2002.
[145] Ferrari BC, Stoner K, Bergquist PL. Applying fluorescence based technology to the recovery and isolation of Cryptosporidium and Giardia from industrial wastewater streams. Water Research. 2006;40:541-8.
[146] Mcclelland RG, Pinder AC. Detection of Low-Levels of Specific Salmonella Species by Fluorescent-Antibodies and Flow-Cytometry. Journal of Applied Bacteriology. 1994;77:440-7.
[147] Veal DA, Deere D, Ferrari B, Piper J, Attfield PV. Fluorescence staining and flow cytometry for monitoring microbial cells. Journal of Immunological Methods. 2000;243:191-210.
[148] Leif R, Vallarino L. Rare-earth chelates as fluorescent markers in cell separation and analysis. In: DS K, P T, editors. Cell Separation Science and Technology, ACS Symposium Series 464, American Chemical Society1991. p. 41-58.
[149] Leif R, Clay SP, Gratzner HG, Haines HG, Rao KV, Vallarino LM. Markers for Instrumental Evaluation of Cells of the Female Reproductive Tract: Existing and New Markers. In: Wied GL, Bahr GF, Bartels PH, editors. The Automation of Uterine Cancer Cytology, Chicago1976. p. 313-44.
[150] Condrau MA, Schwendener RA, Niederer P, Anliker M. Time-Resolved Flow-Cytometry for the Measurement of Lanthanide Chelate Fluorescence .1. Concept and Theoretical Evaluation. Cytometry. 1994;16:187-94.

[151] Condrau MA, Schwendener RA, Zimmermann M, Muser MH, Graf U, Niederer P, et al. Time-Resolved Flow-Cytometry for the Measurement of Lanthanide Chelate Fluorescence .2. Instrument Design and Experimental Results. Cytometry. 1994;16:195-205.
[152] Jin D, Connally R, Piper J. Practical Time-Gated Luminescence Flow Cytometry: II. Experimental Evaluation Using UV LED Excitation. Cytometry Part A. 2007;71A:797-808.
[153] Jin D, Connally R, Piper J. Practical Time-Gated Luminescence Flow Cytometry: I. Concepts. Cytometry Part A. 2007;71A:783-96.
[154] Jin DY, Piper JA, Leif RC, Yang S, Ferrari BC, Yuan JL, et al. Time-gated flow cytometry: an ultra-high selectivity method to recover ultra-rare-event mu-targets in high-background biosamples. Journal of biomedical optics. 2009;14.
[155] Jin D, Ferrari B, Leif R, Yang S, Vallarino LM, WilliamS J, et al. UV LED excited time-gated luminescence flow cytometry: Evaluation for rare-event particle counting - art. no. 68590O. P Soc Photo-Opt Ins. 2008;6859:O8590-O.
[156] Perfetto SP, Chattopadhyay PK, Roederer M. Innovation - Seventeen-colour flow cytometry: unravelling the immune system. Nat Rev Immunol. 2004;4:648-U5.
[157] Ferrari BC, Attfield PV, Veal DA, Bell PJ. Application of the novel fluorescent dye Beljian red to the differentiation of Giardia cysts. J Microbiol Meth. 2003;52:133-5.
[158] Vesey G, Hutton P, Champion A, Ashbolt N, Williams KL, Warton A, et al. Application of Flow Cytometric Methods for the Routine Detection of Cryptosporidium and Giardia in Water. Cytometry. 1994;16:1-6.
[159] Galbraith W, Wagner MCE, Chao J, Abaza M, Ernst LA, Nederlof MA, et al. Imaging Cytometry by Multiparameter Fluorescence. Cytometry. 1991;12:579-96.
[160] Liu LX, Li YH, Sun LG, Li H, Peng X, Qu JL. Fluorescence lifetime imaging microscopy using a streak camera. Multiphoton Microscopy in the Biomedical Sciences Xiv. 2014;8948.
[161] Biskup C, Zimmer T, Kelbauskas L, Hoffmann B, Klocker N, Becker W, et al. Multi-dimensional fluorescence lifetime and FRET measurements. Microscopy research and technique. 2007;70:442-51.
[162] Kato T, Kashida H, Kishida H, Yada H, Okamoto H, Asanuma H. Development of a Robust Model System of FRET using Base Surrogates Tethering Fluorophores for Strict Control of Their Position and Orientation within DNA Duplex. Journal of the American Chemical Society. 2013;135:741-50.
[163] Lakowicz JR. Principles of Fluorescence Spectroscopy. 3rd ed: Springer; 2006.
[164] Bennett R. Instrument to measure fluorescence lifetimes in the millimicrosecond region. Review of Scientific Instruments. 1960;31:1275-9.
[165] Holton MD, Silvestre OR, Errington RJ, Smith PJ, Matthews DR, Rees P, et al. Stroboscopic fluorescence lifetime imaging. Opt Express. 2009;17:5205-16.
[166] James DR, Siemiarczuk A, Ware WR. Stroboscopic Optical Boxcar Technique for the Determination of Fluorescence Lifetimes. Review of Scientific Instruments. 1992;63:1710-6.
[167] Brown Jr G. Simplified system for the measurement of fluorescence lifetimes using the stroboscopic method. Review of Scientific Instruments. 1963;34:414-5.
[168] Sergent N, Levitt JA, Green M, Suhling K. Rapid wide-field photon counting imaging with microsecond time resolution. Opt Express. 2010;18:25292-8.

[169] Suhling K, French PM, Phillips D. Time-resolved fluorescence microscopy. Photochemical & photobiological sciences : Official journal of the European Photochemistry Association and the European Society for Photobiology. 2005;4:13-22.
[170] Principles of fluorescence spectroscopy. Choice: Current Reviews for Academic Libraries. 2007;44:1196-.
[171] Hyppanen I, Soukka T, Kankare J. Frequency-Domain Measurement of Luminescent Lanthanide Chelates. Journal of Physical Chemistry A. 2010;114:7856-67.
[172] Chandler DE, Majumdar ZK, Heiss GJ, Clegg RM. Ruby crystal for demonstrating time- and frequency-domain methods of fluorescence lifetime measurements. J Fluoresc. 2006;16:793-807.
[173] Nunez V, Upadhyayula S, Millare B, Larsen JM, Hadian A, Shin S, et al. Microfluidic Space-Domain Time-Resolved Emission Spectroscopy of Terbium(III) and Europium(III) Chelates with Pyridine-2,6-Dicarboxylate. Analytical chemistry. 2013;85:4567-77.
[174] DeRosa MC, Crutchley RJ. Photosensitized singlet oxygen and its applications. Coordin Chem Rev. 2002;233:351-71.
[175] McCleverty JA. Chemistry of nitric oxide relevant to biology. Chemical reviews. 2004;104:403-18.
[176] Chen HL, Zhao Q, Wu YB, Li FY, Yang H, Yi T, et al. Selective phosphorescence chemosensor for homocysteine based on an iridium(III) complex. Inorg Chem. 2007;46:11075-81.
[177] Qin F, Zhao H, Duan QQ, Cai W, Zhang ZG, Cao WW. New method for measuring time-resolved spectra of lanthanide emission using square-wave excitation. Review of Scientific Instruments. 2013;84.
[178] Liu Q, Feng W, Li FY. Water-soluble lanthanide upconversion nanophosphors: Synthesis and bioimaging applications in vivo. Coordin Chem Rev. 2014;273:100-10.
[179] Zhang L, McKay A, Jin D. High-throughput 3-dimensional time-resolved spectroscopy: simultaneous characterisation of luminescence properties in spectral and temporal domains. RSC Advances. 2013;3:8670-3.
[180] Zhang LX, Mckay A, Jin DY. High-throughput 3-dimensional time-resolved spectroscopy: simultaneous characterisation of luminescence properties in spectral and temporal domains. Rsc Advances. 2013;3:8670-3.
[181] Xiao M, Selvin PR. Quantum yields of luminescent lanthanide chelates and far-red dyes measured by resonance energy transfer. Journal of the American Chemical Society. 2001;123:7067-73.
[182] Xiao M, Selvin PR. An improved instrument for measuring time-resolved lanthanide emission and resonance energy transfer. Review of Scientific Instruments. 1999;70:3877-81.
[183] Svensson FR, Abrahamsson M, Stromberg N, Ewing AG, Lincoln P. Ruthenium(II) Complex Enantiomers as Cellular Probes for Diastereomeric Interactions in Confocal and Fluorescence Lifetime Imaging Microscopy. J Phys Chem Lett. 2011;2:397-401.
[184] Grichine A, Haefele A, Pascal S, Duperray A, Michel R, Andraud C, et al. Millisecond lifetime imaging with a europium complex using a commercial confocal microscope under one or two-photon excitation. Chem Sci. 2014;5:3475-85.
[185] Dragavon J, Amiri M, Marteyn B, Sansonetti P, Shorte S. Fluorescence lifetime imaging to quantify sub-cellular oxygen measurements in live macrophage during

bacterial invasion. Reporters, Markers, Dyes, Nanoparticles, and Molecular Probes for Biomedical Applications Iii. 2011;7910.
[186] Becker W, Su B, Bergmann A, Weisshart K, Holub O. Simultaneous Fluorescence and Phosphorescence Lifetime Imaging. Multiphoton Microscopy in the Biomedical Sciences Xi. 2011;7903.
[187] Baggaley E, Sazanovich IV, Williams JAG, Haycock JW, Botchway SW, Weinstein JA. Two-photon phosphorescence lifetime imaging of cells and tissues using a long-lived cyclometallated (NpyridylCphenylNpyridyl)-C-boolean AND-N-boolean AND Pt(II) complex. Rsc Advances. 2014;4:35003-8.

Chapter 2

Lanthanide-based luminescent materials with long lifetimes in the microsecond range have been demonstrated for time-gated luminescence microscopy imaging [1, 2]. This technique has advantages in suppressing the autofluorescence background while offering high contrast for detection of rare event cells and pathogens [3, 4]. Several advances have been made in the recent years to reduce the system costs with improved simplicity, but the system is not yet accessible routinely to biological labs and only operates in the monochrome mode for single colour imaging.

This chapter describes a practical method to build a multi-colour time-gated luminescence microscope system, and the experimental evaluations to resolve multiple species of microorganisms in the background-free condition. We first designed and engineered an excitation unit based on a high-speed Xenon flash lamp that was synchronized to a purpose-built time-gated luminescence detection unit. We demonstrated that both units were highly compatible and easily adapted to any commercial microscope to perform the time-gated luminescence detection modality. We then carried out dual-colour low-background imaging experiments for simultaneously resolving two pathogenic micro-organisms (*Giardia lamblia* stained with a red europium probe and *cryptosporidium parvum* with a green terbium probe) under a pulsed UV excitation (320-400 nm). We have achieved a better imaging quality by comparing with the UV LED excitation in terms of both signal intensity and imaging contrast. Moreover, we performed an experiment to evaluate its sensitivity and achieve background-free imaging of the single europium-doped Y_2O_2S nanoparticles with average size of 150 nm.

This work was conducted and completed during my first year of PhD candidature based on some earlier achievements in developing earlier versions of time-gated luminescence microscopes in our labs. The uniqueness of my work lies in its simplicity and reproducibility showing a clear reproducible protocol for constructing a multi-colour time-gated imaging modality based on a commercial microscope. The comprehensive evaluation was reported in the form of a peer-reviewed paper in the open-access journal of *Scientific Reports* (by the Nature Publication Group). Following

the success of this work, my colleagues and I have built an identical system at the Dalian University of Technology in China for our collaborators to evaluate their new luminescent probes in the biological systems (our system has been used in their recent paper: *Anal. Chem.*, 2014, 86 (23), pp 11883–11889).

2.1 Contribution to Paper 1

TABEL 2-1 Author contribution summary for paper 1

	L. Z	X. Z	W. D	Y. L	S. L	Z. Y	E. G	J. D	J. P	J. Y	M. V	D. J
Experiment Design	●			●								●
Setup Establishment	●	●										
Data Collection	●	●										
Sample Preparation	●	●	●		●					●	●	
Analysis	●			●								
Manuscript	●			●		●	●	●	●			●

My supervisors have primarily conceived the concept of this work, and I implemented the experimental design. My colleague Xianlin Zheng and I established the optical system and conducted the experimental work. Prof Jingli Yuan, Prof Zhiqiang Ye and Dr Wei Deng provided the lanthanide complexes and supervised me in preparation of biological samples. Our French collaborators, Prof Marc Verelst's group, have synthesized and provided the europium nanoparticles. Dr Yiqing Lu and I have analysed the data and wrote the manuscript. In this project, I have around 80% contribution covering the system design and establishment (20%), sample preparation (20%), data collection (10%), data analysis (20%) and manuscript writing (10%).

2.2 Paper 1

Lixin Zhang, Xianlin Zheng, Wei Deng, Yiqing Lu, Severine Lechevallier, Zhiqiang Ye, Ewa M. Goldys, Judith M.Dawes, James A. Piper, Jingli Yuan, Marc Verelst and Dayong Jin, "Practical Implementaion, Characterization and Applications of a Multi-Colour Time-Gated Luminescence Microscope" ***Scientific Reports***, 2014, DOI:10.1038/srep06597.

SCIENTIFIC REPORTS

OPEN

SUBJECT AREAS:
IMAGING TECHNIQUES
OPTICS AND PHOTONICS

Received
10 March 2014

Accepted
17 September 2014

Published
13 October 2014

Correspondence and requests for materials should be addressed to Y.L. (yiqing.lu@mq.edu.au) or D.J. (dayong.jin@mq.edu.au)

Practical Implementation, Characterization and Applications of a Multi-Colour Time-Gated Luminescence Microscope

Lixin Zhang[1], Xianlin Zheng[1], Wei Deng[1], Yiqing Lu[1], Severine Lechevallier[2], Zhiqiang Ye[3], Ewa M. Goldys[1], Judith M. Dawes[1], James A. Piper[1], Jingli Yuan[3], Marc Verelst[2] & Dayong Jin[1]

[1]Advanced Cytometry Labs, ARC Centre of Excellence for Nanoscale BioPhotonics (CNBP), Macquarie University, Sydney, NSW 2109, Australia, [2]Centre d'Élaboration de Matériaux et d'Etudes Structurales (CERMES - CNRS), Paul Sabatier University, France, [3]State Key Laboratory of Fine Chemicals, School of Chemistry, Dalian University of Technology, Dalian 116024, China.

Time-gated luminescence microscopy using long-lifetime molecular probes can effectively eliminate autofluorescence to enable high contrast imaging. Here we investigate a new strategy of time-gated imaging for simultaneous visualisation of multiple species of microorganisms stained with long-lived complexes under low-background conditions. This is realized by imaging two pathogenic organisms (*Giardia lamblia* stained with a red europium probe and *Cryptosporidium parvum* with a green terbium probe) at UV wavelengths (320–400 nm) through synchronization of a flash lamp with high repetition rate (1 kHz) to a robust time-gating detection unit. This approach provides four times enhancement in signal-to-background ratio over non-time-gated imaging, while the average signal intensity also increases six-fold compared with that under UV LED excitation. The high sensitivity is further confirmed by imaging the single europium-doped Y_2O_2S nanocrystals (150 nm). We report technical details regarding the time-gating detection unit and demonstrate its compatibility with commercial epi-fluorescence microscopes, providing a valuable and convenient addition to standard laboratory equipment.

Autofluorescence in biological samples presents a universal challenge for conventional fluorescence techniques to detect or visualize target species[1–6]. The time-gated luminescence (TGL) technique, which takes advantages of long-lived luminescent probes (e.g. lanthanide complexes) and time-delayed detection, substantially enhances the signal-to-noise ratio and contrast by suppressing the autofluorescence contribution[7–12]. However, the presently reported TGL microscopes can only image one colour at a time, due to the gating schemes and/or imaging devices that only allow monochromatic visualization[8,13–17]. Though multiple colours can be superimposed via image processing[18,19], it requires frequent changing of filters and reduces the efficiency when examining different species, as well as limits the opportunity to investigate their interactions. Meanwhile, the previous TGL microscopes required costly components and sophisticated assembly, which are often inaccessible in most chemical and biological laboratories[20–24]. These issues have been hindering broad implementation of the time-gated imaging technique.

In our previous work, we demonstrated a low-cost true-colour TGL microscope, featuring an ultraviolet light-emitting diode (UV LED) for excitation and a mechanical chopper for time-gating[13,25,26]. In order to simultaneously excite multiple long-lived probes, especially terbium with sensitizing moiety complex that needs a triplet energy around 30,000 cm^{-1} to pump Tb^{3+} to its excited state ($^5D_4$; 20,400 cm^{-1})[25], efficient excitation at 300–340 nm is required; however, the power of currently available UV LEDs at this wavelength range is not strong enough. On the other hand, flash lamps emitting deep UV with high power but low repetition rate (less than 100 Hz) have been used for TGL microscopy[27,28], but the long detection windows prevent efficient collection of lanthanide luminescence typically with decay lifetimes of ~1 ms or less, as well as having stability issues when synchronized to mechanical choppers.

In this work, we report a highly efficient TGL microscopy system for dual-colour low-background imaging. It uses a high-power flash lamp that can be externally triggered at high repetition rate (up to 1 kHz). This system also comprises a purpose designed and optimized time-gating unit that can be simply inserted into a commercial

epi-fluorescence microscope. We apply the new imaging system for simultaneous detection of both *Giardia lamblia* stained with a red-emitting europium complex probe and *Cryptosporidium parvum* stained with a green-emitting terbium complex probe against strong autofluorescent background. Sufficient sensitivity of this combined system is demonstrated by imaging single nanoparticles.

Results

To set up the multi-colour TGL microscope, we built an illuminator featuring a new-generation ceramic xenon flash lamp (FX-4400, Excelitas Technologies) capable of delivering high-power light pulses to excite the sample, and a time-gating unit incorporating a modified mechanical chopper to discriminate long-lived luminescence against rapidly decaying autofluorescence. Both modules were designed and engineered in such a way that they can be directly coupled onto commercial microscopes, for example the Olympus IX71 epi-fluorescence microscope used in our study, to perform TGL imaging with minimum effort required for configuration and alignment.

Optical layout. The schematic diagram of this multi-colour TGL microscope is shown in Figure 1a and 1b. In the excitation phase (Figure 1a), the beam from the xenon lamp passes through a UV band-pass filter (U-360, Edmund), and is reflected by a dichroic mirror (DC shown in Figure 1; 400DCLP, Chroma). Then, it is focused through an objective lens (60×, NA 0.75, Edmund), onto a microscopic slide to excite the specimen. The generated luminescence is collected by the same objective. It is separated from the excitation path by the dichroic mirror, and coupled to the time-gating unit consisting of the chopper, two eyepieces and a digital colour camera (DP71, Olympus). Two eyepieces (Eyepiece 1: ×10, Olympus; Eyepiece 2: RKE 32 mm, wide angle, Edmund) are used to bring down the size of the emission beam, so that the chopper can be placed at the focal spot to block the emission with minimised dead time during the periods of pulsed excitation[13]. When the excitation is off, a short time delay is applied to allow the prompt fading of the autofluorescence background. Therefore, in the detection phase, only the luminescence from the long lifetime lanthanide probes is captured by the camera (Figure 1b). The synchronisation between excitation phase and detection phase should be carefully and accurately carried out. The time sequence used is given in Figure 1c, and the details of synchronisation are described below.

Excitation source. In this system, the ceramic xenon flash lamp used outputs an average power of 60 W over its full spectrum (from 160 nm to 2000+ nm), and more importantly, a high repetition rate up to 1 kHz. It was coupled into the back port of the IX71 microscope, replacing the original mercury lamp and connecting the collimator using a customized adaptor. In order to minimise the optical background and photo-bleaching of the sample, a UV band-pass filter was used to only select the spectral region which contributed to the excitation of lanthanide probes (320–400 nm; see Supplementary Figure S1). The average excitation power entering the rear aperture of the objective lens was measured to be 2.7 mW. It had a reasonably uniform distribution over a sample area of 200 μm in diameter, leading to an excitation intensity of 8.6 W/cm^2.

For comparison, our previously reported system using a UV LED (UVTOP310, 315 ± 15 nm; Sensor Electronic Technology) for

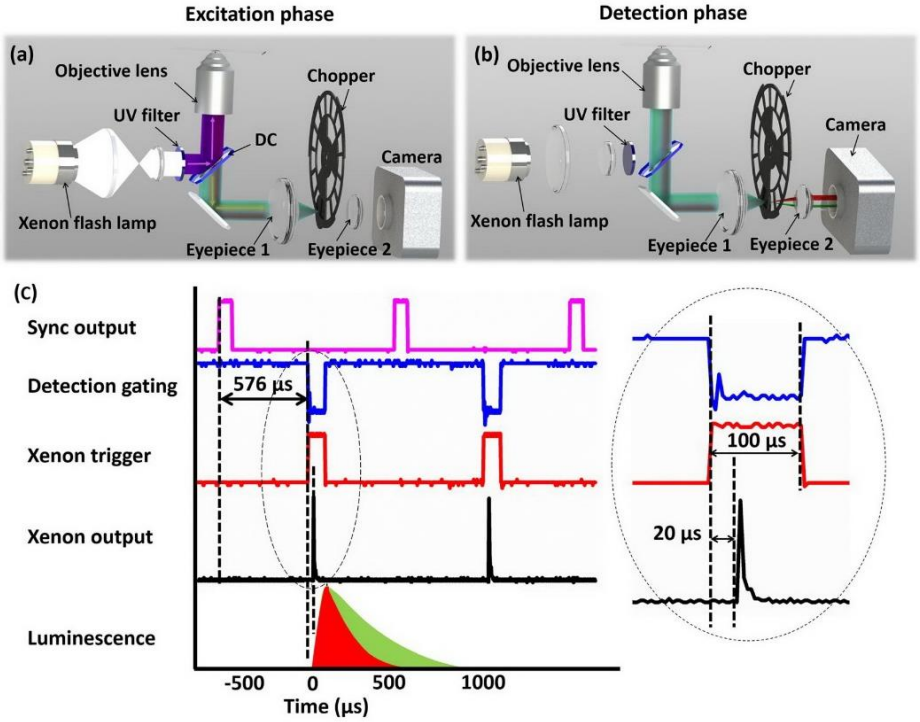

Figure 1 | Schematic diagrams of the multi-colour TGL microscope. (a) In the excitation phase, a pulsed excitation light illuminates the sample, while the chopper stops the luminescence/autofluorescence being captured by camera. (b) In the detection phase, the excitation is turned off, and the chopper allows the luminescence to reach the camera. (c) The time sequence of the system is shown, with every repetition cycle containing a gating window of 88 μs and a detection window of 968 μs. Each flash pulse is released 20 μs after the trigger and last around 17 μs.

excitation[25] was also investigated for multi-colour TGL imaging. Its average excitation power at the rear aperture of the objective lens was measured to be 0.5 mW, hence an excitation intensity of 1.6 W/cm^2.

Chopper modification. In order to achieve optimum performance and compatibility with the xenon flash lamp, we modified a high-speed mechanical chopper (C995, Terahertz Technologies Inc). Originally, this device had 30 blades with a fixed duty cycle of 1 : 1, and it was able to run at a frequency up to 5 kHz. Considering that the highest frequency of the xenon lamp was 1 kHz and the lifetimes of lanthanide probes were in the range of tens to hundreds of μs, we removed 25 blades using ultrafast laser micromachining and only kept one blade out of every six, so that the duty cycle became 1 : 11 (see Supplementary Figure S2). It is worth mentioning that the reduced weight of the chopper blades also helped reduce the vibration of the time-gating unit to some degree.

A plate with a 1-mm-diameter pinhole was attached to the chopper enclosure to increase the chopping efficiency by removing stray light, as well as protecting the device from dust. The highest chopping frequency after modification was measured to be 947 Hz, which yielded 88 μs for gating and 968 μs for detection.

Time-gating unit. Incorporating the modified chopper, a time-gating unit was designed and built, as shown in Figure 2. An aluminium frame was machined to mount the eyepieces, the chopper and the camera, alongside an adaptor for the camera port of a standard microscope, in our case the Olympus IX71. Fine alignment of the components was conducted in the bright-field mode illuminated by a halogen lamp. In the first step, the pair of eyepieces was adjusted to make their focuses completely overlap. Since the eyepieces had the same magnification, this was verified by measuring the beam size at a long distance (e.g. 1 m) away along the optical path, which should remain identical regardless of the presence/absence of the two eyepieces. In the second step, the modified chopper was inserted between the eyepieces, so that its pinhole plate was located exactly at the common focus of the two eyepieces. In the third step, the camera was mounted after the second eyepiece. The imaging quality of the system was examined using a microscopic reticle (grid distortion targets, Thorlabs). The most common optical aberration encountered during the alignment was the "barrel distortion" (see Supplementary Figure S3); however, this could be effectively overcome once all optical components were adjusted to be exactly coaxial. After proper alignment, the obtained field-of-view was 150 × 150 μm^2.

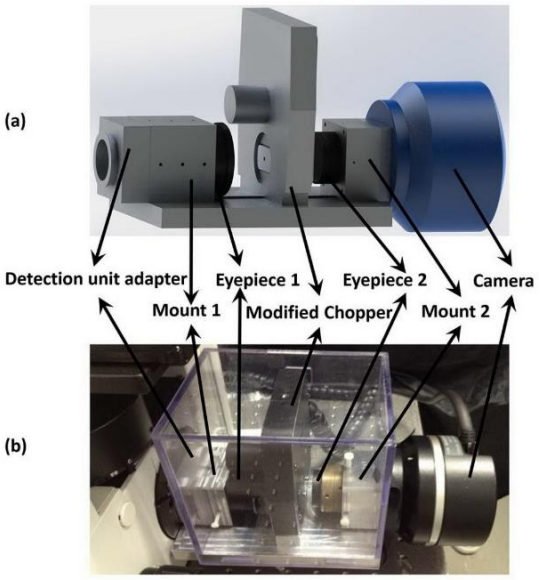

Figure 2 | The time-gating unit consists of two eyepieces, one chopper and one camera, all of which are mounted on a common frame. Top: the schematics; Bottom: a photo of the real system.

Synchronisation. After all the components were properly aligned, synchronisation between the excitation and the time-gated detection was elaborately carried out to ensure maximum contrast enhancement for TGL imaging. As shown in Figure 1c, we first measured the time delay between the *Sync Output* from the chopper controller (which was generated by a built-in sensor in the chopper head for monitoring the rotation of the blades) and the physical opening/blockage of the detection path. The latter was recorded by a photodiode placed after the second eyepiece when the bright-field illumination was switched on. With the modified chopper blades, this delay from the rising edge of *Sync Output* to the blockage of the detection path was determined as 576 μs, which was essentially caused by the different positions of the sensor and the pinhole. Then, we fed the *Sync Output* from the chopper controller to a digital delay generator (DG535, Stanford Research Systems), which sent TTL pulses of 100 μs duration to trigger the xenon lamp. Because of the gas discharge process, there was another time delay from the rising edge of the trigger signal to the time of flashing, which was measured as 20 μs. Finally, we adjusted the delay value between the *Sync Output* channel and the xenon trigger channel while monitoring the level of autofluorescence leakage using a piece of paper as the reference sample. It was found that a delay value of 576 μs (same as the delay between *Sync Output* and chopper blockage) rendered the autofluorescence invisible and allowed the maximum luminescence signal to be captured.

Dual-colour imaging. Two waterborne pathogens, *Giardia lamblia and Cryptosporidium parvum*, were labelled with Eu and Tb luminescent complexes, respectively (see Methods for details). The mixed samples were imaged under xenon flash lamp excitation, with the non-time-gated result shown in Figure 3a and the time-gated result shown in Figure 3b for one typical sample area. To evaluate the signal-to-background ratios in an accurate and objective way, the intensity levels of targets as well as the rest areas were carefully analysed in the separate red and green channels (detailed procedures see Supplementary Information S4). As shown in Figure 3c and 3d, the part of signals that were once submerged under the background clearly stood out after the time-gated mode was applied. The average values given in Figure 3e, after statistically measuring 10 pairs of non-time-gated and time-gated images (complete data see Supplementary Table S1 and S2), indicate the signal-to-background ratio is enhanced by 4.3-folds (from 126 : 44 to 137 : 11) for the red channel, as well as 3.3-folds (from 91 : 45 to 74 : 11) for the green channel, with camera exposure time of 5 seconds. By contrast, previously it took 15 seconds (repetition rate 2.5 kHz, excitation pulse 100 μs, detection window 300 μs) to accumulate enough luminescent signals (average 70 for red and 37 for green) under 315 nm UV LED excitation (see Supplementary Information S5). Therefore, it is calculated that the excitation efficiency of the xenon lamp is 5.9 times in red and 6.0 times in green higher than that of the UV LED, thus more suitable for multi-colour TGL microscopy.

Crosstalk between red (Eu) and green (Tb) channels. We proposed a calibration method to calculate the crosstalk from the emission spectra of lanthanide chelates and the responsivity curves of the true-colour DP71 camera (detailed procedures see Supplementary Information S6). Briefly, 78.6% of the total emission from the Eu complexes is collected into the red channel of the camera, along with

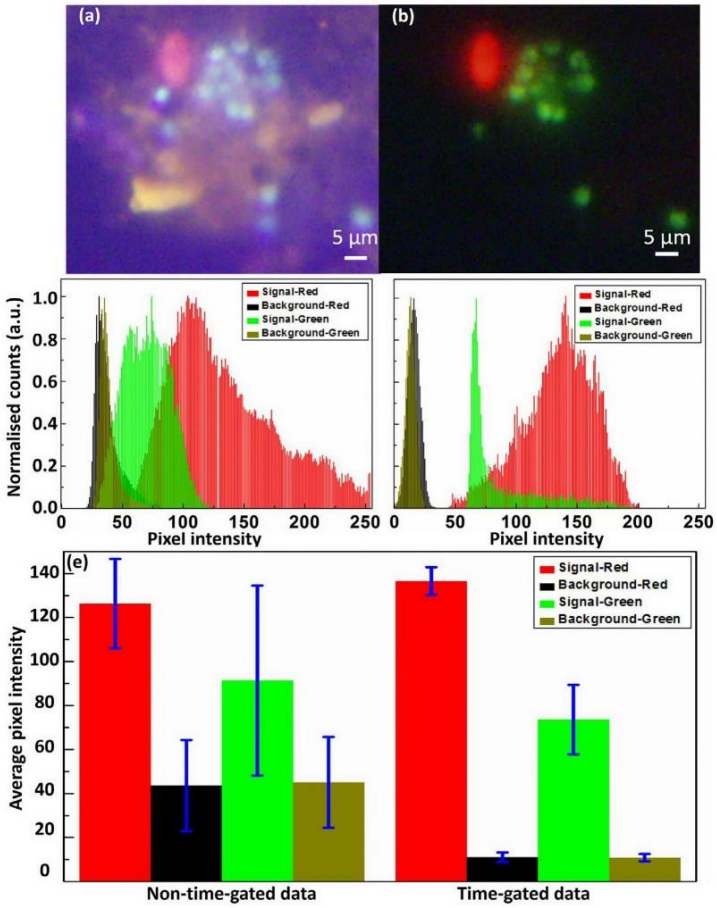

Figure 3 | Two-colour imaging under xenon lamp excitation. (a) and (b) are non-time-gated and time-gated images of *Giardia lamblia* cysts labelled with a red europium probe and *Cryptosporidium parvum* oocysts labelled with a green terbium probe (exposure time: 5 seconds). (c) and (d) show the pixel intensity histograms for the signal area (target cells) and the background area in separate red and green channels for (a) and (b), respectively. (e) is a bar chart showing the average signal and background levels summarised from 10 pairs of non-time-gated and time-gated dual-colour images. Error bars represent ±1 s.e.m.

13.6% and 7.8% into green and blue channels, respectively. Meanwhile, for the Tb complexes, since its emission spectrum has satellite peaks in the blue and red range, 59.9% of the total emission is collected into the green channel, 19.2% into the red channel, and 20.9% into the blue channel. These values can be applied to compensate the original imaging results to achieve more precise quantitative measurement. However, for applications that aim to detect target cells or analytes only, the crosstalk issue may be ignored if the contrast in time-gated images is sufficiently high, as was the case in this study.

Single nanoparticle sensitivity. We further evaluated the sensitivity of the new time-gated luminescence microscope by imaging single nanoparticles. Figure 4 presents a typical result of 150 nm Y_2O_2S:Eu^{3+} nanoparticles under xenon lamp excitation with an exposure time of 30 seconds. While the non-time-gated mode failed to provide enough contrast (Figure not shown), the time-gated mode offered sufficient sensitivity to observe these nanoparticles down to a single one (Figure 4a). Figure 4b enlarges images of the luminescent spots which potentially contain single nanoparticles (others were easily to be identified as aggregation of nanoparticles). Following a literature method[14,29], they were eventually confirmed in the corresponding transmission electron microscopy (TEM) image (Figure 4c), which showed perfect correlation with the luminescence image (Figure 4d; detailed procedures see Supplementary Information S7).

Discussion and Conclusion

In this study, we demonstrate for the first time that simultaneous dual-colour visualisation can be realised in TGL imaging for two species of microorganisms stained with different lanthanide probes. We show that outstanding sensitivity and contrast can be achieved with a new-generation xenon flash lamp that is capable of pulsed excitation at high repetition rate. Our compact time-gating unit provides an easy-to-use and low-cost option to chemists developing lanthanide materials and biologists who wish to eliminate autofluorescence background. Furthermore, the system is also compatible to the automated scanning and lifetime measurement techniques[30,31], to enable high-throughput detection and analysis of multiple target microorganisms. With the rapid progress in lanthanide chemistry, especially the new development of lifetime-tunable lanthanide probes[32], we believe such multi-colour TGL

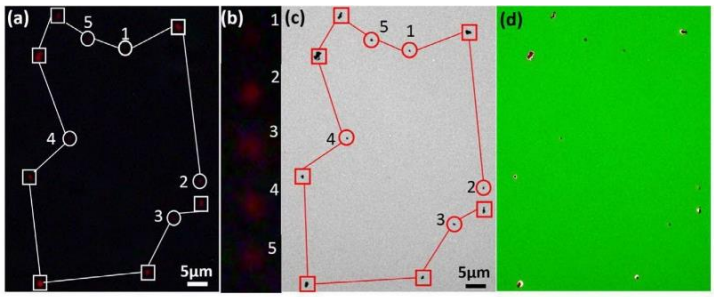

Figure 4 | Imaging results of the Y_2O_2S:Eu nanoparticles. (a) A time-gated image shows a pattern of luminescence spots. The spots marked with circles (numbered as 1 to 5) contain single Eu nanoparticles, while the others marked with squares contain aggregation of nanoparticles. (b) The enlarged images are given for spots 1–5. (c) The TEM image shows the same pattern for the spots of nanoparticles. (d) Co-localisation analysis confirms the perfect match between the time-gated image and the TEM image.

technique will have a broad range of impact on analytical and biosensing applications.

Methods

Immunoluminescent staining of Giardia lamblia. Immunofluorescence staining of *Giardia lamblia* was carried out based on the published method[24] with slight modifications. 30 μL of mouse monoclonal anti-*Giardia* antibody G203 (IgG, cyst-wall specific, 0.44 mg/mL, BTF-bioMérieux), 100 μL of biotinylated goat anti-mouse IgG antibody (1 : 10 dilution; Catalogue Number AP200B, ChemiCon International, Millipore Bioscience Division), and 100 μL of SA-BSA-BHHCT-Eu^{3+} conjugate (50 μg/mL) (the synthesis method was reported in literature[13]) were mixed with 10 μL suspension of *Giardia lamblia* (containing ~2,500 *Giardia lamblia* cysts, BTF-bioMérieux), and incubated at room temperature for 12 hours. In order to separate the Eu-labelled cysts, the FACSAria flow cytometer (Becton Dickinson) was used to sort out the sample prepared above, which yielded ~2,000 stained cysts in 400 μL 1.25% PBS solution.

Immunoluminescent staining of Cryptosporidium parvum. For staining of *Cryptosporidium parvum*, a method similar to that reported in literature[33] was used. In a typical procedure, 10 μL suspension of *Cryptosporidium parvum* oocysts (~10^6 oocysts/mL in PBS, BTF-bioMérieux) was mixed with 20 μL of mouse monoclonal anti-Cryptosporidium antibody C104 (IgG, 0.44 mg/mL; BTF-bioMérieux) and incubated for 24 hours at room temperature. The mixture was then centrifuged (at 12,000 rpm, 5 minutes) and washed with PBS (pH 7.2) three times. After removing the supernatant, 20 μL of 10-fold diluted biotinylated goat anti-mouse IgG antibody was added and incubated for another 24 hours at room temperature, followed by washing and centrifugation. Subsequently, 20 μL of the Tb-labelled streptavidin (1 : 20 dilution of 1 mg/mL kit, LanthaScreen® Tb-Streptavidin, Invitrogen) was added and the suspension was incubated for another 48 hours. Finally, the stained *Cryptosporidium* oocysts were washed three times with PBS.

Preparation of mixed pathogen samples. In order to demonstrate the background suppression feature of our system, a sample exhibiting strong autofluorescence was prepared. Flower petals with different colours of native chromophores were pulverized and mixed with fruit juice, which is also known to be autofluorescent. They were filtered through a centrifugal filter device (UFC30GV00, Millipore) to remove large fragments.

The two stained microorganisms and artificial background samples were mixed and sandwiched between a glass slide and a coverslip. 5 μL of background solution was dropped onto a glass slide. After it dried, 2 μL of the Eu-probe-labelled *Giardia lamblia* cysts was added. 10 minutes later, 2 μL of the Tb-probe-labelled *Cryptosporidium parvum* was dropped on top of the sample, and the whole preparation was covered with a coverslip.

Preparation of single nanoparticle samples. 10 μL of an ethanol solution containing 0.25 mg/mL Eu-doped nanoparticles $Y_2O_2S:Eu^{3+}$ (5% dopants, average size 150 nm)[34] was dropped on the copper grids coated by amorphous carbon. The nanoparticles on the grid were imaged by a transmission electron microscope (TEM, Philips CM10).

1. Gahlaut, N. & Miller, L. W. Time-resolved microscopy for imaging lanthanide luminescence in living cells. *Cytom Part A* **77A**, 1113–1125, doi:10.1002/Cyto.A.20964 (2010).
2. Tian, L. *et al.* Preparation and time-gated luminescence bioimaging applications of long wavelength-excited silica-encapsulated europium nanoparticles. *Nanoscale* **4**, 3551–3557, doi:10.1039/C2nr30233k (2012).
3. Rich, R. M. *et al.* Elimination of autofluorescence background from fluorescence tissue images by use of time-gated detection and the AzaDiOxaTriAngulenium (ADOTA) fluorophore. *Anal Bioanal Chem* **405**, 2065–2075, doi:10.1007/s00216-012-6623-1 (2013).
4. Bunzli, J. C. G. & Eliseeva, S. V. Intriguing aspects of lanthanide luminescence. *Chem Sci* **4**, 1939–1949, doi:10.1039/C3sc22126a (2013).
5. Shinoda, S. Dynamic cyclen-metal complexes for molecular sensing and chirality signaling. *Chemical Society reviews* **42**, 1825–1835, doi:10.1039/C2cs35295h (2013).
6. Cheng, L., Wang, C. & Liu, Z. Upconversion nanoparticles and their composite nanostructures for biomedical imaging and cancer therapy. *Nanoscale* **5**, 23–37, doi:10.1039/c2nr32311g (2013).
7. Lichtman, J. W. & Conchello, J. A. Fluorescence microscopy. *Nature methods* **2**, 910–919, doi:10.1038/nmeth817 (2005).
8. Sagolla, K., Lohmannsroben, H. G. & Hille, C. Time-resolved fluorescence microscopy for quantitative Ca2+ imaging in living cells. *Anal Bioanal Chem* **405**, 8525–8537, doi:10.1007/s00216-013-7290-6 (2013).
9. Vaasa, A. *et al.* Time-gated luminescence microscopy with responsive nonmetal probes for mapping activity of protein kinases in living cells. *Chemical communications* **48**, 8595–8597, doi:10.1039/c2cc33565d (2012).
10. Moore, J. D., Lord, R. L., Cisneros, G. A. & Allen, M. J. Concentration-independent pH detection with a luminescent dimetallic Eu(III)-based probe. *Journal of the American Chemical Society* **134**, 17372–17375, doi:10.1021/Ja307098z (2012).
11. Lechevallier, S. *et al.* Luminescence properties of mesoporous silica nanoparticles encapsulating different europium complexes: application for biolabelling. *J Nanomater*, doi:10.1155/2013/918369 (2013).
12. Rich, R. M. *et al.* Multiple-pulse pumping for enhanced fluorescence detection and molecular imaging in tissue. *Methods*, doi:10.1016/j.ymeth.2013.08.026 (2013).
13. Jin, D. & Piper, J. A. Time-gated luminescence microscopy allowing direct visual inspection of lanthanide-stained microorganisms in background-free condition. *Analytical chemistry* **83**, 2294–2300, doi:10.1021/ac103207r (2011).
14. Deng, W. *et al.* Ultrabright Eu-doped plasmonic Ag@SiO2 nanostructures: time-gated bioprobes with single particle sensitivity and negligible background. *Advanced materials* **23**, 4649–4654, doi:10.1002/adma.201102027 (2011).
15. Wu, J. *et al.* Visible-light-sensitized highly luminescent europium nanoparticles: preparation and application for time-gated luminescence bioimaging. *J Mater Chem* **19**, 1258–1264, doi:10.1039/B815999h (2009).
16. Duncan, M. D., Mahon, R., Tankersley, L. L. & Reintjes, J. Time-gated imaging through scattering media using stimulated raman amplification. *Opt Lett* **16**, 1868–1870, doi:10.1364/Ol.16.001868 (1991).
17. Requejo-Isidro, J. *et al.* High-speed wide-field time-gated endoscopic fluorescence-lifetime imaging. *Opt Lett* **29**, 2249–2251, doi:10.1364/Ol.29.002249 (2004).
18. Soini, A. E., Kuusisto, A., Meltola, N. J., Soini, E. & Seveus, L. A new technique for multiparameter imaging microscopy: use of long decay time photoluminescent labels enables multiple color immunocytochemistry with low channel-to-channel crosstalk. *Microscopy research and technique* **62**, 396–407, doi:10.1002/jemt.10389 (2003).
19. Hanaoka, K., Kikuchi, K., Kobayashi, S. & Nagano, T. Time-resolved long-lived luminescence imaging method employing luminescent lanthanide probes with a new microscopy system. *Journal of the American Chemical Society* **129**, 13502–13509, doi:10.1021/ja073392j (2007).
20. Connally, R., Jin, D. & Piper, J. High intensity solid-state UV source for time-gated luminescence microscopy. *Cytometry. Part A: the journal of the International Society for Analytical Cytology* **69**, 1020–1027, doi:10.1002/cyto.a.20326 (2006).
21. Connally, R. E. & Piper, J. A. Time-gated luminescence microscopy. *Annals of the New York Academy of Sciences* **1130**, 106–116, doi:10.1196/annals.1430.032 (2008).

22. Hu, B. L., He, Y. H. & Liu, Z. Y. NIR area array CCD-based singlet oxygen luminescence imaging for photodynamic therapy. *J Phys Conf Ser* **277**, doi:10.1088/1742-6596/277/1/012011 (2011).
23. Ibanez, G., McBean, J. L., Astudillo, Y. M. & Luo, M. K. An enzyme-coupled ultrasensitive luminescence assay for protein methyltransferases. *Analytical biochemistry* **401**, 203–210, doi:10.1016/J.Ab.2010.03.010 (2010).
24. Lu, Y. *et al.* Automated detection of rare-event pathogens through time-gated luminescence scanning microscopy. in *Cytometry A* Vol. 79, 349–355, doi: 10.1002/Cyto.A.21045 (2011).
25. Jin, D. Y. Demonstration of true-color high-contrast microorganism imaging for terbium bioprobes. *Cytom Part A* **79A**, 392–397, doi:10.1002/Cyto.A.21052 (2011).
26. Jin, D. Y., L, Y. Q., Leif, R. C., Yang, S., Rajendran, M. & Miller, L. W. in *Current Protocols in Cytometry How to build a time-gated luminescence microscope* 67: 62.22:62.22.61–62.22.36. (2014).
27. Beverloo, H. B., Vanschadewijk, A., Vangelderenboele, S. & Tanke, H. J. Inorganic phosphors as new luminescent labels for immunocytochemistry and time-resolved microscopy. *Cytometry* **11**, 784–792, doi:10.1002/cyto.990110704 (1990).
28. Vereb, G., Jares-Erijman, E., Selvin, P. R. & Jovin, T. M. Temporally and spectrally resolved imaging microscopy of lanthanide chelates. *Biophysical journal* **74**, 2210–2222, doi:10.1016/S0006-3495(98)77930-5 (1998).
29. Wu, S. *et al.* Non-blinking and photostable upconverted luminescence from single lanthanide-doped nanocrystals. *Proceedings of the National Academy of Sciences of the United States of America* **106**, 10917–10921, doi:10.1073/pnas.0904792106 (2009).
30. Lu, Y., Xi, P., Piper, J. A., Huo, Y. & Jin, D. Time-gated orthogonal scanning automated microscopy (OSAM) for high-speed cell detection and analysis. *Sci. Rep.* **2**, 837, doi:10.1038/srep00837 (2012).
31. Lu, Y. *et al.* On-the-fly decoding luminescence lifetimes in the microsecond region for lanthanide-encoded suspension arrays. *Nature Communications*, doi:10.1038/ncomms4741 (2014).
32. Lu, Y. *et al.* Tunable lifetime multiplexing using luminescent nanocrystals. *Nature Photonics* **8**, 33–37, doi:10.1038/nphoton.2013.322 (2014).
33. Yuan, J. L., Wang, G. L., Kimura, H. & Matsumoto, K. Highly sensitive time-resolved fluoroimmunoassay of human immunoglobulin E by using a new europium fluorescent chelate as a label. *Analytical biochemistry* **254**, 283–287, doi:10.1006/abio.1997.2444 (1997).
34. Osseni, S. A. *et al.* Gadolinium oxysulfide nanoparticles as multimodal imaging agents for T2-weighted MR, X-ray tomography and photoluminescence. *Nanoscale* **6**, 555–564, doi:10.1039/c3nr03982j (2013).

Acknowledgments

The authors acknowledge Dr. Benjamin Johnston (Macquarie OptoFab Node, Australian National Fabrication Facility) for laser micromachining to modify the optical chopper blades, the financial support from Australian Research Council (DP1095465, LP130100517, and FT130100517), Macquarie University Research Fellowship (Y.L.), and International Macquarie University Research Excellence Scholarships (L.Z. and X.Z.). Y.L. and D.J. acknowledge the International Society for Advancement of Cytometry for support as ISAC Scholars.

Author contributions

Y.L. and D.J. conceived the project, designed the experiments and supervised the research. L.Z., X.Z. and D.J. were primarily responsible for microscopy setups, evaluation, data collection and analysis. L.Z., X.Z., Y.L. and D.J. prepared figures and wrote the main manuscript text. W.D., S.L., J.Y., Z.Y. and M.V. provided the samples and conducted image data analysis. J.M.D., E.M.G. and J.A.P. contributed to data analysis and manuscript preparation.

Additional information

Supplementary information accompanies this paper at http://www.nature.com/scientificreports

Competing financial interests: The authors declare no competing financial interests.

How to cite this article: Zhang, L. *et al.* Practical Implementation, Characterization and Applications of a Multi-Colour Time-Gated Luminescence Microscope. *Sci. Rep.* **4**, 6597; DOI:10.1038/srep06597 (2014).

Practical Implementation, Characterization and Applications of a Multi-Colour Time-Gated Luminescence Microscope

Lixin Zhang[1], Xianlin Zheng[1], Wei Deng[1], Yiqing Lu[1*], Severine Lechevallier[2], Zhiqiang Ye[3], Ewa Goldys[1], Judith M. Dawes[1], James A Piper[1], Jingli Yuan[3], Marc Verelst[2], Dayong Jin[1*]

[1]*Advanced Cytometry Labs, ARC Centre of Excellence for Nanoscale BioPhotonics (CNBP), Macquarie University, Sydney, NSW 2109, Australia*

[2]*Centre d'Élaboration de Matériaux et d'Etudes Structurales (CERMES - CNRS), Paul Sabatier University, France*

[3]*State Key Laboratory of Fine Chemicals, School of Chemistry, D alian University of Technology, Dalian 116024, China*

[*]Email: yiqing.lu@mq.edu.au; or: dayong.jin@mq.edu.au

S1. Xenon lamp excitation spectrum

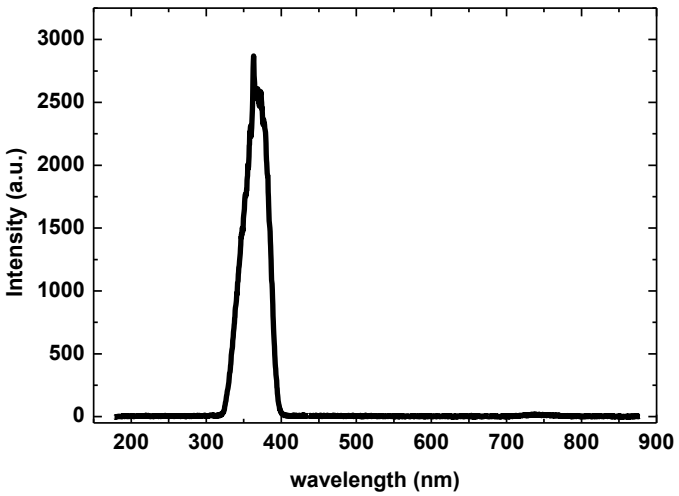

Figure S1. The excitation light from the xenon flash lamp has a spectral region from 320 nm to 400 nm, after passing through a UV band-pass filter (U-360, Edmund)

S2. Modification of chopper blades

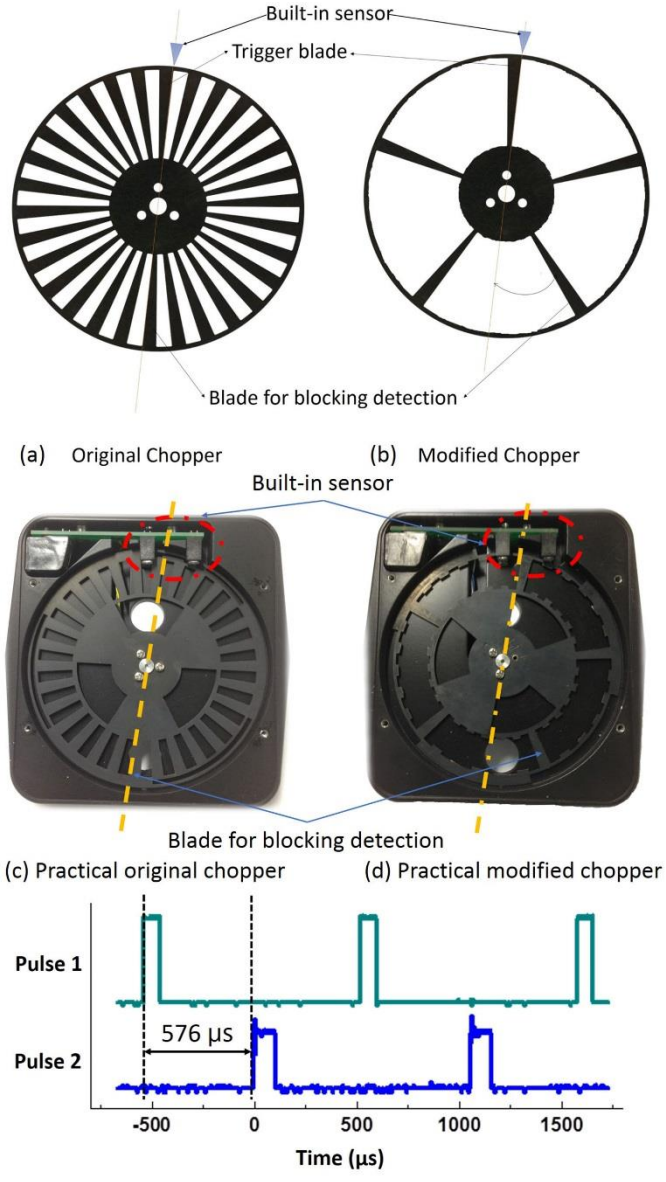

Figure S2. The induced time delay between the sensor trigger blade and the detection blocking blade in the modified chopper

S3. Correction of optical distortion

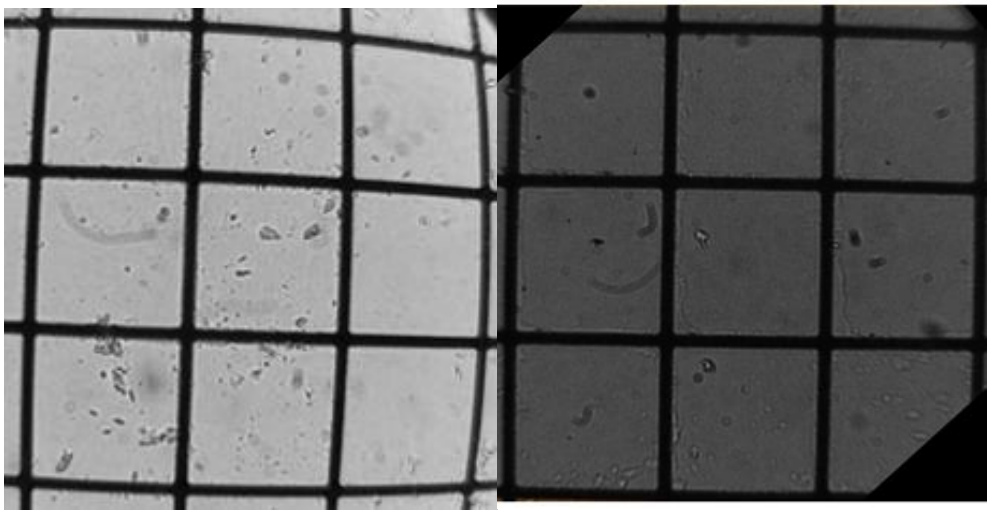

Figure S3. A wide-field image with barrel distortion (left), and its improved image without barrel distortion (right), after all optical components are aligned to be exactly coaxial. Each grid represents 50×50 μm^2.

S4. Image analysis to determine the signal-to-background ratio

The average signal and background levels for the red and the green channels of the images captured under the non-time-gated mode and the time-gated mode were analysed based on the procedures illustrated below, with the two images in Figure S4 as the example. Matlab was used in this study, but other image processing software, such as ImageJ, can also be used.

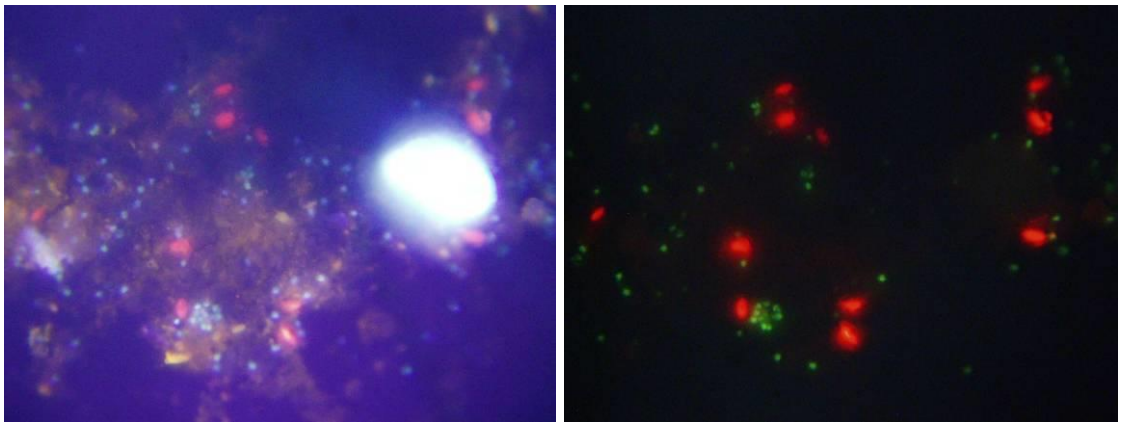

Figure S4. The non-time-gated (left) and time-gated (right) dual-colour images to be referred to in the image analysis demonstration.

S4.1 Analysing signal levels in time-gated images

The time-gated colour image was split into the red, green and blue channels. Figure S4.1-1 shows the monocolour images of the red and green channels, while the blue channel was not considered in the following analysis.

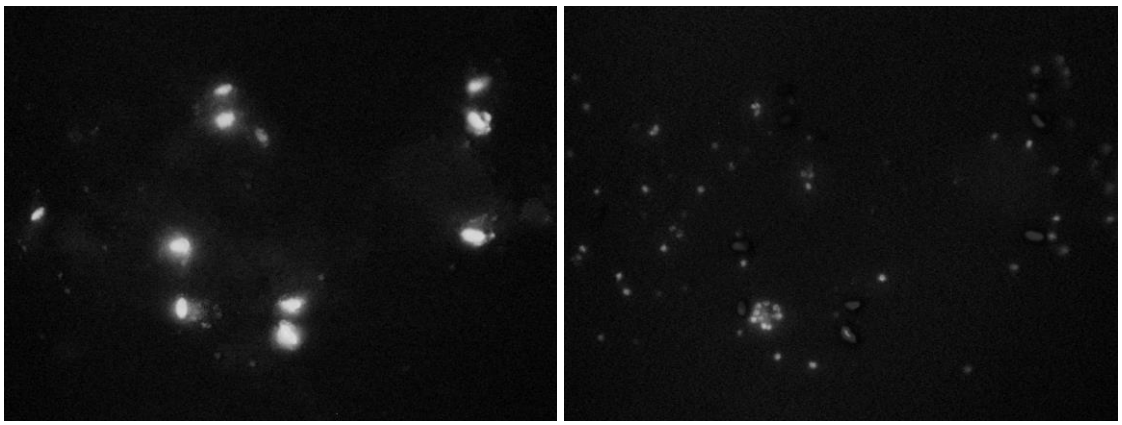

Figure S4.1-1 The red (left) and green (right) channels of the time-gated image.

Image masks with thresholds equal to 0.3 times the maximum intensities in respective channels were applied on these monocolour images to effectively select target cells, as shown in Figure S4.1-2.

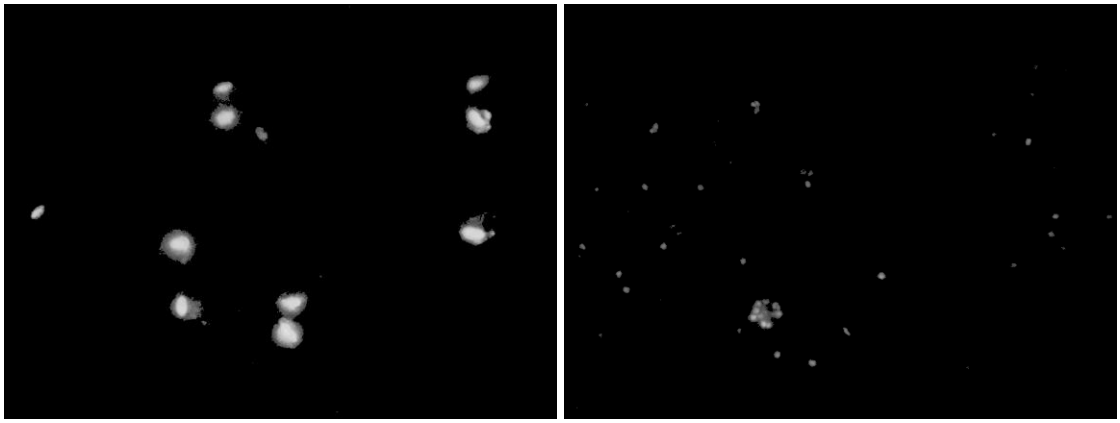

Figure S4.1-2 The time-gated monocolour images with masks to select target cells, for the red channel (left) and the green channel (right).

The maximum, minimum and average signal intensities were obtained for the masked areas.

S4.2 analysing background levels in time-gated images

The above masks were reversed and then applied to the images in Figure S4.1-1 again, to select the non-target areas, as shown in Figure S4.2, before the maximum, minimum and average background intensities were calculated.

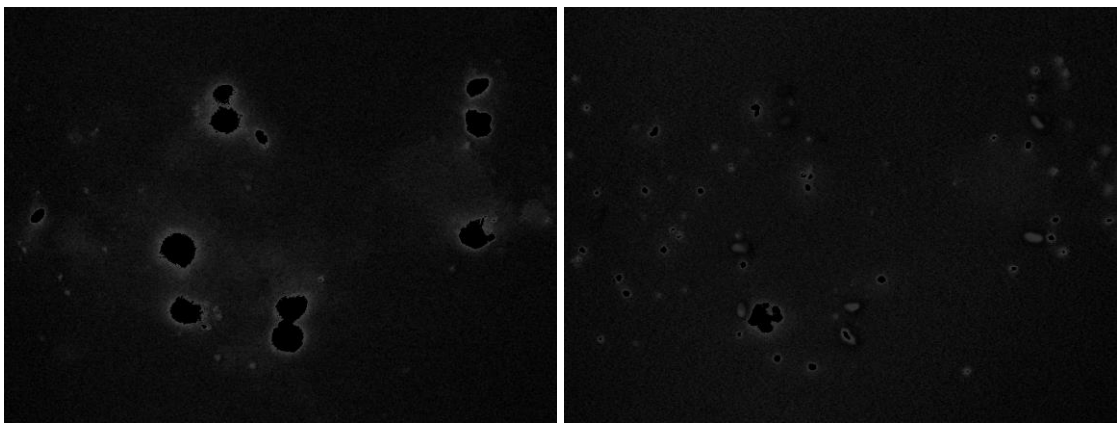

Figure S4.2 The time-gated monocolour images with background areas masked for the red channel (left) and the green channel (right).

S4.3 Analysing signal levels in non-time-gated images

The non-time-gated colour image was split into the red, green and blue channels, as shown in Figure S4.3-1 (again, the blue channel was ignored).

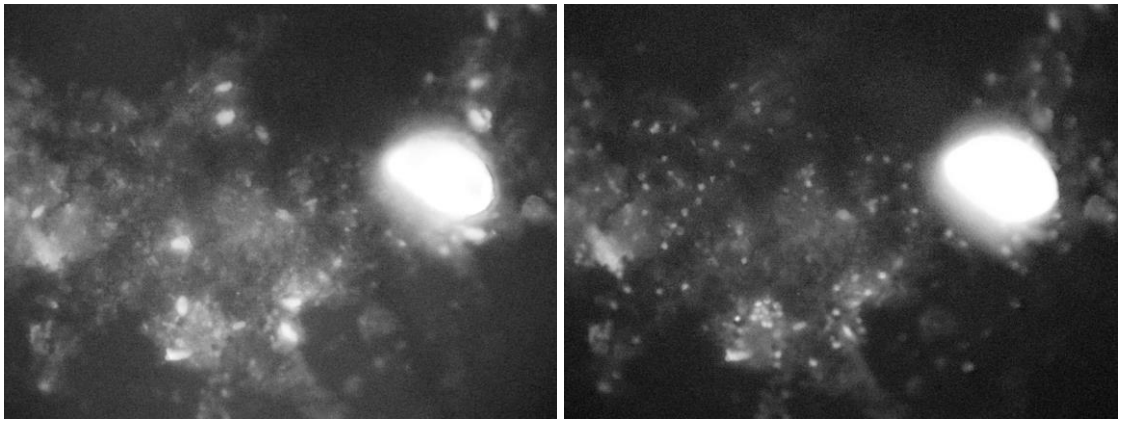

Figure S4.3-1 The red (left) and green (right) channels of the non-time-gated image.

The same masks used in S4.1 were applied to select the areas that contained target cells, and the maximum, minimum and average signal intensities were calculated.

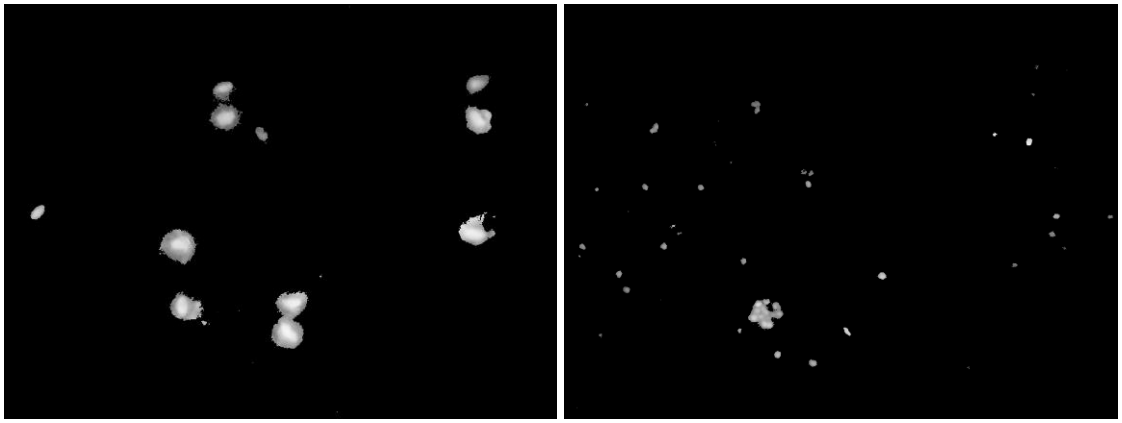

Figure S4.3-2. The non-time-gated monocolour images with masks selecting target cells, for the red channel (left) and the green channel (right).

S4.4 analysing background levels in non-time-gated images

The same masks used in S4.2 were applied to the images in Figure S4.3-1, to select the non-target areas, as shown in Figure S4.4, before the maximum, minimum and average background intensities were calculated.

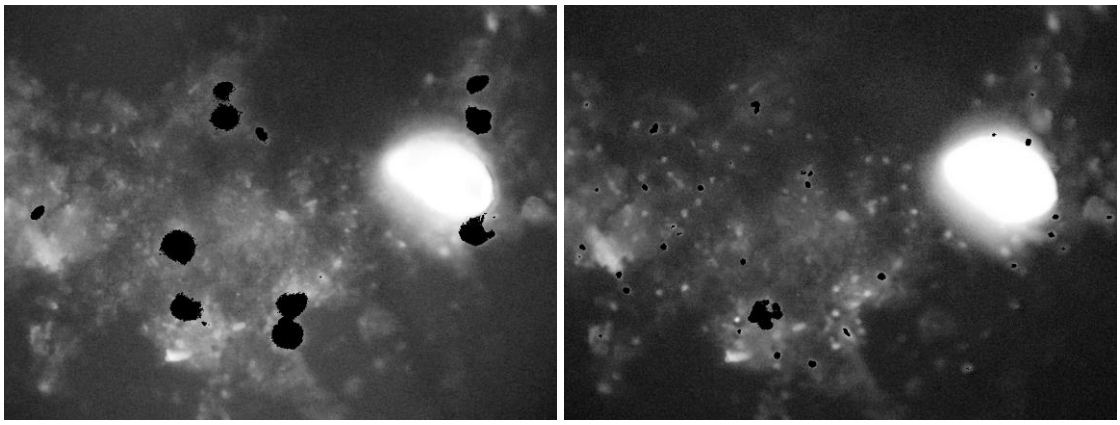

Figure S4.4. The non-time-gated monocolour images with background areas masked for the red channel (left) and the green channel (right).

Table S1. Signal and background levels of the red channel for ten pairs of images under non-time-gated and time-gated modes.

Luminescence from Eu complexes measured in the red channel							
	Image No.	S_max	S_min	S_avg	B_max	B_min	B_avg
Non-time-gated mode	1	252	75	167	255	11	82
	2	221	74	147	183	14	51
	3	168	42	105	126	0	29
	4	239	63	150	254	20	81
	5	219	37	112	107	0	26
	6	217	31	112	182	0	42
	7	219	34	122	109	0	23
	8	219	38	114	118	0	28
	9	226	34	129	173	3	42
	10	208	35	105	128	2	33
Time-gated mode	1	228	69	133	68	0	15
	2	220	67	130	66	0	10
	3	205	62	133	61	0	8
	4	222	67	144	66	0	12
	5	220	67	137	66	0	11
	6	221	67	141	66	0	9
	7	220	67	147	66	0	8
	8	222	67	142	66	0	12
	9	222	67	132	66	0	14
	10	222	67	127	66	0	11

Table S2. Signal and background levels of the green channel for ten pairs of images under non-time-gated and time-gated modes.

Luminescence from Tb complexes measured in the green channel							
	Image No.	S_max	S_min	S_avg	B_max	B_min	B_avg
Non-time-gated mode	1	252	46	144	255	11	84
	2	221	38	101	213	14	52
	3	108	23	71	168	0	29
	4	241	57	190	254	20	82
	5	102	23	58	219	0	27
	6	217	18	79	217	0	43
	7	131	17	41	219	0	24
	8	219	19	64	219	0	30
	9	226	16	107	226	3	44
	10	103	18	58	208	2	34
Time-gated mode	1	194	59	91	58	0	15
	2	111	34	45	33	0	11
	3	178	54	80	53	0	9
	4	114	35	47	34	0	11
	5	206	62	91	61	0	10
	6	184	56	74	55	0	9
	7	181	55	66	54	0	11
	8	188	57	78	56	0	11
	9	179	54	73	53	0	11
	10	189	57	89	56	0	10

S5. Imaging results under UV LED excitation

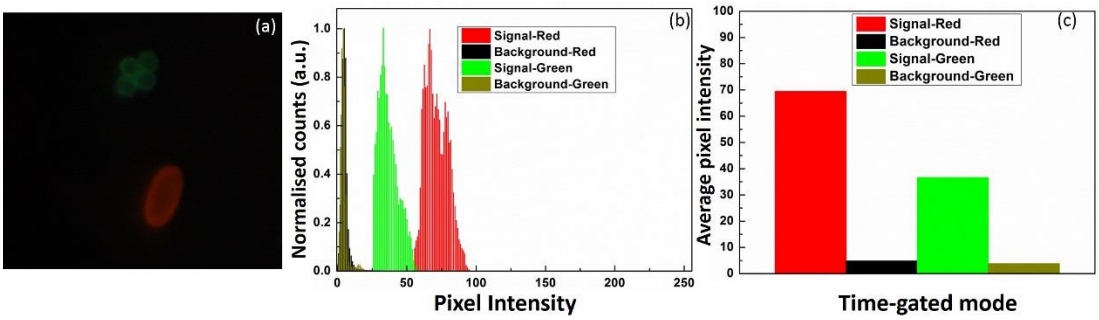

Figure S5. Imaging results under UV LED excitation. (a) Dual-colour time-gated image of Eu-labelled *Giardia* and Tb-labelled *Cryptosporidium*, with an exposure time of 15 seconds. (b) Pixel intensity histograms of the signal and background levels in the red and green channels. (c) Bar chart showing the average signal and background levels. The signal-to-background ratios are 70:5.6 for the red channel and 37:4.2 for the green channel.

S6. Calculation of the crosstalk

In addition to time gating, accurate quantification of the luminescence intensities for the two pathogens requires calibration of the crosstalk between the red and green channels, which is caused by the satellite emission peaks of the Eu and Tb complexes.

The relative responsivity curves for the red, green and blue channels of the Olympus DP71 camera can be found in its user manual available online, as shown in Figure S6.1. The curves were digitized using the GetData Graph Digitizer software.

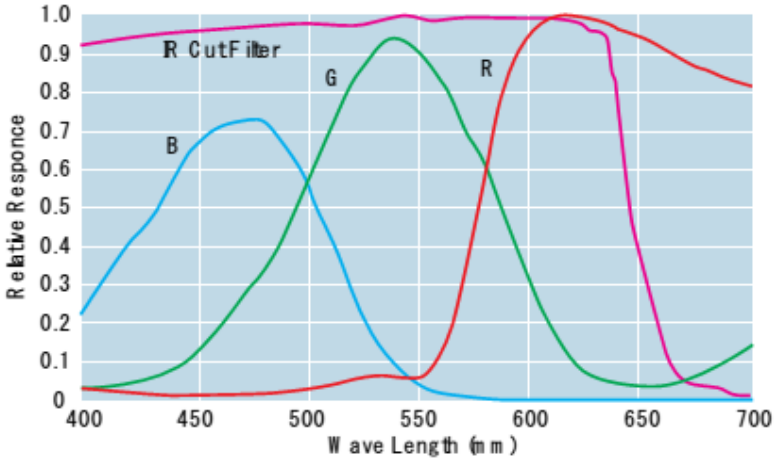

Figure S6.1 Relative responsivity curves for the Olympus DP71 camera.

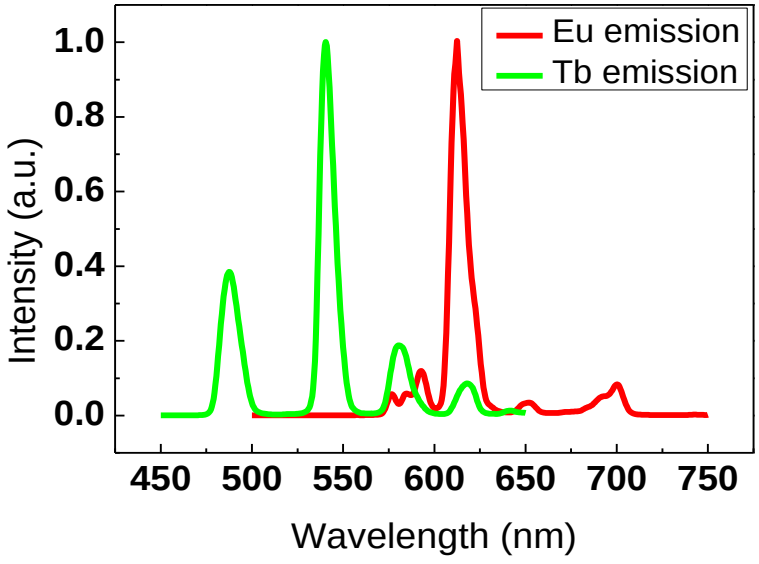

Figure S6.2 Emission spectra of the Eu and Tb complexes.

The emission spectra of the Eu and Tb complexes, as shown in Figure S11, were multiplied by the three responsivity curves, respectively, followed by normalisation, to calculate their contribution proportions to the three colour channels. The results are given in Table S3.

Table S3. The contributions of the Eu and Tb emission to the colour channels of the camera.

	Red Channel	Green Channel	Blue Channel
Eu emission	78.6%	13.6%	7.8%
Tb emission	19.2%	59.9%	20.9%

S7. Co-localization analysis of the nanoparticle images

The time-gated luminescence image of the Eu nanoparticles and its corresponding TEM image were compared using the colocalization function in the ImageJ software. The images were first resized to ensure they covered the identical area, before transformed into 8-bit grey-scale, as shown in Figure S7.

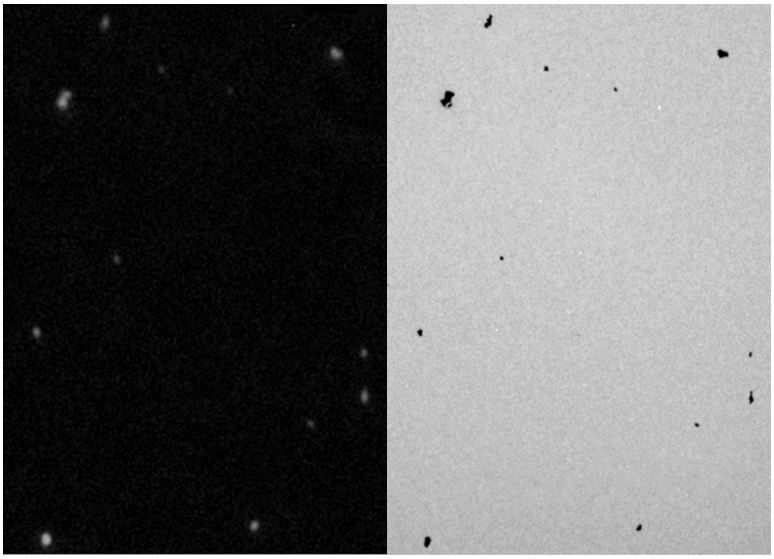

Figure S7. Grey-scale images of the original time-gated luminescence image (left) and the TEM image (right) of the Eu nanoparticles.

They were imported into the colocalization plugin to generate the co-localisation image, as shown in Figure 4d in the main text.

2.3 Remarks

A low-cost dual-colour time-gated luminescence microscope has been realised in this chapter, based on the design and construction of an excitation unit and its synchronized time-gated luminescence detection unit. Both units are low cost and have high compatibility so they can be easily adapted to any commercial microscope to perform time-gated luminescence detection. The system has been applied to simultaneously resolve two pathogenic micro-organisms from complex bio-samples with high contrast. Its high detection sensitivity was further demonstrated by imaging single nanoparticles. This work provides an easy-to-use and low-cost option for biologists and chemists investigating long-lifetime luminescent probes for high sensitivity imaging.

The current system further indicates the need for high-power pulsed excitation sources, such as solid-state light emitting diodes in the 310 nm-330nm region, or new multi-colour luminescent probes with excitation in the visible/near infrared (IR) wavelength range. The latter is desirable to overcome the problem of photo-bleaching of molecular complexes and the detrimental effect on bio-samples induced by the required UV excitation.

This chapter also suggests future work to integrate other measurement and characterisation functionalities to the microscope to collect high-resolution spectral and temporal information of lanthanide probes, materials or labelled cells.

2.4 References

[1] Jin DY. Demonstration of true-color high-contrast microorganism imaging for terbium bioprobes. Cytom Part A. 2011;79A:392-7.
[2] Gahlaut N, Miller LW. Time-resolved microscopy for imaging lanthanide luminescence in living cells. Cytom Part A. 2010;77A:1113-25.
[3] Connally RE, Piper JA. Time-gated luminescence microscopy. Annals of the New York Academy of Sciences. 2008;1130:106-16.
[4] Jin D, Piper JA. Time-gated luminescence microscopy allowing direct visual inspection of lanthanide-stained microorganisms in background-free condition. Analytical chemistry. 2011;83:2294-300.

Chapter 3

Lanthanide-doped upconversion materials, which show good photo-stability, long luminescence lifetime and narrow linewidth emission spectra, have been extensively investigated and developed for lasers, sensing and lighting applications [1-4]. The last 10 years have witnessed major developments in nanomaterials, leading to mono-disperse upconversion nanocrystals for bio-medical applications [5, 6]. However, the details of the upconversion mechanisms remain unclear, due to their multiple energy levels, the interplay of multiple dopants as sensitizers and activators, and complex photon-relaxation process. Normally the spectra and lifetimes of upconversion emission are measured independently; this characterization process is slow and does not provide in-depth relationships between different optical parameters.

This chapter describes an integrated time-resolved spectroscopy and imaging system for simultaneous measurements of temporal and spectral information from luminescent materials. Time-resolved spectroscopy has been realised by incorporating an integrated multichannel photon-sensing device, a 32-channel PMT as a linear array detector attached to the spectrometer to replace the conventional CCD camera. A high-resolution imaging system has been realized by using a single avalanche photodiode (APD) in our home-built laser scanning confocal microscopy system. The time-resolved measurements, data acquisition process and inter-system switching have been synchronized automatically by LabVIEW-based programming. To demonstrate the powerful utility of this system, a sample of mono-disperse hexagonal-shaped upconversion nanocrystals (NaYF4: Yb20%, 2%) with 40 nm diameter were tested. It took less than 1 minute for the system to complete 50 data acquisitions and construct a time-resolved 3-dimensional graph (lifetime, spectrum and intensity). Moreover, guided by the imaging modality, the system has been demonstrated for site-specific slide-based characterization of upconversion luminescence at different excitation power intensities.

This work was implemented and completed during my second year of PhD study. This instrumentation project is a timing development for high speed, efficient and high-resolution characterisation of the new generations of lanthanide-doped upconversion nanoscale and micro-scale materials. The experimental design and evaluation results

were published in the journal of *RSC Advances* in 2013. To further demonstrate the broad utility of my setup, some additional but unpublished data on the characterization of down-conversion luminescence using this system are also appended to the end of this chapter.

3.1 Contributions to Paper 2

TABLE 3-1 Author contribution summary for paper 2.

	L.Z	A. M	D.J.
Project idea	●		●
Experimental Design and system setup	●		
Data Acquisition	●	●	
Data Analysis	●	●	●
Main text writing	●	●	●
Figures and Supporting Info	●		●

My supervisor A/Prof Dayong Jin conceived the core concept, and I devised the whole optical and electronics control system as well as the performance evaluations, occupying 40% of the whole contribution. My co-supervisor Dr Aaron Mckay supervised me in the LabVIEW programming to realise the system synchronization and data acquisition, with contribution of 25%. My supervisors and I analysed the data and wrote the manuscript, occupying 20% of the whole contribution. In this project, I have more than 80 % contributions.

3.2 Paper 2

Lixin Zhang, Aaron McKay and Dayong Jin. “High-throughput 3-dimensional time-resolved spectroscopy: simultaneous characterization of luminescence properties in spectral and temporal domains”. *RSC Advances*, 2013, 3, 8670-8673.

RSC Advances

RSC Publishing

COMMUNICATION

View Article Online
View Journal | View Issue

High-throughput 3-dimensional time-resolved spectroscopy: simultaneous characterisation of luminescence properties in spectral and temporal domains†

Cite this: *RSC Advances*, 2013, **3**, 8670

Received 6th February 2013,
Accepted 17th April 2013

DOI: 10.1039/c3ra40637g

www.rsc.org/advances

Lixin Zhang, Aaron McKay and Dayong Jin*

Lanthanide luminescence is presented in full spectral and temporal detail by challenging the limits of low-light sensing and high-speed data acquisition. A robust system is demonstrated, capable of constructing high-resolution time-resolved spectra with high throughput processing. This work holds real value in advancing characterisation capability to decode interesting insights within lanthanide materials.

By meeting the stringent requirements in lighting, telecommunication, electroluminescent devices, analytical sensors and bio-imaging set-ups, the luminescence properties of lanthanide-doped materials have attracted significant research efforts both at the fundamental and applied levels.[1] The unique luminescent properties of lanthanide materials offer sharp emission spectrum, large Stokes shifts, exceptionally long lifetime, and upconversion generation that stem from their ladder-like energy levels and sophisticated energy transfer processes. Traditional spectroscopic approaches of either luminescence spectra or lifetime decay rates at individual wavelengths are insufficient to understand the rich chemical physics. This deficiency as result of lacking of robust instrumentation development remains a major barrier for the field of material science and applications.[1]

The inorganic nanocrystal matrix, such as $NaYF_4$, co-doped with ytterbium (Yb^{3+}) and erbium (Er^{3+}), or thulium (Tm^{3+}) rare-earth ions represent a new generation of lanthanide-doped upconversion nanocrystals.[2–9] They have recently attracted significant research interests in many fields including bio-detection,[10] bio-imaging,[11,12] anti-counterfeiting security,[13,14] solar cells,[15] and 3-D displays.[16] In the $NaYF_4$:Yb/Er system, a network of closely spaced Yb ions sensitises with infrared radiation at a wavelength of 980 nm and couples *via* non-radiative resonance to neighbouring Er ions. In contrast with organic dye fluorophores, the Er ion has multiple excited states with remarkably long (sub-ms) lifetimes, so that upconversion nanocrystals are able to stepwise absorb two or more near-infrared photons, and display blue-shifted emission in the visible spectrum.

Fundamental to fully understand the mechanisms behind upconversion process in Ln-doped nanocrystals, one must overcome the difficulties that result from multiple energy levels of the lanthanide material itself and the complicated photon relaxation process associated with multiple sensitised photons travelling within a network of thousands of interacting nano-scaled sensitisers and emitters, which together are influenced by the large surface-to-volume ratio common in nanoparticle science.[17] Practically, there are two major properties of the upconversion luminescence that provide opportunities for advanced bio-imaging.[12] Firstly, in the spectral domain, narrow-bandwidth anti-Stokes-shifted emission allows efficient colour separation from the autofluorescence. The second advantage lies in a million-fold difference between the much longer lifetimes of upconversion nanocrystals and shorter endogenous fluorophores lifetimes that make up the autofluorescence background ($\sim$1 ms *cf.* $\sim$3 ns). Therefore an optical time-gated approach allows almost complete suppression of the autofluorescence and excitation background. From an application perspective, it becomes critical to characterise simultaneously the spectral and lifetime characteristics of Ln-doped nanocrystals as a unifying picture.

To date the luminescence properties, especially that of the lifetime and spectral characteristics of Ln-doped nanocrystals have been reported with a measure of mutual exclusivity. For example the spectral properties have been report of similar doped nanocrystals with resolutions of 1–5 nm,[18,19] although acquisition times have either been unreported or with dwell times much longer than sub-millisecond lifetime of many lanthanide-doped upconversion nanocrystals. Alternatively, lifetime measurement techniques regardless of excitation method employ a scanning monchromator[20,21] or a selection of band-pass filters[22,23] to build spectral information only after many scans at the expense of spectral resolution or signal throughput. Gustavsson *et al.*, for example, tested the fluorescence decay of a dimethylquaterphenyl solution in cyclohexane in 10 nm bands over a range of 70 nm.[19] There have been several characterisation suites suitable for pico- and nano-second lifetimes which utilise expensive high-speed

Advanced Cytometry Laboratories, MQ BioFocus Research Centre & MQ Photonics Research Centre, Macquarie University, Sydney, NSW 2109, Australia.
E-mail: dayong.jin@mq.edu.au

† Electronic supplementary information (ESI) available. See DOI: 10.1039/c3ra40637g

imagers and polychromators for nanoparticles and quantum dots.[24,25] These systems contain complex ultrafast pulse lasers and are generally prohibitively expensive. For long-lifetime measurements, current methods based on digital oscilloscopes,[26] time-gated intensified CCD cameras,[18] or photomultiplier tube (PMT) scanning monochrometer[27] can test spectrum, lifetime,[27–30] or even construct 3-D time-resolved spectrum,[28] however the throughput, sensitivity and resolution of these systems are still not sufficient.

In this work, we report a viable approach for obtaining time-resolved spectra with high sensitivity, resolution and throughput. We incorporate an integrated multi-channel photon-sensing device, a Hamamatsu 32-channel PMT, as a linear array detector behind a spectrometer (1200 lines per mm, MicroHR (Automated), Horiba). This provides high spectral resolution as well as allowing simultaneous detection of lifetime decays. To challenge the real-time simultaneous 32-channel data analysis, we employ two 16-channel programmable DAQ cards with 1.25 MHz bandwidth per channel (PXIe-6358, National Instruments). In addition, the DAQ cards also provided means to synchronise the pulsed laser source, spectrometry scanner, and data acquisition over many cycles so that sufficient signal strength could be accumulated to detect low concentration of lanthanide materials (detailed setup description and schematic layout Fig. S1 are provided in the ESI†).

To demonstrate the powerful utility of this system, we coupled the spectrometer fibre to a purpose-built upconversion confocal laser scanning system similar to the ref. 8, and tested the 40-nm hexagonal phase $NaYF_4$:$Yb_{20\%}$,$Er_{2\%}$ upconversion nanocrystals on microscope slides (transmission electron microscope image of the nanocrystals are provided as Supplementary Fig. S2, ESI†). The samples were produced using a modified user-friendly synthesis method *via* the solvothermal route.[8,16]

Fig. 1 recorded the most comprehensive upconversion luminescence spectrum with high-resolution lifetime-decay curves for each wavelength to our knowledge. It took less than 1 min for our automated system to complete 50 acquisitions and construct the 3-D spectrogram. This demonstrates the extremely high throughput achieved by the system design. Supplementary Fig. S3, ESI† selectively display another three sets of data collected under different laser excitation powers (29 mW, 19 mW and 14 mW; equivalent to average power density values in the range of 2.8–5.7 $\times$ 10^4 W cm^{-2}) of pulsed excitation. According to our previous knowledge,[7,9] the radio-metric spectra were strongly power dependent, which was further confirmed by this work as shown in Supplementary Fig. S4, ESI†. Increasing the excitation radiation from relatively low (14 mW peak power) to relatively high levels (39 mW peak power), the power-dependent ratio of red-to-green integrated intensities increased from 0.9 to 1.4. The 3-D figures clearly display the upconversion luminescence behaviours on each energy level after 78 μs pulses of 980 nm excitation (at 500 Hz pulse repetition rate). According to the simplified energy level diagram (see inset of Fig. 1), the green (Er^{3+} $^4F_{7/2} \rightarrow {}^2H_{11/2}$, $^4S_{3/2} \rightarrow {}^4I_{15/2}$) and red ($Er^{3+}$ $^4F_{7/2} \rightarrow {}^2H_{11/2}$, $^4S_{3/2} \rightarrow {}^4F_{9/2} \rightarrow {}^4I_{15/2}$) emissions arise from sequential two-photon upconversion processes;[29]

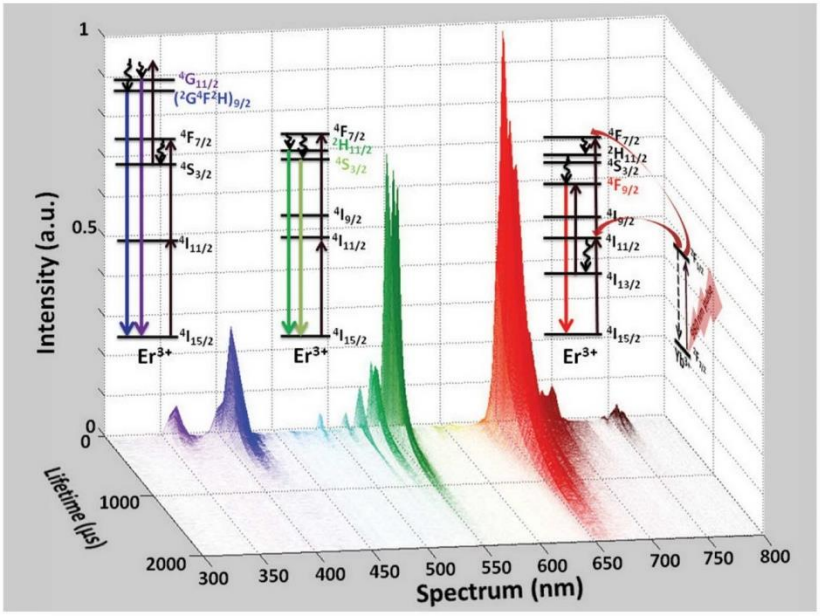

Fig. 1 The 3-dimensional time-resolved luminescence spectra from NaYF4:Yb/Er nanocrystals with the simplified energy levels shown in inset. The pseudo colours were added to match different wavelength colours for improved spectrum presentation, and transparency factor was adjusted according to the intensity values on each colour channels for improved visibility on lifetime decays.

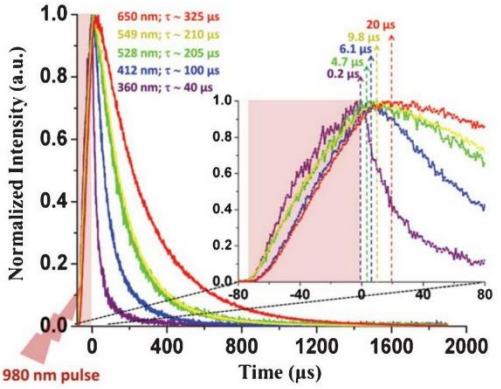

Fig. 2 The normalised time-resolved decaying curves from different emission wavelengths at 360 nm, 412 nm, 528 nm, 549 nm and 650 nm. For simplicity, the lifetime values were calculated by fitting to mono-exponential decay algorithm.

interestingly, due to the high power density we reached in the range of 0.72 to 1.98 $\times$ 10^6 W cm^{-2} the characteristic ultraviolet emission with a spectral peak measured at 360 nm (Er^{3+} $^4G_{9/2}$, $^2K_{15/2}$, $^2G_{7/2} \rightarrow {}^4G_{11/2} \rightarrow {}^4I_{15/2}$) and violet emission at 412 nm (Er^{3+} $^4G_{9/2}$, $^2K_{15/2}$, $^2G_{7/2} \rightarrow {}^4G_{11/2} \rightarrow (^2G^4F^2H)_{9/2} \rightarrow {}^4I_{15/2}$) arise clearly from step-wise sequential three-photon upconversion processes.

The high-resolution spectrum profile decays in the temporal domain at 3-nm spectral resolution, providing in-depth information across neighbourhood emission bands to monitor lifetime behaviours. The lifetime-decay curves have a 1-μs temporal resolution and accuracy better than 1 μs set by the intrinsic electronics bandwidth: 1 MHz bandwidth of the PMT current-to-voltage pre-amplifier and a per-channel data acquisition rate of 1.25 MHz. The lifetime decays follow poly-exponential curves mainly due to the multiple long-lived excited states of activator (Er) ions and relaxations between them during the process of each decay. Fig. 2 selectively displays the upconversion luminescence decay curves on the emission wavelength of 360 nm, 412 nm, 528 nm, 549 nm and 650 nm representing the ultra violet (UV), violet, green, yellow, and red emissions respectively. The red clearly decays slower than the green, which results were consistent with our previous observations.[9] The yellow emission ($^4S_{3/2} \rightarrow {}^4I_{15/2}$) decays slight longer than green emission ($^2H_{11/2} \rightarrow {}^4I_{15/2}$), also consistent with literatures.[30] The two emission bands at 360 nm (Er^{3+} $^4G_{9/2}$, $^2K_{15/2}$, $^2G_{7/2} \rightarrow {}^4G_{11/2} \rightarrow {}^4I_{15/2}$) and 412 nm ($Er^{3+}$ $^4G_{9/2}$, $^2K_{15/2}$, $^2G_{7/2} \rightarrow (^2G^4F^2H)_{9/2} \rightarrow {}^4I_{15/2}$) as result of the three-photon upconversion process however decay time, τ, much shorter with $\sim$40 μs and $\sim$100 μs, respectively.

Furthermore, the system also recorded the featured high-resolution rise times of upconversion emissions resulting from energy transfer upconversion (ETU) and indirect pumping of the metastable-emitting levels of erbium.[30] After pulsed excitation, there are still sufficient sensitised photons travelling within Yb networks or intermediate states of Er ions waiting to be (further) up-converted. This further leads to the remarkably extended intensity peaks following the excitation laser pulse. The UV, violet, green, yellow and red emissions reach their intensity peaks at 0.2 μs, 6.1 μs, 4.7 μs, 9.8 μs, and 20 μs after the excitation pulse respectively (shown in the inset of Fig. 2). By taking a detailed analysis of the rising slopes of different wavelengths, the number and rate of each cascade upconversion steps can be asserted. The UV rapidly follows 980 nm excitation energy pulse with minimum delay (only 0.2 μs) in intensity peak, which indicates very fast population of the metastable $^4G_{9/2}$, $^2K_{15/2}$, $^2G_{7/2}$. The violet and red emissions follow the excitation relatively slower than the other threes, which suggests the fact that the multiphonon non-radiative relaxations ($^2H_{11/2}$, $^4S_{3/2} \rightarrow {}^4F_{9/2}$ and $^4I_{11/2} \rightarrow {}^4I_{13/2}$ for red, and $^4G_{11/2} \rightarrow (^2G^4F^2H)_{9/2}$ for violet) were slow.

In conclusion, to meet the increasing requirements for advanced characterisation of luminescence lanthanide materials, such as the current, fast growing field of upconversion nanocrystals,[31] we have demonstrated the next generation of spectroscopy systems for simultaneously recording multiple lifetime decay curves and high-resolution emission spectrum. The relationships between multiple excited states and complicated photon transfer process can be better understood using our system which can be used to rapidly discover and accurately investigate the unique properties within a variety range of luminescence materials. To our best knowledge, this work is the first quantitative report showing the 3-D time-resolved full-emission spectra with lifetime and high-resolution spectrum peaks in upconversion nanocrystals. Therefore, this work holds significant value in advancing instrumentation design, as well as broadly impacting the chemistry and material sciences.

Acknowledgements

The authors wish to acknowledge Deming Liu for the preparation of upconversion nanocrystals, Prof. Jim Piper, Dr. Yiqing Lu, Yujia Liu, Prof. Ewa Goldys, Prof. Judith Dawes, Jiangbo Zhao, and Henrique Thadeu for constructive technical discussions. L. Zhang and D. Jin acknowledge financial support from the International Macquarie University Research Excellence Scholarship (iMQRES), Macquarie University Research Infrastructure Block Grants (RIBG) 2011, and the Australian Research Council (Discovery Project DP 1095465).

Notes and references

1 S. V. Eliseeva and J.-C. G. Bunzli, *Chem. Soc. Rev.*, 2010, **39**, 189.
2 L. Sun, H. Dong and C.-H. Yan, *Nanoscale*, 2013, DOI: 10.1039/C3NR34069D.
3 W. Deng, L. Sudheendra, J. Zhao, J. Fu, D. Jin, I. M. Kennedy and E. M. Goldys, *Nanotechnology*, 2011, **22**, 325604.
4 J. Zhou, Z. Liu and F. Li, *Chem. Soc. Rev.*, 2012, **41**, 1323.
5 H. X. Mai, Y. W. Zhang, L. D. Sun and C. H. Yan, *J. Phys. Chem. C*, 2007, **111**, 13721.
6 J. Peng, Y. Sun, Q. Liu, Y. Yang, J. Zhou, W. Feng, X. Zhang and F. Li, *Nano Res.*, 2012, **5**, 770.
7 E. P. Schartner, D. Jin, H. Ebendorff-Heidepriem, J. A. Piper, Z. Lu and T. M. Monro, *Nanoscale*, 2012, **4**, 7448.

Electronic Supplementary Material (ESI) for RSC Advances

High-throughput 3-Dimentional Time-resolved Spectroscopy: Simultaneous Characterization of Luminescence Properties in Spectral and Temporal Domains

Supplementary information

Lixin Zhang[a], Aaron McKay[a], Dayong Jin*[a]

Fig. S1 illustrates the principle and simplified layout of a purpose-built microscopy system. Briefly, it incorporates three basic functions: wide-field microscopy imaging, laser scanning confocal microscopy imaging, and time-resolved spectral measurement. Wide-field imaging is used to find locations of interests when preparing lanthanide samples on a microscopy slide; scanning confocal imaging is then used to zoom in to detect nanoparticles.

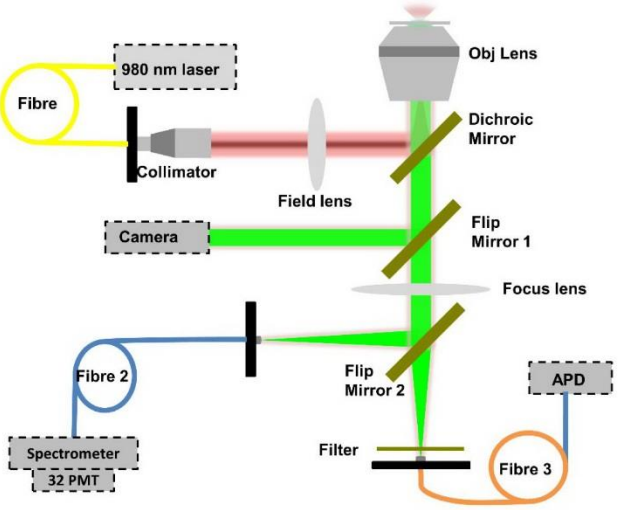

Figure S1. The schematic optical layout for slide-based microscopy imaging system capable of time-resolved spectrum measurement: it has been developed from a x-y-z 3-D stage based scanning microscope via epi-fluorescence configuration, incorporating both wide-field illumination and confocal illumination through a switching lens.

The illumination from a fibre-coupled single-mode diode laser (350 mW, 975 nm, LEO Photonics Co., Ltd) was collimated by a commercial collimator (F240FC-780, NA=0.5, Thorlabs) and focused onto the microscopy slide by an objective lens (60×, 0.75 NA, Edmund Optics) via a dichroic mirror (FF01-842/SP-25, Semrock). The fluorescent image was collected and projected onto a colour CCD camera (2.11 MP, Ds-Vi1, Nikon) reflected by the flip mirror 1 after passing through the dichroic mirror for alignment. Here, the viewing field was enlarged by inserting a field lens in excitation beam to construct a telescope structure with the help of objective lens. Then the flip mirror 1 would be moved out of the optical path, and the optical signal was launched on to an avalanched photodiode (APD) (SPCM-AQRH-14-FC, PerkinElmer Optoelectronics) via 50-μm core diameter optical fibre for confocal imaging of upconversion nanoparticles without flip mirror 2, or to an larger core fibre (600-μm core diameter) and then to a grating-based spectrometer (1200 lines/mm, MicroHR automated, Horiba) for spectrum analysis with flip mirror 2 in optical path. Instead of using a CCD camera (e.g., as a spectroscopy setup), or a single element detector (e.g., as a monochrometer setup), we used a high-gain 32-channel photomultiplier tube (PMT) linear array (H11460, Hamamatsu) was utilised to capture the luminescence decay curves from each wavelength band simultaneously. The spectral resolution was 3 nm, and the temporal resolution was 1 μs (limited by the 1-MHz pre-amplifier bandwidth of PMTs). The photo-electron gain of the PMT array was set to 10^6 V/A. To support real-time data acquisition and analysis in high speed, two 16-channel analog-to-digital data acquisition (DAQ) cards (1.25 MHz bandwidth per channel; PXI e-6358, National Instruments) were connected to a personal computer (i5-core; 4 GB memory; Windows 7 operating system).

The programming work has focused on the synchronisation between the laser excitation pulse sequence, spectroscope grating-mirror scanning, and the data acquisition and accumulation from the 32-channel PMT array. The program was implemented in LabVIEW (version 2010, National Instruments) by controlling two output channels (to control the laser and grating mirror) and all 32 input channels (connected to 32 channels of the PMT array) of the two DAQ cards. The DAQ cards were also software controlled

Electronic Supplementary Material (ESI) for RSC Advances

using customised LabVIEW code. To generate a sequence of pulsed laser illumination, a software-based analog function generator was programmed. Both the duty cycle and the repetition rate of the laser diode were controlled according to the experiment requirements. For the results shown in this work, the pulse width was 78 µs and repetition rate was 500 Hz. The arrangement between the grating and the 32-channel PMT array allow approximately 100 nm to be collected simultaneously; each channel capturing emission decays for 3.125 nm spectral bands. The grating mirror position was stepped to collect sequential 100 nm bands to give the broad 300–800 nm spectrum at high resolution as shown in Figure 1 and Figure S3.

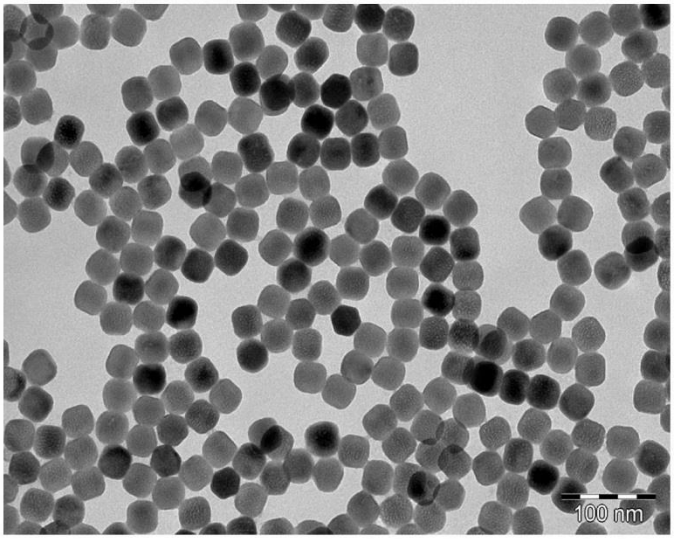

Figure S2. TEM image of hexagonal NaYF4: Yb(20%),Er(2%) nanocrystals

The hexagonal phase $NaYF_4$:$Yb_{20\%}$,$Er_{2\%}$ upconversion nanocrystals with average size of 40 nm were produced using a modified user-friendly synthesis method via the solvothermal route.

Electronic Supplementary Material (ESI) for RSC Advances

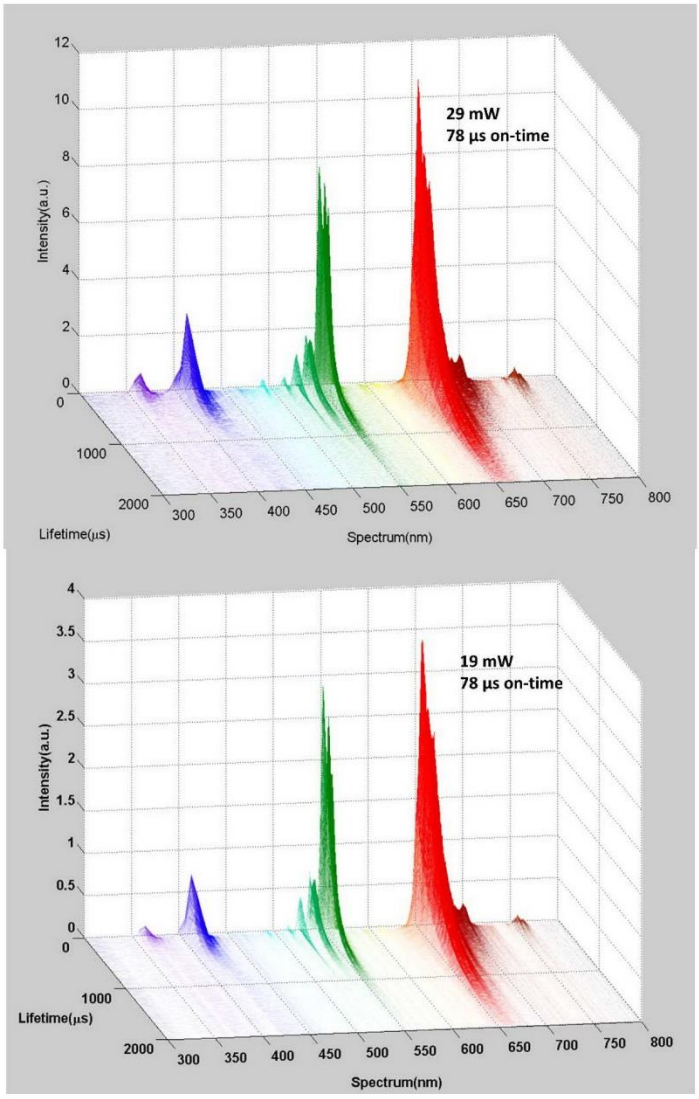

Electronic Supplementary Material (ESI) for RSC Advances

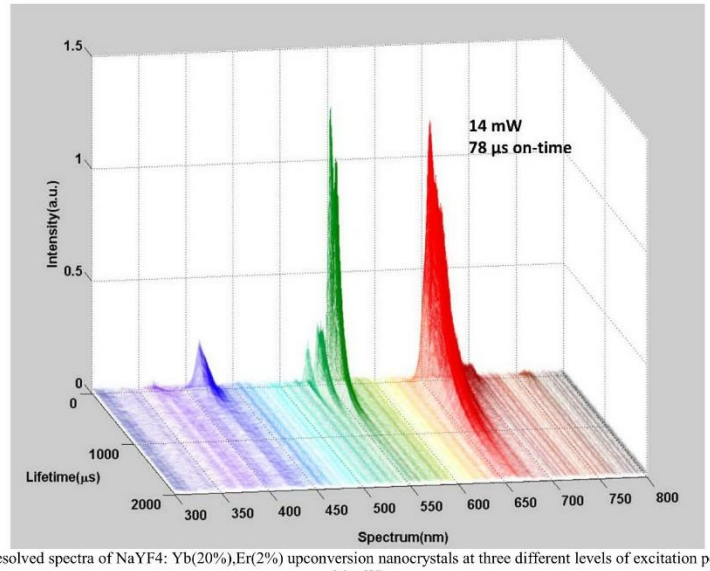

Figure S3. The 3-D time-resolved spectra of NaYF4: Yb(20%),Er(2%) upconversion nanocrystals at three different levels of excitation powers (29 mW, 19 mW, and 14 mW)

Electronic Supplementary Material (ESI) for RSC Advances

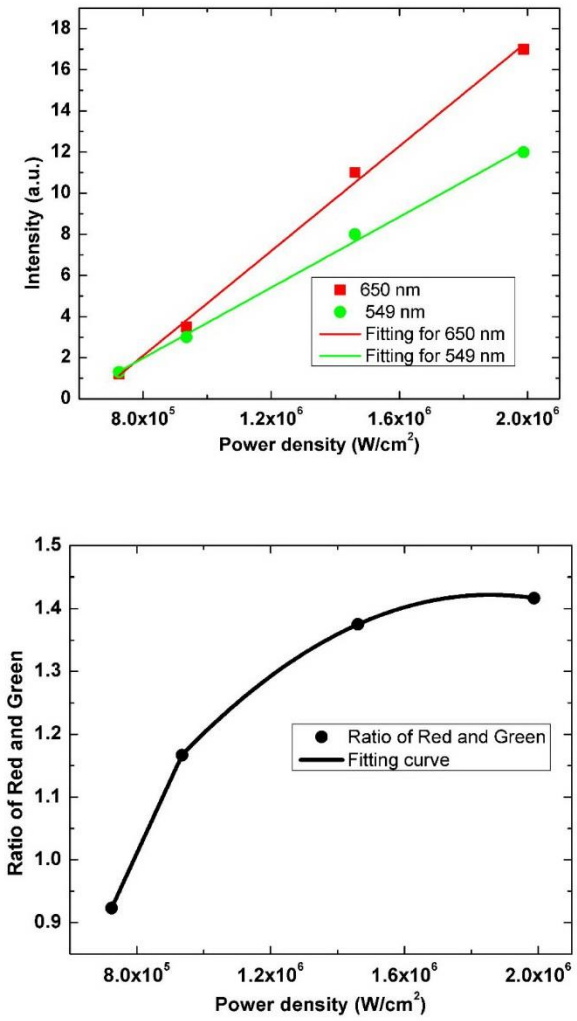

Figure.S4 Power dependence of ratio-metric luminescence intensity of Er-doped upconversion nanocrystals
The left one shows the power dependence of green and red emission, individually; the right one shows the ratio of red and green emission.

Electronic Supplementary Material (ESI) for RSC Advances

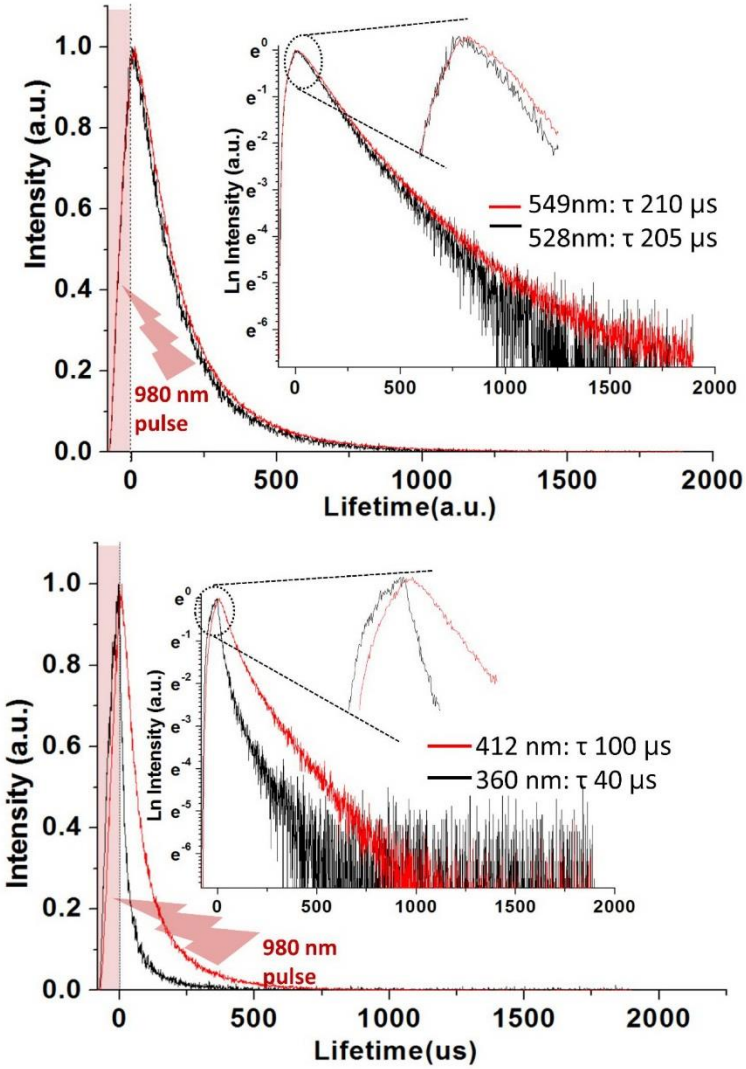

Figure.S5 the typically lifetime curves (at Linear and Log scales) of 360 nm, 412 nm, 528 nm and 549 nm emissions
The top figure makes a comparison of lifetimes for 528 nm and 549 nm emission wavelengths: The red clearly decays slower than the green; some difference in intensity peak positions. The bottom one compares the lifetimes of 412 nm and 360 nm: there are obvious differences on the decay time and intensity peak position.

8 S. Wu, G. Han, D. J. Milliron, S. Aloni, V. Altoe, D. V. Talapin, B. E. Cohen and P. J. Schuck, *Proc. Natl. Acad. Sci. U. S. A.*, 2009, **106**, 10917.

9 J. Zhao, Z. Lu, Y. Yin, C. McRae, J. A. Piper, J. M. Dawes, D. Jin and E. M. Goldys, *Nanoscale*, 2013, **5.**

10 D. K. Chatterjee, M. K. Gnanasammandhan and Y. Zhang, *Small*, 2010, **6**, 2781.

11 S. Jiang, Y. Zhang, K. M. Lim, E. K. Sim and L. Ye, *Nanotechnology*, 2009, **20**, 155101.

12 Z. Song, Y. G. Anissimov, J. Zhao, A. V. Nechaev, A. Nadort, D. Jin, T. W. Prow, M. S. Roberts and A. V. Zvyagin, *J. Biomed. Opt.*, 2013, **18**, 061215.

13 W. J. Kim, M. Nyk and P. N. Prasad, *Nanotechnology*, 2009, **20.**

14 T. Blumenthal, J. Meruga, P. Stanley May, J. Kellar, W. Cross, K. Ankireddy, S. Vunnam and Q. N. Luu, *Nanotechnology*, 2012, **23**, 185305.

15 W. Zou, C. Visser, J. A. Maduro, M. S. Pshenichnikov and J. C. Hummelen, *Nat. Photonics*, 2012, **6**, 560.

16 F. Wang, Y. Han, C. S. Lim, Y. Lu, J. Wang, J. Xu, H. Chen, C. Zhang, M. Hong and X. Liu, *Nature*, 2010, **463**, 1061.

17 F. Wang, R. R. Deng, J. Wang, Q. X. Wang, Y. Han, H. M. Zhu, X. Y. Chen and X. G. Liu, *Nat. Mater.*, 2011, **10**, 968.

18 P. L. T. M. Frederix, M. A. H. Asselbergs, W. G. J. H. M. Van Sark, D. J. Van den Heuvel, W. Hamelink, E. L. De Beer and H. C. Gerritsen, *Appl. Spectrosc.*, 2001, **55**, 1005.

19 T. Gustavsson, A. Sharonov and D. Markovitsi, *Chem. Phys. Lett.*, 2002, **351**, 195.

20 J. Buckers, D. Wildanger, G. Vicidomini, L. Kastrup and S. W. Hell, *Opt. Express*, 2011, **19**, 3130.

21 X. Liu, B. J. Chen, E. Y. B. Pun and H. Lin, *Opt. Mater.*, 2013, **35**, 590.

22 Q. Y. Zhang, T. Li, Z. H. Jiang, X. H. Ji and S. Buddhudu, *Appl. Phys. Lett.*, 2005, **87.**

23 C. N. Fleming, K. A. Maxwell, J. M. DeSimone, T. J. Meyer and J. M. Papanikolas, *J. Am. Chem. Soc.*, 2001, **123**, 10336.

24 Q. D. Zheng, H. M. Zhu, S. C. Chen, C. Q. Tang, E. Ma and X. Y. Chen, *Nat. Photonics*, 2013, **7**, 234.

25 D. F. Underwood, T. Kippeny and S. J. Rosenthal, *J. Phys. Chem. B*, 2001, **105**, 436.

26 V. Mahalingam, R. Naccache, F. Vetrone and J. A. Capobianco, *Opt. Express*, 2012, **20**, 111.

27 F. S. Choa, J. Y. Fan, P. L. Liu, J. Sipior, G. Rao, G. M. Carter and Y. J. Chen, *Appl. Phys. Lett.*, 1996, **69**, 3668.

28 K. Senechal-David, S. J. Pope, S. Quinn, S. Faulkner and T. Gunnlaugsson, *Inorg. Chem.*, 2006, **45**, 10040.

29 Y. Li, J. Zhang, X. Zhang, Y. Luo, X. Ren, H. Zhao, X. Wang, L. Sun and C. Yan, *J. Phys. Chem. C*, 2009, **113**, 4413.

30 A. Bednarkiewicz, D. Wawrzynczyk, A. Gagor, L. Kepinski, M. Kurnatowska, L. Krajczyk, M. Nyk, M. Samoc and W. Strek, *Nanotechnology*, 2012, **23**, 145705.

31 A. Gnach and A. Bednarkiewicz, *Nano Today*, 2012, **7**, 532–563.

3.3 Additional information (unpublished results)

Apart from the three-dimensional time-resolved spectra we presented in the published paper, their corresponding two dimensional figures are shown here: intensity in terms of spectrum (upper figure), and intensity in terms of lifetime (lower figure)

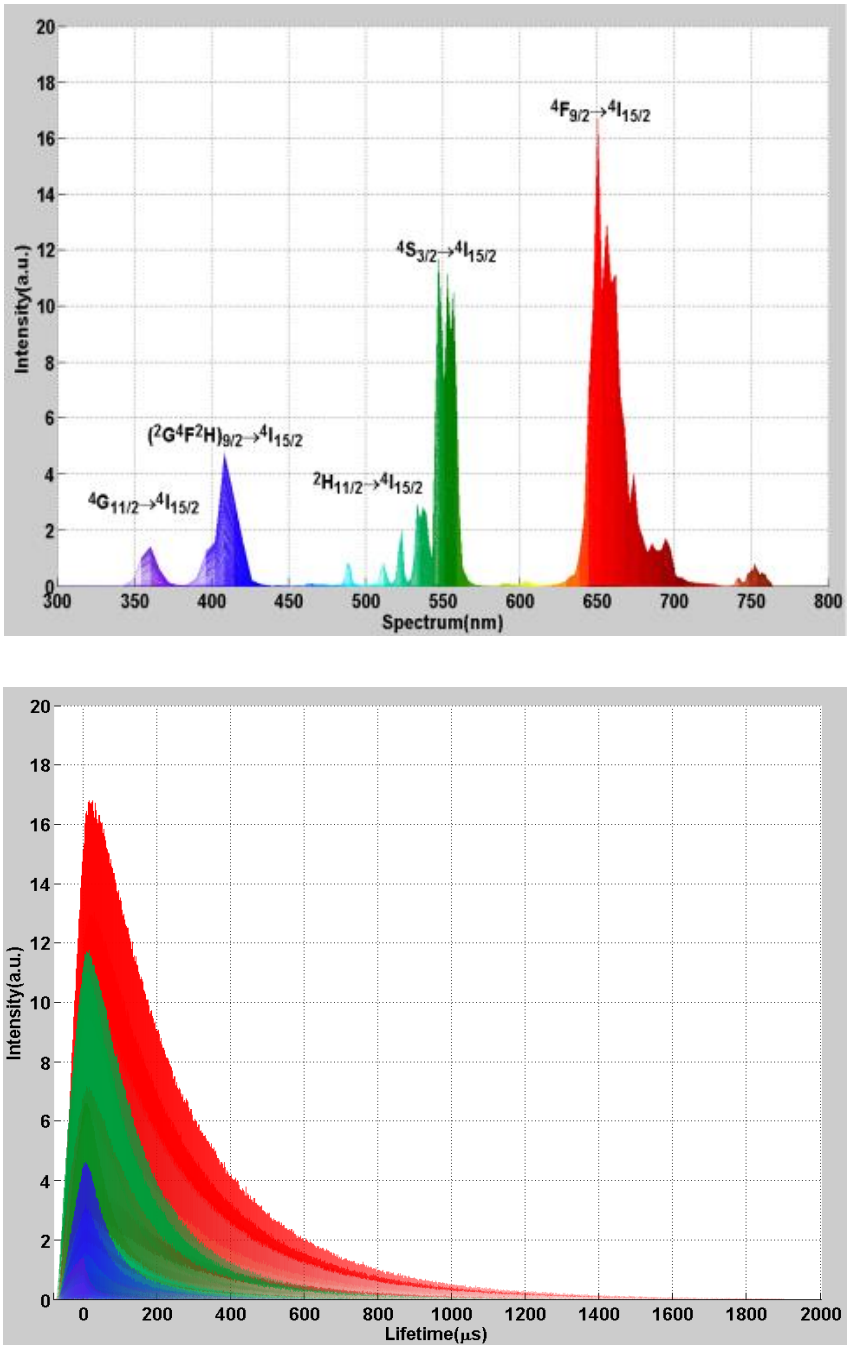

Figure. S3-1 two dimensional information for the NaYF4: Yb2%, Er2%: intensity vis wavelength (upper) and intensity vis lifetimes (lower).

Apart from the characterisation for the lanthanide doped upconversion nanocrystals, I have used this system to characterise long-lived down-conversion luminescence and sensitized luminescence based on the luminescence resonance energy transfer (LRET) process from europium complex doped microspheres. These luminescence lifetime coded microspheres are useful in simultaneous analysis of multiple biomolecules and analytes in a single test. The original work was published by my colleagues at the Advanced Cytometry Labs at Macquarie (*Nature Communications*, DOI: 10.1038/ncomms4741). The microspheres were prepared by my colleagues using europium complex BHHCT as donor and a hexafluorophosphate salt of cationic coumarin as acceptor dyes encapsulated into porous polystyrene beads. By pulsing an ultraviolet (UV) light emitting diode as the excitation source, my setup was modified to excite the down-conversion microspheres at 365 nm. The time-resolved spectroscopy system supports the collection of the time-resolved long-lifetime emissions in red. The figures below recorded the 3-D time-resolved spectra from two different batches of LRET microspheres at different donor-to-accept doping ratios. The UV pulses are 78 μs at repetition rate of 250 Hz. From the comparison figures of time-resolved spectra, the luminescence lifetime for microspheres with donor/acceptor ratios of 1:0.25 is longer than the one with donor/acceptor ratios of 1:1.2 due to the less LRET effect.

The purpose of this experiment was to use the comprehensive time-resolved spectral data to calculate the energy transfer efficiency within a single microsphere. But due to the inaccuracy and difficulty of controlling the acceptors' distribution and uniformity as well as the photo-bleaching problem, this experiment was not concluded by the time of my PhD thesis submission.

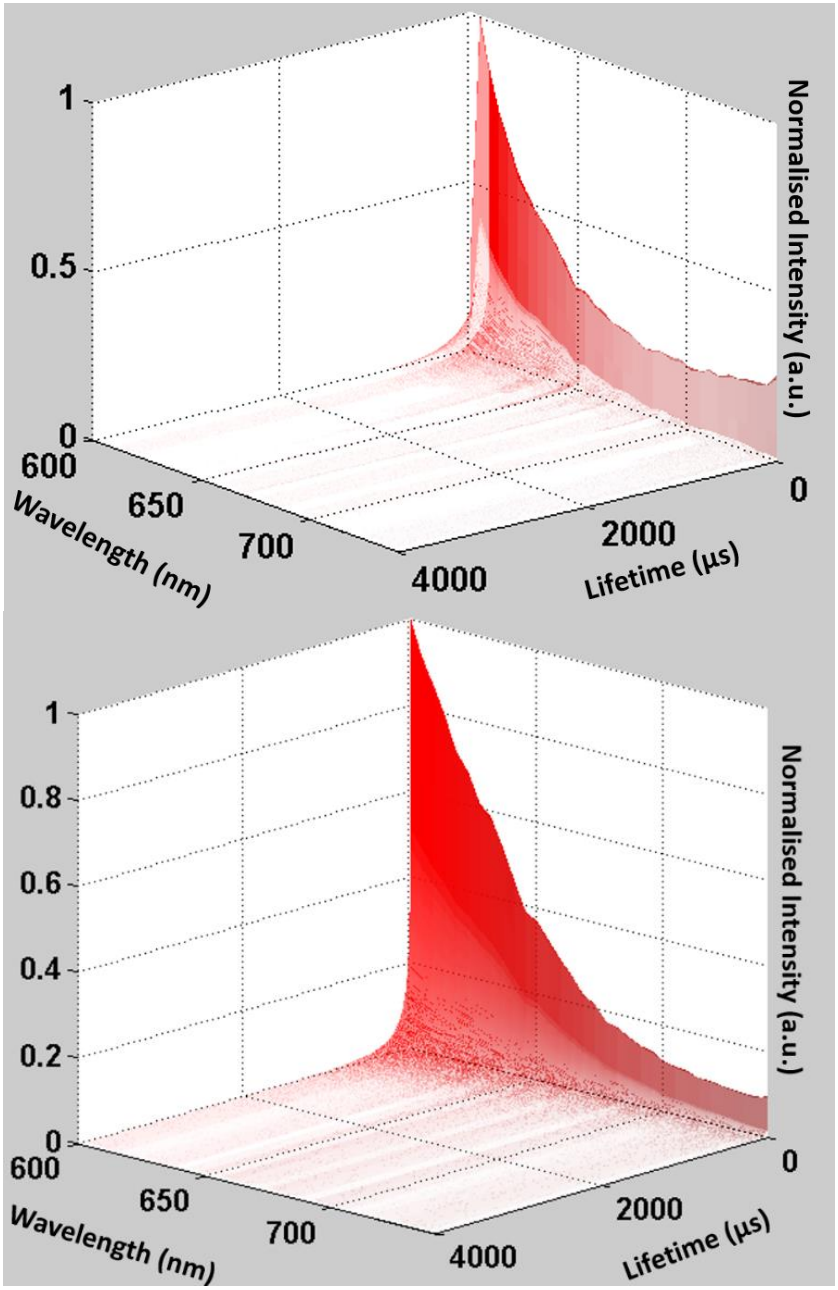

Figure. S3-2 time-resolved spectra of 15 µm LRET microspheres with donor/acceptor ratios of 1:0.25 (top) and 1:1.2 (bottom).

3.4 Remarks

The high-throughput time-resolved spectroscopy system has been described in this chapter. This engineering work is based on the careful design and application of a multi-channel PMT linear array detector as well as integration and synchronizations of different measurement modalities. This system can simultaneously measure temporal and spectral luminescence intensities from long-lived luminescent materials with both high speed and high resolution. We have verified its performance in studying both upconversion nanocrystals using the 980 nm laser excitation and down-conversion microspheres using the pulsed 365 nm UV LED excitation.

The current system still requires further optimization and the integration of other characterization modalities towards a fully automatic system with self-correlated functionalities to performance advanced nanoscale characterization of luminescent nano- and micro- materials. A mathematical algorithm should be developed and applied via the control programming to calibrate the experimental data in both intensity and corresponding wavelength values, instead of the current manual operation.

Apart from the high throughput feature of this system for building 3-D time-resolved spectra, this robust system can also implement imaging characterisation for the lanthanide doped materials by incorporating the laser scanning confocal microscope and wide field microscope. The extension of this work with additional features has been presented in the next chapter.

3.5 References

[1] Liu Q, Feng W, Li FY. Water-soluble lanthanide upconversion nanophosphors: Synthesis and bioimaging applications in vivo. Coordin Chem Rev. 2014;273:100-10.
[2] Zhu H, Chen X, Jin LM, Wang QJ, Wang F, Yu SF. Amplified Spontaneous Emission and Lasing from Lanthanide-Doped Up-Conversion Nanocrystals. Acs Nano. 2013;7:11420-6.
[3] Cui YJ, Chen BL, Qian GD. Lanthanide metal-organic frameworks for luminescent sensing and light-emitting applications. Coordin Chem Rev. 2014;273:76-86.
[4] Zhu H, Lin CC, Luo W, Shu S, Liu Z, Liu Y, et al. Highly efficient non-rare-earth red emitting phosphor for warm white light-emitting diodes. Nature communications. 2014;5:4312.
[5] Gargas DJ, Chan EM, Ostrowski AD, Aloni S, Altoe MV, Barnard ES, et al. Engineering bright sub-10-nm upconverting nanocrystals for single-molecule imaging. Nature nanotechnology. 2014;9:300-5.
[6] Sun Y, Zhu XJ, Peng JJ, Li FY. Core-Shell Lanthanide Upconversion Nanophosphors as Four-Modal Probes for Tumor Angiogenesis Imaging. Acs Nano. 2013;7:11290-300.

Chapter 4

The sophisticated energy transfer and luminescence mechanisms that lead to many unique optical properties of lanthanide materials are still not completely quantified. This requires both novel design to synthesize new materials and robust setups for advanced characterisations under different external conditions with high resolution.

While Chapters 2 and 3 studied the unique optical properties of photon down-converting and photon upconverting materials in both spectral and lifetime domains, Chapter 4 here explores the optical properties of lanthanide materials with high spatial precision (resolution) and under the different excitation power intensities.

We first designed and synthesized a library of colour-barcoded upconversion micro-rods (the synthesis was done by our collaborators at National University of Singapore), and I further upgraded my characterization system by adding a laser scanning confocal imaging modality. The laser confocal scanning microscopy method can provide high resolution for characterizing selected sections on a single micro-rod for nanoscale time-resolved analysis. I carried out comprehensive measurements for different designs of micro-rods and confirmed no energy transfer happening between the neighbourhood sections in one rod doped by different lanthanide acceptors (Tm3+ and Er3+). In this system, I realized a self-correlated method for imaging and analysis: the wide field microscope is useful for rapid identification of the targets/areas of interest, and the laser scanning confocal microscope is used to inspect a specific area with high resolution, which is followed by the application of lifetime measurement. This work has been published in the prestigious *Journal of America Chemistry Society* 2014 with my role as the 2nd author in charge of optical characterisations.

Moreover, closely working with my colleagues at the Advanced Cytometry Labs at Macquarie University, I have also contributed my characterisation platform for the power dependence study of upconversion materials, which has led to another co-authored paper published in the prestigious journal of *Nature Nanotechnology*. In this work I characterised the power-dependent properties of the highly doped upconversion crystals (Supplementary Figure S6). This provides further evidence that a high excitation irradiance can moderate the concentration quenching for brighter

upconversion materials. I have further applied my system and demonstrated that highly-doped single nanocrystals could be directly imaged by the wide field microscope (Supplementary Figure S10).

4.1 Contributions to Paper 3

TABLE 4-1 Author contribution summary for paper 3.

	Y. Zhang	L. Zhang	R. Deng	J. Tian	Y. Zong	D. Jin	X. Liu
Experiment Design	•						
Material Synthesis	•		•	•	•		
Optical Characterisation		•				•	
Data Analysis	•	•	•		•		•
Main Manuscript	•	•				•	•
Figures and Supporting Info	•	•	•	•	•		

In this project, I contributed the optical characterisation aspect of this project by upgrading the system developed in Chapter 3 by adding a laser scanning confocal microscope. I carried out all the optical characterisations, data collection and data analysis, which takes account of around 30 % of the whole contribution.

4.2 Paper 3

Yuhai Zhang, **Lixin Zhang**, Reren Deng, JingTian, Yun Zong, Dayong Jin and Xiaogang Liu. “Multicolor Barcoding in a Single Upconversion Crystal”, *J. Am. Chem. Soc.* 2014, 136, 4893-4896.

JACS
JOURNAL OF THE AMERICAN CHEMICAL SOCIETY
Communication
pubs.acs.org/JACS

Multicolor Barcoding in a Single Upconversion Crystal

Yuhai Zhang,[†] Lixin Zhang,[‡] Renren Deng,[†] Jing Tian,[§] Yun Zong,[∥] Dayong Jin,[‡] and Xiaogang Liu*[,†,∥,⊥]

[†]Department of Chemistry, National University of Singapore, 3 Science Drive 3, Singapore 117543, Singapore
[‡]Advanced Cytometry Laboratories, MQ Photonics Research Centre and MQ Biofocus Research Centre, Macquarie University, Sydney, NSW 2109, Australia
[§]Laboratory of Advanced Materials, Fudan University, 220 Handan Road, Shanghai 200433, China
[∥]Institute of Materials Research and Engineering, 3 Research Link, Singapore 117602, Singapore
[⊥]Center for Functional Materials, NUS (Suzhou) Research Institute, Suzhou, Jiangsu 215123, China

Supporting Information

ABSTRACT: We report the synthesis of luminescent crystals based on hexagonal-phase $NaYF_4$ upconversion microrods. The synthetic procedure involves an epitaxial end-on growth of upconversion nanocrystals comprising different lanthanide activators onto the $NaYF_4$ microrods. This bottom-up method readily affords multicolor-banded crystals in gram quantity by varying the composition of the activators. Importantly, the end-on growth method using one-dimensional microrods as the template enables facile multicolor tuning in a single crystal, which is inaccessible in conventional upconversion nanoparticles. We demonstrate that these novel materials offer opportunities as optical barcodes for anticounterfeiting and multiplexed labeling applications.

Barcoding materials have been widely used as luminescent probes for multiplexed assays in biological species because of their distinct optical characteristics.[1] The use of these materials for anticounterfeiting applications has also attracted much attention in recent years.[2] However, their application in practical settings has been largely hindered by high-cost materials fabrication, low reaction yields, complex instrumentation setup, and high background noise when excited by common ultraviolet or visible light sources.[3]

Lanthanide-doped upconversion materials may provide a much needed solution for the above-mentioned problems.[4] First, their fabrication methods are typically based on low-cost bottom-up processes and can be easily scaled up for massive production.[5] Second, the morphology of the upconversion materials is highly tunable with features ranging from nanosized particles to microscale rods,[6] allowing for direct decoding without the concern of the diffraction limit using conventional optical microscopes. The third aspect is that upconversion materials feature large anti-Stokes shifts and long lifetimes, leading to largely reduced background noise.[7] Furthermore, the ability to tune the emission wavelength from UV−vis to NIR spectral regions offered by photon upconversion enables the generation of a large, diverse library of optical barcodes. Despite their promise, it has been challenging to prepare multicolored upconversion barcodes using a single spherical nanoparticle due to the resolution limit of conventional optical microscopes. Herein, we report the rational design and synthesis of multicolor-banded upconversion barcodes based on tip-modified hexagonal-phase $NaYF_4$ microrods with different activators doped at the tips (Scheme 1). With varying sets of activators, we prepare a library of single-crystal-based upconversion barcodes comprising different combinations of three primary colors (red, green, and blue) that are easily readable with conventional optical microscopes. We also demonstrate the use of these optical materials as barcodes for security inking and cell tracking applications.

Regular light microscopes generally have the best spatial resolution of ~200 nm constrained by the optical diffraction limit.[8] To resolve two emission features (or spots), the two

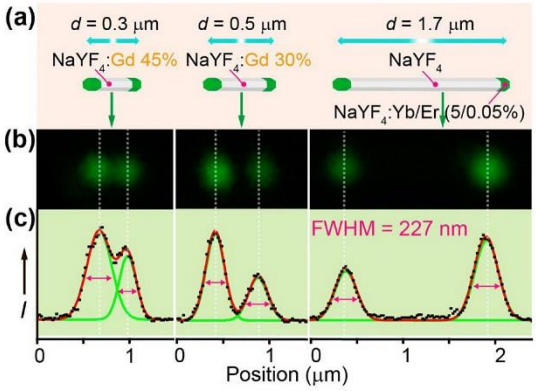

Figure 1. (a) Schematic design for determining the diffraction limit of the microscope using three tip-modified microrods with different spacer lengths (d = 0.3, 0.5, and 1.7 μm). (b) Upconversion micrographs of the three microrods showing the emission dots from the tips. (c) Their corresponding emission spectra indicating the degree of the spatial overlap between the two emission dots. The point spread function (red line) of the intensity profile is fitted with a Gaussian function (green line), and the full width at half-maximum (fwhm) is taken as the resolution. The average fwhm of the six spots is 227 nm, in good agreement with the theoretical value (196 at 550 nm estimated using an oil objective lens with a numeric aperture of 1.4). Note that the length of the spacer is tuned by Gd doping at varied concentrations.

Received: February 12, 2014
Published: March 19, 2014

dx.doi.org/10.1021/ja5013646 | J. Am. Chem. Soc. 2014, 136, 4893−4896

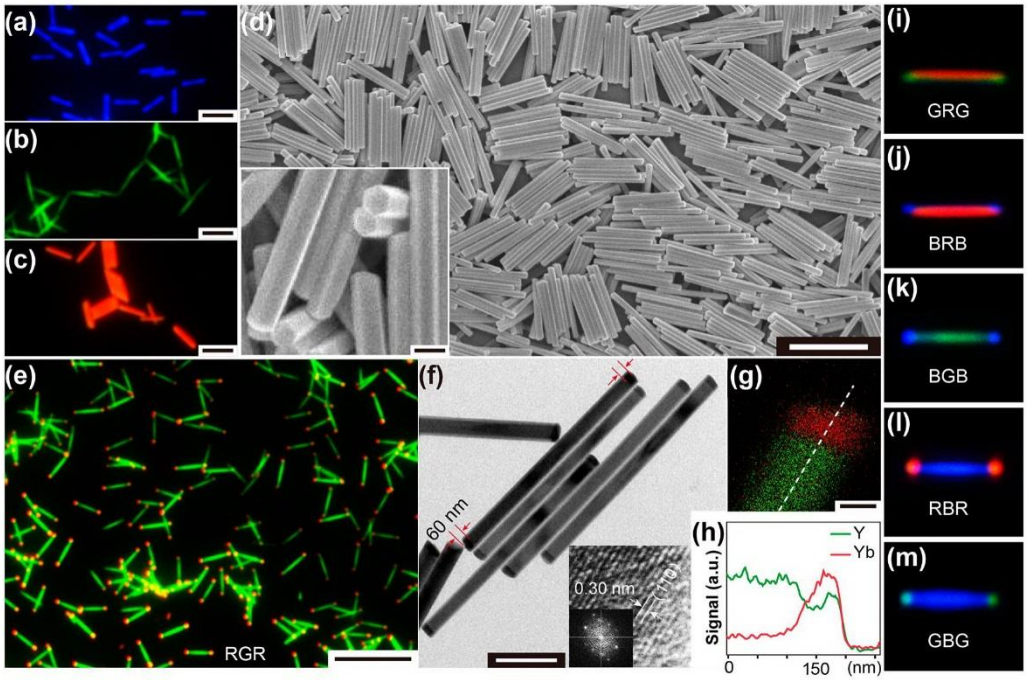

Figure 2. (a–c) Optical micrographs of the parent $NaYF_4$ upconversion microrods doped with Yb^{3+}/Tm^{3+} (20/0.2 mol %), Yb^{3+}/Er^{3+} (5/0.05 mol %), and Yb^{3+}/Er^{3+} (50/0.05 mol %), respectively. Scale bars in a-c are 2 μm. (d) A typical SEM image of the $NaYF_4$ microrods. Scale bar is 2 μm. Inset shows the hexagonal prism morphology of the rods. Scale bar is 200 nm. (e) Optical micrographs of dual-color (RGR) emitting $NaYF_4$ microrods after the end-on epitaxial growth with $NaYF_4$:Yb/Er precursors. Scale bar is 5 μm. Note that the red-emitting tips are heavily doped with 50 mol % of Yb^{3+}, while the green-emitting segment is doped with 5 mol % of Yb^{3+}. (f) TEM image of the tip-modified microrods (Inset: HRTEM image and corresponding Fourier-transform diffractogram of the segment joint). Scale bar is 500 nm. (g, h) Elemental mapping and corresponding EELS line scan conducted on a single tip-modified microrod. Scale bar in g is 50 nm. (i–m) Optical micrographs showing five additional sets of dual-color-banded upconversion microrods, obtained by varying the composition of the dopants. Note that the appearance of a tinge color at the tip junction is due to the chromatic aberration and limited resolution of the microscope.

emitting objects need to be separated by a distance larger than the diffraction limit. Otherwise, the microscope would not have the necessary resolution power to distinguish them. In our design, we utilize $NaYF_4$ microrods with a length of ~2 μm as spacers to grow tip-modified rods that can exhibit distinguishable dual-color emissions. To confirm this, we synthesized three types of microrods with emitting tips separated by spacers of different lengths (Figures 1 and S1). It was found that as the length of the spacer increases from 0.3 to 1.7 μm, the two emitting spots are gradually resolved from one merged spot into two independent spots. Considering the compromise of synthetic yield induced by Gd^{3+} doping (detailed discussion in Supporting Information),[6a] we chose a 1.7-μm spacer in this work for multicolor tuning on a single upconversion crystal. The use of the 1.7-μm spacer for the growth of tip-modified rods overcomes the diffraction limit, allowing different emission colors easily resolvable at the single crystal level.

The lanthanide-doped $NaYF_4$ microrods were prepared by a well-established hydrothermal method.[9] Emissions from individual rods doped with different sets of lanthanides can be identified owing to the strong upconversion luminescence of the hexagonal-phase microrods (Figures 2a–c and S2). Scanning electron microscopic imaging reveals the high uniformity of the as-synthesized microrods (~1.9 μm in length and ~140 nm in diameter) (Figure 2d). Note that the length of the rods can be tuned from 0.3 to 2 μm using the gadolinium doping approach (Figure S1).[10] Furthermore, we found that upon addition of α-$NaYF_4$ nanoparticles (Figure S3) as the precursors, successive end-on growth of the β-$NaYF_4$ microrods can be achieved, as evidenced by the optical microscopic images (Figure 2e). This can be attributed to favorable epitaxial growth along the long [001] axis of the crystal. Transmission electron microscopy (TEM) imaging shows two dark-colored tips of the segmented rods, attributable to the high contrast of heavily Yb^{3+}-doped $NaYF_4$ (Figures 2f and S12). High-resolution TEM reveals the single-crystalline nature of the rod with a d-spacing of 0.30 nm, corresponding to the (110) plane of β-$NaYF_4$ (JCPDS No. 16-0334). X-ray diffraction data suggest that the α-$NaYF_4$ precursors are completely consumed after the hydrothermal reaction (Figure S4).

To confirm the tip growth onto the parent microrod, we intentionally doped Yb^{3+} with large concentration disparities, into the β-$NaYF_4$:Yb/Er microrod (5 mol % of Yb^{3+}) and the α-$NaYF_4$:Yb/Er nanoparticle precursor (50 mol % of Yb^{3+}), respectively (Figure S4). Elemental mapping by STEM was performed on the resulting hybrid rods. The difference in the elemental distribution of Yb^{3+} and Y^{3+} over the rod tip clearly indicates the presence of a junction (Figure 2g). The line scan and spot scan analyses reveal the Yb abundance (40%) in the new tip, which is in good agreement with the Yb content in

dx.doi.org/10.1021/ja5013646 | J. Am. Chem. Soc. 2014, 136, 4893–4896

Scheme 1. Design of the Bottom-up Synthesis of a Dual-Color-Banded Hexagonal-Phase $NaYF_4$:Yb/Er Upconversion Microrod through an Oriented Epitaxial Growth Method[a]

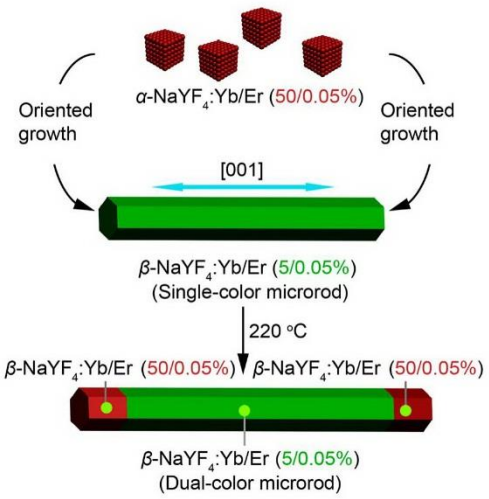

[a]As cubic-phase $NaYF_4$ nanoparticles tend to dissolve at elevated temperatures due to low thermal stability, they could be used as precursors for successive growth of hexagonal-phase $NaYF_4$ tips at both ends of the microrods.

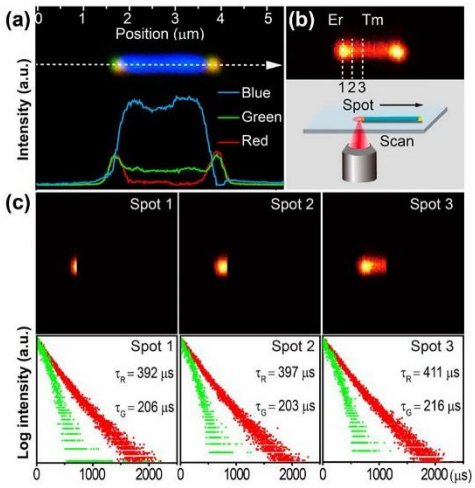

Figure 3. (a) Wide-field luminescence image of a single microrod exhibiting YBY dual-color upconversion emission. Note that the color component of the emission can be resolved by RGB acquisition. (b) Confocal microscope image of a different dual-color microrod. (c) The corresponding green ($^4S_{3/2}$) and red ($^4F_{9/2}$) emission lifetimes in three different areas (marked with spot 1, 2, 3 shown in b) of the microrod. Note that spot 1 contains only Er^{3+}. Spot 2 contains Er^{3+} and a small amount of Tm^{3+}. Spot 3 is codoped with Er^{3+} and a large amount of Tm^{3+}.

α-$NaYF_4$ precursors (Figures 1h and S5). Importantly, the use of α-$NaYF_4$ nanoparticle precursors rather than lanthanide ionic solutions is critical for high yield synthesis of the segmented microrods, as the direct use of ionic precursors leads to phase separation dominant in the crystal growth process

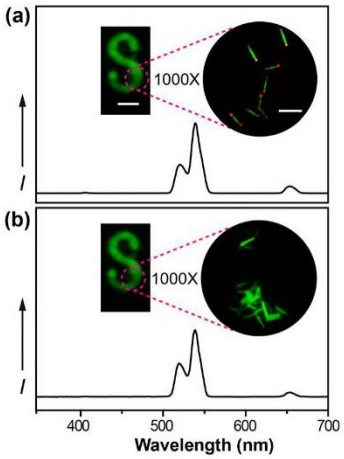

Figure 4. (a) Luminescence image of a stamped letter S generated with dual-color microrods (shown in 1000× magnified image) as the ink. The corresponding upconversion emission spectrum is also shown. Scale bars are 3 μm (right) and 3 mm (left). (b) Luminescence image of a control sample generated with single-color microrods as the ink. Note that the emission spectra (or bulk color appearance) of these two patterns are almost identical. However, their differences in spatial distribution are clearly distinguishable under high magnification.

(Figure S6).[11] It is worth noting that the introduction of luminescent tips of different composition not only enhances the color contrast of the parent microrod but also expands the scope of multicolor upconversion at the single crystal level. Using the step-by-step epitaxial growth method, we synthesized a series of dual-color upconversion microrods displaying different combinations of three primary colors (Figure 2i–m).

As an added benefit, the dual-color upconversion microrod provides a platform to investigate the possibility of energy transfer at the tip junction. To this end, we synthesized YBY-color rods (Y and B denote yellow emission of the tips and blue emission of the parent rod, respectively) (Figure 3a). Using a confocal microscope (Figure S7), three different spots (Labeled as 1, 2, 3) at the region of the tip junction can be selectively focused and scanned (Figure 3b). Notably, the use of different band-pass filters allows us to analyze the individual emission peak of Er^{3+}, for example, green emission at 545 nm ($^4S_{3/2} \rightarrow {}^4I_{15/2}$) and red peak at 655 nm ($^4F_{9/2} \rightarrow {}^4I_{15/2}$) (Figure S8). We obtained essentially unaltered lifetimes of Er^{3+} recorded at three different spots (Figures 3c and S9), indicating that there is no crosstalk between Tm^{3+} and Er^{3+} activators even at the tip junction. We reason that the intrinsic small absorption cross sections ($\sim 10^{-21}$ cm^2) of lanthanide ions and the relatively large donor–acceptor separation at the tip junction are mainly responsible for the inefficient energy transfer between Tm^{3+} and Er^{3+}.[12]

We further demonstrated the use of the as-synthesized multicolor microrods as barcodes for anticounterfeiting application.[13] Note that these microrods are dispersible in dimethyl sulfoxide solvent, providing a transparent ink solution under ambient light conditions (Figure S10). As a proof-of-concept experiment, we stamped a solution containing RGR dual-color emitting $NaYF_4$:Yb/Er microrods (Yb^{3+}/Er^{3+}: 5/0.05 mol % for the green-emitting part and Yb^{3+}/Er^{3+}: 50/0.05 mol % for the red-emitting ends) as the security ink onto a paper substrate to

dx.doi.org/10.1021/ja5013646 | J. Am. Chem. Soc. 2014, 136, 4893–4896

create an "S" pattern. As a control, we generated an identical pattern using green-color emitting $NaYF_4$:Yb/Er (10/0.05 mol %) microrods. When exposed to 980-nm laser light, the two patterns are almost indistinguishable based on emission spectral comparison or color appearance under low magnification (Figure 4a). Remarkably, we could clearly tell the two patterns apart when zoomed in under high magnification (Figure 4b). These experiments revealed that the dual-color spatially coded microrods can provide added security protection, enabling almost instant verification of patterned features. On a separate note, these microrods can be internalized by cancer cells, posing positive implications in the quest for multiplexed optical labels (Figure S11 and Movie S1).

Our findings could bring a better understanding of epitaxial growth to other lanthanide-based anisotropic crystals. The fact that these solution-processable multicolor-banded microrods with good crystalline properties can be easily made on a large scale suggests the prospects of using upconversion phosphor barcodes for optical labeling applications, where low-cost manufacturing of the materials with multilevel optical features is essential. We expect an increased effort dedicated to the investigation of these materials in the near future.

■ ASSOCIATED CONTENT

Supporting Information

Additional experimental details. This material is available free of charge via the Internet at http://pubs.acs.org.

■ AUTHOR INFORMATION

Corresponding Author

chmlx@nus.edu.sg

Notes

The authors declare no competing financial interest.

■ ACKNOWLEDGMENTS

This study was supported by the National University of Singapore (R-143-000-427), the Ministry of Education (R-143-000-453), the Singapore-MIT Alliance, and the Agency for Science, Technology, and Research (R-143-000-366). We thank H. H. Kim, W. F. Yang, and X. W. Liu for technical support.

■ REFERENCES

(1) (a) Nam, J.-M.; Thaxton, C. S.; Mirkin, C. A. *Science* **2003**, *301*, 1884. (b) Agasti, S. S.; Liong, M.; Peterson, V. M.; Lee, H.; Weissleder, R. *J. Am. Chem. Soc.* **2012**, *134*, 18499. (c) Kim, S. H.; Shim, J. W.; Yang, S. M. *Angew. Chem., Int. Ed.* **2011**, *50*, 1171. (d) Pregibon, D. C.; Toner, M.; Doyle, P. S. *Science* **2007**, *315*, 1393.

(2) (a) Osberg, K. D.; Rycenga, M.; Bourret, G. R.; Brown, K. A.; Mirkin, C. A. *Adv. Mater.* **2012**, *24*, 6065. (b) Creran, B.; Yan, B.; Moyano, D. F.; Gilbert, M. M.; Vachet, R. W.; Rotello, V. M. *Chem. Commun.* **2012**, *48*, 4543.

(3) (a) Haase, M.; Schäfer, H. *Angew. Chem., Int. Ed.* **2011**, *50*, 5808. (b) Gorris, H. H.; Wolfbeis, O. S. *Angew. Chem., Int. Ed.* **2013**, *52*, 3584. (c) Park, Y. I.; Nam, S. H.; Kim, J. H.; Bae, Y. M.; Yoo, B.; Kim, H. M.; Jeon, K.; Park, H. S.; Choi, J. S.; Lee, K. T.; Suh, Y. D.; Hyeon, T. *J. Phys. Chem. C* **2013**, *117*, 2239. (d) Bogdan, N.; Vetrone, F.; Ozin, G. A.; Capobianco, J. A. *Nano Lett.* **2011**, *11*, 835. (e) Chen, G.; Ohulchanskyy, T. Y.; Liu, S.; Law, W.; Wu, F.; Swihart, M. T.; Agren, H.; Prasad, P. N. *ACS Nano* **2012**, *6*, 2969. (f) Hao, J.; Zhang, Y.; Wei, X. *Angew. Chem., Int. Ed.* **2011**, *50*, 6876. (g) Li, L.; Wu, P.; Hwang, K.; Lu, Y. *J. Am. Chem. Soc.* **2013**, *135*, 2411. (h) Zhou, J.; Liu, Z.; Li, F. *Chem. Soc. Rev.* **2012**, *41*, 1323. (i) Liu, Y.; Zhou, S.; Tu, D.; Chen, Z.; Huang, M.; Zhu, H.; Ma, E.; Chen, X. *J. Am. Chem. Soc.* **2012**, *134*, 15083.

(4) (a) Zhang, F.; Haushalter, R. C.; Haushalter, R. W.; Shi, Y.; Zhang, Y.; Ding, K.; Zhao, D.; Stucky, G. D. *Small* **2011**, *7*, 1972. (b) Podhorodecki, A.; Banski, M.; Noculak, A.; Sojka, B.; Pawlik, G.; Misiewicz, J. *Nanoscale* **2013**, *5*, 429. (c) Wang, F.; Deng, R.; Wang, J.; Wang, Q.; Han, Y.; Zhu, H.; Chen, X.; Liu, X. *Nat. Mater.* **2011**, *10*, 968. (d) Hu, W.; Lu, X.; Jiang, R.; Fan, Q.; Zhao, H.; Deng, W.; Zhang, L.; Huang, L.; Huang, W. *Chem. Commun.* **2013**, *49*, 9012. (e) Teng, X.; Zhu, Y.; Wei, W.; Wang, S.; Huang, J.; Naccache, R.; Hu, W.; Tok, A. I. Y.; Han, Y.; Zhang, Q.; Fan, Q.; Huang, W.; Capobianco, J. A.; Huang, L. *J. Am. Chem. Soc.* **2012**, *134*, 8340. (f) Saboktakin, M.; Ye, X.; Chettiar, U. K.; Engheta, N.; Murray, C. B.; Kagan, C. R. *ACS Nano* **2013**, *7*, 7186. (g) Chan, E. M.; Han, G.; Goldberg, J. D.; Gargas, D. J.; Ostrowski, A. D.; Schuck, P. J.; Cohen, B. E.; Milliron, D. J. *Nano Lett.* **2012**, *12*, 3839. (h) Schäfer, H.; Ptacek, P.; Eickmeier, H.; Haase, M. *Adv. Funct. Mater.* **2009**, *19*, 3091. (i) Ye, X.; Collins, J. E.; Kang, Y.; Chen, J.; Chen, D. T. N.; Yodh, A. G.; Murray, C. B. *Proc. Natl. Acad. Sci. U.S.A.* **2010**, *107*, 22430. (j) Liu, Y.; Tu, D.; Zhu, H.; Chen, X. *Chem. Soc. Rev.* **2013**, *42*, 6924.

(5) (a) Dai, Y.; Xiao, H.; Liu, J.; Yuan, Q.; Ma, P. a.; Yang, D.; Li, C.; Cheng, Z.; Hou, Z.; Yang, P.; Lin, J. *J. Am. Chem. Soc.* **2013**, *135*, 18920. (b) Liu, Q.; Sun, Y.; Yang, T.; Feng, W.; Li, C.; Li, F. *J. Am. Chem. Soc.* **2011**, *133*, 17122. (c) Anderson, R. B.; Smith, S.; May, P. S.; Berry, M. T. *J. Phys. Chem. Lett.* **2014**, *5*, 36.

(6) (a) Wang, F.; Han, Y.; Lim, C. S.; Lu, Y.; Wang, J.; Xu, J.; Chen, H.; Zhang, C.; Hong, M.; Liu, X. *Nature* **2010**, *463*, 1061. (b) Wang, L.; Li, Y. *Nano Lett.* **2006**, *6*, 1645. (c) Zhang, F.; Wan, Y.; Yu, T.; Zhang, F.; Shi, Y.; Xie, S.; Li, Y.; Xu, L.; Tu, B.; Zhao, D. *Angew. Chem., Int. Ed.* **2007**, *46*, 7976. (d) Zhang, C.; Lee, J. Y. *ACS Nano* **2013**, *7*, 4393. (e) Na, H.; Woo, K.; Lim, K.; Jang, H. S. *Nanoscale* **2013**, *5*, 4242. (f) Xiao, Q.; Zheng, X.; Bu, W.; Ge, W.; Zhang, S.; Chen, F.; Xing, H.; Ren, Q.; Fan, W.; Zhao, K.; Hua, Y.; Shi, J. *J. Am. Chem. Soc.* **2013**, *135*, 13041. (g) Zhou, J.; Chen, G.; Wu, E.; Bi, G.; Wu, B.; Teng, Y.; Zhou, S.; Qiu, J. *Nano Lett.* **2013**, *13*, 2241. (h) Stanton, I.; Ayres, J. A.; Therien, M. J. *Dalton Trans.* **2012**, *41*, 11576.

(7) (a) Auzel, F. *Chem. Rev.* **2004**, *104*, 139. (b) Beurer, E.; Grimm, J.; Gerner, P.; Güdel, H. U. *J. Am. Chem. Soc.* **2006**, *128*, 3110. (c) Eliseeva, S. V.; Bünzli, J.-C. G. *Chem. Soc. Rev.* **2010**, *39*, 189. (d) Wang, F.; Liu, X. *Chem. Soc. Rev.* **2009**, *38*, 976.

(8) (a) Caillat, L.; Hajj, B.; Shynkar, V.; Michely, L.; Chauvat, D.; Zyss, J.; Pellé, F. *Appl. Phys. Lett.* **2013**, *102*, 143114. (b) Cui, J.-M.; Sun, F.-W.; Chen, X.-D.; Gong, Z.-J.; Guo, G.-C. *Phys. Rev. Lett.* **2013**, *110*, 153901.

(9) Wang, X.; Zhuang, J.; Peng, Q.; Li, Y. *Nature* **2005**, *437*, 121.

(10) (a) Chen, D.; Yu, Y.; Huang, F.; Yang, A.; Wang, Y. *J. Mater. Chem.* **2011**, *21*, 6186. (b) Zeng, S.; Ren, G.; Xu, C.; Yang, Q. *CrystEngComm* **2011**, *13*, 4276.

(11) (a) Johnson, N. J.; Korinek, A.; Dong, C.; van Veggel, F. C. *J. Am. Chem. Soc.* **2012**, *134*, 11068. (b) Li, C.; Yang, J.; Quan, Z.; Yang, P.; Kong, D.; Lin, J. *Chem. Mater.* **2007**, *19*, 4933.

(12) (a) Su, Q.; Han, S.; Xie, X.; Zhu, H.; Chen, H.; Chen, C.-K.; Liu, R.-S.; Chen, X.; Wang, F.; Liu, X. *J. Am. Chem. Soc.* **2012**, *134*, 20849. (b) Wang, J.; Deng, R.; MacDonald, M. A.; Chen, B.; Yuan, J.; Wang, F.; Chi, D.; Hor, T. S. A.; Zhang, P.; Liu, G.; Han, Y.; Liu, X. *Nat. Mater.* **2014**, *13*, 157. (c) Xie, X.; Liu, X. *Nat. Mater.* **2012**, *11*, 842. (d) Xie, X.; Gao, N.; Deng, R.; Sun, Q.; Xu, Q.-H.; Liu, X. *J. Am. Chem. Soc.* **2013**, *135*, 12608.

(13) (a) Lu, Y.; Zhao, J.; Zhang, R.; Liu, Y.; Liu, D.; Goldys, E. M.; Yang, X.; Xi, P.; Sunna, A.; Lu, J.; Yu, Shi.; Robert, C. L.; Huo, Y.; Shen, J.; Piper, J. A.; Robinson, J. P.; Jin, D. *Nat. Photonics* **2013**, *8*, 32. (b) Deng, R.; Liu, X. *Nat. Photonics* **2014**, *8*, 10. (c) Zhao, J.; Jin, D.; Schartner, E. P.; Lu, Y.; Liu, Y.; Zvyagin, A. V.; Zhang, L.; Dawes, J. M.; Xi, P.; Piper, J. A.; Goldys, E. M.; Monro, T. M. *Nat. Nanotechnol.* **2013**, *8*, 729. (d) Zhang, Y.; Liu, X. *Nat. Nanotechnol.* **2013**, *8*, 702. (e) Liu, Y.; Ai, K.; Lu, L. *Nanoscale* **2011**, *3*, 4804. (f) Meruga, J. M.; Cross, W. M.; May, P. S.; Luu, Q.; Crawford, G. A.; Kellar, J. J. *Nanotechnology* **2012**, *23*, 395201. (g) Wang, J.; Wei, T.; Li, X.; Zhang, B.; Wang, J.; Huang, C.; Yuan, Q. *Angew. Chem., Int. Ed.* **2014**, *53*, 1616.

SUPPORTING INFORMATION

Multicolor Barcoding in a Single Upconversion Crystal

Yuhai Zhang, Lixin Zhang, Renren Deng, Jing Tian, Yun Zong, Dayong Jin, and Xiaogang Liu*

Department of Chemistry, National University of Singapore, 3 Science Drive 3, Singapore 117543, Singapore; Advanced Cytometry Laboratories, MQ Photonics Research Centre and MQ Biofocus Research Centre, Macquarie University, Sydney, NSW 2109, Australia; Laboratory of Advanced Materials, Fudan University, 220 Handan Road, Shanghai 200433, China; Institute of Materials Research and Engineering, 3 Research Link, Singapore 117602, Singapore; Center for Functional Materials, NUS (Suzhou) Research Institute, Suzhou, Jiangsu 215123, China

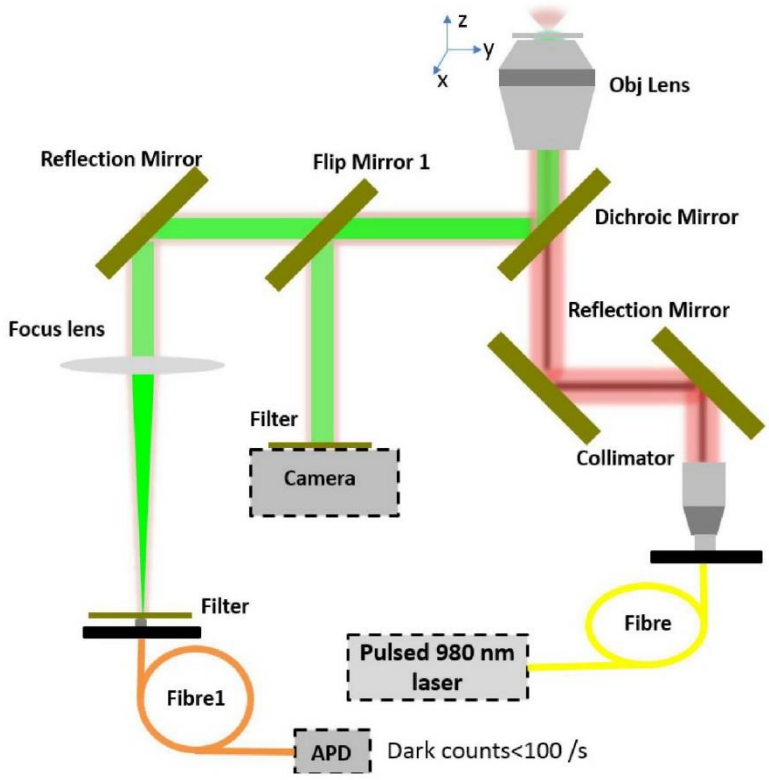

Figure S7. Simplified layout of a home-made upconversion characterization system. The system incorporates three basic functions: wide-field microscopy imaging, laser scanning confocal imaging, and lifetime measurement system. This wide-field imaging is used to pinpoint the locations of interest from a large area. The scanning confocal imaging is then used to zoom in and scan the detailed area of a single microrod, and therefore the sensitive lifetime measurement can be achieved to characterize the emitting features at high spatial resolution.

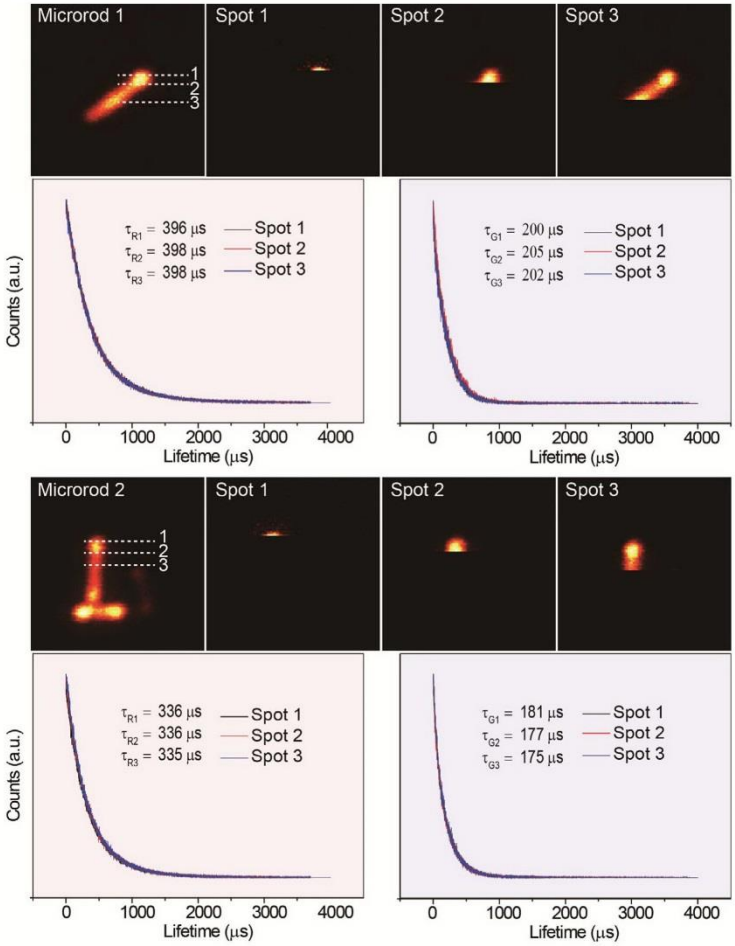

Figure S9. Additional lifetime measurements on two single tip-modified $NaYF_4$ microrods (Yb^{3+}/Tm^{3+}:20/0.2 mol% for parent rods, and Yb^{3+}/Er^{3+}:20/2 mol% for the tips). The emission lifetimes were measured at three different areas (marked with spot 1, 2, 3) of the microrods. Note that spot 1 contains only Er^{3+}. Spot 2 contains Er^{3+} and a small amount of Tm^{3+}. Spot 3 is co-doped with Er^{3+} and a large amount of Tm^{3+}. The lifetimes obtained from the energy levels ($^4S_{3/2}$ and $^4F_{9/2}$) of Er^{3+} are denoted as τ_G and τ_R, respectively. The overlap of the decay curves indicates that there is no energy transfer between different activators at the tip junction.

4.3 Additional information (unpublished results)

To characterise these novel multi-colour barcoded upconversion materials, the optical system with high resolution capability and high detection efficiency was required. Here, we provide the self-correlated imaging function in my home-built characterisation system for accurate and fast determination of targets. We firstly applied the wide field microscope to rapidly find the targets (micro-rods with two ends doped by activators Er^{3+} and middle section doped by activators Tm^{3+}), as shown in figure S4.1 (a) with three positions labelled by P1, P2 and P3, and then applied the laser scanning confocal microscope to provide detailed areas by zooming in these three specific positions, as shown in figure S3.1 (b-left) for P3, (c) for P1 and (d) for P2, with imaging resolution of 408 nm shown in figure b (right).

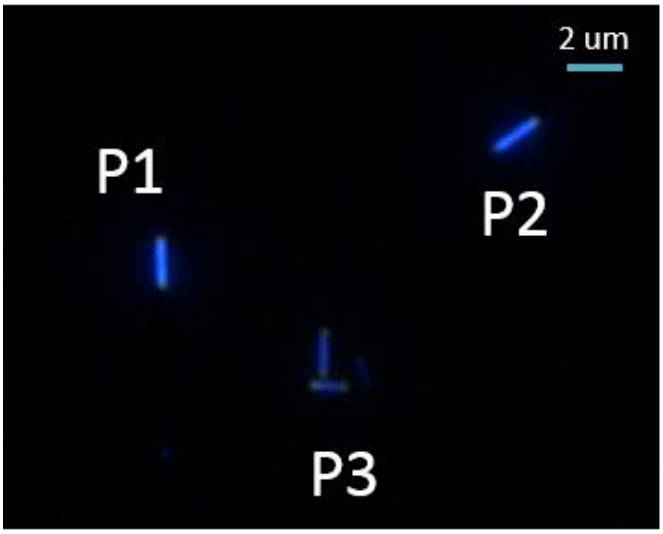

(a)Wide field imaging for micro-rods with positions labelled by P1, P2 and P3

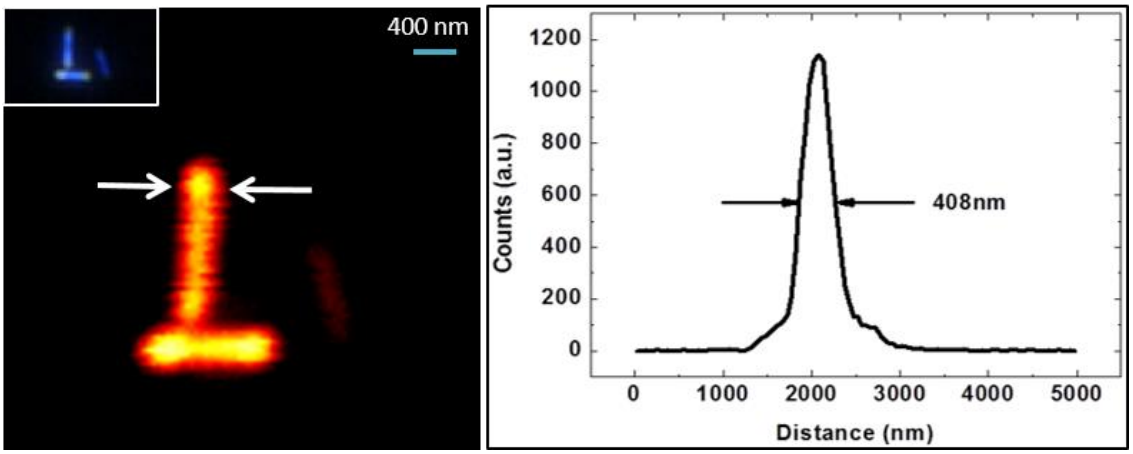

(b)Confocal imaging for position P3 (left) and the imaging resolution of 408 nm (right)

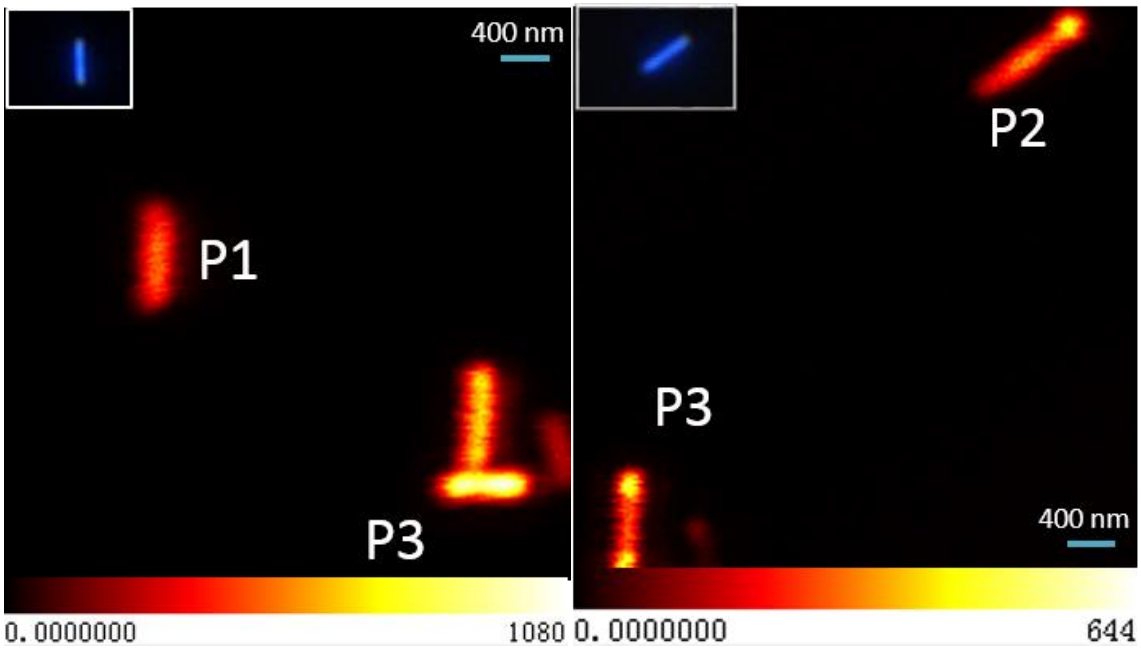

(c)Confocal imaging for P1 *(d) confocal imaging for P2*

Figure S4.1 wide field imaging micro-rods and corresponding confocal imaging (colour in figure b-d means intensity)

To study the energy transfer between two neighbouring sections in a single rod doped with different activators (Er^{3+} and Tm^{3+}), we firstly distinguished the different doped sections using laser scanning confocal modality in preparation for the lifetime measurements at each doped section. Figure S 4.2 (a) shows the confocal imaging for one micro-rod with all the emissions (the red colour means intensity).

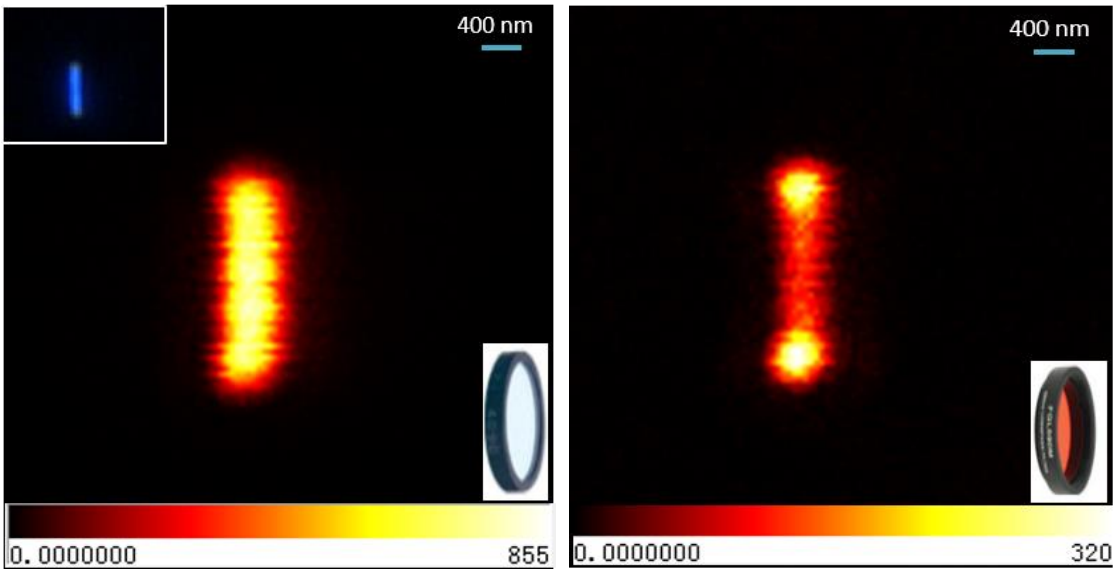

(a) Imaging for full emissions *(b) imaging for red emission*

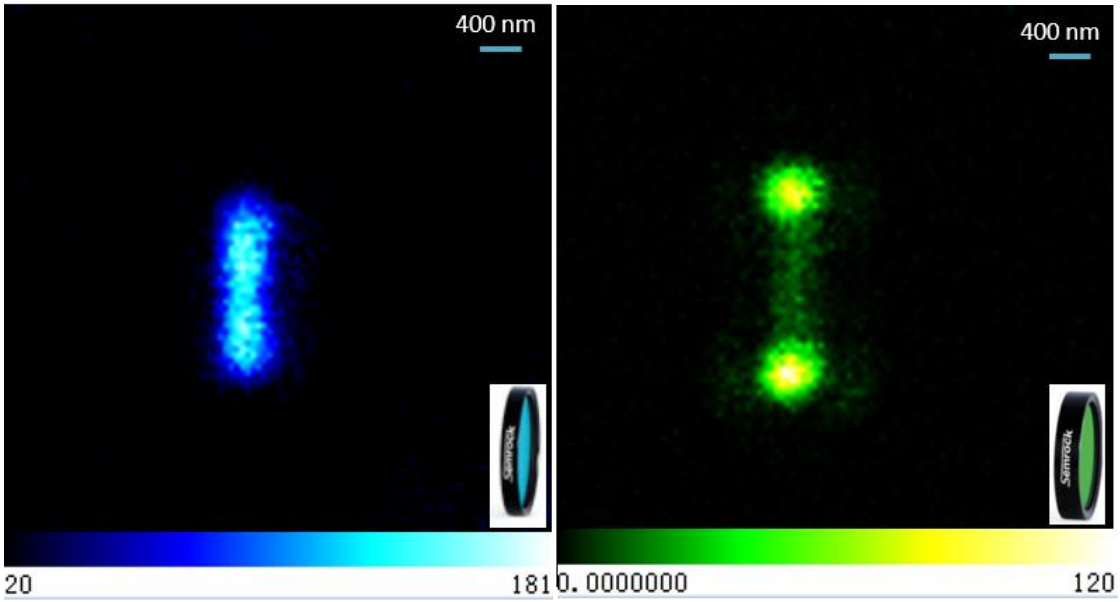

(c)Imaging for blue emissions *(d) imaging for green emission*

Figure S4.2 confocal imaging for determination of different doped sections. Here, blue emission (455nm and 475 nm) from doped Tm^{3+} ions; the green emission 545 nm and red emissin from Er3+ ions; both ions have red emission at 650 nm but with red emission from Tm^{3+} much weaker).

Due to the different emissions of these two doped activators (Tm^{3+} and Er^{3+}), the different doping sections can be recoginised by implementing a confocal imaging scan with different emission filters. Figure S4.2 (b) is the confocal image for red emission with two ends (Er^{3+} doped) stronger than the middle part (Tm^{3+} doped); figure S4.2 (c) shows the confocal image with blue emission from Tm^{3+} ions; and figure 4.2 (d) is the confocal image with green emission from doped Er^{3+}ions. Clearly, the doped sections could be observed and determined, and then the lifetime measurement at these two doped sections and their junction was closely followed to determine whether there is energy transfer between these two doped activators.

4.4 Contributions to Paper 4

TABEL 4-2 Author contribution summary for paper 4

	J.Z.	D.J.	E.P.S.	Y.L.	Y.L.	A.V.Z.	Z.L.	J.M.D.	P.X.	J.A.P.	E.M.G.	T.M.M.
Project Design		●										●
Materials	●					●						
System Setup	●	●	●	●	●				●			●
Data Collection	●	●	●	●	●		●					
Analysis	●	●	●	●	●	●	●	●	●	●	●	●
Manuscript & Figures	●	●	●	●	●			●		●	●	●
Modelling	●	●									●	
Supplementary Information	●	●				●	●				●	

In this work, I built the upconversion wide-field microscope, and did the power-dependent imaging analysis leading to Figure S6 and single nanoparticle imaging shown as Figure S10. I contributed 5% of data collection and 5% data analysis, occupying 10% of the whole contribution.

4.5 Paper 4

Jiangbo Zhao, Dayong Jin, Erik P. Schartner, Yiqing Lu, Yujia Liu, Andrei V. Zvyagin, **Lixin Zhang,** Judith M. Dawes, Peng Xi, James A. Piper, Ewa M. Goldys and Tanya M. Monro. "Single-nanocrystal sensitivity achieved by enhanced upconversion luminescence", *Nature Nanotechnology*, DOI:10.1038/NNANO.2013.171.

nature nanotechnology

LETTERS

PUBLISHED ONLINE: 1 SEPTEMBER 2013 | DOI: 10.1038/NNANO.2013.171

Single-nanocrystal sensitivity achieved by enhanced upconversion luminescence

Jiangbo Zhao[1], Dayong Jin[1]*, Erik P. Schartner[2], Yiqing Lu[1], Yujia Liu[1,3], Andrei V. Zvyagin[1], Lixin Zhang[1], Judith M. Dawes[1], Peng Xi[3,4], James A. Piper[1], Ewa M. Goldys[1] and Tanya M. Monro[2]

Upconversion nanocrystals convert infrared radiation to visible luminescence, and are promising for applications in biodetection[1-3], bioimaging[4-7], solar cells[8-10] and three-dimensional display technologies[8,9,11]. Although the design of suitable nanocrystals has improved the performance of upconversion nanocrystals[10,12-14], their emission brightness is limited by the low doping concentration of activator ions needed to avoid the luminescence quenching that occurs at high concentrations[15,16]. Here, we demonstrate that high excitation irradiance can alleviate concentration quenching in upconversion luminescence when combined with higher activator concentration, which can be increased from 0.5 mol% to 8 mol% Tm^{3+} in $NaYF_4$. This leads to significantly enhanced luminescence signals, by up to a factor of 70. By using such bright nanocrystals, we demonstrate remote tracking of a single nanocrystal with a microstructured optical-fibre dip sensor. This represents a sensitivity improvement of three orders of magnitude over benchmark nanocrystals such as quantum dots[17].

Lanthanide-doped upconversion nanocrystals[8,9] are typically doped with ytterbium (Yb^{3+}) sensitizer ions, which absorb infrared radiation and non-radiatively transfer their excitation to activator ions such as erbium (Er^{3+}), thulium (Tm^{3+}) or holmium (Ho^{3+}). Although recent advances in synthesis have led to accurate control of upconversion nanocrystal morphology, crystal phase and emission colours[7,11,15,16,18–21], it has been difficult to achieve strong upconversion luminescence. Attempts to overcome this problem include coating nanocrystals with an inert/active shell to minimize surface quenching[12,14,22,23], or using noble metal nanostructures to enhance the energy transfer rate by surface plasmons[24,25]. However, these approaches do not address the intrinsic limitation of concentration quenching[15,16,18], where brightness decreases with increasing dopant density beyond the optimal concentration threshold. The optimal Tm^{3+} concentration in $NaYF_4$ host lattices is low, in the range of ~0.2–0.5 mol% at excitation irradiance below 100 W cm^{-2} (with ~20–40 mol% Yb^{3+})[16,26–29]. Such nanocrystals have small numbers of activators and therefore produce weak upconversion emission.

Here we present evidence that upconversion luminescence can be significantly enhanced by using much higher activator concentrations under relatively high-irradiance excitation. We have found that this previously unexplored regime achieves a new balance between the sensitizers, activators and excitation irradiance, and can overcome the widely reported concentration quenching in upconversion[15,16,18,26–29]. As a result, it has been possible to realize high bright upconversion luminescence in 8 mol% Tm^{3+}-doped $NaYF_4$ nanocrystals co-doped with 20 mol% Yb^{3+}. Their high brightness originates from a combination of high excitation intensity, increased activator concentration, and accelerated sensitizer–activator energy transfer rate arising from the decreased average minimum distance between adjacent Ln^{3+} ions. This significantly enhanced upconversion has enabled the remote detection of a single nanocrystal using a fibre dip sensor.

Hexagonal-phase $NaYF_4$ nanocrystals were synthesized with Tm^{3+} concentrations in the range ~0.2–8 mol% co-doped with 20 mol% Yb^{3+} (Supplementary Section S1 and Fig. S1). A single-mode continuous-wave 980 nm diode laser beam launched into a suspended-core microstructured optical fibre (Fig. 1) produced excitation irradiance values of up to 2.5×10^6 W cm^{-2}. The uniform ~40 nm nanocrystals dispersed in cyclohexane (39 pM) were drawn into the holes in the fibre for upconversion luminescence measurements (Supplementary Section S2). This brings the nanocrystals into the vicinity of sufficiently high intensity guided light, and also provides a platform suitable for efficiently collecting their emission. At 2.5×10^6 W cm^{-2} irradiance, we observed that the 8 mol% Tm^{3+} nanocrystals generate a previously unreported bright upconversion emission that is much stronger than in 0.5 mol% Tm^{3+} nanocrystals (the 802 nm emission is increased by a factor of 70, Fig. 1c). In contrast, at a low excitation of 10 W cm^{-2}, our results (Supplementary Fig. S2) show that the upconversion intensity as a function of Tm^{3+} concentration first increases and then decreases above 0.5 mol% Tm^{3+}, consistent with previous reports[16,26–29]. This observation indicates that efficient upconversion emission can be realized at a high activator doping, but only when sufficient irradiance is provided (~1×10^6 W cm^{-2}, achieved in laser scanning microscopy). Sufficient excitation irradiance can unlock otherwise dark activators, thereby enhancing the upconversion brightness (Supplementary Fig S3). This effect is independent of nanocrystal size (from tens to several hundreds of nanometres), surface conditions and synthesis conditions (Supplementary Sections S3, S4, Figs S3–S7).

To understand the relationship between the upconversion signal, activator concentration and excitation irradiance, we collected a matrix of power-dependent (1.6×10^4 W cm^{-2} to 2.5×10^6 W cm^{-2}) luminescence spectra for same sized ~40 nm upconversion nanocrystals at varying Tm^{3+} concentrations. The spectra, which are similar to those in Fig. 2b were decomposed into individual Gaussian peaks (Fig. 2c). These were divided into three groups according to the initial Tm^{3+} levels: the $^3H_4$ group, comprising a single peak at 802 nm, the $^1G_4$ group, with 650 nm and 480 nm peaks, and the $^1D_2$ group, with peaks at 455 nm, 514 nm, 744 nm and 782 nm (see Fig. 2a for a simplified diagram of transitions in the Yb^{3+}–Tm^{3+} system). The integrated intensity ratios of the $^1D_2$

[1]Advanced Cytometry Laboratories, MQ Photonics Research Centre and MQ BioFocus Research Centre, Macquarie University, Sydney, New South Wales 2109, Australia, [2]Institute of Photonics and Advanced Sensing and School of Chemistry and Physics, University of Adelaide, Adelaide, South Australia 5005, Australia, [3]School of Biomedical Engineering, Shanghai Jiao Tong University, Shanghai, China, [4]Department of Biomedical Engineering, College of Engineering, Peking University, Beijing 100871, China. *e-mail: dayong.jin@mq.edu.au

LETTERS NATURE NANOTECHNOLOGY DOI: 10.1038/NNANO.2013.171

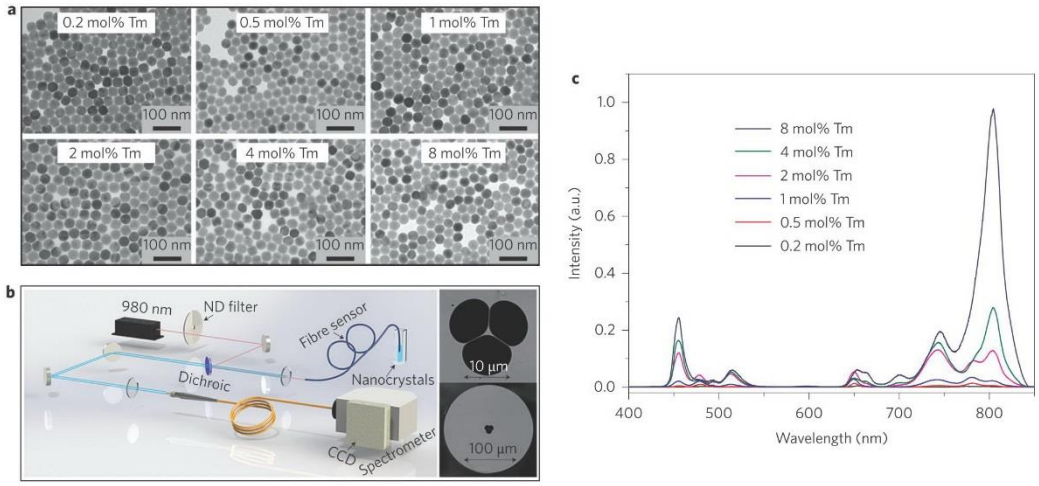

Figure 1 | Highly Tm^{3+}-doped $NaYF_4$ nanocrystals exhibit enhanced upconversion in a suspended-core fibre. a, Transmission electron microscopy images of monodispersed $NaYF_4$:Yb/Tm nanocrystals at different doping levels. All nanoparticles have a similar average size with a narrow size distribution. **b**, Schematic of the experimental configuration for capturing upconversion luminescence of $NaYF_4$:Yb/Tm nanocrystals using a suspended-core microstructured optical-fibre dip sensor. The continuous-wave 980-nm diode laser is targeted at the suspended core. Light propagates along the length of the fibre and interacts with the upconversion nanocrystals located within the surrounding holes. The excited upconversion luminescence is coupled into the fibre core and the backward-propagating light is captured by a spectrometer. Inset: scanning electron microscope images showing a cross-section of the F2 suspended-core microstructured optical fibre at different magnifications. The fibre outer diameter is 160 μm with a 17 μm hole and 1.43 μm core. **c**, Upconversion spectra of a series of $NaYF_4$:Yb/Tm nanocrystals with varied Tm^{3+} concentrations under an excitation irradiance of 2.5×10^6 W cm^{-2}, showing a steady increase in upconversion luminescence with increasing Tm^{3+} content from 0.2 mol% to 8 mol%.

to $^3H_4$ and $^1G_4$ to $^3H_4$ groups (Fig. 2d) show a decreasing contribution of emissions from the $^1G_4$ and $^1D_2$ groups with increasing Tm^{3+} content compared to $^3H_4$ emission. This suggests that the respective population ratios of $^1D_2$ and $^1G_4$ levels to $^3H_4$ decrease in these conditions, to a point where the 8 mol% Tm^{3+} nanocrystals mainly produce the $^3H_4$ (802 nm) emission within our excitation range. We also note that the emission ratios of $^1G_4$:$^3H_4$ and $^1D_2$:$^3H_4$ increase with excitation irradiance in all samples. This suggests that, with increasing excitation irradiance, the population of $^1D_2$ and $^1G_4$ levels increases faster than the population of $^3H_4$. These trends also suggest that a low activator concentration causes an energy transfer bottleneck: at increasing excitation powers the $^3H_4$ level eventually reaches its full capacity to release the 802 nm emission energy (Fig. 2e), and, in order to release any additional energy transferred from Yb^{3+}, the higher energy level emissions in Tm^{3+} ($^1G_4$ and $^1D_2$) become progressively activated. At higher Tm^{3+} concentrations the decay rate of the $^3H_4$ population increases, and this shifts the bottleneck to proportionately higher excitation energies.

Moreover, we have confirmed that the absolute conversion efficiency strongly increases with increasing irradiance, which is attributed to increased excited-state populations of sensitizer and activator ions. The absolute conversion efficiency is defined as the ratio of the emitted to absorbed power (Supplementary Section S5 and Fig. S8)[14]. The absolute conversion efficiency in the low concentration (0.5 mol%) sample reaches a plateau at 3×10^2 W cm^{-2}, whereas in the high concentration (4 mol%) sample it continues to increase within this range. We also measured the power-dependent relative upconversion efficiency for the different nanocrystal samples (Fig. 3a). Increasing the excitation irradiance from 1.6×10^4 W cm^{-2} to 2.5×10^6 W cm^{-2} enhances the overall upconversion luminescence intensity by factors of 5.6, 71 and 1,105 for 0.5 mol%, 4 mol% and 8 mol% Tm^{3+}, respectively. Additionally, this figure indicates that the partitioning of excitation energy flux between the 'effective' 980 nm quanta actually producing upconversion and those 980 nm quanta that are lost on other processes (such as various non-radiative recombination and unobserved emissions) changes dramatically with excitation irradiance and concentration of Tm^{3+} ions. Importantly, at high excitation and high Tm^{3+} doping level, the fraction of excitation energy producing upconversion emission is increased. This shows that upconversion is more efficient at high excitation and for high Tm^{3+} doping. The effect is observed to be especially strong for the 8 mol% Tm^{3+} samples, as is evident from the extremely steep slope above 2×10^6 W cm^{-2} excitation irradiance. Figure 3b shows the same integrated upconversion intensity per Tm^{3+} ion for different Tm^{3+} doping levels. Although the observation of significant enhancement in upconversion intensity from 0.2 mol% to 1 mol% may be due to the fact that upconversion from five photon excitations, previously reported in 0.2 mol% Tm^{3+} (refs 30–32), was not collected in this work, the increase from 1 mol% to 2 mol% clearly shows that the energy transfer efficiency from Yb^{3+} sensitizers to Tm^{3+} activators has been significantly enhanced. This work has therefore shown that the decreased excited sensitizer-to-excited activator distance has indeed increased the energy transfer efficiency, which makes a significant contribution to enhancing the overall conversion efficiency.

To verify that increasing the excitation irradiance enhances the upconversion luminescence and changes the optimal activator/sensitizer concentration ratio, we formulated the rate equations in a generalized upconverting Yb^{3+}–Ln^{3+} system (Supplementary Section S6 and Fig. S9a). In our model the lanthanide ion (activator) is represented by three states—Ln_0, Ln_1 and Ln_2—with equal energy spacing $E_2 - E_1 = E_1 - E_0$, and the upconversion emission takes place from the excited Ln_2 state to the ground Ln_0 state. The lanthanide ions are excited by energy transfer from the excited states of Yb^{3+} (Yb_1) populated by transitions from the ground-state Yb_0, which have the same energy spacing of $E_1 - E_0$. Using our rate equations,

NATURE NANOTECHNOLOGY DOI: 10.1038/NNANO.2013.171 LETTERS

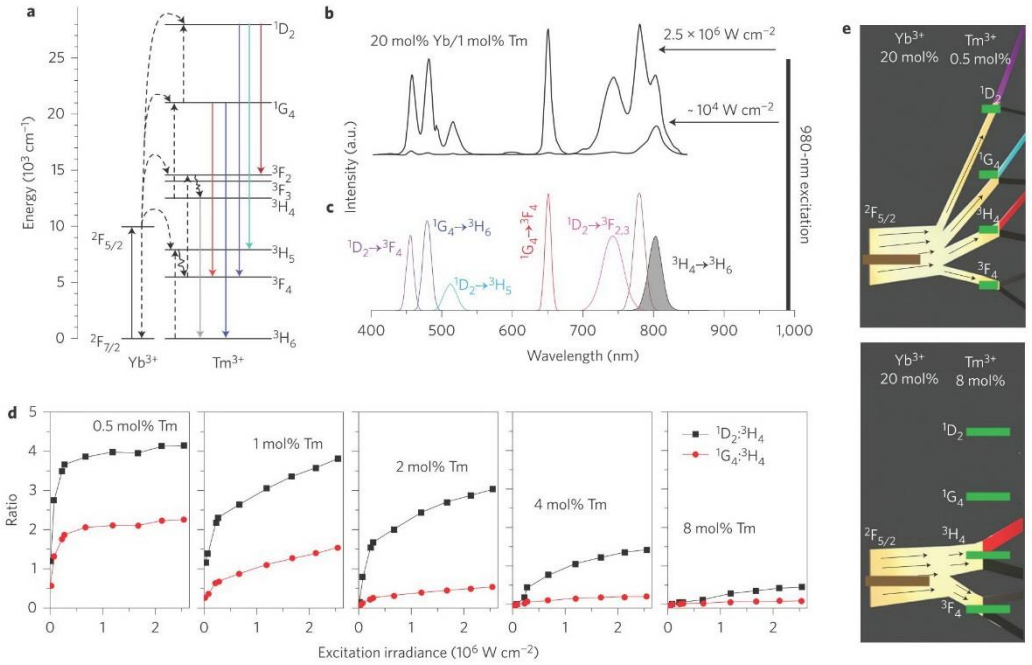

Figure 2 | Analysis of power-dependent multiphoton upconversion. a, Simplified energy-level scheme of $NaYF_4$:Yb/Tm nanocrystals indicating major upconversion processes. Dashed lines indicate non-radiative energy transfer, and curved arrows indicate multiphonon relaxation. **b**, Typical evolution of spectra for 1 mol% Tm^{3+} as a function of excitation, showing substantial growth of emissions from the $^1G_4$ and $^1D_2$ levels with increasing excitation from 1×10^4 W cm^{-2} to 2.5×10^6 W cm^{-2}. **c**, Decomposition of the spectra into individual Gaussian peaks. Integrated intensities are given by I_λ where λ is the peak wavelength. Different transitions are indicated by the colours shown in the energy-level scheme in **a**. For example, the shaded area represents the $^3H_4 \rightarrow {}^3H_6$ transitions. **d**, Intensity ratios of the $^1D_2$ to $^3H_4$ classes $(I_{455} + I_{514} + I_{744} + I_{782})/I_{802}$ and $^1G_4$ to $^3H_4$ classes $(I_{480} + I_{660})/I_{802}$ as a function of excitation irradiance. **e**, Diagram illustrating energy transfer between the ensemble of Yb^{3+} and Tm^{3+} ions and subsequent radiative and non-radiative pathways. Top (bottom) panels: low (high) Tm^{3+}/Yb^{3+} ratio. In the case of a low Tm^{3+}/Yb^{3+} ratio, the limited number of Tm^{3+} ions creates an energy transfer bottleneck, due to the limited capacity of Tm^{3+} to release energy from the $^3F_4$ and $^3H_4$ states. Thus, at increasing excitation, alternative energy loss channels (radiative and non-radiative) involving higher states $^1G_4$ and $^1D_2$ progressively switch on. Brown, excitation light; green, simplified energy levels; red, blue and purple, radiative energy flux; grey, radiative flux not observed in this work; black, non-radiative energy loss.

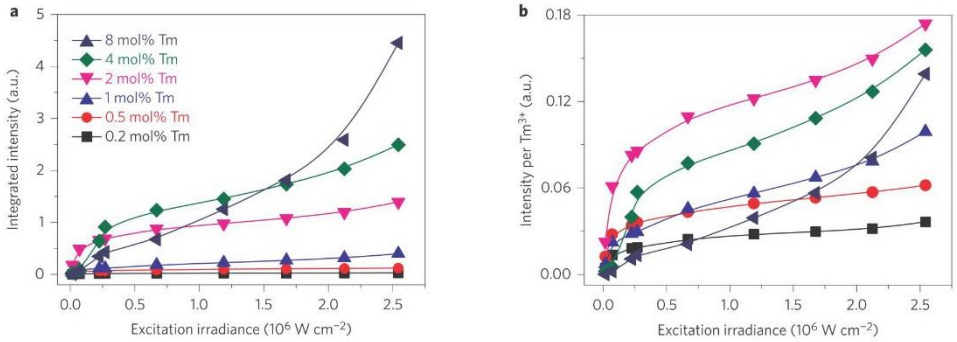

Figure 3 | Analysis of power-dependent upconversion efficiency. a, Integrated upconversion luminescence intensity (~400–850 nm) as a function of excitation irradiance for a series of Tm^{3+}-doped nanocrystals. All samples have the same volume and number of nanocrystals. **b**, As in **a**, but divided by the concentration of Tm^{3+} ions. Under an excitation irradiance of 2.5×10^6 W cm^{-2}, 2 mol% Tm^{3+} has the highest relative upconversion efficiency, whereas the strongest upconversion signal is observed in 8 mol% Tm^{3+} due to the larger number of activators available with sufficient excitation.

the population in the Ln_2 state is expressed in terms of the density of lanthanide ions in the ground state, the excited Yb^{3+} population, excitation irradiance and various intrinsic macroscopic rate constants, such as the energy transfer and upconversion rates. The experimental and simulated upconversion luminescence intensities show concentration quenching at low irradiance, but increase at

LETTERS NATURE NANOTECHNOLOGY DOI: 10.1038/NNANO.2013.171

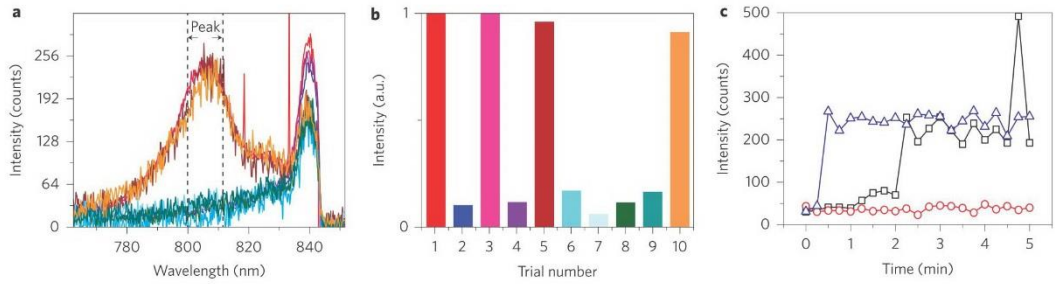

Figure 4 | Detecting a single nanocrystal in a suspended-core microstructured fibre dip sensor. a, Results of 10 trials of loading 3.9 fM nanocrystal solution into the fibre dip sensor. Four positive trials, shown in red, magenta, dark red and orange, show comparable ~800–810 nm emission peaks, and six trials result in consistent background noise baselines (presented in the remaining colours). The baseline level is due to scattering of 980-nm excitation. **b**, Normalized nanocrystal emission integrated from ~800 to 810 nm. The four positive trials shown in red, magenta, dark red and orange produce intensities of ~250 with a low coefficient of variation (CV) of 4.7%, and high signal-to-noise ratio of >8. **c**, Time-dependent dynamics of three independent trials. Red: trial with no nanocrystals observed (only background is observed). Blue: one nanocrystal appears shortly after the start of the trial. Black: single nanocrystal appears in the fibre after 2 min, followed by a second at ~5 min; one of the nanocrystals then exits the observation volume.

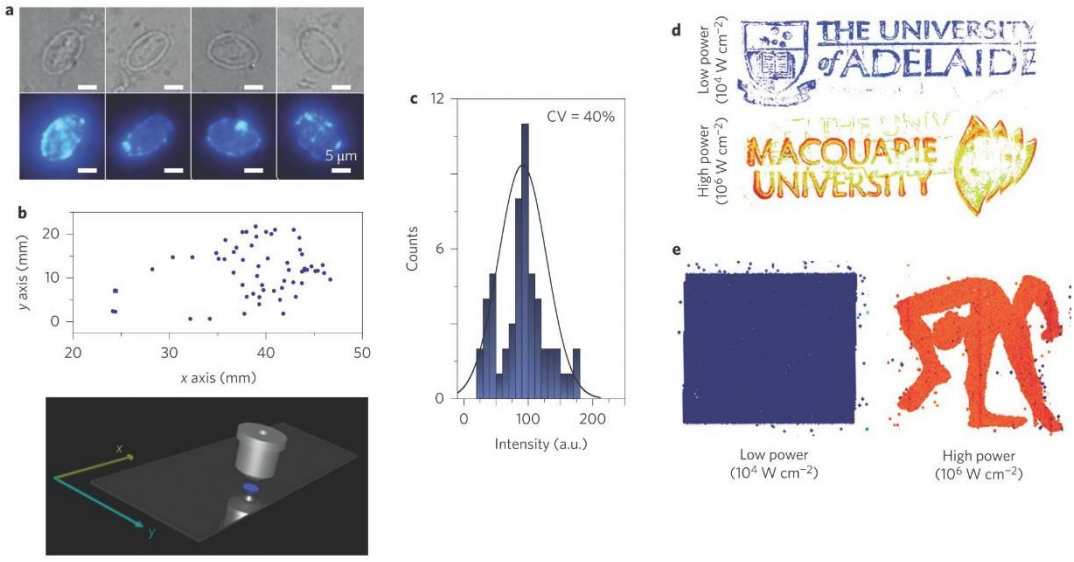

Figure 5 | Proof-of-principle experiments demonstrating a broad spectrum of applications. a, Images of *Giardia lamblia* cells labelled with antibody-conjugated 4 mol% Tm^{3+} upconversion nanocrystals under transmission (top) and luminescence (bottom) modes. The 980-nm wide-field excitation and upconversion detection yield negligible autofluorescence background, so absolute signal intensities of each single microorganism (see histogram in **c**) provide quantification of the level of surface antigens. **b**, Individual cells localized on a glass slide by a scanning cytometry system (top), and its schematic (bottom). Targeted cells are symbolized by blue dots. **c**, Histogram showing the quantification results of the population of nanocrystal-labelled *Giarida lamblia* (CV, coefficient of variation). **d**, Demonstrations of security inks using the power-dependent optimal Tm^{3+} concentration. Low-concentration (0.2 mol% Tm^{3+}) nanocrystals were used to stain the masking pattern (University of Adelaide logo), which is visible under both low-power illumination (top) and high-power illumination (bottom). High-concentration (4 mol% Tm^{3+}) nanocrystals were used to stain the hidden pattern (Macquarie University logo), which is over 10 times brighter than the masking pattern. At this dynamic range the masking pattern is almost unnoticeable. **e**, Nanocrystal solution 'security inks' were used in an inkjet printer with 0.5 mol% Tm^{3+} nanocrystals as a rectangular mask to confound the signal image from 8 mol% Tm^{3+} nanocrystals. At laser scanning confocal setting (>1 × 10^6 W cm^{-2}), the hidden trademark image of the 8 mol% Tm^{3+} nanocrystals becomes visible and dominant.

high irradiance, in agreement with our observations (Supplementary Fig. S9b–f). Moreover, the simulations show increasing relative upconversion efficiency with increasing excitation irradiance (Supplementary Fig. S9g), which is in agreement with Fig. 3a. To the best of our knowledge, this is the first analytical approach to describe the upconversion quenching process at increasing activator concentrations and excitation powers.

We have demonstrated that these bright nanocrystals can significantly extend the detection limit in a fibre-based dip sensor, a novel nanoscale sensing platform for clinical point-of-care, chemical and

NATURE NANOTECHNOLOGY DOI: 10.1038/NNANO.2013.171 LETTERS

biological applications[17]. The detection limit for fluorescent quantum dots in such sensors was earlier reported to be ~10 pM due to competing autofluorescence background from the fibre itself. In this work the fibre autofluorescence problem is avoided by using 980 nm excitation and 802 nm emission of Tm^{3+}, wavelengths that are well separated from the glass background fluorescence (Supplementary Fig. S11). To investigate the achievable detection limit, we measured our brightest 8 mol% Tm^{3+} nanocrystals at 3.9 fM dilution in ten identical fibre dip sensors (Supplementary Section S8). The respective 802 nm peaks (Fig. 4a) show a consistent intensity of 250 ± 30 counts in four experiments, whereas six other experiments show a consistent background level of ~30 counts (Fig. 4b). We attribute these strongly quantized values of the peak intensity (~220 net counts) to the observation of single nanocrystals in these four trials. To confirm this hypothesis we calculated the average number of particles expected to be located within the detection volume in a microstructured fibre, and found this to be 0.55, consistent with our observations of a single nanocrystal in 40% of trials. The Poissonian probability of observing two or more nanocrystals in a single trial for our average of 0.55 particles is 11%. To validate our assignment further, we set up an experiment to continuously monitor the 802 nm upconversion intensity during sample intake as the holes of the fibre fill with the nanocrystal suspension by capillary action (Fig. 4c). One of these trials (red) showed the background signal only, indicating that in this trial no nanocrystals entered the detection volume. The second (blue) showed a single nanocrystal appearing in the detection volume halfway through the experiment. The third (black) showed one nanocrystal entering the detection region, followed by a second one after 6 min; one nanocrystal is then observed to exit while the other continues to be observed. The signal of both combined nanocrystals is 470 ± 30 (440 net counts), twice the single nanocrystal net count of 220. These experiments show that high brightness of upconversion emission achieved at sufficient irradiance excitation enables, for the first time, the detection of a single high Tm^{3+}-doped nanocrystal within the fibre platform. Furthermore, these single nanocrystals are bright enough to be visible to the naked eye and could be recorded by a low-cost digital camera in a wide-field microscopy system (Fig. S10 in Supplementary Section S7).

This exceptional nanocrystal brightness provides compelling advantages to a wide range of fields including immunofluorescence imaging (Fig. 5a), rare event cell detection and quantification (Fig. 5b,c), document security (Fig. 5d) and security printing (Fig. 5e). We demonstrated that the new ultrabright upconversion nanocrystals provide high-contrast biolabels. To this end, *Giardia lamblia* cells were labelled by nanocrystals conjugated to suitable monoclonal antibodies (G203). Figure 5a shows the labelled Giardia cells imaged by a scanning system at only 0.1 s exposure time by a standard charge-coupled device (CCD) camera. The absence of autofluorescence background at 980 nm excitation enabled the quantification of the absolute signal intensities of each single microorganism, as well as quantification of the level of surface antigens (Fig. 5c)[33]. Single labelled cells on a glass slide have been detected within 3 min without background interference (Fig. 5b). This shows that these bioprobes are capable of rare event detection. Moreover, excitation-dependent upconversion has also enabled a new approach to 'security inks' (Fig. 5d,e), because the highly doped (>4 mol%) Tm^{3+} nanocrystals remain dark unless high infrared excitation irradiance is used, in contrast to low doped nanocrystals (Fig. 5d). Additionally, the nanocrystal suspensions can be dispersed in traditional inkjet printer inks to print highly secure trademarks/images on papers/plastics (Fig. 5e).

In conclusion, we have demonstrated a novel approach to significantly enhance the upconversion luminescence of nanocrystals, by increasing the activator concentration in combination with elevated irradiance excitation ($\sim 1 \times 10^6$ W cm^{-2}). The microstructured fibre dip sensor used here easily achieves such excitation intensities, making it possible to detect single nanocrystals while probing subcellular fluid volumes. These results show that the nanocrystals can be detected at one end of the fibre as they enter the fibre from the other end, enabling measurements to be made from a significant distance, and leading the way to *in vivo* measurements. Highly Ln^{3+}-doped nanocrystals at sufficient irradiance excitation have strong potential for use as photostable, background-free and extremely bright labelling probes for bioimaging. Furthermore, this work presents a new approach for understanding and predicting the behaviour of lanthanide-based upconversion systems, and provides new directions both for nanoscale sensing and the materials science of Ln^{3+}-doped nanomaterials.

Received 13 May 2013; accepted 26 July 2013;
published online 1 September 2013

References

1. Zhang, C., Yuan, Y., Zhang, S., Wang, Y. & Liu, Z. Biosensing platform based on fluorescence resonance energy transfer from upconverting nanocrystals to graphene oxide. *Angew. Chem. Int. Ed.* **50,** 6851–6854 (2011).
2. Wu, S. W. *et al.* Non-blinking and photostable upconverted luminescence from single lanthanide-doped nanocrystals. *Proc. Natl Acad. Sci. USA* **106,** 10917–10921 (2009).
3. Stepuk, A. *et al.* Use of NIR light and upconversion phosphors in light-curable polymers. *Dental Mater.* **28,** 304–311 (2012).
4. Nyk, M., Kumar, R., Ohulchanskyy, T. Y., Bergey, E. J. & Prasad, P. N. High contrast *in vitro* and *in vivo* photoluminescence bioimaging using near infrared to near infrared up-conversion in Tm^{3+} and Yb^{3+} doped fluoride nanophosphors. *Nano Lett.* **8,** 3834–3838 (2008).
5. Wang, M. *et al.* Immunolabeling and NIR-excited fluorescent imaging of HeLa cells by using $NaYF_4$:Yb,Er upconversion nanoparticles. *ACS Nano* **3,** 1580–1586 (2009).
6. Yang, Y. M. *et al. In vitro* and *in vivo* uncaging and bioluminescence imaging by using photocaged upconversion nanoparticles. *Angew. Chem. Int. Ed.* **51,** 3125–3129 (2012).
7. Tian, G. *et al.* Mn^{2+} dopant-controlled synthesis of $NaYF_4$:Yb/Er upconversion nanoparticles for *in vivo* imaging and drug delivery. *Adv. Mater.* **24,** 1226–1231 (2012).
8. Haase, M. & Schäfer, H. Upconverting nanoparticles. *Angew. Chem. Int. Ed.* **50,** 5808–5829 (2011).
9. Auzel, F. Upconversion and anti-Stokes processes with *f* and *d* ions in solids. *Chem. Rev.* **104,** 139–173 (2004).
10. Zou, W. Q., Visser, C., Maduro, J. A., Pshenichnikov, M. S. & Hummelen, J. C. Broadband dye-sensitized upconversion of near-infrared light. *Nature Photon.* **6,** 560–564 (2012).
11. Wang, F. *et al.* Simultaneous phase and size control of upconversion nanocrystals through lanthanide doping. *Nature* **463,** 1061–1065 (2010).
12. Vetrone, F., Naccache, R., Mahalingam, V., Morgan, C. G. & Capobianco, J. A. The active-core/active-shell approach: a strategy to enhance the upconversion luminescence in lanthanide-doped nanoparticles. *Adv. Funct. Mater.* **19,** 2924–2929 (2009).
13. Liu, X. *et al.* Breakthrough in concentration quenching threshold of upconversion luminescence via spatial separation of the emitter doping area for bio-applications. *Chem. Commun.* **47,** 11957–11959 (2011).
14. Boyer, J. C. & van Veggel, F. C. Absolute quantum yield measurements of colloidal $NaYF_4$: Er^{3+}, Yb^{3+} upconverting nanoparticles. *Nanoscale* **2,** 1417–1419 (2010).
15. Wang, F. & Liu, X. Upconversion multicolor fine-tuning: visible to near-infrared emission from lanthanide-doped $NaYF_4$ nanoparticles. *J. Am. Chem. Soc.* **130,** 5642–5643 (2008).
16. Zhang, H., Li, Y., Lin, Y., Huang, Y. & Duan, X. Composition tuning the upconversion emission in $NaYF_4$:Yb/Tm hexaplate nanocrystals. *Nanoscale* **3,** 963–966 (2011).
17. Schartner, E. P., Ebendorff-Heidepriem, H., Warren-Smith, S. C., White, R. T. & Monro, T. M. Driving down the detection limit in microstructured fiber-based chemical dip sensors. *Sensors* **11,** 2961–2971 (2011).
18. Wang, F. *et al.* Tuning upconversion through energy migration in core–shell nanoparticles. *Nature Mater.* **10,** 968–973 (2011).
19. Ye, X. C. *et al.* Morphologically controlled synthesis of colloidal upconversion nanophosphors and their shape-directed self-assembly. *Proc. Natl Acad. Sci. USA* **107,** 22430–22435 (2010).
20. Yan, C., Dadvand, A., Rosei, F. & Perepichka, D. F. Near-IR photoresponse in new up-converting CdSe/$NaYF_4$:Yb,Er nanoheterostructures. *J. Am. Chem. Soc.* **132,** 8868–8869 (2010).

21. Gorris, H. H., Ali, R., Saleh, S. M. & Wolfbeis, O. S. Tuning the dual emission of photon-upconverting nanoparticles for ratiometric multiplexed encoding. *Adv. Mater.* **23,** 1652–1655 (2011).
22. Wang, F., Wang, J. A. & Liu, X. G. Direct evidence of a surface quenching effect on size-dependent luminescence of upconversion nanoparticles. *Angew. Chem. Int. Ed.* **49,** 7456–7460 (2010).
23. Mai, H. X., Zhang, Y. W., Sun, L. D. & Yan, C. H. Highly efficient multicolor up-conversion emissions and their mechanisms of monodisperse $NaYF_4$:Yb,Er core and core/shell-structured nanocrystals. *J. Phys. Chem. C* **111,** 13721–13729 (2007).
24. Priyam, A., Idris, N. M. & Zhang, Y. Gold nanoshell coated $NaYF_4$ nanoparticles for simultaneously enhanced upconversion fluorescence and darkfield imaging. *J. Mater. Chem.* **22,** 960–965 (2012).
25. Zhang, F. *et al.* Fabrication of $Ag@SiO_2@Y_2O_3$:Er nanostructures for bioimaging: tuning of the upconversion fluorescence with silver nanoparticles. *J. Am. Chem. Soc.* **132,** 2850–2851 (2010).
26. Yin, A., Zhang, Y., Sun, L. & Yan, C. Colloidal synthesis and blue based multicolor upconversion emissions of size and composition controlled monodisperse hexagonal $NaYF_4$:Yb,Tm nanocrystals. *Nanoscale* **2,** 953–959 (2010).
27. Mahalingam, V., Vetrone, F., Naccache, R., Speghini, A. & Capobianco, J. A. Colloidal Tm^{3+}/Yb^{3+}-doped $LiYF_4$ nanocrystals: multiple luminescence spanning the UV to NIR regions via low-energy excitation. *Adv. Mater.* **21,** 4025–4028 (2009).
28. Kramer, K. W. *et al.* Hexagonal sodium yttrium fluoride based green and blue emitting upconversion phosphors. *Chem. Mater.* **16,** 1244–1251 (2004).
29. Liang, L. F., Wu, H., Hu, H. L., Wu, M. M. & Su, Q. Enhanced blue and green upconversion in hydrothermally synthesized hexagonal $NaY_{1-x}Yb_xF_4:Ln^{3+}$. *J. Alloys Comp.* **368,** 94–100 (2004).
30. Chen, X. & Song, Z. Study on six-photon and five-photon ultraviolet upconversion luminescence. *J. Opt. Soc. Am. B* **24,** 965–971 (2007).
31. Chen, G. Y., Somesfalean, G., Zhang, Z. G., Sun, Q. & Wang, E. P. Ultraviolet upconversion fluorescence in rare-earth-ion-doped Y_2O_3 induced by infrared diode laser excitation. *Opt. Lett.* **32,** 87–89 (2007).
32. Qin, G. S. *et al.* Intense ultraviolet upconversion luminescence from Yb^{3+} and Tm^{3+} codoped amorphous fluoride particles synthesized by pulsed laser ablation. *Opt. Commun.* **242,** 215–219 (2004).
33. Lu, Y., Xi, P., Piper, J. A., Huo, Y. & Jin, D. Time-gated orthogonal scanning automated microscopy (OSAM) for high-speed cell detection and analysis. *Sci. Rep.* **2,** 837 (2012).

Acknowledgements

The authors thank D. Birch, D. Inglis, N. Vella, A. Nadort, R. Field, M. Nguyen, D. Liu, C. Yan and J. Shen (Olympus Australia) for sample characterization, H. Ebendorff-Heidepriem for providing the suspended-core fibres, which were fabricated at the OptoFab node of the Australian National Fabrication Facility (ANFF), and A. Nechaev (Lomonosov Moscow State University of Fine Chemical Technologies, Russia) for bulk crystal preparation. J.Z. acknowledges a Macquarie University Research Excellence Scholarship, and D.J. and J.P. acknowledge support from the Australian Research Council (DP1095465, LP130100517). P.X. acknowledges support from the '973 program' of China (2011CB707502, 2011CB809101) and T.M. acknowledges the support of an ARC Federation Fellowship.

Author contributions

D.J. and T.M. conceived the project, designed the experiments and supervised the research. J.Z., E.S., Y.Lu and D.J. were primarily responsible for data collection and analysis. D.J., E.G., J.Z. and T.M. prepared figures and wrote the main manuscript text. J.Z., E.G., A.Z. and D.J. were primarily responsible for supporting information and numerical simulations. All authors contributed to data analysis, discussions and manuscript preparation.

Additional information

Supplementary information is available in the online version of the paper. Reprints and permissions information is available online at www.nature.com/reprints. Correspondence and requests for materials should be addressed to D.J.

Competing financial interests

The authors declare no competing financial interests.

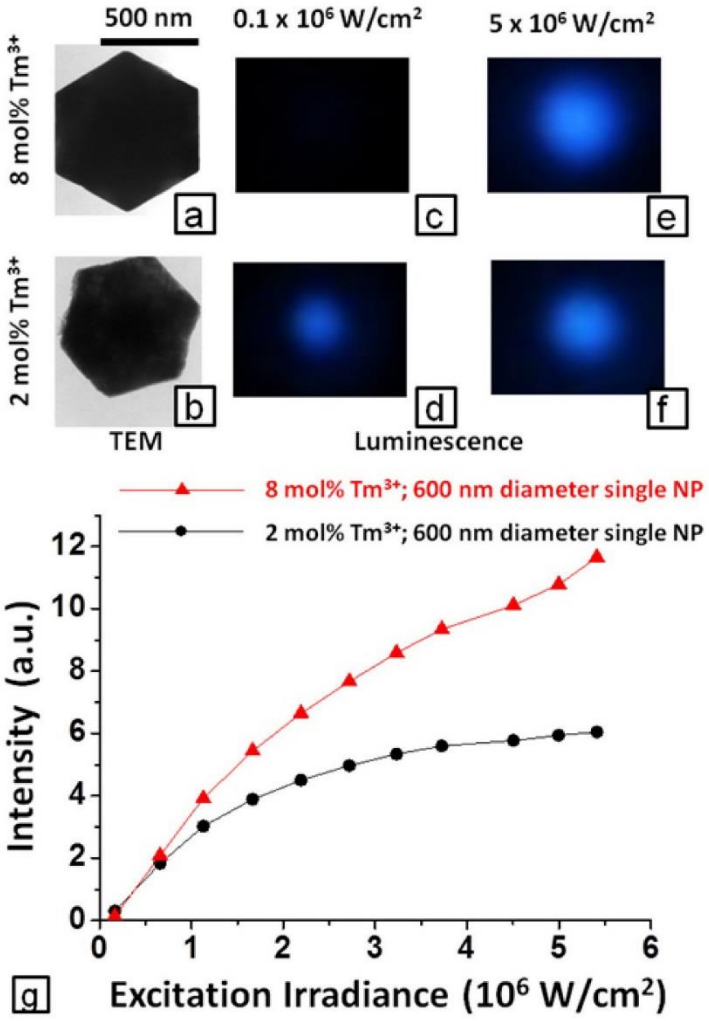

Fig S6. Power dependent single bulk crystal measurement under wide-field upconversion luminescence microscope. *Figures a) and b) are the TEM images of as-prepared bulk crystals at Tm^{3+} doping concentration of 8 mol% and 2 mol% respectively (same samples as Fig S3 d and f); c) and d) are the luminescence images in the visible range (400 ~700nm) at excitation power density of 0.1 × 10^6 W/cm^2 and e) and f) are taken at higher excitation of 5 × 10^6 W/cm^2 for 8 mol% Tm^{3+} and 2 mol% Tm^{3+} single bulk crystals, respectively. All the luminescence images are produced at the same CCD exposure time of 60 milliseconds. g) power-dependent intensities (integrated over 400~850 nm range) of the same single bulk crystals measured by a single-photon counting avalanche diode.*

7. Single nanoparticle imaging results

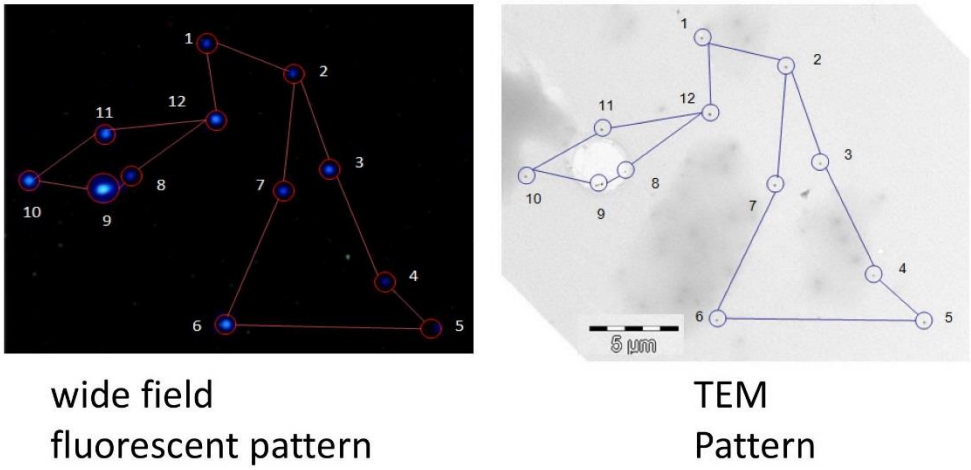

Fig S10. Single nanoparticle detection in wide-field microscopy. a) *Laser scanning microscopy image (excitation at 980 nm) of a 4 mol% Tm^{3+} doped nanocrystals on a glass slide.* ***b)*** *A corresponding TEM image of the same area.*

4.6 Additional information (unpublished results)

Apart from the single nanoparticle imaging shown in published paper, we actually carried out imaging of single nanoparticles using our upconversion wide field microscope. The figure S 4.3 shows the wide field imaging with five single upconversion nanocrystals (NaYF4: Yb20%, Tm 4%) with size of 40 nm: the original fluorescence imaging is inserted (left top corner), and their corresponding intensities are shown in three-dimensional figure by using ImageJ software. The figure S4.4 shows another wide field imaging for upconversion nanocrystals and their corresponding TEM pattern for confirmation of single/multiple nanocrystals. These provide the extra evidence that the high brightness could be obtained for these densely doped upconversion materials under the high excitation power.

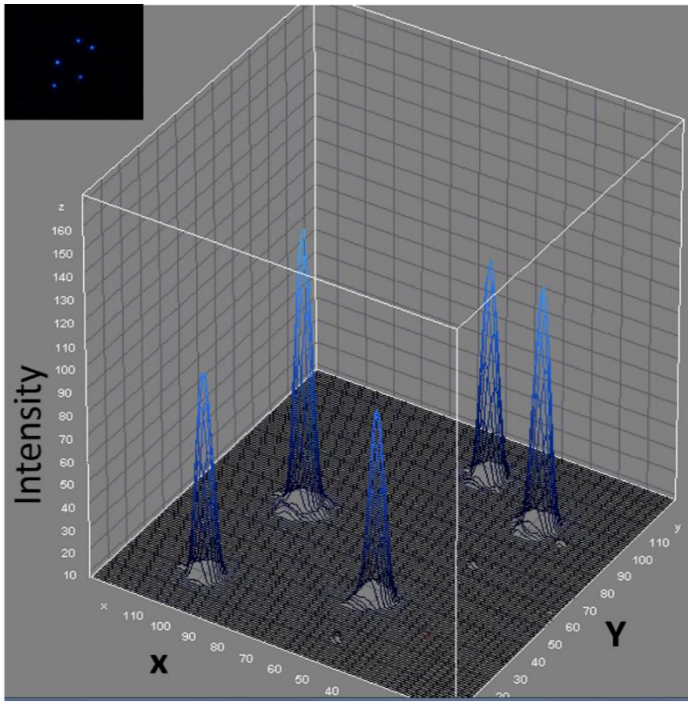

Figure S 4.3 single upconversion nanoparticle (NaYF4: Yb20%, Tm4%) imaging. The inserted figure on the left top corner shows the wide field imaging for the single nanocrystals, and their intensities are displayed in the 3-D figure by ImageJ software.

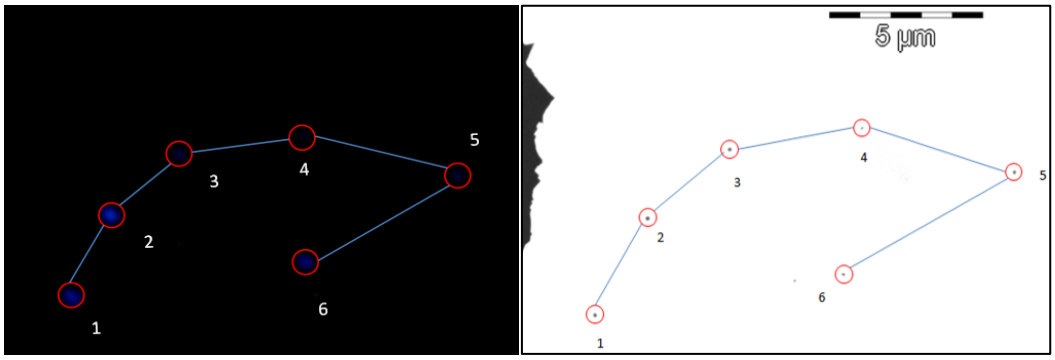

Figure S4.4 wide field imaging for upconversion nanocrystals (left) under 980 nm excitation; and corresponding TEM pattern (right).

4.7 Remarks

Our optical system has been further upgraded and applied to characterise lanthanide based upconversion micro-rods and nanocrystals at high resolution and under different excitation power intensities. I first used the system to characterise upconversion micro-rods, and with high optical resolution and lifetime measurements I confirmed there is no energy transfer between two closely sections doped with different activators. The self-correlated imaging and analysis functions incorporated in one system can rapidly find the points of interest, and then accurately zoom in to inspect an area to measure the luminescence lifetime. The wide field microscope was useful to study the power-dependent properties of highly-doped upconversion nanoparticles with single nanoparticle sensitivity, which provides further evidence that the high excitation irradiation alleviates the problem of concentration quenching in lanthanide-doped upconversion nanocrystals.

The current system has scope for further optimization and integration of other optical modalities towards more powerful and comprehensive characterisation. For example, the confocal scanning range can be ideally increased to achieve large area detection, and ideally the system would be automatically controlled with multi-channel detectors applied to increase the sample analysis throughput. Meanwhile, the targets of interest from wide field imaging would be conveniently and automatically selected for further confocal imaging with higher resolution.

In the view of upconversion materials, some other optical parameters, such as energy transfer efficiency, excitation dipole orientation and emission polarization, are still unclear. Therefore, the corresponding measurements should be carried out by designing an efficient optical system. The Appendix presents two current projects for the measurement of energy transfer efficiency and emission polarization for upconversion materials.

Chapter 5. Conclusions and Perspectives

5.1 Summary

Lanthanide complexes and luminescence nanomaterials have been intensively developed over the last decade for bio- sensing and imaging applications. Their unique optical properties, including long luminescence lifetime (microseconds), large stokes and anti-stokes shifts and sharp spectral emission lines, are highly attractive for achieving ultra-sensitive detections, but only when appropriate design of excitation source, optics, and detection systems with control electronics is implemented. From the perspective of fundamental research, the details of the luminescence mechanisms involving multiple energy levels and complicated photon relaxation process are still unclear, due to the lack of effective optical systems for comprehensive characterisation.

To address these demands, my thesis has focused on developing and implementing advanced optical systems based on the time-gated luminescence and time-resolved luminescence approaches in the microsecond region. Two prototype instruments have been successfully engineered and validated by applications.

To ensure high throughput, compatibility and stability but also reduce the complexity and cost for the time gated luminescence (TGL) imaging applications, I designed and built a multi-colour TGL microscope for simultaneous observation of multiple species of microorganisms stained with long-lived complexes. We first designed and engineered an excitation unit based on a high-speed Xenon flash lamp that was synchronised to a purpose-built time-gated detection unit. Both units feature high compatibility and can be easily adapted to any commercial microscope for TGL imaging. We then demonstrated dual-colour background-free imaging of two types of micro-organisms stained with red-emitting europium complex and green-emitting terbium complex respectively. Moreover, we verified the detection sensitivity by imaging the single 150 nm europium-doped nanoparticles. This engineering work provides a clear protocol for constructing a multi-colour time-gated imaging system which is low-cost, simple and reproducible, and easily accessible for biological and

chemical laboratories. As result, this system has been recently duplicated for biochemical research at our collaborators' labs at Dalian University of Technology in China. The majority of results from this work have been reported in the paper published in *Scientific Reports* 2014.

In parallel, to comprehensively characterise lanthanide-based luminescent materials, I have designed and built a time-resolved spectroscopy system based on a multi-modality fluorescence microscope capable of high-speed acquisition of high-resolution time-resolved spectra from both down-conversion and upconversion lanthanide-doped luminescence materials. We first applied an integrated multi-channel photon-sensing device (a 32 channel PMT as a linear array detector) to replace the traditional camera in the spectrometer for simultaneously collecting the spectra and the lifetimes at each wavelength. We then replaced the single-channel avalanche photodiode (APD) with this purpose-built time-resolved spectrometer for signal collection in our home-built laser scanning confocal microscopy system. Using this system, we acquired the first 3-dimensional time-resolved spectra from a sample of mono-disperse hexagonal-phase $NaYF_4$: Yb20%, Er2% upconversion nanocrystals. It took less than 1 minute for the system to complete 50 data acquisitions to construct a time-resolved spectrum with high spectral and temporal resolution. Moreover, we showed the information-rich self-correlated time-resolved spectra obtained by this system were valuable to study the luminescence resonance energy transfer (LRET) efficiency for down-conversion doped single microspheres. To the best of our knowledge, this is the first quantitative measurement of spectra and lifetime decay curves from luminescent lanthanide materials. The majority of results from this work have been reported in the paper published in *RSC Advances* 2013.

To provide nanoscale characterization capabilities to explore the sophisticated photon-emitting mechanisms in lanthanide nanomaterials, I upgraded my system for time-resolved luminescent lifetime detection using a laser scanning microscope and a wide field microscope. This was verified to study the energy transfer effects on the boundary of colour-barcoded heterogeneous upconversion micro-rods. The laser scanning confocal microscope provides high resolution scanning of selected sections on a micro-rod for time-resolved lifetime analysis. We implemented comprehensive measurements to compare lifetime changes from different designs of micro-rods and

confirmed no energy transfer happening between two neighbourhood sections doped with different activators. Moreover, we demonstrated that self-correlated imaging and analysis functions incorporated in the system can rapidly localize the points of interest before a zoom in analysis by the laser scanning confocal microscope to measure the luminescence lifetime. Furthermore, using my upconversion wide-field microscope I demonstrated single particle sensitivity achieved by directly imaging highly doped upconversion nanocrystals. The system is also suitable for an analysis of power-dependence to study highly doped upconversion crystals with higher emission intensity under intense power irradiation. This work provides an advanced characterisation modality to study lanthanide doped luminescence materials with high resolution. The majority of results from this work have been reported in the papers (my role as co-author) published in *Journal of American Chemical Society* 2014 and *Nature Nanotechnology* 2013.

In summary, my PhD program for the last three and half years focused on instrumentation engineering, and I have advanced both time-gated luminescence approach and time-resolved characterization methods in the context of integrated microscopy and spectroscopy systems. My work has transformed robust microscopy designs and provided stable reproducible devices for end-users in material chemistry and cell biology labs. My work has also resulted in advanced characterization systems to enable high-speed high-resolution acquisition of temporal and spectral luminescence properties from long-lived luminescence materials, leading to new tools for fundamental research to study photon luminescence mechanisms. There is large scope for further optimization of this multi-modality optical characterization system towards automatic, high-throughput and high-sensitivity characterization by incorporating multichannel detection and manipulation capabilities.

5.2 Future Work

The results of this multidisciplinary research program also suggest a range of future opportunities in exploring advanced optical instruments/techniques towards better understanding of luminescence mechanisms for lanthanide-doped nanomaterials. We have identified three opportunities for the near future. These include exploration of emission lifetimes of upconversion nanomaterials at different excitation power levels, quantitative measurement of the energy transfer efficiency between the sensitizers and activators within upconversion nanocrystals, and emission polarisation properties of lanthanide doped up-conversion crystals.

Indeed, for each of these opportunities, I have established new instrumentation and methods, and obtained some preliminary results, which form three appendices presented at the end of this thesis.

Appendix I.

The upconversion luminescence lifetimes are independent of the excitation power

6.1 Introduction

Luminescence lifetime, as an important indicator for understanding the photon-emission mechanisms of luminescence materials, has also been extensively applied in the application field of photonics sensing recently. For example, fluorescence lifetime imaging microscopy (FLIM) and lifetime-barcoding multiplexing techniques take the advantage of the lifetime signatures to distinguish different targets stained by probes with different lifetimes [1, 2]; the luminescence resonance energy transfer (LRET) scheme can be used to tune the lifetimes [3] or measure the lifetime changes in absence or presence of acceptors to calculate the energy transfer efficiencies. Lifetime measurement is much more robust than intensity measurement due to the fact that it is independent to intensity of emitters. There is a knowledge gap to characterize the dependence of luminescence lifetimes in the microsecond region on the excitation power intensity.

Recently, Schuck et al reported the decrease of luminescence lifetimes for upconversion nanocrystals (NaYF4: Yb20%, Er2%) when power density increased from 1 W/cm^2 to 1 MW/cm^2 [4]. The authors applied the band-pass emission filters (540±20 nm and 650 with ±20 nm) to separately select green and red emissions for lifetime measurement. Nevertheless, each emission band involves different photon relaxation processes or/and different excited states, therefore the filter-based lifetime measurement only gives an average result. To study the relationship between the excitation power and emission lifetime, it is desirable to extract the emission lifetimes from each excited state and analyse its dependence on a large range of excitation power intensities.

In this proof-of-the-principal study, I applied a microstructure optical-fibre based spectroscopy system based on the time-resolved spectrometer established in Chapter 3 and examined the luminescence lifetimes of two different types of upconversion

nanocrystal (NaYF4: Yb20%, Er2% and NaYF4: Yb30%, Tm0.5%, Nd1%). The microstructure optical fibre provides a large dynamic range of excitation power intensities, and the 3-D time-resolved system provides a high resolution of 3 nm for the accurate high-throughput lifetime measurement of emissions covering the visible emission region. After extracting the narrow-band (3 nm) lifetime decay curves with various excitation power intensities, the luminescence decay curves did not show obvious changes.

6.2 Materials and Methods

6.2.1 Upconversion nanocrystals

Sample I: the β-phase dual-doped upconversion nanocrystals NaYF4: Yb20%, Er2% with simplified energy level diagram shown in Figure 6-1(a).

Sample II: the β-phase tri-doped upconversion nanocrystals NaYF4: Yb30%, Tm0.5%, Nd1% with typical emission spectrum shown in figure 1(b).

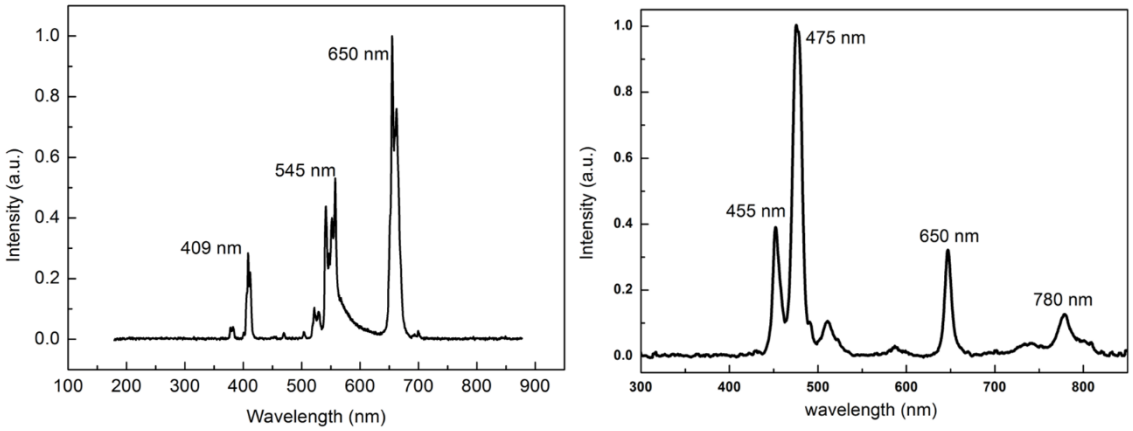

Figure 6-1. Emission spectra for two types of upconversion nanocrystals: (a) emission spectrum for NaYF4: Yb20%, Er2% upconversion nanocrystals with three main emission bands with emission peaks at 409 nm, 545 nm, and 650 nm; (b) emission spectrum for NaYF4: Yb30%, Tm0.5%, Nd1% with four main emission bands with emission peaks at 455 nm, 475 nm, 650 nm and 780 nm.

6.2.2 Optical characterisation system

Our slide/fibre-based time-resolved spectroscopy system was applied to perform the time-resolved spectra measurement, as shown in Figure 6-2.

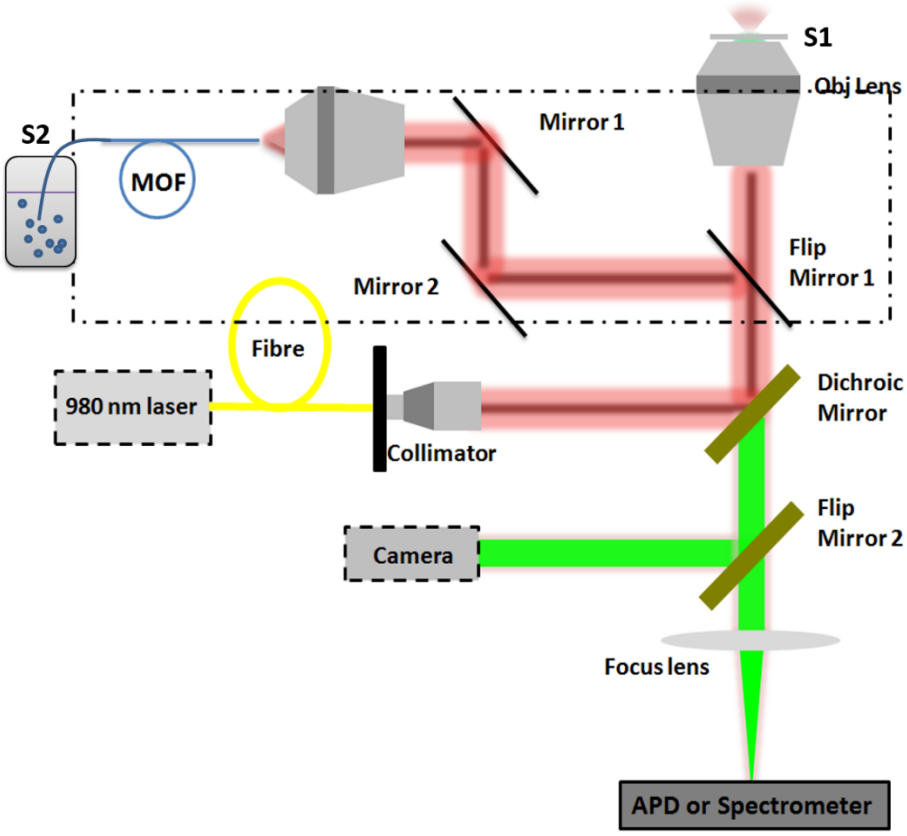

Figure 6-2. Slide/fibre based time-resolved spectroscopy system. For slide based system, the samples are excited on a glass slide with a three-dimensional stage, while for fibre based system, the samples are excited inside the microstructured optical fibre (MOF). The switch between these two systems is realized by a Flip Mirror 1.

The slide-based measurement was used to capture the decay curves of NaYF4: Yb20%, Er2% nanocrystals under three different excitation intensities (5, 10 and 15 MW/cm^2). The fibre-based system was applied to measure the tri-doped nanocrystals with five excitation power intensities ranging from 20 kW/cm^2 to 200 kW/cm^2.

6.3 Results and Discussions

Shown in Figure 5-3, under the excitation power intensities of 5 MW/cm^2, 10 MW/cm^2 and 15 MW/cm^2, we compared the luminescence decay curves at 545 nm (Figure 6-2 a) and 650 nm (Figure 6-2b), respectively, and found no obvious changes for either emission peaks from NaYF4: Yb30%, Er2% upconversion nanocrystals.

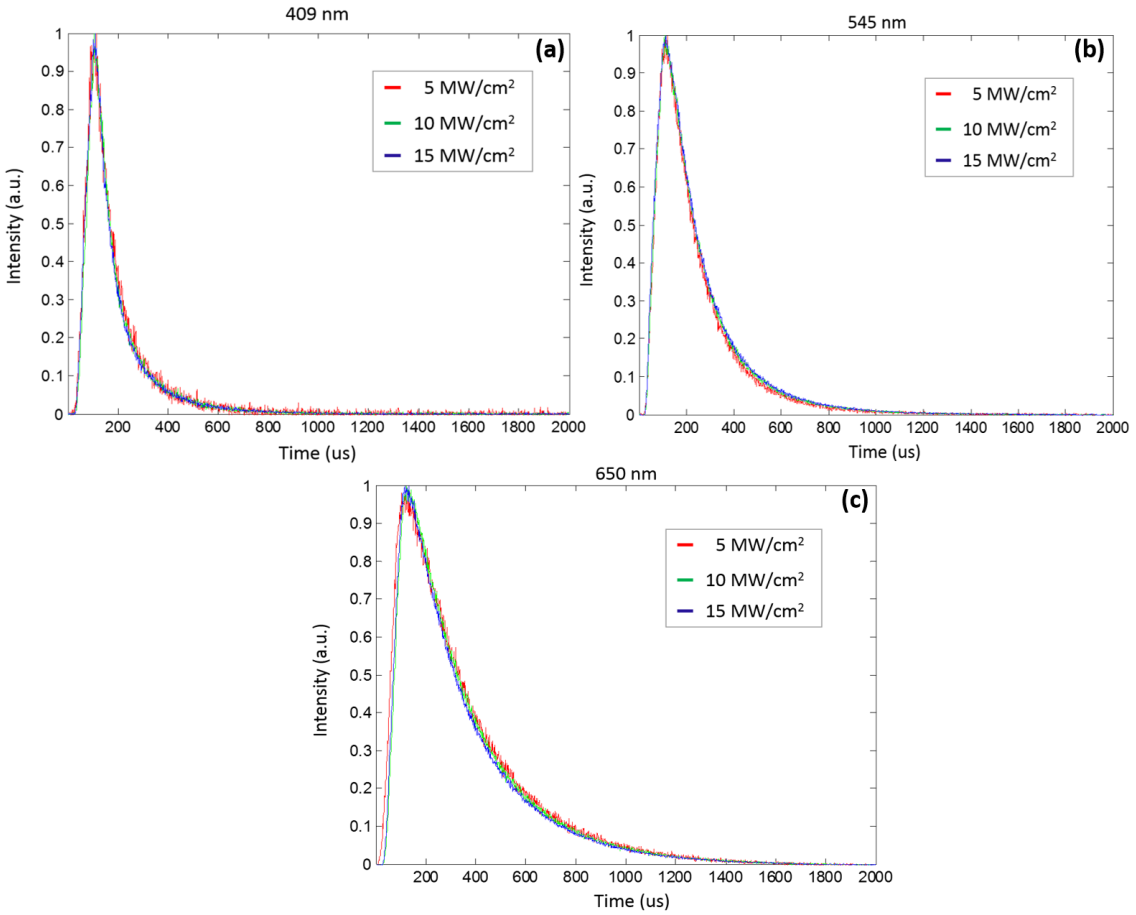

Figure 6-3. Comparison of luminescence decay curves under different excitation intensities at two different emission wavelengths (a) 409nm, (b) 545 nm and (c) 650 nm from the NaYF4: Yb30%, Er2% upconversion nanocrystals.

Shown in Figure 6-4, under the excitation power intensities of 20kW/cm^2, 30 kW/cm^2, 50 kW/cm^2, 100 kW/cm^2, 200 kW/cm^2, we compared the luminescence decay curves at 455 nm, 475 nm, 650 nm and 780 nm, and did not observe obvious changes on the decay curves for each emission peaks from the tri-doped upconversion nanocrystals NaYF4: Yb30%, Tm0.5%, Nd1%,

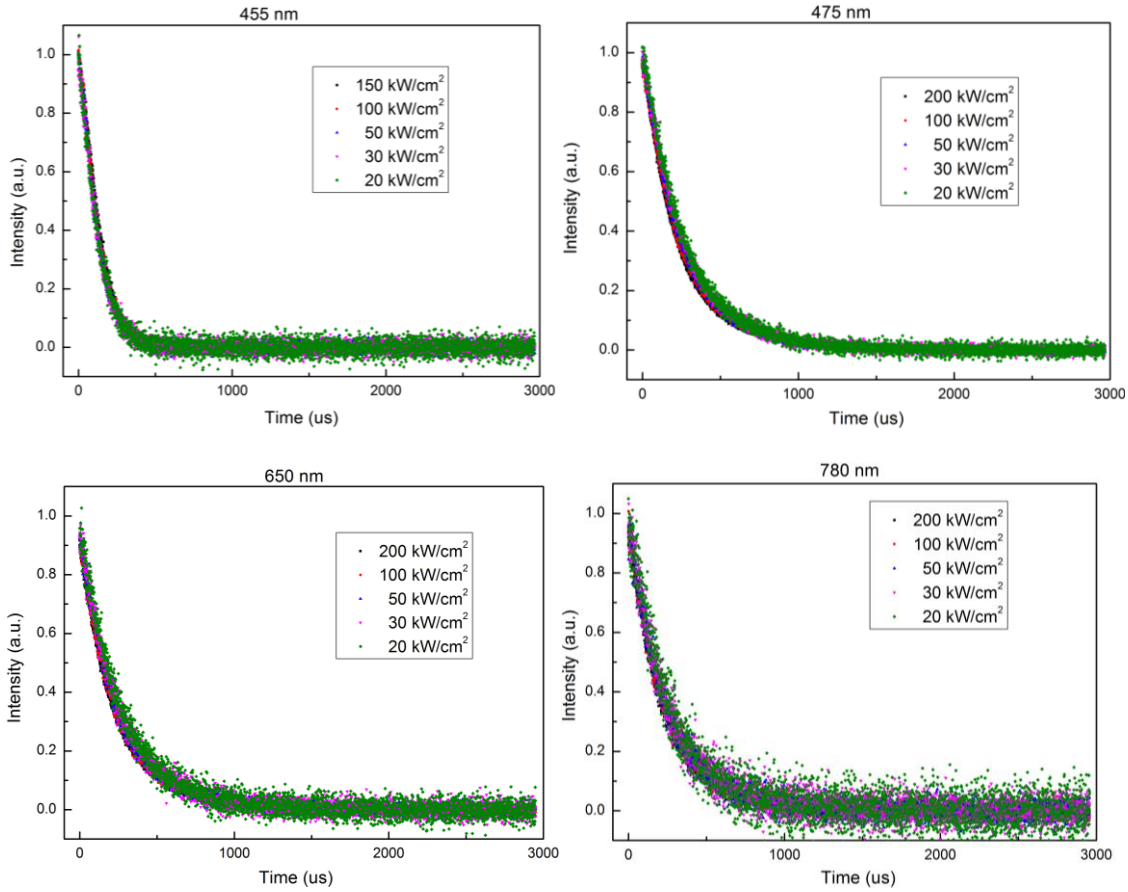

Figure 6-4. Comparison of luminescence decay curves under different excitation power densities at four different emission wavelengths 455 nm, 475 nm, 650 nm and 780 nm from the NaYF4: Yb30%, Tm0.5%, and Nd1% tri-doped upconversion nanocrystals.

6.4 Conclusions

Using our time-resolved spectroscopy system by simultaneously collecting the luminescence decay curves at each visible emission wavelengths (spectral resolution of 3.3 nm), we provided evidence that the luminescence decay lifetime is independent of the excitation power intensities for two different types of upconversion nanocrystals. These results were obtained with excitation power intensities ranging from 20 kW/cm^2 to several MW/cm^2. These results are controversial to the reported results by Schuck et al [4]. Our experiments using relatively higher power intensity range that may reach the saturation excitation for upconversion nanocrystals, and therefore, more comprehensive investigations are needed to study the effect of lower excitation power intensities on the luminescence lifetimes.

6.5 References

[1] Lu YQ, Zhao JB, Zhang R, Liu YJ, Liu DM, Goldys EM, et al. Tunable lifetime multiplexing using luminescent nanocrystals. Nature Photonics. 2014;8:33-7.

[2] Svensson FR, Abrahamsson M, Stromberg N, Ewing AG, Lincoln P. Ruthenium(II) Complex Enantiomers as Cellular Probes for Diastereomeric Interactions in Confocal and Fluorescence Lifetime Imaging Microscopy. J Phys Chem Lett. 2011;2:397-401.

[3] Lu Y, Lu J, Zhao J, Cusido J, Raymo FM, Yuan J, et al. On-the-fly decoding luminescence lifetimes in the microsecond region for lanthanide-encoded suspension arrays. Nature communications. 2014;5:3741.

[4] Gargas DJ, Chan EM, Ostrowski AD, Aloni S, Altoe MV, Barnard ES, et al. Engineering bright sub-10-nm upconverting nanocrystals for single-molecule imaging. Nature nanotechnology. 2014;9:300-5.

Appendix II.

Activators' quantum yield measurement in upconversion nanocrystals

7.1 Introduction

Lanthanide-doped upconversion nanocrystals are typically doped with ytterbium (Yb^{3+}) sensitizer ions, which absorb infrared radiation and non-radiatively transfer their excitation to activator ions such as erbium (Er^{3+}), thulium (Tm^{3+}) or holmium (Ho^{3+}). Upconversion nanocrystals have been extensively studied in the recent decade due to their excellent optical properties, including long lifetime, sharp emission spectra, good photo-stability and large anti-stokes shift.

One of the current bottleneck challenges lies in its relatively low upconversion efficiency. Strategies, such as coating nanocrystals with an inert shell to minimize surface quenching [1], using noble metal nanostructures to enhance the energy transfer rate by surface plasmon resonance [2], and using high efficient crystal host to minimize the internal energy loss [3], have been reported to enhance the upconversion efficiency. The upconversion process involves sophisticated process of photon absorption by sensitizer ions, energy transfer and back transfer, internal and external quenching, and photon emissions from multiple excited states of activators. Strategies to improve the upconversion efficiency requires techniques to diagnose where the photon energy gets lost. Advanced measurements for quantum yield (QY), radiative rates and non-radiative rates have become a challenge.

In this work, we applied the micro-cavity based photonics method to directly measure the QY of activators (Er^{3+} ions) doped in upconversion nanocrystals ($NaYF_4$: Yb20%, Er2%). By measuring the luminescence lifetimes and studying the variations of radiation rates at different cavity lengths, this method can be used to obtain the absolute QY of activators (Er^{3+}) at different emission bands. Since the overall QY is a result of energy transfer efficiency times the QY of activators, this method also provides a means to measure the energy transfer efficiency from the sensitizer to the activators. Therefore,

the method provides a diagnostics tool for understanding the upconversion luminescence process and efficiency.

7.2 Materials and Methods

7.2.1 Upconversion nanocrystals

The hexagonal-phased NaYF4: Yb20%, Er2% upconversion nanocrystals with average size of 40 nm are measured by TEM, and their TEM image and simplified energy levels are shown in Figure 7-1 with emission spectra shown in Figure 6-1 (a).

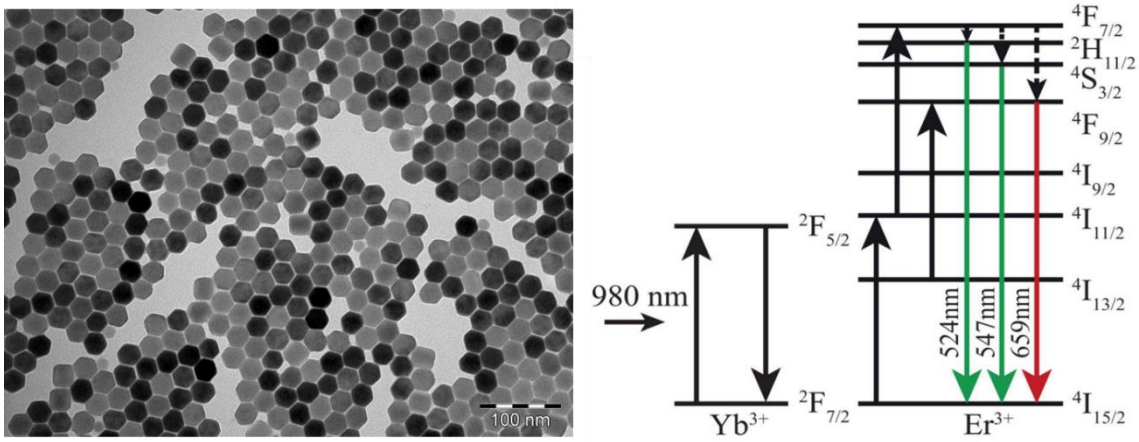

Figure 7-1. The hexagonal-phased NaYF4: Yb20%, Er2% upconversion nanocrystals with size of 40 nm: (a) their TEM image; and (b) simplified energy level.

7.2.2 Micro-cavity and sample preparation

Illustrated in Figure 7-2 (a), the micro-cavity is formed by one plano-convex lens and one coverslip. The plano-convex lens was coated by a thin layer of silver (thickness 80 nm) on the curved surface providing a high reflectivity of approximately 95%; and the glass coverslip (thickness 170 µm) was coated by a thin layer of silver (thickness 30 nm) providing an efficient excitation and emission with a transmission of approximately 25% [4]. The spherical surface of the lens on the top provides a tunable cavity length by laterally moving the micro-cavity with respect to the laser focus controlled by the nanoscale positioning stage.

The procedure of preparing micro-cavity samples involves five steps after the silver coating by vapour deposition method. 1) well mix the upconversion nanocrystals and UV-curable optical glue by ultra-sonication for 20 minutes; 2) drop 10 µL of the

mixture onto the silver coated coverslip; 3) place the convex lens on the top of the mixed sample to form a sandwich structure; 4) illuminate the sandwich structured sample with UV light for 30 minutes to cure the mixture solution into solid; 5) test the quality of this sandwich structured sample by wide field image with white light illumination (a successful sample preparation was shown in Figure 7-2 (b) with regular interference rings).

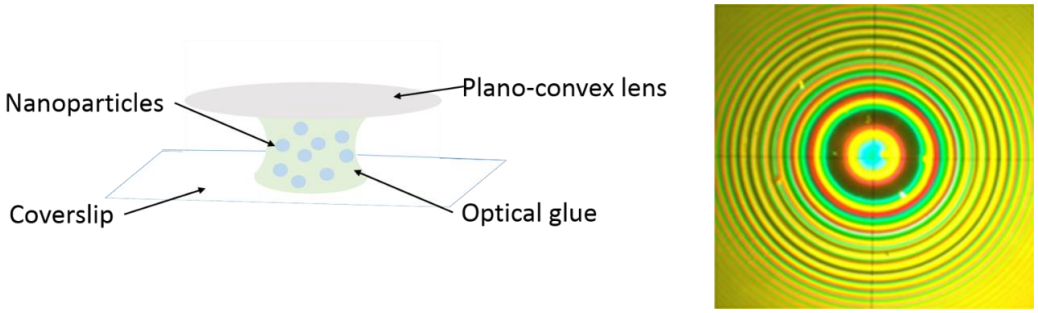

Figure 7-2. Schematic diagram of micro-cavity (left): the microcavity is formed by one plano-convex lens and one coverslip with nanoparticles sandwiched. Wide field image of micro-cavity sample under white light illumination with regular interference rings (right).

7.2.3 Optical characterisation setup

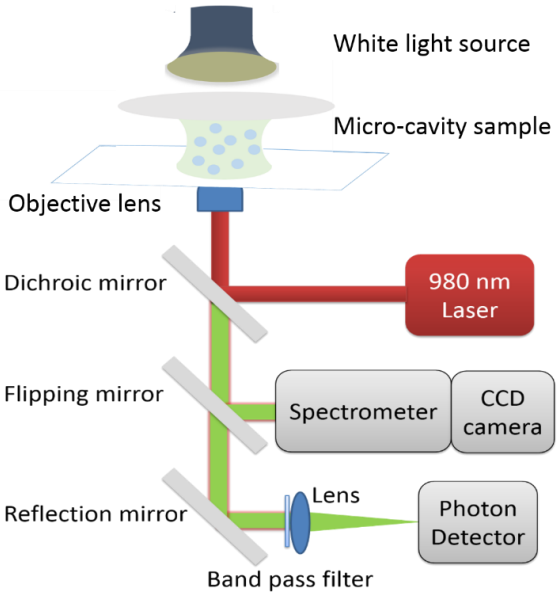

Figure 7-3. Scheme of experimental setup, including a laser scanning confocal microscope for selectively imaging a targeted area through the micro-cavity, a time-

resolved optical detection system for the lifetime measurement, and a spectrometer system for determination of the cavity length.

As illustrated in the schematic Figure 7-3, the setup is based on a home-built laser scanning confocal microscope, a time-resolved detection using a single photon counting detector, and a spectrometer. The laser scanning confocal system is used to determine the position of different cavity lengths for lifetime measurement. And selected positions of interest were marked by lines on the confocal images, shown in Figure 7-4 (a) and Figure 7-4 (b) for the green emission band (through a band pass filter (FF01-540/20)) and red emission band (through a band pass filter 641/50) respectively. Time-resolved measurements were carried out with luminescence lifetime decay curves captured at each pixel along the marked lines, and the spectrometer was then used to determine the cavity lengths for these pixels of interest by capturing the maximum transmission spectra of white light illumination.

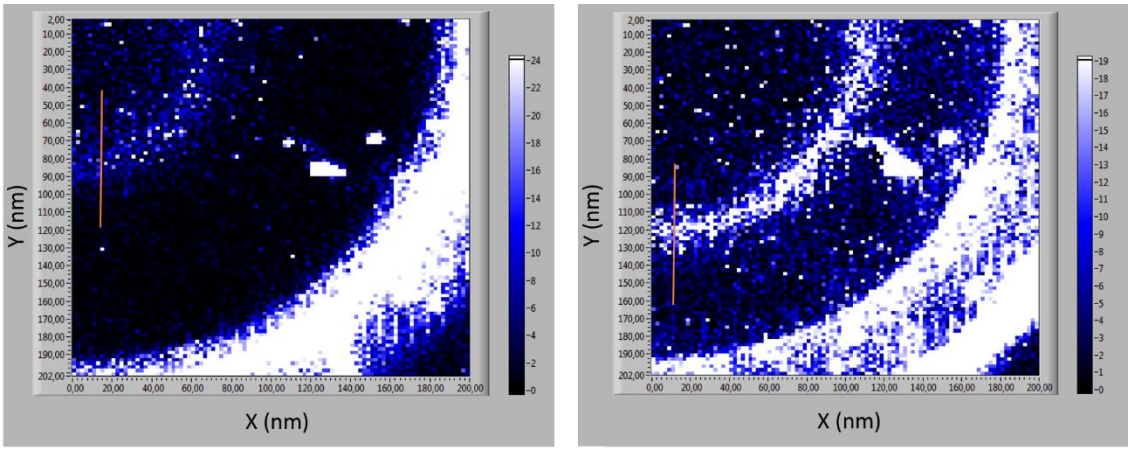

Figure 7-4. Confocal images with selected positions marked by red lines for lifetime measurement. (a) Confocal imaging for green emission band (530 nm to 550 nm) (b) confocal imaging for red emission band (615 nm to 661 nm).

7.3 Results and Discussions

Figure 5-9 shows the relationship between the luminescence lifetimes (y axis) of each pixels of interest with different cavity length (x axis), measured according to the red (Figure 5-9 a) and green (Figure 5-9 b) emission bands for the NaYF4:Yb20%, Er2% upconversion nanoparticles. The increase of cavity length led to decreased upconversion luminescence lifetime. According to the theoretical modelling and curve fitting analysis

shown by solid lines in Figure 7-5, we obtained the Er^{3+} activators' quantum yield values for both green and red two emission bands. For green emission around 545 nm, the quantum yield was measured as 13.7 ±2%; for red emission around 650 nm, the quantum yield was measured as 15.2±2%. The system also resulted in the calculated free space lifetime 129 ± 3 μs and 219± 6 μs for green emission and red emission bands respectively, which values are consistent to the literature reports [5, 6]indicating the accuracy of the micro-cavity based method. Moreover, we applied the bootstrapping calculations to obtain the average values and standard deviations of quantum yields by randomly choosing 70% of experimental data points for curve fitting, with results shown in Figure 7-6.

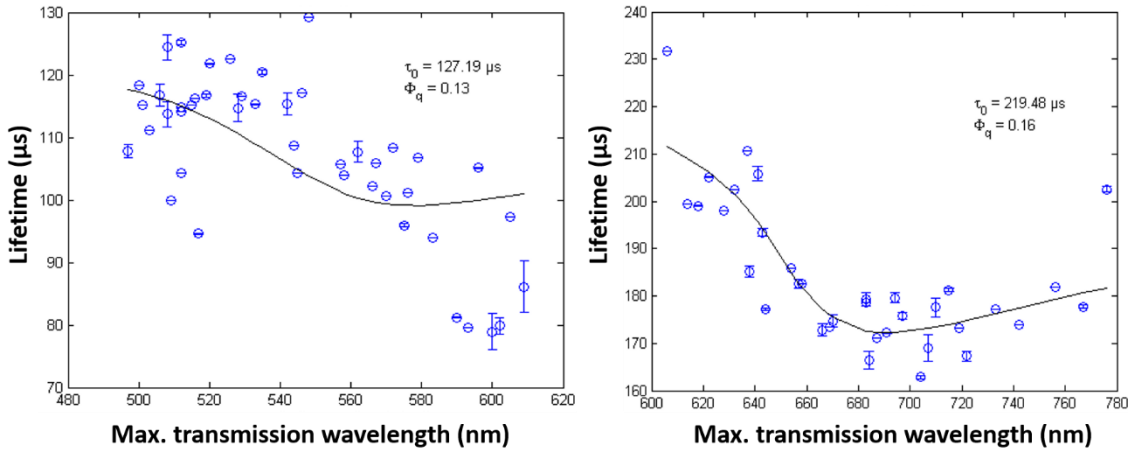

Figure 7-5. Luminescence lifetimes vs cavity lengths for the measurement of NaYF4: Yb20%, Er2% upconversion nanocrystals sandwiched within the micro-cavity. (a) Lifetime curves for green emission (x nm to xx nm); (b) lifetime curves for red emission (x nm to xx nm). Blue circle dots are the experimental data and dark lines are the theoretical fitting curves.

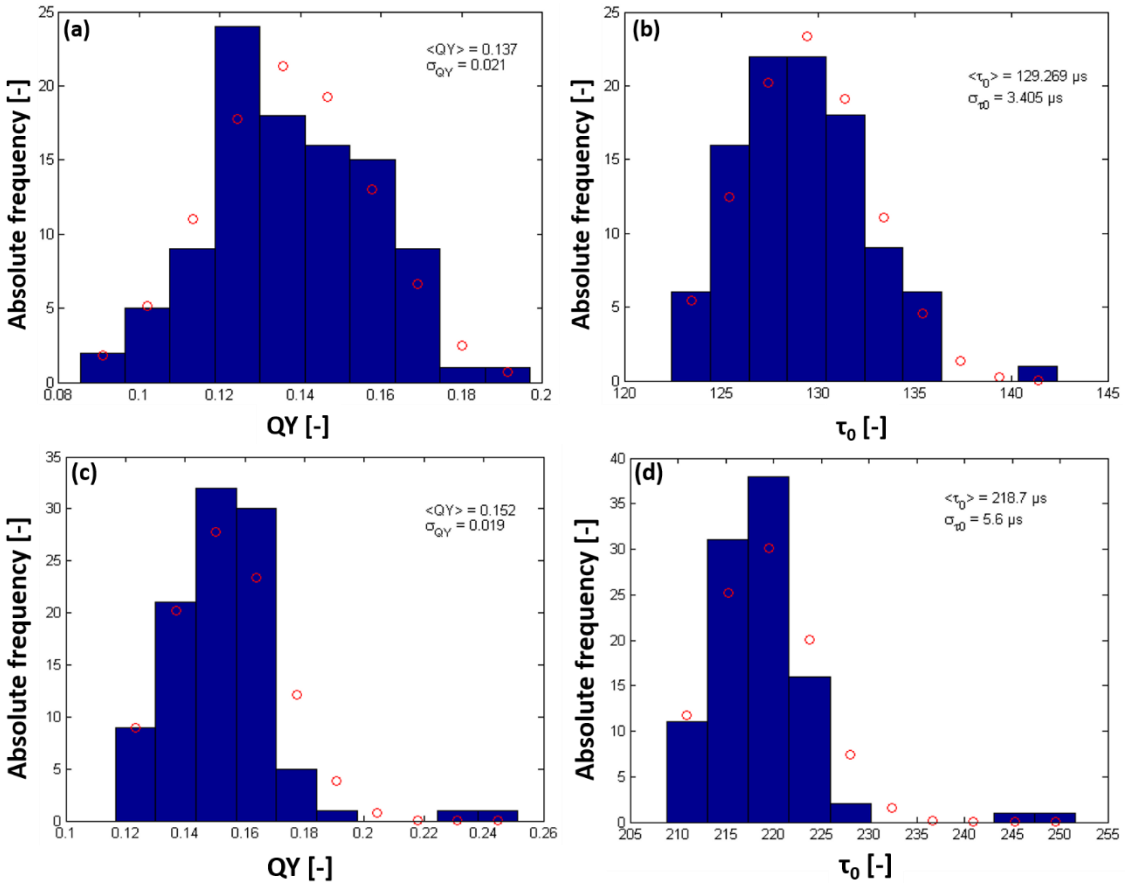

Figure 7-6. Bootstrapping calculation to obtain the average QY values and lifetime values for both green and red emissions.

7.4 Conclusions

Micro-cavity based method provides a direct QY measurement for doped activators (Er^{3+}) in upconversion nanocrystals ($NaYF_4$: Yb20%, Er2%). The method is both robust and accurate in determining the activators' QY and free space lifetimes, which benefits from the statistics analysis using pixel by pixel based lifetime measurements within a series of varied micro-cavity length. Since the overall QY can be measured using the traditional methods[7-9], the activators' QY values will provide an opportunities to measure the upconversion luminescence process through quantitatively calculation of the energy transfer efficiency between Yb and Er ions, non-radiative rates and radiation rates from excited states. This provides a new nanoscale characterisation tool for upconversion materials science aiming to deliberately synthesize high quality more efficient nanoparticles.

7.5 References

[1] Chen DQ, Huang P. Highly intense upconversion luminescence in Yb/Er:NaGdF4@NaYF4 core-shell nanocrystals with complete shell enclosure of the core. Dalton T. 2014;43:11299-304.
[2] Lu D, Cho SK, Ahn S, Brun L, Summers CJ, Park W. Plasmon enhancement mechanism for the upconversion processes in NaYF4:Yb(3+),Er(3+) nanoparticles: Maxwell versus Forster. Acs Nano. 2014;8:7780-92.
[3] Wang J, Deng R, MacDonald MA, Chen B, Yuan J, Wang F, et al. Enhancing multiphoton upconversion through energy clustering at sublattice level. Nature materials. 2014;13:157-62.
[4] Bar S, Chizhik A, Gutbrod R, Schleifenbaum F, Chizhik A, Meixner AJ. Microcavities: tailoring the optical properties of single quantum emitters. Analytical and bioanalytical chemistry. 2010;396:3-14.
[5] Liu LX, Qin F, Zhao H, Lv TQ, Zhang ZG, Cao WW. Shell thickness dependence of upconversion luminescence of beta-NaYF4:Yb, Er/beta-NaYF4 core-shell nanocrystals. Opt Lett. 2013;38:2101-3.
[6] Zhang L, McKay A, Jin D. High-throughput 3-dimensional time-resolved spectroscopy: simultaneous characterisation of luminescence properties in spectral and temporal domains. RSC Advances. 2013;3:8670-3.
[7] Zhao J, Jin D, Schartner EP, Lu Y, Liu Y, Zvyagin AV, et al. Single-nanocrystal sensitivity achieved by enhanced upconversion luminescence. Nature nanotechnology. 2013;8:729-34.
[8] Nadort A, Sreenivasan VK, Song Z, Grebenik EA, Nechaev AV, Semchishen VA, et al. Quantitative imaging of single upconversion nanoparticles in biological tissue. PloS one. 2013;8:e63292.
[9] Boyer JC, van Veggel FCJM. Absolute quantum yield measurements of colloidal NaYF4: Er3+, Yb3+ upconverting nanoparticles. Nanoscale. 2010;2:1417-9.

Appendix III.

Characterisation of luminescence polarisation properties of upconversion micro-rods and nanocrystals

8.1 Introduction

Under a polarised excitation, a single emitter will generally emit polarised luminescence. However, the emission polarisation property will get lost for multiple emitters randomly distributed even under a polarised excitation beam. Therefore anisotropic emissions are observed in most cases. When multiple rare earth ions as luminescence photon sensitisers and emitters are co-doped within a sodium yttrium fluoride crystal by randomly replacing the yttrium ions[1, 2], we would expect that the polarised emissions from multiple single emitters superimpose in a non-coherent manner and become unpolarised as a whole. But recently Zhou *et al.* observed the polarisation property of luminescence emissions from the NaYF4: Yb20%, Tm2% upconversion micro-rods by rotating wavelength-sensitive half wave plate placed before one polariser and the detector[3]. This result makes us to think whether the individual emitters at a certain concentration (distance) and crystal orientation have already started to interact with each other.

With this interesting question, we design a new characterisation system and conducted a series of experiments for comprehensive and quantitative characterisations of a variety of upconversion materials. We first built a wide-field upconversion microscope based on a layout of two identical objectives, instead of epi-fluorescence configuration. This layout avoids possible polarisation changes at each reflecting surface. Among different effects we account for mismatch reflection for each polarisation and a change of phase due to the different depth that the electromagnetic field undergoes at each mirror. We then carried out a comprehensive study on the emission polarisation of upconversion micro-rods (length 2 μm and diameter 150 nm). We measured both the orientation of the linear polarisation and the elliptical polarisation component of the emission signal. These measurements are done at each wavelength in order to quantitatively determine their polarisation directions. Moreover,

we explored the relationship between doping concentration and emission polarisation by synthesising a series of upconversion micro-rods with different sensitiser/activator concentrations. Furthermore, we have also examined the effect of excitation powers/polarisations on the emission polarisation of upconversion micro-rods.

8.2 Materials and Methods

8.2.1 Upconversion materials

Two series of upconversion micro-rods (NaYF4:Yb, Tm) were prepared with (i) six different Yb doping concentrations from 10 % to 60% with the Tm doping concentration fixed at 2 mol%; and (ii) two different Tm concentrations from 0.5% and 8 % with the Yb concentration fixed at 5 mol%. Figure 8-1 shows the typical morphology, typical emission spectrum and fluorescence images of upconversion micro-rods with length of 2 µm and diameter of 150 nm.

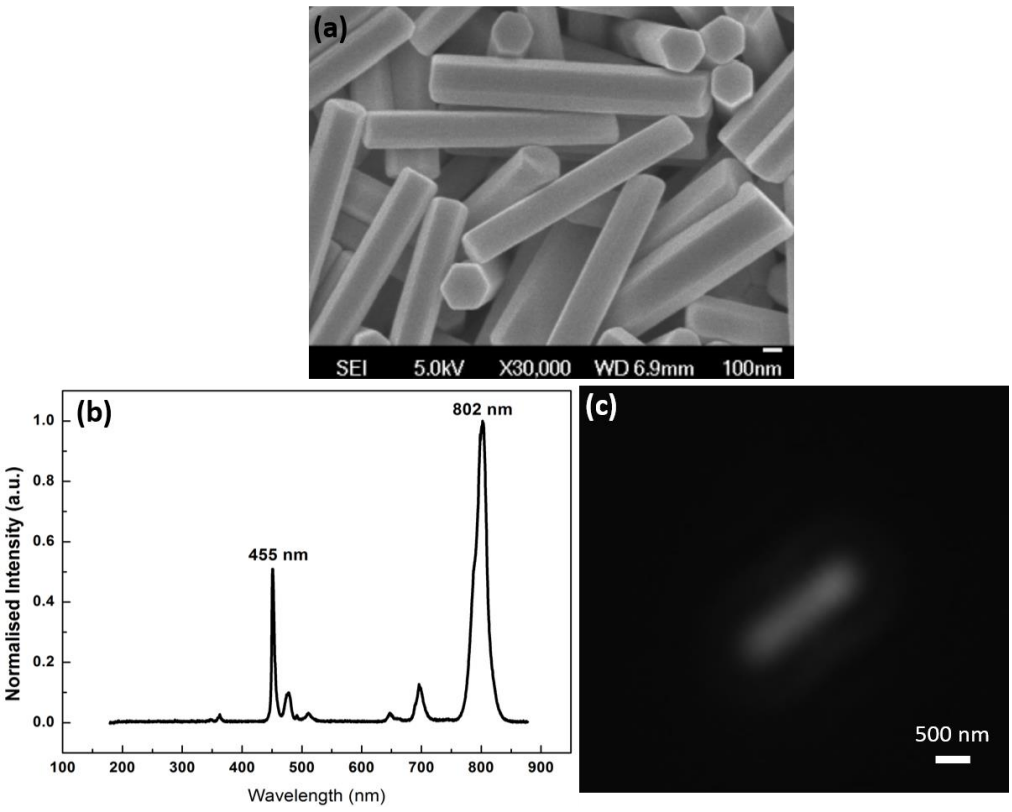

Figure 8-1. (a) scanning electron microscope (SEM) image for upconversion micro-rod with length of 2 µm and diameter of 150 nm; (b) the typical emission spectrum of NaYF4:Yb, Tm upconversion micro-rods; (c) fluorescence image of one micro-rod at 802 nm emission.

8.2.2 Optical characterisation system

Figure 8-2 shows the schematic diagram of our characterisation system. The excitation source is a linear polarised beam from a laser diode (BLP976-PAG900, Thorlabs). The output of the laser beam is collimated. Thus the beam is in paraxial regime that allows selecting the different polarisations after crossing a half wave plate (HWP) (AHWP05M-980, thorlabs) and a quarter wave plate (QWP 1) (AQWP05M-980, Thorlabs). The polarised excitation beam excites the sample (S) slide on a piezo nano-poistioning stage with three translation axis (MAX311D, Thorlabs) after being focused by an objective lens (60×, 0.75 NA, Edmund) (Ob1). The generated upconversion luminescence signal is collected by another identical objective lens (Ob2) placed exactly opposite to the Ob1. The fluorescence will then pass through a polariser for measuring linear polarisation component before being captured by camera (Lu165, Lumenera). To measure the elliptic component in the fluorescence signal, a quarter wave plate (QWP 2) is required before the polariser and the camera, as shown in Figure 8-2.

Accurate alignment of the emission optical path with respect to the excitation path is critical to this experiment. The system alignment for excitation and emission paths was carried out independently. The optics in the excitation part allows any linear polarisation based on tuning the half waveplate and the quarter waveplate: horizontal, diagonal, vertical, anti-diagonal, right circular and left circular polarised directions. The alignment of the optics for the emission collection was carried out in an auxiliary setup. The polariser is aligned just in front of the CCD. Its rotation allows analysing each polarization component. The quarter wave plate (QWP 2) is calibrated for each particular emission wavelength of interest. After calibration, the polariser and the quarter wave plate are added to the principal system.

This system without the quarter wave plate is used for measuring the linear component of the polarisation via the first two Stokes parameters. The quarter wave plate (QWP 2) allows measuring the third Stokes parameter - the ellipticity component of the polarisation. This complete set of measurements give us a full description quantitatively and qualitatively of the emission polarisations.

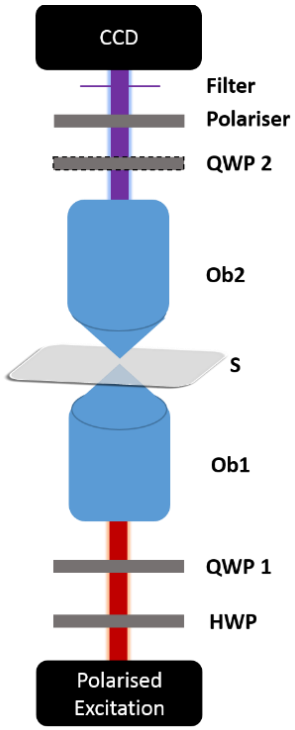

Figure 8-2. The schematic diagram of wide-field imaging system for polarisation characterisation. HWP: half waveplate at 980 nm; QWP 1: quarter waveplate at 980 nm; Ob1 and Ob2 are identical objective lens; S: sample; QWP2: quarter waveplate.

8.3 Results and Discussions

We used different polarised excitation beam to carry out the measurement, with preliminary result shown in Figure 8-3. It is worth to mention that the amplitude range in Figure 8-3 is from 0.90 to 1. Therefore, there is a slightly linear polarisation at 802 nm emission by measuring first two stokes parameters of emission from NaYF4: Yb30%, Tm2% micro-rod. To fully determine the polarisation, we need to carry out further measurement for the third Stokes parameter. Due to the slightly linear polarisation, if the sum of the three Stokes parameters is close to ±1, the emission would be almost circularly polarised; while if it is close to zero, this means the fluorescence signal is fully or almost depolarised.

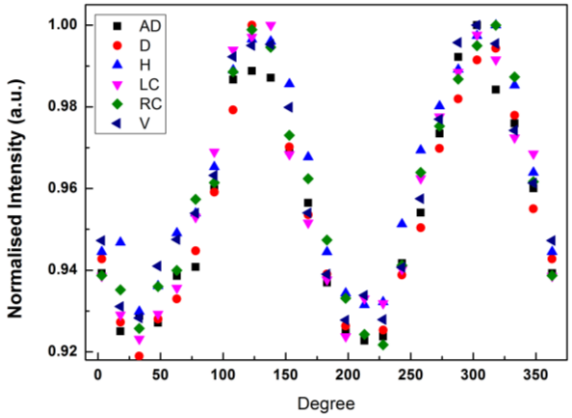

Figure 8-3. Emission polarisation at 802 nm under excitations with six polarised directions shown in Cartesian coordination. AD: anti-diagonal polarisation; D: diagonal polarisation; H; horizontal polarisation; LC: left circular polarisation; RC: right circular polarisation.

8.4 Conclusions

The slight linear polarised emission at 802 nm can be observed from the 30% Yb 2% Tm upconversion micro-rods. This may indicate an exciting optical phenomenon for the rare earth ions doped upconversion materials. More comprehensive characterisations are needed to explore the mechanisms driving such an interesting phenomenon. More evidence needs to be collected to reveal whether different doping concentrations induced different emission polarisation.

8.5 References

[1] Jiang T, Song W, Liu S, Qin W. Synthesis and upconversion luminescence properties study of NaYbF4:Tm3+ crystals with different dopant concentration. Journal of Fluorine Chemistry. 2012;140:70-5.
[2] Zhao J, Lu Z, Yin Y, McRae C, Piper JA, Dawes JM, et al. Upconversion luminescence with tunable lifetime in NaYF4:Yb,Er nanocrystals: role of nanocrystal size. Nanoscale. 2013;5:944-52.
[3] Zhou J, Chen G, Wu E, Bi G, Wu B, Teng Y, et al. Ultrasensitive polarized up-conversion of Tm(3+)-Yb3+ doped beta-NaYF4 single nanorod. Nano letters. 2013;13:2241-6.